N° d'ordre NNT : 2016LYSEI088

THESE de DOCTORAT DE L'UNIVERSITE DE LYON
opérée au sein de
l'INSA de Lyon
et délivrée en partenariat international avec
l'Université de Tohoku

Ecole Doctorale N° 162
Mécanique – Energétique – Génie Civil - Acoustique

Spécialité de doctorat : Génie Mécanique

Soutenue publiquement le 20/09/2016, par :
Paul Profizi

Development of a Numerical Model of Single Particle Impact with Adhesion for Simulation of the Cold Spray Process

---

Devant le jury composé de :

Tanguy, Anne	Professeur des Universités	INSA de Lyon	Présidente
Alart, Pierre	Professeur des Universités	Université de Montpellier	Rapporteur
Bergheau, Jean-Michel	Professeur des Universités	ENISE	Rapporteur
Feyel, Frédéric	Directeur de Recherche	Groupe SAFRAN	Examinateur
Combescure, Alain	Professeur des Universités	INSA de Lyon	Directeur de thèse
Ogawa, Kazuhiro	Professeur des Universités	Université de Tohoku	Co-directeur de thèse
Nelias, Daniel	Professeur des Universités	INSA de Lyon	Invité
Elguedj, Thomas	Professeur des Universités	INSA de Lyon	Invité

Département FEDORA – INSA Lyon - Ecoles Doctorales – Quinquennal 2016-2020

SIGLE	ECOLE DOCTORALE	NOM ET COORDONNEES DU RESPONSABLE
CHIMIE	**CHIMIE DE LYON** **http://www.edchimie-lyon.fr** Sec : Renée EL MELHEM Bat Blaise Pascal 3e etage secretariat@edchimie-lyon.fr Insa : R. GOURDON	M. Stéphane DANIELE Institut de Recherches sur la Catalyse et l'Environnement de Lyon IRCELYON-UMR 5256 Équipe CDFA 2 avenue Albert Einstein 69626 Villeurbanne cedex directeur@edchimie-lyon.fr
E.E.A.	**ELECTRONIQUE, ELECTROTECHNIQUE, AUTOMATIQUE** **http://edeea.ec-lyon.fr** Sec : M.C. HAVGOUDOUKIAN Ecole-Doctorale.eea@ec-lyon.fr	M. Gérard SCORLETTI Ecole Centrale de Lyon 36 avenue Guy de Collongue 69134 ECULLY Tél : 04.72.18 60.97 Fax : 04 78 43 37 17 Gerard.scorletti@ec-lyon.fr
E2M2	**EVOLUTION, ECOSYSTEME, MICROBIOLOGIE, MODELISATION** **http://e2m2.universite-lyon.fr** Sec : Safia AIT CHALAL Bat Darwin - UCB Lyon 1 04.72.43.28.91 Insa : H. CHARLES Safia.ait-chalal@univ-lyon1.fr	Mme Gudrun BORNETTE CNRS UMR 5023 LEHNA Université Claude Bernard Lyon 1 Bât Forel 43 bd du 11 novembre 1918 69622 VILLEURBANNE Cédex Tél : 06.07.53.89.13 e2m2@ univ-lyon1.fr
EDISS	**INTERDISCIPLINAIRE SCIENCES-SANTE** **http://www.ediss-lyon.fr** Sec : Safia AIT CHALAL Hôpital Louis Pradel - Bron 04 72 68 49 09 Insa : M. LAGARDE Safia.ait-chalal@univ-lyon1.fr	Mme Emmanuelle CANET-SOULAS INSERM U1060, CarMeN lab, Univ. Lyon 1 Bâtiment IMBL 11 avenue Jean Capelle INSA de Lyon 696621 Villeurbanne Tél : 04.72.68.49.09 Fax :04 72 68 49 16 Emmanuelle.canet@univ-lyon1.fr
INFOMATHS	**INFORMATIQUE ET MATHEMATIQUES** **http://infomaths.univ-lyon1.fr** Sec :Renée EL MELHEM Bat Blaise Pascal 3e etage infomaths@univ-lyon1.fr	Mme Sylvie CALABRETTO LIRIS – INSA de Lyon Bat Blaise Pascal 7 avenue Jean Capelle 69622 VILLEURBANNE Cedex Tél : 04.72. 43. 80. 46 Fax 04 72 43 16 87 Sylvie.calabretto@insa-lyon.fr
Matériaux	**MATERIAUX DE LYON** **http://ed34.universite-lyon.fr** Sec : M. LABOUNE PM : 71.70 –Fax : 87.12 Bat. Saint Exupéry Ed.materiaux@insa-lyon.fr	M. Jean-Yves BUFFIERE INSA de Lyon MATEIS Bâtiment Saint Exupéry 7 avenue Jean Capelle 69621 VILLEURBANNE Cedex Tél : 04.72.43 71.70 Fax 04 72 43 85 28 Ed.materiaux@insa-lyon.fr
MEGA	**MECANIQUE, ENERGETIQUE, GENIE CIVIL, ACOUSTIQUE** **http://mega.universite-lyon.fr** Sec : M. LABOUNE PM : 71.70 –Fax : 87.12 Bat. Saint Exupéry mega@insa-lyon.fr	M. Philippe BOISSE INSA de Lyon Laboratoire LAMCOS Bâtiment Jacquard 25 bis avenue Jean Capelle 69621 VILLEURBANNE Cedex Tél : 04.72 .43.71.70 Fax : 04 72 43 72 37 Philippe.boisse@insa-lyon.fr
ScSo	**ScSo*** **http://recherche.univ-lyon2.fr/scso/** Sec : Viviane POLSINELLI Brigitte DUBOIS Insa : J.Y. TOUSSAINT viviane.polsinelli@univ-lyon2.fr	Mme Isabelle VON BUELTZINGLOEWEN Université Lyon 2 86 rue Pasteur 69365 LYON Cedex 07 Tél : 04.78.77.23.86 Fax : 04.37.28.04.48

*ScSo : Histoire, Géographie, Aménagement, Urbanisme, Archéologie, Science politique, Sociologie, Anthropologie

Acknowledgments

I would first like to thank both my supervisors, without whom none of this would have been possible and for the incredible opportunity they gave me with this double degree.

I am honored to have been under the supervision of Prof. Alain Combescure, one of the bests in this field, his incredible experience and wisdom. His patience also, and relaxed way of handling problems throughout these three years and a half. I know I am not even near having learned everything I can from him. Thanks to him also for proposing this double degree to start with, right when I was simply looking for a funny simulation subject on which to spend my few months of Master research. I thank him for being the best fit I could have hoped for in a supervisor.

I can never thank enough Prof. Kazuhiro Ogawa for taking me in as a double degree student in his laboratory. This has been one of the best experiences of my life and I think I have learned a lot from my time here be it in terms of international culture or in terms of scientific knowledge. I have been able to expand my skills and interests in the best environment due to his patience and kindness. I just wish I had taken time to learn Japanese more intensively so as to take profit of his experience and my time in his laboratory even more.

I thank my examiners too, first Prof. Yu Fukunishi, Prof. Toshiyaki Hashida, Prof. Kazuo Hokkirigawa and Prof. Jean-Yves Cavaillé for the Japanese defense, for their patience and their understanding as well as informed input on my work during my many presentations. I know that without them the quality of my paper and presentation would not be even nearly the same. I thank them for the way these felt more like conversations between specialists rather than actual defenses. I hope I managed to answer all their concerns and fill all the gaps they pointed out to me.

For the French defense I must thank Prof. Anne Tanguy, who kindly accepted to be my jury's president, without whom I could not have defended my thesis, but also Dr. Frédéric Feyel for accepting to be one of my examiners (and for hiring me). Thanks also to Prof. Daniel Nelias and Prof. Thomas Elguedj for coming to the defense and for their numerous questions and comments. I particularly have to thank Prof. Pierre Alart and Prof. Jean-Michel Bergheau for reviewing this paper and giving me their hindsight on my research.

I also have to thank Prof. Jean-Yves Cavaillé for his help with my double degree and all he has done for me in the name of ELyT Lab which really feels like a big family, and the awesome ELyT Schools which are the reason why I started this double degree in the first place, and where I met some of my best Japanese friends. Thank you also for your counsel regarding my future career decisions.

Thanks to everyone at LaMCoS with me during my Master internship and first year of Ph.D., many of whom have now long set sail, thanks for the laughs, thanks for the help, thanks for the great atmosphere in that open-space, thank you to those who were still there when I came back to welcome me.

Thanks also to everyone at Ogawa lab, thanks for their help in making me feel at home and discover life in Japan and life in a Japanese laboratory. It really was an incredible journey. Thanks to Ichikawa sensei, for being forever helping, be it for experiments or administrative problems where my Japanese skills would prove lacking. Thanks also to Homma san, especially her patience and kind help whenever I would forget something or need help with my procedures.

Finally I would like to thank my family, my parents for supporting me and giving me all I needed in life to get where I am today, my brother and sister and my friends in France for

helping with my transition to a life on the other end of the world by staying forever available and listening to all my adventures, good or bad, with an ever comprehensive ear, a necessity especially during the few short times I got homesick.

To conclude, I wish everyone to be as lucky with their opportunities in life as I have been until now.

Summary

In the context of the Cold Spray process, a numerical model of a single particle impact is developed in the software Europlexus. The point of interest is the adhesion of the particle to the substrate, thus an adhesive interaction model is also created. The impact model uses the Smooth Particle Hydrodynamics and/or the Finite Elements methods, with a Johnson-Cook material law, commonly used for metals at high strain rates, which takes into account strain hardening, strain rate hardening and thermal softening. The adhesive interaction is based on a Griffith and Dugdale-Barenblatt cohesive model with energy dissipation and a limit on the cohesive stress. Using this model it is shown that in the case of fast dynamics and deformable bodies, not only the adhesion parameters but also the type of model has an influence on the results. The adhesion model is also, contrary to previous works, linked with an actual physical mechanism known to induce adhesion in Cold Spray: a shear stress instability at the interface. This is done by adding an activation criterion to the cohesive model. This criterion is defined as a local drop in yield strength on either element in contact (particle or substrate element). Only when this criterion is locally met are the cohesive stresses applied and cohesive energy dissipated. The result is the apparition of a critical velocity, under which adhesion cannot occur due to either not enough initial kinetic energy to create an instability at the interface, or not enough adhesive surface created to keep the particle from rebounding. For the model to localize and undergo shear banding/shear instability, a damage value is added to the material law. Two damage models are implemented, a Johnson-Cook ductile failure model, and a shear failure model. Simulations of shear banding in a dynamically compressed tilted cylinder show the ability of the obtained material model to initiate and propagate a shear instability. Following the damage model, an erosion criterion is also implemented in the cohesive model to remove the cohesive stresses from highly damaged parts of the adhesive surface. This results at very high impact speeds in a maximal velocity above which the interfacial material is too damaged to sustain enough adhesion and prevent the particle from rebounding. These two criteria combined are then tested in a parametric study at impact speeds ranging from 100 $m.s^{-1}$ to 1000 $m.s^{-1}$. A deposition behavior similar to the Cold Spray process is then observed, with a range of low velocities without any adhesion of the particle, then a critical speed initiating a velocity range of adhesion of the particle, and finally a maximum speed above which the interface is too damaged to sustain the adhesion. The impact model is thus validated for the simulation of the adhesion of a single particle during the Cold Spray process.
In complement to the numerical study, a set of experimental observations is carried out to better understand the actual microstructural dynamics and changes at the interface of 1 mm copper particles impacted by the Single Particle Impact Testing System on a copper substrate. Using hardness testing and Electron Backscatter methods, the local microstructure and mechanical properties around the interface are investigated. The hardness variation across impacted samples is compared to the results given by a simulation of the exact same impact cases, and conclusions are given on the validity of using the macroscopic Johnson-Cook model for modeling the behavior of a mesoscopic microstructure. The local effect of a shear band on the hardness is not observed. In a second time, using EBSD maps of the same indented samples, the local grain size on the indentations is measured and the link between grain size and hardness is made. It is shown that no clear effect is present and thus that the Johnson-Cook model is sufficient and no grain dynamics model is required for the impact model to be accurate.

In a last part, the elements and methodology for using the model in parametric studies are presented, as well as some directions and ideas to follow, and experiments to carry out in parallel to improve the current knowledge on the adhesion mechanism in Cold Spray, be it for metallic particles or other materials.

KEYWORDS fast dynamics, adhesion, cold spray, SPH, Johnson-Cook, shear banding, EBSD, microindentation

Résumé

Dans le cadre du procédé de revêtement de surface Cold Spray, un modèle numérique d'impact de particule sur substrat à haute vitesse est créé, ainsi qu'une nouvelle interaction adhésive, dans le logiciel de dynamique explicite du CEA Europlexus. Le modèle utilise des Éléments Finis et la méthode sans maillage SPH (Smoothed Particle Hydrodynamics) avec la loi matériau de Johnson-Cook, couramment utilisée pour modéliser les métaux à des vitesses de déformation élevées et prenant en compte le durcissement plastique, le durcissement en vitesse de déformation, et l'assouplissement thermique. L'interaction adhésive est basée sur les modèles de zone cohésive de Dugdale-Barenblatt et Griffith, avec une limite sur la contrainte cohésive et la rupture de l'adhésion dictée par l'énergie dissipée. L'étude de cette interaction dans le cas des corps déformables à haute vitesse de déformation montre que le type de modèle cohésif utilisé impacte directement et de façon très prononcée les résultats du calcul. L'interaction adhésive est ensuite liée à un mécanisme physique connu pour être la raison majeure de l'adhésion entre métaux lors du procédé Cold Spray : l'instabilité en cisaillement à l'interface de contact (présente dans la simulation grâce à une loi d'endommagement). Pour ce faire, un critère d'activation de l'adhésion est créé, basé sur une chute de la valeur locale de limite élastique du matériau. Ce critère permet de retrouver le phénomène de vitesse critique nécessaire pour l'adhésion de la particule lors du procédé. Un critère de rupture de l'adhésion supplémentaire est ajouté, basé sur la valeur de l'endommagement dans les éléments collés, et permet de retrouver le phénomène de vitesse maximale pour l'adhésion de la particule. Le modèle complet, construit sur des principes physiques, est ainsi capable de simuler le phénomène d'adhésion Cold Spray. Des tests de dureté et images EBSD sont aussi présentés et comparés aux résultats numériques afin de valider les différentes hyothèses du modèle.

Dans le premier chapitre, le procédé de Cold Spray est décrit, ainsi que différentes méthodes expérimentales disponibles étant utilisées dans l'étude des propriétés des revêtements et de leur microstructure. Il n'existe que peu d'études sur les méthodes numériques pour les impacts adhésifs à très grande vitesse, et de plus celles disponibles utilisent des codes commerciaux pour lesquels les limitations du code ou les modèles exacts utilisés sont mal connus. Par exemple, pour le traitement des contacts, les codes explicites utilisent généralement une méthode de pénalisation qui dissipe nécessairement une certaine quantité d'énergie qui n'est pas toujours contrôlée et qui pourtant peut être de l'ordre de grandeur de l'énergie cinétique restante dans la particule après rebond. C'est pourquoi certaines de ces simulations doivent être considérées avec précaution. Ce constat est aussi valable pour les modèles d'adhésion/de zones cohésives. Ainsi le premier et principal but de ce travail de recherche est de développer et d'étendre ces modèles dans le code explicite de dynamique rapide Europlexus pour les Eléments Finis et les Smoothed Hydrodynamics Particles, afin de quantifier la qualité de différents modèles numériques et matériaux et les comparer sur des cas pratiques pour valider l'approche. Il existe aussi un manque de connaissances sur les propriétés matériaux au niveau de l'interface entre le substrat et la particule impactée. Le second objectif de cette recherche est donc d'observer l'évolution de la microstructure et dureté à travers un échantillon de particules impactées par la méthode Cold Spray.

Le deuxième chapitre présente plus en détail les outils numériques introduits dans le contexte, afin de préciser la façon dont ils sont implémentés ou ont été modifiés. Sont décrits :

la géométrie 3D de boule impactant un substrat, les conditions limites absorbantes sur le substrat, et les paramètres matériau utilisés. Une section importante du chapitre présente le modèle d'adhésion, point novateur de cette thèse, avec le critère d'épuisement de l'énergie disponible, le critère d'activation de l'adhésion liant le phénomène d'adhésion à un phénomène physique choisit, et le critère d'érosion de l'adhésion qui profite de la variable d'endommagement du modèle matériau. Ce chapitre montre qu'à cause de la taille de maille en jeu, une représentation correcte des déformations à l'intérieur de la bande de cisaillement ne sont ni nécessaires ni bénéfiques pour le modèle global. Les lois entrant en jeu dans la simulation de bandes de cisaillement sont complexes et assez nouvelles. Le modèle développé ici ne détecte ainsi que le démarrage de la localisation avec une chute de la limite élastique, et n'est pas conçue pour recréer avec précision le comportement à l'intérieur de la bande du matériau ayant localisé.

Dans le troisième chapitre, les différentes implémentations décrites du chapitre deux sont validées grâce à des tests numériques : barre de Hopkinson, test de traction et simulation de localisation par bande de cisaillement. Un premier modèle d'impact sans adhésion est aussi étudié. Le comportement du modèle d'adhésion est caractérisé grâce à des tests de complexité croissante. Les conclusions obtenues sont les suivantes :

— L'implémentation de la loi de Johnson-Cook avec adoucissement thermique et son lien avec la méthode SPH est a été validée par la comparaison des résultats des simulations de barre de Hopkinson obtenus avec ceux venant de simulations EF avec et sans adoucissement thermique. Une comparaison des courbes de tests de traction avec celles obtenues sous Abaqus Explicit viennent aussi renforcer cette validation.
— Le code des lois d'endommagement et leur comportement ont été vérifiés en simulant une apparition de bande de cisaillement lors de la compression dynamique d'un cylindre incliné. Une validation quantitative n'a cependant pas été tentée au vue du nombre trop important de paramètres à régler/trouver pour pouvoir comparer aux résultats expérimentaux utilisant du Ti6Al4V. Le choix est donc fait d'utiliser au possible les lois et paramètres déjà utilisés dans les études de bande de cisaillement/localisation dans l'aluminium et le cuivre.
— Le modèle d'impact de particule a été créé et son comportement en terme de déformation en fonction du maillage, sans adhésion, est bon à des vitesses d'impact inférieures à environ 700 $m.s^{-1}$ mais ne converge plus voire ne finit pas le calcul pour des vitesses supérieures. Cet effet est en grande partie dû à l'utilisation d'une formulation Lagrangienne totale pour les SPH en solide. L'implémentation d'une formulation Lagrangienne Mise à jour a été démarrée mais non finie.
— Enfin le modèle d'adhésion a été validé à son tour sur différents cas dont un cas d'impact 1D analytique, un cas 2D élastique, un cas 3D élastique puis un cas 3D élasto-plastique. L'influence des paramètres du modèle (énergie surfacique et contrainte adhésive maximale) a été montrée. Le modèle est au final capable de simuler une zone d'adhésion contenue entre une vitesse minimale (critique) d'impact et une vitesse maximale (d'érosion), comme dans le procédé Cold Spray.

Dans le quatrième chapitre, le double objectif des mesures expérimentales est proposé : étudier le changement de microstructure dans la particule pour différentes vitesses d'impact, ainsi que son lien avec l'adhésion; obtenir des variations de dureté à travers les échantillons et les lier à la taille de grain locale, pour ainsi conclure quant à la nécessité d'utiliser un modèle de dynamique des grains. Ces essais sont effectués sur des particule de cuivre impactées sur des

substrats cuivre à 230 et 457 m.s^{-1}.

En termes de microstructure, il est clair que les particules subissent un raffinement de taille de grains, mais pas uniquement au niveau de l'interface particule-substrat. Près de cet interface cependant se crée une région de grain avec un niveau de déformation nul avec une vitesse d'impact croissante, probablement par un processus de recristallisation dynamique et de bande de cisaillement. Ces régions sont de l'ordre de dizaines de microns de large et situées en majorité sur les parties les plus cisaillées de la surface de contact, sur les côtés. Le lien entre ces zones à déformation nulle et une adhésion locale n'est cependant pas claire et mérite de plus amples investigations.

Des mesures de variation de dureté sont effectuées et montrent que la particule et le substrat subissent de l'écrouissage et un raffinement des grains près de l'interface. Ainsi le raffinement des grains et l'écrouissage sont probablement liés. Cependant ces mesures ne montrent pas de changement local au niveau de l'interface, ou bien celui-ci est perdu dans le bruit ou perdu entre les pas d'indentation. Des régions sans déformation peuvent pourtant être vues dans les images EBSD le long de l'interface pour les impacts à haute vitesse, d'une largeur d'une dizaine de microns. Ainsi, bien que certaines indentations se situent sur cette zone, celle-ci ne semble pas avoir d'impact important sur la dureté locale. Les simulations d'impact montrent une chute locale de la limite d'élasticité près de l'interface, qui si liée à la dureté, n'est pas observée expérimentalement. Ceci est expliqué par le fait que les simulations ne considèrent pas le refroidissement post-impact de la particule, ainsi le lien entre simulation et expérimentation nécessite un post-traitement des résultats de simulations prenant en compte le refroidissement. Malgré cela, la dépendance de la dureté avec la taille locale de grain peut être vue comme faible ou inexistante, ce qui permet de conclure sur la validité de la loi matériau de Johnson-Cook pour ce type de simulation. Les lois d'endommagement nécessitent cependant quelques réglages afin d'obtenir un comportement matériau proche de celui utilisé durant les expériences.

Dans le dernier chapitre, on démontre que le modèle créé est hautement polyvalent et montre un potentiel fort en tant qu'outil d'étude du phénomène d'adhésion pour les impacts à haute vitesse du Cold Spray et que l'objectif a ainsi été atteint. Cependant le modèle requiert de nombreux paramètres d'entrée, chacun devant être considéré attentivement et lié autant que possible à des résultats expérimentaux :

— Les paramètres numériques de la méthode EF ou SPH ont une influence directe sur les résultats. Une attention particulière doit être portée sur la mise en place d'une étude de convergence avant d'utiliser un ensemble de paramètres pour une étude paramètrique. L'influence de ces derniers peut aussi dépendre du type de loi matériau utilisée : ainsi ajouter un processus d'endommagement et de localisation renforce l'effet sur les résultats de la taille de maille choisie. Il serait ainsi utile de tout d'abord effectuer une série de tests simples sur une nouvelle loi matériau avant d'utiliser cette dernière dans le modèle d'impact.

— Les paramètres matériaux, ici ceux de la loi de Johnson-Cook et de la loi d'endommagement, nécessitent un choix éclairé et doivent provenir autant que possible de tests effectués sur les matériaux utilisés lors des impacts expérimentaux.

MOTS-CLÉS dynamique rapide, adhésion, cold spray, SPH, Johnson-Cook, bande de cisaillement, EBSD, microindentation

Contents

List of Figures

List of Tables

Chapter 1

Introduction

The first chapter aims at introducing all the basic and advanced concepts necessary for a good comprehension of the work done during this thesis. It is divided in four parts. First, the Cold Spray process will be introduced: the circumstances around its discovery and development, a description of the usual cold spray apparatus, its advantages and disadvantages compared to other coating processes, and finally the current knowledge and hypotheses surrounding the adhesion of the material after projection.
In a second time, the experimental tools used for investigation of the adhesion process will be reviewed and explained: the Single Particle Impact Testing System (SPITS) developed by Ogawa laboratory will be presented with its advantages over a standard Cold Spray spraying machine for studying single particle adhesion, then the Electron Backscatter Diffraction method and its use in the investigation of microstructure change and shear banding near the interface, and finally the Hardness Testing method for nanoindentations throughout the impacted specimens and its use in improving the numerical model.
In the third part the numerical basic concepts and tools involved in this work are introduced and described.
In the fourth and final part, a review will be given of the most important and most recent numerical studies of particle impact during Cold Spray, then the first models made with their use and limits, and finally the most recent models introducing a cohesive model which will be the most useful for comparison of the results of the model created here.

Contents

1.1 The Cold Spray process

The work done during this thesis is dedicated to creating a numerical model, with the development of all the necessary numerical tools, able to simulate the adhesion of a particle during the Cold Spray coating process. The next section is there to present what is exactly this so-called ”Cold Spray” process, where it comes from, why it is called ”cold”, why it is a versatile subject worth studying in regards to many issues such as power efficiency or durability in fields ranging from aeronautics to solar cells or 3D printing, and finally why a new numerical tools are required and useful in improving such a process.

1.1.1 Coating technologies

The Cold Spray technique is a coating process, by definition a method by which the surface of an object (the substrate), is modified by adding a new layer of material (same or different) onto it. It is different from other surface treatment processes such as shot-peening or chromising which only modify the characteristics of the already present surface [TIL 06].

Coating processes are used in various industrial fields such as power plants, aeronautics, aerospace, or automobiles, where high efficiency and energy loss reduction problems are of uttermost importance. The structural components are submitted to critical conditions in severe environments, high temperatures, pressures or corrosive fluids. These extreme conditions give birth to extreme aging mechanisms (fatigue, creep, oxidation, corrosion, erosion, abrasion... etc) that need to be reduced for higher product efficiency and longer lifetime. Reducing the frequency at which these critical components have to be repaired or changed can lead to economical and even ecological benefits.

One good example in which the Cold Spray technique is used is for the turbine blades in gas power plants, where the power conversion efficiency of the burning of the gas is linked to the maximum temperature at which it can function. The material used for turbine blades and other critical structural components is typically a Nickel alloy which can withstand very high temperatures. To allow for even higher working temperatures, Thermal Barrier Coatings consisting of a thin layer of ceramic material is applied to the surfaces of the blades. Thanks to the refractory properties of the ceramics coatings, the Nickel alloy can still resist while the surrounding gas temperature can be increased by around 200°C: the overall power plant efficiency is hence improved. Figure 1.1 shows a typical blade turbine with its ceramic coating and a temperature profile through the obtained structure. In this same manner the efficiency of an aircraft engine may be increased by 6-12% thereby saving up to $250,000 per year in fuel costs on a large aircraft engine. The economic inducement to find a successful coating is therefore high (see for instance www.dynacer.com).

1.1.2 Discovery and development

The Cold Spray process derives from experimental observations made in the 1980s in Russia at the Institute of Theoretical and Applied Mechanics of the Russian Academy of Sciences in Novosibirsk, by Dr. Anatolii Papyrin and his colleagues who were studying mixed gas flow dynamics and its interaction with immersed bodies in a wind tunnel at supersonic speeds, that is the effect of introducing dust and different materials as particles on air flow

(a)

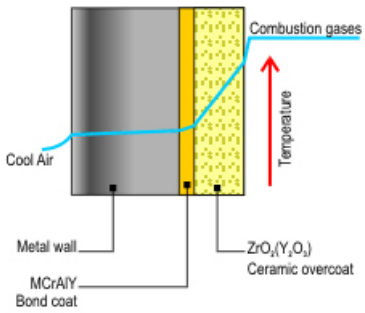

(b)

Figure 1.1: A gas turbine blade with a ceramic Thermal Barrier Coating (a) and the obtained temperature profile (b)

and surface interaction. The point was to investigate problems stemming from aeronautics and other fields where it was shown that the presence of particles in a flow would alter its behavior significantly compared to behaviors given by models created for pure flows. During their study they discovered that, for high enough wind velocities, certain types of particles would create a solid agglomerate on the impacted surface of the immersed object. A detailed summary of the research that led to this discovery is given in [PAP 07] and [CHA 07].

They quickly realized the importance of this finding and issued a US patent for the Cold Spray process in 1994, and a European patent in 1995, after having successfully deposited a wide range of pure metals, metal alloys, and composites on different substrate materials and studied and demonstrated the feasibility of this new process for various applications, which will be presented in the next sections. A consortium was then created in the US with major companies of the aircraft and others industries to establish the first US cold spray research group under the supervision of Dr. Papyrin to study and measure the properties of cold sprayed coatings. [PAP 07, CHA 07]

Nowadays many research centers around the world are equipped with a cold spray facility and are actively studying coating properties, to try and improve the process efficiency or find new applications. The cold spray process is considered part of the additive manufacturing field

and as such is seen as part of the most promising technologies of the next decades by major governing entities and companies, giving this research field a good support and innovation capability. An excellent resource for finding out more about the Cold Spray process and the different actors involved would be the Thermal Spray Society, the European Thermal Spray Association or the Japan Thermal Spray Society (see for instance http://etsa-thermal-spray.org/ and http://www.jtss.or.jp/).

1.1.3 Description of the process

The basic principle, as can be understood from the circumstances around its origin, is to use metal (or more recently ceramic or even polymer) powder particles to form a dense coating by means of ballistic impingement upon a suitable substrate. The powders usually range in size from 5 to 100μm (or even smaller for ceramics and nanometers for polymers) and are accelerated by injection into a high velocity stream of gas (usually air, nitrogen or helium). This high velocity gas stream is generated through the expansion of a pressurized, preheated gas through a converging-diverging nozzle. The pressurized gas is expanded to supersonic velocity, with an accompanying decrease in pressure and temperature. The powder particles, initially carried by a separate gas stream, are injected into the nozzle either prior to or downstream from the throat. The particles are then accelerated by the main nozzle gas flow and are impacted onto a substrate after exiting the nozzle (Figure 1.2). Upon impact, the solid particles deform and create a bond with the substrate in a process described in section 1.1.5. As the process continues, particles keep impacting the substrate and form bonds with previously deposited material, resulting in a build-up and an uniform coating with high bond strength and a porosity that can be very little or high depending on the desired coating properties.
The term 'cold spray' has first been used to describe this process due to the relatively low temperatures (typically 900 °K) of the expanded gas stream that exits the nozzle, but also describes the low temperatures that the particles subsequently undergo (around 600 °K). As will be shown in section 1.1.5, the time the particles spend in the heated carrier gas has indeed been shown not to be long enough for the particle to heat significantly, and post-impact microstructure observations have shown no sign of significant melting of the particles due to plastic deformations upon impact. The process is thus 'cold' only by comparison with other thermal spraying techniques such as HVOF or plasma spraying, but still remains the coldest in terms of temperatures involved and is the only one that does not melt the particles before impact. [HER 11]

Remark: A distinction is usually made between high and low pressure cold spray, which as the name indicates, work at different initial carrier gas pressures and use different kinds of gas, resulting in different attainable impact speeds and different material coating capabilities.

A comparison in terms of gas temperatures and particle velocities attained with cold spray compared to other conventional thermal spray techniques can be seen in Figure 1.3

1.1.4 Advantages and limits

The advantages of Cold Spray over other thermal coating processes are of course linked to the relatively low temperature (under melting temperature) to which the matter is subjected

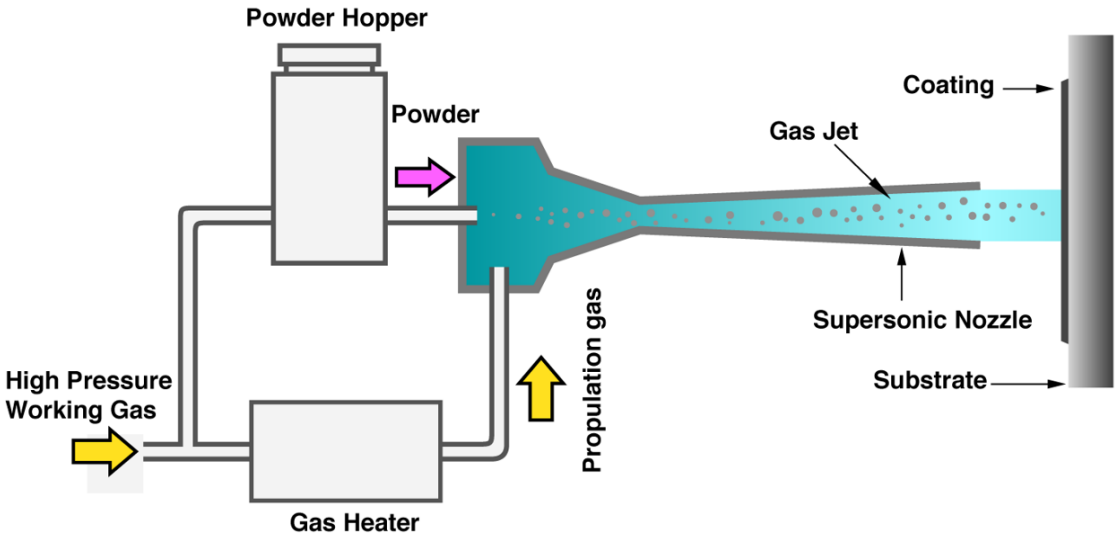

Figure 1.2: Schematic of the High Pressure Cold Spray apparatus

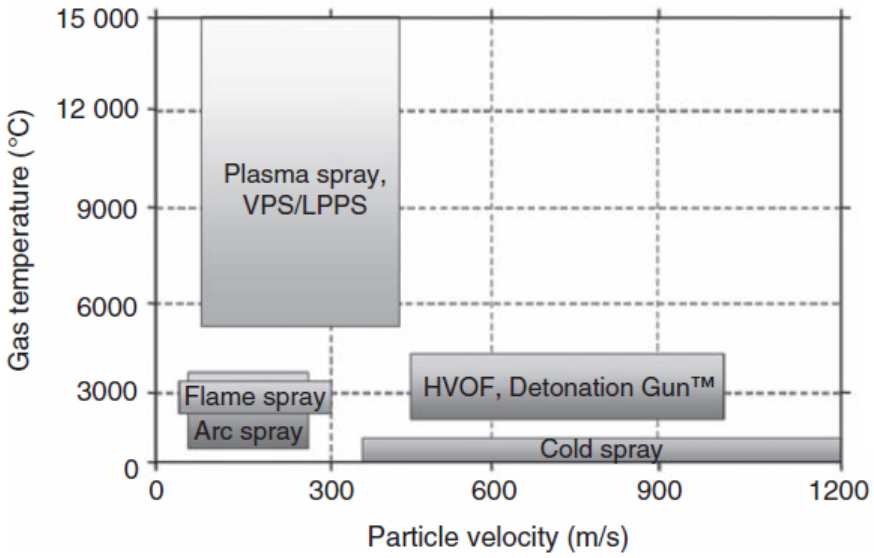

Figure 1.3: Comparison of approximate gas temperatures and particle velocities for cold spray and for conventional thermal spray techniques [ALK 98, ITO 16]

during the coating creation (see section 1.1.5).

As a result, the Cold Spray offers specific characteristics [CHA 07], such as:
- High deposition efficiencies, high deposition rates (up to some μ m per second), high coating densities, high bonding strengths, high coating conductivity, high corrosion resistance, high strength and hardness;
- Minimal surface preparation required and no or little masking, short standoff distance, no grit blast, no phase changes ([KIM 05] gives an example for WC-Co coatings), no oxidation, no grain growth (grain size is usually smaller after cold spray) (more details on that in chapter Experimental observations);
- Flexibility in substrate-coating selection;
- Minimum thermal input to the substrate, which can be useful for temperature sensitive materials;
- Possible compressive residual stresses (see for example [XIE 15]);
- Very-thick coatings can be obtained (up to several mm or cm), linking it to the 3D printing industry and direct fabrication of parts;
- Collection and re-use of projected but not bonded particles makes a powder utilization of 100% theoretically possible;
- Operational safety is increased because of the absence of high-temperature gas jets, radiation, and explosive gases (even though for use of nano-sized particles protective respiratory equipment is advised).

These different characteristics make the Cold Spray process an unique candidate for producing and repairing a wide range of industrial parts.

There are however of course some disadvantages to using this technique:
- Most cold-sprayed metallic coatings have a lower tensile strength and a lower ductility than the bulk material;
- The adhesive strength between a cold sprayed coating and a substrate tends to decrease with increasing coating thickness;
- The deposition mechanism of metallic particles is not yet completely understood;
- Pure ceramics and some alloys (such as work-hardening alloys) can not or have been until now very difficult to process. Several techniques have been specifically developed for these materials, such as mixing the ceramics powders with metal, or modifying the spraying process itself. In [LIU 15], a vacuum cold spray deposition process was used to spray ceramics and showed high deposition efficiencies.

However the lack of fundamental understanding of the bonding mechanisms of ceramic particles during coating deposition still limit this kind of method;
- Cold-sprayed coatings on ceramic substrates show only limited bond strength;
- High quality coatings are usually produced with expensive helium as a carrier gas in order to achieve the impact velocities necessary for deposition, diminishing its economic advantage over other processes;
- Spraying complex shapes and internal surfaces can prove difficult;

As a conclusion, the Cold Spray process is very well suited for many applications, but its

relative novelty and remaining limitations for some materials do not yet always make it the best economical or engineering option for industries, as is the case with any industrial process. As such, from an engineering point of view it is important to remember that this process will not become a miracle solution for every problems, and a mix of different solutions is usually the best choice.
Still, the point of this presentation of the process is to show why it has become a center of attention for industrials and research laboratories, and remains a promising technology which requires improvement.

1.1.5 The adhesion mechanism

The previous sections showed the benefits and limits of the Cold Spray process, and that one of its best advantages is its capacity to work under melting temperature. However, one of the biggest limitations yet stems from the lack in understanding, description and modeling of the physical processes leading to the adhesion of a particle during impact. The timescale and sizes involved during the impact are indeed of the order of micrometers and nanoseconds, which make it impossible with current technology to observe directly the dynamics involved. Research has thus concentrated on post-impact observations and analytical and numerical simulations, and has managed to give some useful information on the physics involved in particle adhesion. We will here see what are the different scientific facts that have been gathered and the different hypotheses put forward by the Cold Spray community to try and explain these observations.

This study was concentrated on the case of impact of metal on metal, which is yet the one for which the most information is available in the literature.

During the impact, due to the high speed, the kinetic energy is transformed by way of material deformation in elastic energy and then dissipated by plastic deformations. At the speeds and contact pressures involved, the bonding mechanisms involved are similar to those in explosive cladding or shock wave compaction as it is linked to the extremely high plastic deformations the interface is submitted to.
Several phenomena could be responsible for mechanical adhesion of two surfaces, such as atomic inter-diffusion or local melting of the interface resulting in a weld, but these have been shown not to play a significant role [KLI 05]:

Indeed the melting at the interface has been shown to be inexistent or really limited at the speeds involved, this by microstructure observations [GRU 04] and numerical simulations of the impact (see section 1.4.1). This means that the adhesion phenomenon is more likely to be a solid-state process.

As for atomic inter-diffusion, it has been shown that the metal-metal inter-diffusion coefficient at temperatures near the melting point is of the order of 10^{-15} to $10^{-13} m^2.s^{-1}$, and for a typical particle/substrate contact time of 40 ns with micron-sized particles as in Cold Spray, the atomic inter-diffusion distance is between 0.004 and 0.1 nm. Since this distance is only a fraction of the inter-atomic distance, atomic diffusion at the particle/substrate interface should be excluded as a dominant particle-substrate bonding mechanism [XIE 14].

This leaves the most widely accepted explanation for solid adhesion of metals in Cold Spray: an Adiabatic Shear Instability at the interface, or Shear Band [ASS 03, CHA 07], leading to solid adhesion of the contacting surfaces. Solid adhesion between two materials requires clean

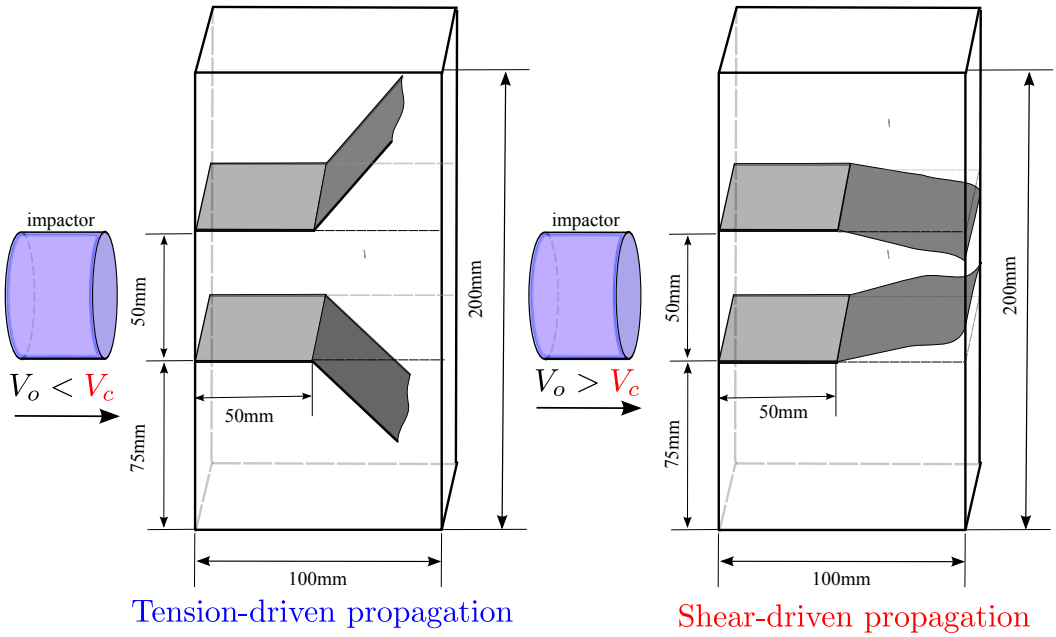

Figure 1.4: Kalthoff fast impact experiment [KAL 87]

conforming surfaces under high contact pressures. The high impact speed already procures very high contact pressures. As for the conforming, clean surfaces, they are obtained due to the afore-mentioned Adiabatic Stress Instability, or Shear Band, at the interface.

Adiabatic shear bands (ASB) are regions where very large shearing occurs as a result of intense dynamic loading of metals and alloys. As in the example of a particle impact, very high load rates and shear deformations develop from the beginning of the contact. These high plastic deformations lead to a heating of the contacting surfaces, heat which will try to dissipate in the rest of the material. The shear deformation however, occurs at a rate which is too high to allow the heat to be evacuated away from the sheared zone by conduction. Hence the generated heat leads to a localized process of intense thermal-softening, eventually counteracting the strain hardening and leading to loss in material strength, in its turn leading to more shear localization (see figure 1.6): this is typical of an instability mechanism. The formation of this type of intense shear localization is often a precursor to catastrophic failures in structural engineering. The well known Kalthoff experiments [KAL 87] (Figure 1.4) represent a typical shear band localization leading to failure: they occur only in the case of very fast impact of the projectile and they are highly localized [HAB 12] (Figure 1.5).

On the other hand these highly localized straining can also be used for fabrication purposes for example during conventional machining, metal-forming, cold spray, high velocity shaping [WRI 03], but the localization has then to be perfectly controlled and monitored.

This failure mechanism that structural engineers will try to avoid, is seen as beneficial in this case since it causes a jetting of the softened material out of the contacting zone (Figure 1.7). This jetting of the highly softened material removes the impurities previously present at the interface, and give the clean and conforming surfaces needed for solid adhesion. It has also been shown [GRU 03, CHA 05] that during the jetting, flow instabilities can result in local mixing of the two contacting materials, giving more surface for adhesion and some mechanical interlocking, thus increasing adhesive strength (Figure 1.8) 1.7). This process of adiabatic shear stress instability

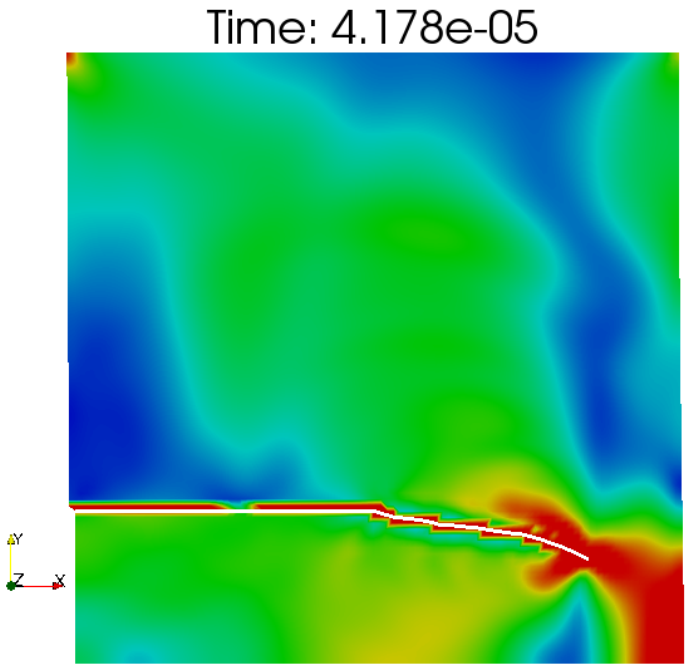

Figure 1.5: Shear bands formation for 32.41 m/s velocity [HAB 12]

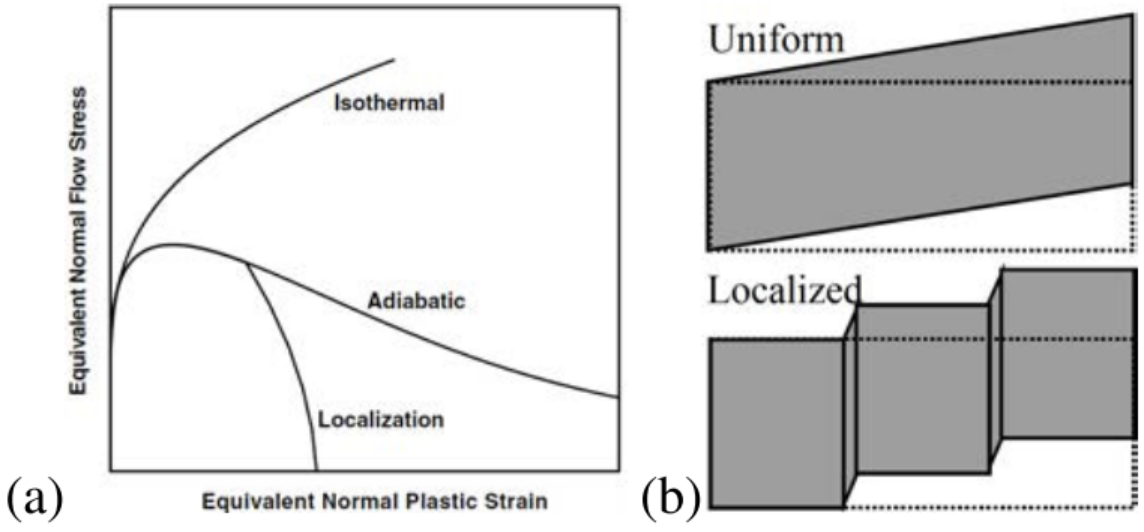

Figure 1.6: (a) Typical stress-strain curves in a normal strain hardening material (Isothermal), an adiabatically softened material (Adiabatic) and in a material undergoing an adiabatic shear localization (Localization); (b) schematics of the uniform and the localized simple shears [CHA 05].

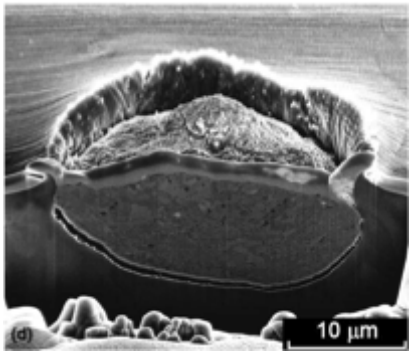

Figure 1.7: Jet formation in a Cu on Al impact at 500 m/s [XIE 14]

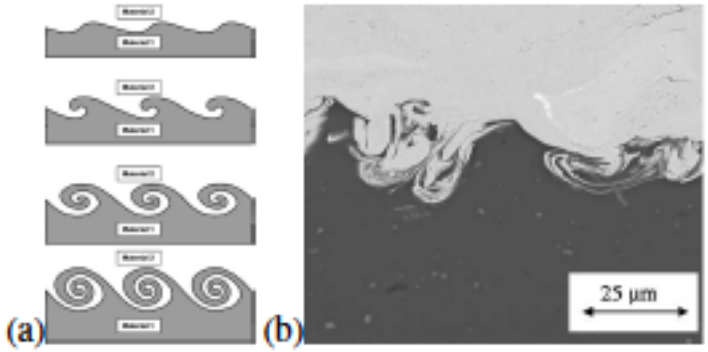

Figure 1.8: Material Mixing at interface [GRU 03, CHA 05]

leading to adhesion is the most studied and simulated (for instance see [XIE 14]), it has however been shown on cases of impact of copper particles on AL substrates that it does not explain all observed behaviors, as in the case of an impact of copper on aluminum [XIE 14], which should according to ASB criteria not lead to adhesion at the speed for which it is experimentally observed. The reason for adhesion in this case is that the hard particle penetrates deep enough in the soft material to be embedded in it.

As a conclusion, it can be said that according to current knowledge, the main mechanism behind adhesion of metals in the Cold Spray process in the formation of an Adiabatic Shear Band, or Adiabatic Shear Stress Instability, at the particle/substrate interface due to the high impact speed. This mechanism induces solid adhesion, some possible mixing and localized mechanical interlocking. In some specific cases however this is not enough to explain adhesion, and other mechanisms are to be expected to play a role, even if globally less significant.

1.2 Experimental investigation methods

The Cold Spray process is a relatively new technology and is extensively studied by different companies and laboratories around the world. The usual method is to spray a certain material on another chosen material and try a wide range of spraying parameters (gas pressure and temperature, preheating of the substrate... etc) to see if a coating is possible, and if it is, characterize its different wished for properties such as hardness, bonding strength, conductivity. The tools used to characterize the coatings are typically Scanning Electron Microscopes, X-Ray Diffraction, Indentors for hardness, Peeling or Scratching machines for bonding strength...
Of all of these, two methods have been used for this work: Electron Backscatter Diffraction (EBSD) and hardness testing by nanoindentation. This section gives quick descriptions of each of them with references, and examples of their use in existing papers on characterization of cold sprayed coatings or related topics.

1.2.1 Electron Backscatter Diffraction

Electron backscatter diffraction (EBSD) (see http://www.ebsd.com/) is based on the observation of patterns made by Kikuchi bands, bands created when submitting the surface of a specimen to an electron beam with a high inclination angle (typically 70 °). The electrons penetrate the surface and are reflected by the first few crystal planes, giving the reflected electrons trajectories that depend on the crystalline structure and orientation of the specimen where hit by the beam. Kikuchi lines or bands were first studied in 1928 by Kikuchi when observing diffraction of electrons by thin films of mica, but the pattern variations and dependence to tilting angle were obtained over 60 years ago [ALA 54]. Cameras were then used to observe the patterns more quickly and efficiently [DIN 92], and the development of rapid automated pattern recognition and analysis linked to the increase in computer capacity and control of the microscope beam enabled area scans of a sample surface to be obtained rapidly and automatically with commercially available systems. The EBSD acquisition hardware generally comprises a sensitive CCD camera, and an image processing system for pattern averaging and background subtraction. The software controls the data acquisition by scanning the beam over the sample in a raster, obtaining and solving the diffraction patterns at each point, and storing the data. Further software is then required to analyze, manipulate and display the data. The algorithms and parameters behind the analysis of the observed Kikuchi bands and their

translation to comprehensible orientation maps is beyond the scope of this presentation but can be found in [DIN 92, HUM 04].

The so-called "Orientation maps" or EBSD maps obtained give many different informations on the microstructure of the scanned area of the sample, all based on an analysis of the variations in local crystalline orientation. The typical orientation maps (OIM) obtained and associated results used in this work can be brought down to:

- The grain map, depicting the individual grains, as approximated by the analysis software by looking at the point-to-point change in orientation. If this change in crystalline orientation is above a given value (typically 15°), the measurement points will be seen as belonging to different grains.
- The Inverse Pole Figure map (IPF), which associates a color with each local orientation, as a function of crystalline orientations.
- The Image Quality (IQ) map, charting the quality of the observed EBSD pattern, with a low value indicating an unclear diffraction pattern due to wrong SEM or camera acquisition settings, a poor sample preparation, or simply a deformed crystal structure due to local plastic deformation and defects.
- The Confidence Index (CI) map, giving a value depicting how sure the software is that the given solution is the right material and orientation among all the geometrical possible solutions for the local observed pattern.
- The Kernel Average Misorientation map (KSAM), gives for each point the average of all the misorientations with neighboring points (the kernel). The size of this kernel can be modified and can have an impact on results. It is used to evaluate the levels of deformation (seen as changes in crystalline orientation in a grain).
- The Grain Average Misorientation map (GAM) gives for each grain the average of the fore-mentioned misorientation.
- The Grain Orientation Spread (GOS), gives the spread in orientation over a grain. It has been found useful to assess the level of plastic deformation inside a grain. (http://www.ebsd.com/)

The precision of these maps depend on the step-size between two measurement points and can go down to nanometers, but the scanned area is then reduced accordingly to keep the amount of data manageable. The quality of the results also crucially depends on the quality of the surface preparation, which has to be polished as flat as possible (typically ending with variations in tens of nanometers), and on the quality of the SEM measurement. Skill and experience are thus required to obtain meaningful results at the grain sizes involved here.

A review of a few studies using EBSD measurement, relevant to this work, can start with [HUM 04], which describes the viability of EBSD for characterization of fine-scale microstructures. The conclusion of the paper is that if using the newest available instrumentation and data analysis tools, grains of $0.1\mu m$ can be measured by EBSD with an acceptable error in grain size measurement. The fully automated data acquisition and analysis make it easier to get statistically significant data from thousands of grains compared with other techniques such as TEM (Transmission Electron Microscopy). It is already being extensively used to characterize sub-micrometer-grained materials produced by severe deformation processes, with its capacity to select specific areas of interest being particularly useful in materials with heterogeneous microstructures such as those produced by stir welding.

EBSD has also already been used to study the microstructure of Shear Bands. In [LIN 07],

hat-shaped specimens of a hot-rolled Interstitial Free (explain IF) steel were dynamically compressed in a split Hopkinson bar at high strain rates to induce the formation of adiabatic shear bands. Observations of the microstructure around the shear bands were made, and the article proposes the occurrence of Progressive subgrain misorientation recrystallization as the best explanation for the development of an ultrafine-grained structure. In [XUE 08], hat-shaped specimens of 304 stainless steel were also compressed using a split Hopkinson bar to create adiabatic shear bands. They observed with OIM maps a gradient in grain and subgrains orientation in the vicinity of the band, with a crystal structure increasingly oriented in the same direction as the shear band. Both these papers conclude on the fact that regular EBSD equipment is usually not suitable for the study of the internal microstructure of shear bands (TEM should be preferred), since it is highly deformed and extremely refined, but is sufficient for the study of the change in microstructure surrounding the band. The size of the shear band, the size of refined grains, and the misorientation gradient also all depend on the initial grain size and microstructure of the studied material.

Furthermore, several studies have been carried out on full coatings with EBSD equipment, such as in this study of the properties of copper coatings as function of particle impact velocity [JAK 15], which could for example be used for comparison with future full coating simulations. This paper concludes on the effect of spraying parameters on the microstructure by stating that for low cold spray velocities, shear straining and limited recrystallization lead to grain shapes which conform to the flow impact direction, whereas at higher temperatures (understand higher impact velocities) thermal softening leads to more efficient recrystallization and larger and more equiaxed grains. Observation of the same kind of behavior for particles sprayed by SPITS (see 1.2.3) is one the goals of the present research, as explained in section Electron Backscatter Diffraction observations.

The methodology further used in this thesis was inspired by several papers, such as [ZOU 09] with its use of EBSD for particle/particle interface dynamic recrystallization evaluation for nickel. Grain size refinement was observed with as-received particles (5-22 μm in diameter) having an average initial grain size of 1-5 μm, and ultrafine grains of 100-200 nm in size observed in the particle-particle boundaries after spraying. Its EBSD observations imply that the formation of the ultrafine grains is attributed to dynamic recrystallization in the process of deformation, rather than static recrystallization during the heating and cooling process, because the typical feature of the grains formed by static recrystallization is nearly strain/defect free, and therefore has a high EBSD pattern quality, whereas in their case the particle-particle boundaries showed a very low pattern quality. They also found that the most likely mechanism for that dynamic recrystallization is rotational (Figure 1.9), thanks to orientation profiles along grains showing a progressive change in rotation. The link is made with the rotational dynamic recrystallization model of Meyers and al. [AND 94, MIS 08] and previously presented [LIN 07]. It also stated that experiments of dynamic recrystallization suggest that the recrystallized grain size (D_R) may be estimated using a simple relationship [HUM 04]:

$$(\sigma/G).(D_R/b)^n = K \tag{1.1}$$

where σ is the applied stress, n and K are constants (0.8 and 15 respectively), b is the Burgers vector magnitude (0.255 nm for copper, 0.25 nm for nickel, 0.286 nm for aluminum), and G is the shear modulus (44.7 GPa for copper, 76 GPa for nickel, 25.5 GPa for aluminum). In the cold spray process, σ is the mean pressure during impact, which can be approximately calculated by [BOR 03]:

$$\sigma = 1/2\rho v^2 \tag{1.2}$$

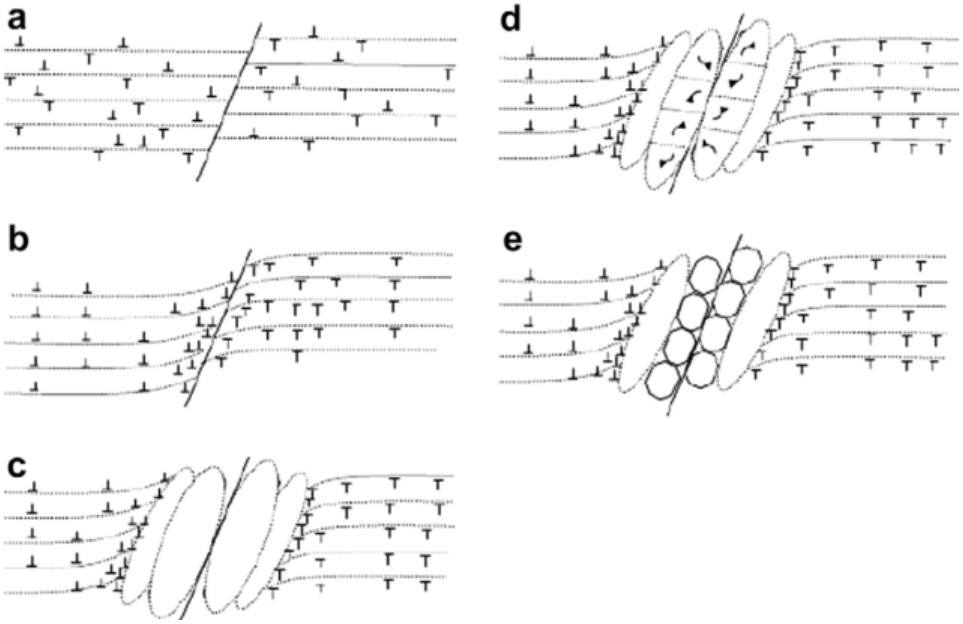

Figure 1.9: Schematic diagram showing the proposed mechanism of dynamic recrystallization in nickel particles during cold spraying: (a) uniform microstructure with low dislocation density before spraying; (b) dislocation propagation and progressive lattice rotation upon impact; (c) dislocation accumulation and formation of elongated subgrains to accommodate deformation; (d) elongated subgrains subdivided into equiaxed subgrains and rotated to accommodate further deformation; (e) formation of highly misoriented grains and equiaxed grains [ZOU 09].

where ρ is the density of materials (8960 kg.m^{-3} for copper, 8908 kg.m^{-3} for nickel, 2710 kg.m^{-3} for aluminum) and v is the average velocity of the particles at the onset of impact. They estimated this way a dynamic recrystallized grain size (D_R) of about 200 nm for v=750 m.s^{-1}, which is in agreement with their EBSD observations. The same approach will be used to assess the size of the observed microstructure as it should be a consequence of the same physical phenomenon. The detailed coupled SPH-FEM analysis will provide precise data on the local contact pressure loading : this can then be used across the contact surface to predict the grain size change according to equation (1.1).

Another source of inspiration (see also 1.2.2) is [ROK 15], where EBSD maps of cold sprayed 7075 Aluminum coatings were not as intensely used as in the previous paper, but rather served as microstructure maps on which the results of nano and micro hardness indentations were mapped. The influence of the position in the coating (depth) on the mechanical properties was investigated, concluding that particle interiors showed a larger grain size and higher dislocation density compared to particle-particle interface regions, that particle interface regions had a roughly 0.5 GPa higher nanohardness compared to particle interiors, attributed to local grain boundary strengthening caused by the dynamic recrystallization (thus hardness values should increase when approaching impact interface and smaller grain size regions.

A recent review on the evaluation of high velocity impact induced microstructure evolution during deposition of cold spray coatings can be found in[LUO 14] for further information on the different mechanisms found in different materials and their implications.

Quantitative evaluation of deformations by EBSD is also the center of recent research, but it is only yet viable in a statistical way on a huge homogeneous zone, and/or with previous tests for calibration at different strains and strain rates, for different known conditions, rendering it not applicable to our case [WIL 06, MIK 15, YOD 10, KAM 06].

As a conclusion, it can be said that the EBSD method has been shown to be a powerful tool to evaluate microstructural changes in cold sprayed coatings or even impacted single particles and in the study of shear bands, giving grain size information and a qualitative estimation of deformations. It has however yet a limited use in quantitative estimation of the deformation gradients. Thus the goal here will not be to get a quantitative information on the deformation gradients in an impacted sample, but, as explained in the experimental section, to give an estimate of the grain refinement in particles impacted by SPITS for different impact speeds, and assess the presence and eventually size of an adiabatic shear band at the particle-substrate interface, and its link with critical velocity, as well as the rotational dynamic recrystallization model.

1.2.2 Hardness testing - Micro indentation

One source for basics of hardness testing is [CHA 99, OLI 11]. It gives different methods, different indentation strategies and many practical indications. These indications are very important as hardness measurements are very sensitive to the experimentalist skill and have to be done with extreme care. In hardness testing, the applied forces should be in Newtons (N). In most papers however they are expressed in terms of kilogram force (kgf) (or just kilograms), gram force (gm) or pond (p), where 1 kgf = 1000 gf = 1000 p = 9.81 N. In this work, because of the software used, everything will be expressed in Newtons. For indentation tests, the hardness is evaluated by the amount of permanent deformation, or plastic flow of the material. This amount may be determined by measuring the depth of the indentation or by measuring the area. As the test material becomes softer, the depth of penetration becomes greater and the projected

area increases. For Microhardness testing, the applied load in the indenter is no greater than 1 kgf. As a rule, microhardness is evaluated by measuring the area of he indentation rather than the depth. For the Vickers test, a constant load of between 10gf and 1kgf (100mN to 10N) is commonly applied. The indentation load has to be applied correctly [GOL 11a]. There is a clear dependency of the result onto the applied load level, and the methodology described in [GOL 11a] is recommended.

One thing to consider is that during an indentation, the material undergoes plastic deformation all around the indented zone, resulting in a modification of material parameters around the indent, which can influence the results of further indentations carried out in the surrounding of the first.

This is why norms on spacing between indentations were created, and followed during the present work: ISO 6507-1 dictates a distance between each indentation superior to 3 times the indentation diameter for steel, alloys and copper, and a distance between each indentation of more than 6 times the indentation diameter for light metals such as aluminum.

The influence of the edge of the specimen also has to be considered, resulting in a minimum distance of 2.5 times the indentation diameter between the indentation center and the edge of the specimen for steel, alloys and copper. This value changes to 3 times the indentation diameter for light metals such as aluminum.

A second norm exists, ASTM E384, where one single less restrictive criterion is described as 2.5 times the indentation diameter between centers of indents or the center of an indent and the specimen edge, be it for steel, copper, aluminum or any metal.

It was decided during this work to follow the more restrictive ISO norm. The method has been experienced for indentation mapping on Ti coating [GOL 11b]

[ZOU 10a, ZOU 10b, ROK 15] have used hardness testing for evaluation of Cold Spray coatings.

In this research a nanoindentation method will be used. The effect of indentation size has to be considered [AJA 04]. There is a norm on distance between indents which leads to a minimal step size and density of points: this will then give a limit on the precision of measurements across the interface.

As a conclusion, hardness tests can be useful to assess variations in mechanical properties across a coating or impacted Cold Spray particles. It should be kept in mind however that comparison of results between tests is difficult or even meaningless due to the high influence of surface preparation, loading conditions, hardness machine, indenter, etc... In this study, quantitative conclusions will thus be avoided, despite a few general trends on relative hardness variation across each sample and its relation to the change in local grain size.

1.2.3 The Single Particle Impact Testing System

The previous sections described some the experimental methods used in the study of cold sprayed coatings, namely EBSD and hardness testing. The research made investigated the change in microstructure of the particles as well as hardness variations, in full coatings or in single splats. One limit of these techniques is that the impact speed of particles can only be approximated from empirical equations using spraying parameters because of the size of the particles used. The impact speed is however maybe the most important parameter required to link the experimental observations with numerical simulations of particle impact.
Ogawa laboratory saw an interest in developing an apparatus that could spray a single particle on a substrate and monitor the impacting velocity. The SPITS (Single Particle Impact Testing

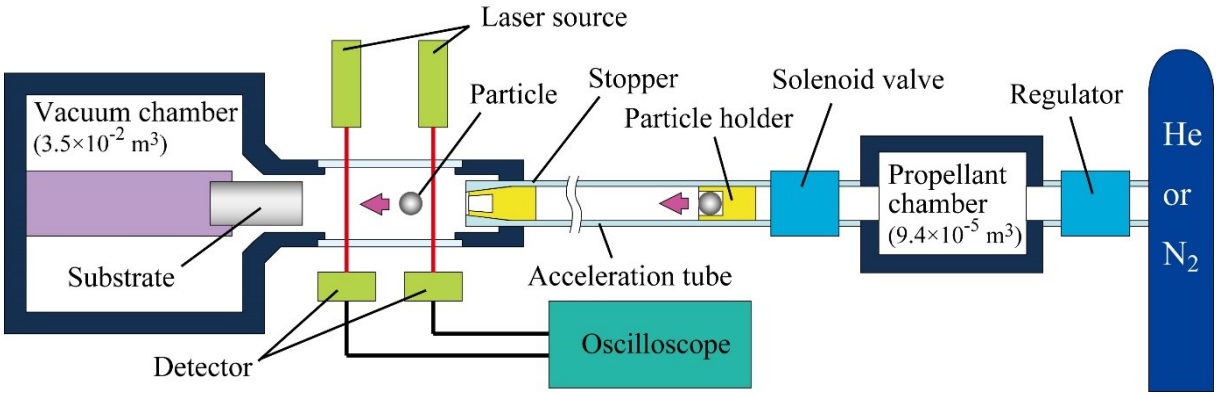

Figure 1.10: Diagram of the SPITS apparatus from [ITO 16]

System), created during the Ph.D. work of Dr. Kiyohiro Ito [ITO 16], aimed at creating an environment where a maximum of variables involved in the particle impact and adhesion are known. It consists in a modified one stage spraying system, using either Helium or Nitrogen as a carrier gas, accelerated through a nozzle, pushing a holder containing a particle of a diameter of 1 mm through a 2 m long acceleration tube. The holder is decelerated inside the acceleration tube, leaving only the particle to go hit the substrate. Two lasers at the exit of the tube measure the velocity of the particle. Impact speeds from $180 m.s^{-1}$ to $600 m.s^{-1}$ can be obtained. A diagram of the apparatus can be seen in Figure 1.10.

Using this equipment, the critical speed for several material couples was measured, and the samples of the impacted single particles were observed in terms of change in shape as a function of impact velocity. The well-defined impact conditions were used to reveal the factors involved in adhesion of pure aluminum and copper particles on five different substrate materials, and it was shown that the removability of the natural oxide films on the substrates is one of the dominant factors. This ”removability” of the natural oxide film for each substrate was measured by looking at oxygen concentration near the surface before and after different Argon sputtering times. Different substrate materials required different sputtering times to completely remove any trace of oxygen and so of oxide near the surface. The materials were then classified and this tendency was linked to the difference in critical velocity for bonding of a particle of a particular material. More than 20 times more energy was for example required to completely remove the oxide film on Al and Ti substrates than on Ni substrates. Another dominant factor was also found to be the amount of plastic deformation involved, making softer materials easier to successfully deposit.

In conclusion, the observations made using that equipment when assessing the dominant factors in particle bonding do agree quite well with the hypothesis of Shear Banding as a main driving force for adhesion. A softer material will more readily localize and the material jet will more easily clean the oxides from the contact area if the oxide film requires less energy to remove.

It was although observed that in a few cases (as in a copper particle impacting aluminum), mechanical trapping of the particle inside the substrate due to high penetration was the main reason for adhesion, meaning that if the main driving force, the adiabatic instability is not the only cause for adhesion, and rather a combination of processes should be used to model correctly all of the possibilities.

Because of all the available data and impacted samples, of the precisely known impact

speeds, and of the size of the particles making it easier to observe and perform indentations onto, it was decided for this study to use a few of the available samples to conduct an small experimental plan described in experimental chapter.

1.3 Numerical concepts

As previously explained, the experimental study of the particle adhesion mechanism during Cold Spray is possible but difficult, due to the time and spatial scales involved. A good way of testing and verifying hypotheses is too conduct numerical simulations of the problem. In the following section, several important numerical concepts used during this thesis work are presented, so the reader can get a general idea of the makings of an adequate numerical model and its possible limitations.

1.3.1 Explicit dynamics formulation

At the center of most numerical simulations is the notion of discretization. We shall consider here the evolution of a mechanical system with time. Knowing the state of the system for one instant and the equations of time evolution of the parameters we shall now describe the numerical method used to approximate time evolution of the mechanical state.

All the numerical time integrations developed in this work are based on the explicit Newmark time integrator (Newmark scheme ($\beta = 0, \gamma = 0.5$) [HUG 12]). It will be quickly presented here. If the solution of a system is entirely known at a point t_n in time (the displacement vector $[U_n]$, the speed vector $[V_n]$ and the acceleration vector $[A_n]$) of the problem is known, then the equilibrium at the next time step t_{n+1} is:

$$\underline{\underline{M}}^{n+1}\overrightarrow{A}^{n+1} = \vec{F}_{ext}^{n+1} - \vec{F}_{int}^{n+1} + \vec{F}_{link}^{n+1} + \vec{F}_{contact}^{n+1} \tag{1.3}$$

where $\vec{F}_{ext}^{n+1}$ is the external force vector, $\vec{F}_{int}^{n+1}$ the internal force, $\vec{F}_{link}^{n+1}$ the permanent link forces and $\vec{F}_{contact}^{n+1}$ the contact forces if they exist. Let us observe that all quantities on the right hand side are evaluated at the end of the times step (index n+1). Equation 1.3 gives the acceleration vector at the end of the time step. The mass matrix M is invariant diagonal and computed only once, at the beginning of the computation. The explicit computations hence do not need any matrix storage and solver except for the contact solving when Lagrange multipliers are used. Let us observe that the internal, link and contact forces have to be known at time n+1. This is the case if one uses an explicit time integrator because the new configuration is already known at the start of time step t_{n+1} since the displacements are given by:

$$\vec{U}^{n+1} = \vec{U}^{n} + \Delta t \vec{V}^{n+1/2} \tag{1.4}$$

in which the velocities at the mid time step $\vec{V}^{n+1/2}$ are given by:

$$\vec{V}^{n+1/2} = \vec{V}^{n} + \frac{\Delta t}{2}\vec{A}^{n} \tag{1.5}$$

The computation of the contact forces is a bit more complex but the chosen method shall be explained later. This method is conditionally stable: the time step must be small enough to respect the Courant's condition so that the time integration is stable. This time step depends on the numerical method chosen for spatial discretization. For finite elements it is well known for

example that the compressive waves should not cross more than one element during one time step.

A different choice ($\beta = 0.25$ and $\gamma = 0.5$) of the parameters of the Newmark scheme would have resulted in methods called "implicit", in which a new state is first guessed, the error made is computed, and a new guess is made, leading to an iterative process of trial and error evaluation. These two methods have well known different advantages and disadvantages: they will not be discussed here. The explicit formulation is generally best suited and most used for transient problems with discontinuities (contacts) and large strains. [BEL 13]

1.3.2 Spatial Discretization

The spatial discretization of the problem is the way in which the system is discretized spatially, in parts for which the behavior can be estimated by known mathematical equations.

1.3.2.1 The Finite Elements method

An excellent reference on Finite Elements is [BEL 13]. The Finite Element method is a weak discretization method which ensures the equilibrium equations in a weak form. The body is decomposed in "simple" elements in which the kinematic fields (displacements, velocities, and accelerations) are assumed to vary between the nodes with simple a priori chosen functions. Once these kinematic field are known on can compute the strains and hence the stresses anywhere within the elements. The process requires a spatial integration scheme generally based on a Gauss rule. This rule uses the values of the integrand on a finite number of points within the element. The process relies essentially on an element by element process and on an assembly step which permits to solve the global equilibrium equation. The mass matrix M of the system is assembled from the element ones. The internal forces are computed element by element and then summed on the nodes to get the global internal load (Equation (1.6).

$$\vec{f}_{int}^{elem} = \int_{V_{n+1}^{elem}} \mathbf{B}^{\mathbf{T}} \sigma_{n+1} dx \tag{1.6}$$

where V_{n+1}^{elem} is the volume of the element at the end of the time step, $\mathbf{B}^{\mathbf{T}}$ the transpose of the discretized divergence operator expressed on the final deformed geometry n+1 and σ_{n+1} the Cauchy stress at the end of the time step. All these quantities can be simply evaluated once the displacements are known at the end of the current time step.

1.3.2.2 The SPH method

The SPH method has been introduced by Monaghan in the late seventies [GIN 77]. It has been used for many years and applied for the development of many physical models with very different topologies [P. 01, JOH 96, JOH 02, MON 09]. This type of method relies on a strong formulation of equilibrium equations: hence the boundary conditions are not easy to enforce. It is a meshless approach which involves only nodes (the SPH points). A good review of these meshless methods can be found in [LIU 05] or in [IDE 03]. The strains at each point are calculated from the displacement field of all the points located in a sphere B of radius h centered on the point (h being, of course, greater than the standard distance between two points). Any function $f(\mathbf{x})$ of the coordinate $\mathbf{x}$ is represented by the following integral:

$$f(\mathbf{x}) \simeq \int_B f(\mathbf{x}') W((\mathbf{x} - \mathbf{x}'), h) d\mathbf{x}' \tag{1.7}$$

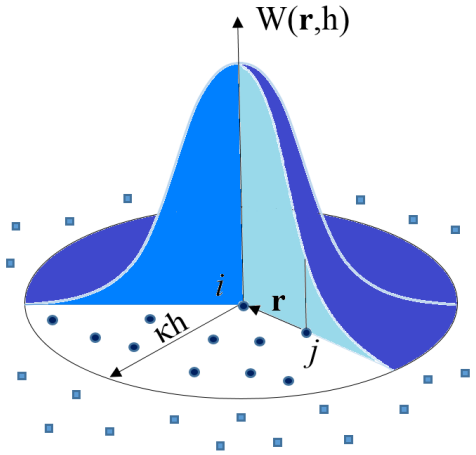

Figure 1.11: The kernel function W

in which $W(\mathbf{x},h)$ is the kernel function which imitates the Dirac function (δ). In order to guarantee a consistent solution, W must possess the following properties:

- Normalization

$$\int_B W((\mathbf{x}-\mathbf{x}'),h)d\mathbf{x}' = 1 \tag{1.8}$$

- Symmetry

$$W((\mathbf{x}-\mathbf{x}'),h) = W((\mathbf{x}'-\mathbf{x}),h)\nabla[W((\mathbf{x}-\mathbf{x}'),h)] = \nabla[W((\mathbf{x}'-\mathbf{x}),h)] \tag{1.9}$$

- Dirac limit

$$\lim_{h\to 0} W((\mathbf{x}-\mathbf{x}'),h) = \delta(\mathbf{x}-\mathbf{x}') \tag{1.10}$$

- Compact support

$$W((\mathbf{x}),h) = 1 \; h > \kappa h \tag{1.11}$$

A typical kernel function is shown in Figure 1.11. The equation chosen to represent this function is:

$$w(r_{ij},h) = C\begin{cases} \frac{3}{2}\left[\frac{2}{3} - \left(\frac{r_{ij}}{h}\right)^2 + \frac{1}{2}\left(\frac{r_{ij}}{h}\right)^3\right] & \text{if } 0 \le \frac{r_{ij}}{h} \le 1 \\ \frac{1}{4}\left[2 - \frac{r_{ij}}{h}\right]^3 & \text{if } 1 < \frac{r_{ij}}{h} < 2 \\ 0 \;\; \text{otherwise} \end{cases} \tag{1.12}$$

with $r_{ij} = \|\mathbf{x_i} - \mathbf{x_j}\|$ and $C = 1/\pi h^3$ in 3D. Let us consider SPH node i and approximate the integral in Equation (1.7) numerically using the quadrature formula given in Equation (1.13):

$$f(\mathbf{x_i}) = \Sigma_{j\in B_i} f(\mathbf{x_j}) W(\mathbf{x_i} - \mathbf{x_j})\omega_j \tag{1.13}$$

In Equation (1.13), B_i is the sphere of radius $h = \kappa h$ centered on i. j is a node belonging to this sphere. Point j is associated with an elementary volume ω_j. The gradients of a function are approximated in a similar way:

$$\nabla f(\mathbf{x_i}) = \Sigma_{j\in B_i} f(\mathbf{x_j}) \nabla W(\mathbf{x_i} - \mathbf{x_j})\omega_j \tag{1.14}$$

This type of formulation was first developed for the simulation of large displacements of fluids and gases [MON 09]. The material models, in general, had no memory effects and all the physical models studied were highly dissipative. The first applications to solids showed that the previous formalism led to artificial fracture mechanisms, even in the case of a linear elastic material with no damage model. This defect, known as tensile instability, was corrected [VIG 09] by introducing an appropriate renormalization of the kernel functions, a total Lagrangian formulation of the solid mechanics equations and some artificial viscosity. In addition, a series of auxiliary points (stress points, positioned like Gauss points) helps eliminate the hourglass modes which can appear in some cases for solid mechanics. When one chooses this stress point type of implementation, the SPH nodes are associated with the kinematic variables while the stress points are associated with the static variables (along with the associated history variables). We will not give any further details on the formulation, which can be found, e.g., in [LIU 10, MAU 06] for volume formulations and in [CAL 11, CAL 13, MAU 08] for shell formulations. In this research, we chose the initial normalized 3D formulation (without stress points). This choice is justified by the existence of very large plastic strains which occur in the simulations, which dissipate enough energy to prevent hourglass modes from developing. For the fluid formulation one can refer to [VID 07] where the updated Lagrangian form is very well described as well as the corrected total Lagrangian formulation.

1.3.3 Contact

This section is devoted to a brief description of formulations for contact in explicit dynamics. We will first describe two methods for detecting the contact situations and then explain one method to determine the contact forces.

1.3.3.1 The Pinball contact detection method

The contact method used between two bodies modeled with SPH is the Pinball method [BEL 91], which consists in surrounding each material point at which contact is likely to occur by a small sphere whose radius is chosen as the same as the radius associated to the SPH node. The method then only consists in checking for inter-penetration of these spheres to detect contact. The Pinball method is slightly more complicated for FE as the Pinball radius has to be computed in function of the volume or characteristic volume of the element. The contact forces also have to be distributed on the different nodes of the element, whereas for SPH there is only one node per element.

During the computation, simple geometrical checks are performed on the distance between two Pinballs, by comparing it to the sum of the Pinball radii. If penetration occurs then the penetration value is given to the contact forces algorithm, which will here use Lagrangian multipliers as seen in 1.3.3.3.

1.3.3.2 The Sliding Surfaces contact detection method

When simulating the impact of a hard on soft material, or soft on hard material, or simply for comparison purposes, a faster solution is to model one or both of the contacting bodies with FE rather than SPH. In this case, a more efficient and precise contact algorithm can be used, the Sliding Surfaces technique [HAL 85, BEN 90]. This method consists as choosing a slave body

which will be represented by its points (the SPH body is then the logical choice if there is one), and choosing a master body of which the external faces will be stored (the need for defined faces with normals is why this technique is not used for SPH contacting SPH).

During the computation, expensive geometrical penetration tests are performed between slave points and master faces, and if penetration occurs, the contact is stored and may be solved once more by the Lagrangian multipliers method.

1.3.3.3 Contact force prediction : the Lagrange multipliers approach

There are at least two strategies to compute the contact forces. The easiest and most used one is the penalty method which consists in adding two opposite forces acting against the interpenetration which are proportional to this interpenetration and to a contact stiffness. These methods are easy to implement and efficient because they act locally between a pair of nodes but they have two drawbacks: the contact stiffness is a parameter of the model and it is not always easy to tune and some energy is consumed during the contact. The will not be used in this work. The Lagrange Multiplier approach has no parameter but implies a small system resolution at each time step: it is hence more complicated to implement efficiently but it is energy conserving. Contact forces will here always be computed by means of the Lagrange multiplier technique. When two surfaces are glued or come in contact, a contact energy term is added to the energy of the system. Let $S_{contact}$ be the contact surface and $\lambda_{contact}$ be the associated surface loads over the contact interface, and let V_{n_1} and V_{n_2} be the normal velocities of the two colliding objects. The expression of the contact energy is:

$$W_{contact} = \int_{S_{contact}} \underline{\lambda_{contact}}^T (\underline{V_{n_1}} - \underline{V_{n_2}}) dS \tag{1.15}$$

For SPH bodies, this equation is to be discretized based on the SPH points located on the external surfaces of the objects, which consist simply of series of SPH points. With this very simple approach, contacts between surfaces boil down to contacts between points. This approach simplifies the definition of the contact normal along which repulsive forces have to be applied, which becomes the direction between the two SPH/Pinball centers.

For FE bodies, however, when using the Sliding Surfaces contact detection algorithm, the contact is between a slave point and a master element surface, which gives a system to be solved on all degrees of freedom involved in the general contact, since a node of a master surface might belong to several elements under contact. The repulsive force are then distributed along the different nodes of the master surface, with a normal to contact taken as the normal to the surface.

The forces are computed to ensure no further penetration of the contacting bodies. In the case without friction, the condition is written:

$$W_{contact} = \int_{S_{contact}} \lambda_{contact} . (\underline{V_1} - \underline{V_2}) \underline{n_{12}} dS \tag{1.16}$$

where $\underline{n_{12}}$ is the normal to the contact, oriented from body 1 to body 2 with $\underline{V_1}$ and $\underline{V_2}$ as the speeds of the nodes associated to Pinballs 1 and 2 for a Pinball contact. In case of master slave context let us define 1 as the master index, then $\underline{n_{12}}$ is oriented outward from the master surface and normal to the master surface at the contact point. The contact energy has to be integrated in time for each time step to ensure proper energy balance. It is easy for permanent links.

$$W_{link}^{n->n+1} = \int_{t_n}^{t_{n+1}} dt \int_{S_{link}} \lambda_{link} . (\underline{V_1} - \underline{V_2}) \underline{n_{12}} dS \tag{1.17}$$

The most simple and usual approximation is to consider that the Lagrange multiplier is a constant function of time in each time step. Equation 1.17 then becomes:

$$W_{link}^{n->n+1} = \lambda_{link} \int_{t_n}^{t_{n+1}} dt(\int_{S_{link}} (\underline{V_1} - \underline{V_2}) \underline{n_{12}} dS) \tag{1.18}$$

The surface S as well as the normal is changing with time. The most common simplification is to choose these values to be constant in time and to take their value at the end of the step. Equation 1.18 then becomes:

$$W_{link}^{n->n+1} = \Delta t \lambda_{link} \int_{S_{link}^{n+1}} (\underline{V_1^{n+1}} - \underline{V_2^{n+1}}) \underline{n_{12}^{n+1}} dS \tag{1.19}$$

The presence of non permanent contacts changes the equations to be solved for equilibrium for the time-step. The contact condition is now unilateral and writes (in absence of friction):

$$(\underline{V_1} - \underline{V_2}).\underline{n_{12}} \leq 0. \tag{1.20}$$

In this case of unilateral contact, the use of equation 1.19 leads to highly oscillating responses. The usual practice is to replace the velocities at time (n+1) by the velocities at time $(n + \frac{3}{2})$ [CAL 11]. Equation 1.19 is replaced by:

$$W_{contact}^{n->n+1} = \Delta t \lambda_{contact} \int_{S_{contact}^{n+1}} (\underline{V_1^{n+\frac{3}{2}}} - \underline{V_2^{n+\frac{3}{2}}}) \underline{n_{12}^{n+1}} dS \tag{1.21}$$

The link forces are related to the Lagrange multipliers $\lambda_{contact}$ or λ_{link} by the following relation:

$$\vec{F}_{link} = \mathbf{C}^T \lambda_{link} \tag{1.22}$$

where C is a matrix containing the components of $\underline{n_{12}}$. The same relation applies to the contact forces. The λ (link or contact) are the solution of the following linear system:

$$\mathbf{H}\lambda = w \tag{1.23}$$

where the matrix H and the right hand side w write:

$$\mathbf{H} = \mathbf{C}.\mathbf{M}-1.\mathbf{C}T \tag{1.24}$$

$$w = \frac{2}{(dt_n + dt_{n+1}} \mathbf{C}(V_{n+\frac{1}{2}} - \mathbf{M}-1(F_{ext} - F_{int}) \tag{1.25}$$

If the links do not change in time the matrix C does not change with time and hence the matrix H can be inverted only once in the computation. If the problem has contacts and large displacements the matrix H has to be often changed and hence inverted. Nevertheless if the number of λ is reasonable this is not a severe drawback. A specific method is used to detect a rebound occurring between time step n and n+1, and prevent application of the repulsive contact force as they become unnecessary. The algorithm computes the virtual speeds the nodes would undergo if no contact forces were applied and tests the new n+1 virtual configuration for penetration.

1.3.4 Material laws

There are many material models which can be used in fast impacts. The Mie Gruneisen model is one of the best known models for hyper velocity impacts. We shall limit ourselves to a very classical model valid for fast dynamics, the Johnson Cook's one.

1.3.4.1 The Johnson-Cook material law

The material model used in all the simulations is based on the Johnson-Cook's generic model. The material deforms plastically with the stress deviator. The integration of the constitutive relation is carried out using the radial recovery technique. The strain hardening of the material is a function of the logarithm of the equivalent plastic strain rate and of a certain power of the temperature:

$$\sigma_Y = (A + Bp^N)(1 + CLog\left[\frac{\dot{p}}{\dot{p}_0}\right])\left[1. - (\frac{T - T_0}{T_{melt} - T_0})^M\right] \tag{1.26}$$

where p denotes the accumulated plastic strain and T the temperature. This model has 8 material parameters: A, B, C, N, M, $\dot{p_0}$ (the reference strain rate), T_0 (the reference temperature) and T_{melt} (the melting point in ^oK). Adiabatic heating was assumed because the impact phenomena being considered are very fast and there is not enough time for heat conduction to take place during the simulation. We chose to convert 90% of the variation in plastic work into an increase in temperature. This ratio is commonly chosen because a portion of the plastic work is consumed in mechanisms other than temperature increase, but other ratios can be used. Thus, this model enables thermal softening to occur in the case of large plastic strains.

1.3.4.2 Material failure laws

A large number of failure models is available. A good review can be seen in [LEM 90, LEM 06]. These classical laws must be adapted to the specific case of Cold Spray where the material experiences very fast strain rates and extreme temperatures. As seen in [YIL 11, YIL 14], a failure law is useful or even necessary to correctly predict the deformation of the particle and particularly the material instability present at the contact interface. These criteria will be extended for the prediction of adhesion.

1.4 Numerical studies of particle impact

The Cold Spray technique is relatively new, but old enough for a lot of numerical studies to have already been performed, to try and help answer the main remaining questions regarding what happens to the particle or particles during impact. This section will present a few of the most relevant previous studies, the limitations they faced, and finally how the model developed here is part of a very few recent studies trying to address some of these limitations.

1.4.1 First particle impact models

The first type of models created with the intent of simulating Cold Spray aim at correctly predicting the dynamics of the impact of a particle on a substrate, a non-trivial problem since it involves both contacts and extreme deformations. This is the logical first step, to verify the viability of the numerical models for predicting the behavior of different materials in a specific context. They are thus limited to the comparison of final deformations with the ones obtained in experiments, and observe the occurrence of phenomena such as jetting for metals. The variation of temperature, yield stress and plastic flow are monitored near the contacting surfaces to detect

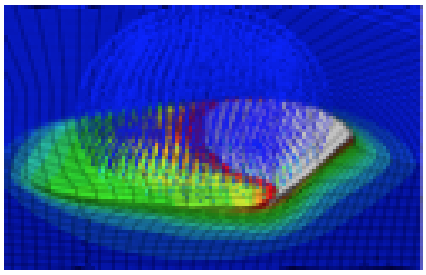

Figure 1.12: SPH simulation of 45 ° inclined impact at 400m/s of 25μm Al particle on CU substrate [XIE 14]

possible melting, and find what specific mechanisms arise upon getting to the critical speed. The specific notion of adhesion is however absent from the model.

In such papers, as in [GRU 03] for metals, the critical velocity is linked to the formation of a particle/substrate interfacial jet composed of both the particle material and the substrate material. These simulations show that high contact pressures and good interfacial jetting, linked with larger kinetic energies for the particle, appear to be the major factors controlling the strength of interfacial bonding and the deposition efficiency. It also provides an hypothesis of interfacial instability due to differing viscosities resulting in interfacial roll-ups and vortices, promoting interfacial bonding by increasing the contact area and giving rise to material mixing and mechanical interlocking as already explained in the particle adhesion mechanism section. It also shows that in cases such as copper on aluminum, the high penetration of the particle in the substrate may lead to a rivet-like mechanism and embedding of the particle, reducing the critical particle velocity.

Already limitations arise for this kind of approach: as explained in the paper itself, the parameters for the material laws used are not always available and limit the capacity in predicting correctly the smallest details of the material behavior, for example, as seen in 1.3.4.2 and even if that particular paper does not use material failure laws, it is very difficult to predict a post-failure behavior with high precision. Furthermore, a FE method with adaptive remeshing is used, prone to its own disadvantages like computation cost and influence of remeshing parameters.

These kinds of studies are however useful in giving an insight on the dynamics to be expected and are the best tool for testing material laws for uncommon materials such as ceramics or polymers.

More recent studies of this kind focus on improving the numerical method used [LI 09], improving the material laws used (for example by introducing material failure [YIL 11]), or even modify the particle impact basic model by introducing new concepts such as accounting for the presence of an oxide film to study its influence on deformation behavior [LI 07]. Other studies have looked at the influence of the angle of impact and shown its influence on several key characteristics of a Cold Spray coating like obtained density and residual stresses[LI 10, XIE 14].

While the results and conclusions made in the above works are interesting and can give quality information on impact dynamics and variations in material parameters during impact, and can help identify that the mechanism responsible for adhesion is most likely an adiabatic instability at the interface with material jetting, they however do not actively study the adhesion mechanism as such and give a way for engineers to quantitatively predict the critical speed.

1.4.2 Finding a criterion for adhesion

Following studies have thus been aimed at defining a criterion for adhesion, and design equations predicting the value of the critical speed.

One of the first attempts gave a formula for critical speed [ASS 03], where critical speed is a function of density, melting temperature, initial temperature and ultimate strength, with coefficients derived from sets of numerical simulations. These give for a given material the variation of critical velocity as a function of small variations in the parameters. Simulations of impacts indicate the impact speed at which adiabatic instability occurs at the interface, and based on the hypothesis that adiabatic instability is the reason for adhesion in Cold Spray, this speed can be said to be the critical speed for adhesion of the particle. This approach is limited by several constraints: it is based on the assumption that SSI is the main cause for adhesion (however that assumption is common to most models), the model is assumed to be sufficiently precise for detection of an SSI, and no adhesive forces were used in the contact [SCH 09]. This means that there is no size effect, which is contradicted by the experiments.

1.4.3 Introducing a cohesive model

The drawback of all the models introduced in the last section, however precise and efficient they might be, is that they do not account for the actual adhesion we are trying to study here. Indeed, they can reproduce with great detail the variations of shape, penetration, even defect density and so on in the impacted particle and even multiple impacted particles, and might give an idea of the likelihood of adhesion, but they do not actually implement adhesive forces at the particle-substrate or particle-particle interface during the computation.
It is only recently that researchers started using models for the actual adhesive behavior at the interface. The works which remain rather preliminary can be seen in [YIL 14, MAN 11].

In [MAN 11], a 2D SPH model of the impact is used, and a Dugdale-Barenblatt cohesive model is put between the particle and the substrate (see figure 1.13). This resulted in a velocity window for adhesion, surrounded by two rebound zones, showing that this cohesive model is able to reproduce the Cold Spray critical and maximum velocities. It used however an SPH interaction to model the contact, which is not the most precise and reliable contact method, it also started adhesion as soon as contact occurred, giving an adhesive surface equal to the contact surface even at very low speeds, and the energy dissipated, although stated as a parameter, had apparently no influence on the cohesive algorithm, and was only used to compare the rebound energy and the adhesive energy at final computational time.

In [YIL 14], a 3D model made with Abaqus is used with a cohesive zone based on a critical cohesive stress where adhesion breaks. The influence of this maximum cohesive stress on the critical velocity is studied, and the link with the experimental cohesive strength is made. Conclusions a minimal surface adhesive energy are drawn from the rebound energy and the remaining adhesive surface. Once again the adhesive surface is initially equal to the surface in contact. The strong point of this article is its use of damage and the quality of the deformations obtained.

A paper worth mentioning is [CHA 02] in which several cohesive models are presented in the context of metal-ceramics cohesive interfaces.

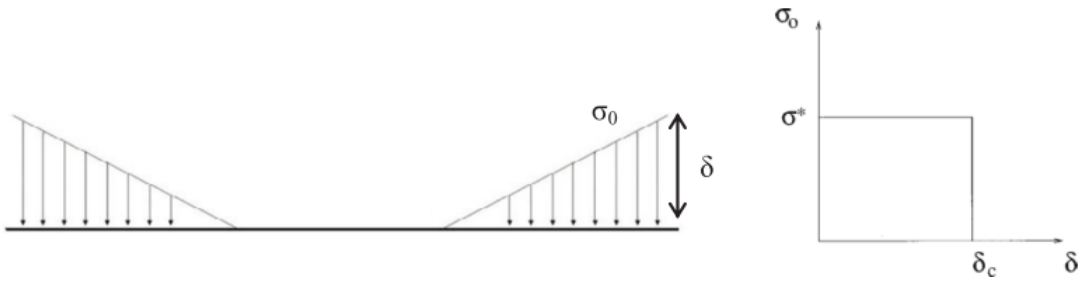

Figure 1.13: Cohesive model used in [MAN 11]

1.4.4 Adhesive models - Cohesive zones

As in fracture mechanics, the adhesion energy is characterized by a surface adhesion energy denoted G_C. The Griffith model consists in keeping the link active as long as the energy which is dissipated in opening the contact remains less than $G_C S_{adhes}$ (where S_{adhes} is the adhesion surface between the two points in contact). For a pair of SPH points in contact with radii R_1 and R_2 respectively, this adhesion surface is determined by Equation (1.27):

$$S_{adhes} = \frac{\pi}{2}(R_1^2 + R_2^2) \tag{1.27}$$

The Barenblatt model introduces a cohesive stress σ_c which is active only during opening. In this case, there is an associated critical opening gap_c beyond which the cohesive forces cease to be active. These three quantities are related according to the following equation:

$$G_C = \sigma_c \, gap_c \tag{1.28}$$

These models shall be used and studied in the case of dynamic impact with adhesion.

1.5 Novelty of this research

In this chapter, the Cold Spray process has been described, as well as different experimental methods available which have been used to investigate coating properties and microstructure. There has been but little research on the numerical methods for fast impact adhesion, as all the papers in the literature use commercial codes not knowing the inner limitations of the codes nor what are exactly the models within the codes. For instance the contact treatment in dynamic explicit codes are based on penalization which necessarily dissipates some unknown amount of energy, which may be of the order of magnitude of the energy remaining for the rebound after impact. Hence these simulations should be considered with some care. The same holds for the adhesion models. Thus the first and main goal of this research work is to develop and extend these models in a research FEM-SPH fast dynamic code (Europlexus) to quantify the quality of the different numerical and material models and compare them with in house experiments to validate the whole approach. There is also a lack of knowledge of the material properties across the interface between the substrate and the impact particulate. The second aim of this research work is then to give an observation of the evolution of microstructure and hardness across the interface of a single impacted particle after its deposition by Cold Spray.

Chapter 2

Presentation of the model

In this second chapter, the model developed is presented.
The different numerical tools described in the previous chapter
and used here are detailed while giving the geometry, boundary
conditions, and material parameters used.
The most important section explains the adhesive model
developed in details.

Contents

2.1 Particle impact model

In this section the impact model developed and used is presented, acting both as a presentation of the tools used and as a summary of the numerical developments undertaken during this work (except for the adhesion model which is described in the second part of this chapter).

2.1.1 Geometry

The geometry of the model is chosen as 3D, with the particle a ball of radius R_b initially above a cuboid substrate of lengths L_s and height H_s, as shown in figure 2.1.

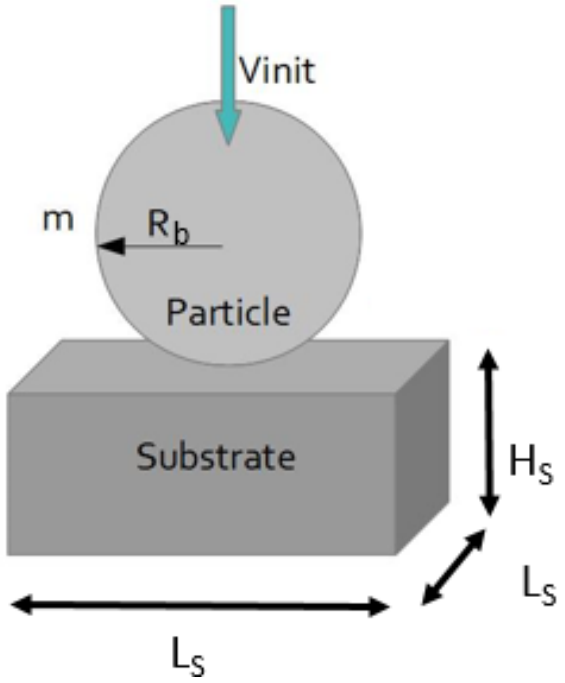

Figure 2.1: Geometry of the impact model

2.1.2 Boundary conditions

The ball is given an initial velocity V_{init}.

To simulate the effect of a semi-infinite substrate (and remove the influence of rebounding pressure waves as the substrate is usually some magnitudes larger than the particle) without making it ten times larger than necessary, elastic impedances have also been used on every side but the impacted one to absorb pressure waves normal to the boundary.

These impedances consist, in the case of finite elements, of a layer of boundary elements with no thickness which will apply a fictitious external pressure $p = -\rho c v_n$, where ρ is the density of the material at the boundary (i.e. the substrate material), c is the speed of sound and v_n is the normal component of local velocity at the boundary. The "internal" forces due to the absorbing boundary are finally computed by spatial integration of a modified pressure $\pi = (p + p_{old})/2$, where p_{old} is the value of π at the previous time integration step. It is worth mentioning that since the speed of sound c is declared as a constant, care in dimensioning the mesh should still be taken for effects modifying its local value (as thermal softening and damage

stiffness degradation), not to reach these boundaries, resulting in a minimal size of the substrate chosen as a little more than the plasticized zone for each impact case.

In the case of SPH elements, absorbing boundaries elements are not available, so the absorbing conditions were directly implemented as a new set of forces computed during the SPH routine after internal forces, with the local resulting force on a given SPH node defined by (2.1), where ρ is the material density, E is the Young modulus, $\vec{v_i}$ is the node speed vector, $\vec{n}$ is the local normal to the boundary (defined by the user as either $\vec{X}$, $\vec{Y}$, $\vec{Z}$, or a combination of them), and $\pi {R_{SPH}}^2$ is the surface area defined by the SPH radius. This last part is the weak point of that implementation since the resulting total surface on which the absorbing condition is effective is smaller than the real one due to the voids in the SPH lattice. This issue has not yet been answered, however absorbing conditions are applied to the three first layers of the substrate on each concerned side, in the same manner as boundary conditions are usually declared on three layers for solid SPH [MAU 12], resulting in an actual absorbing surface area actually larger than necessary.

$$f_{imp}(i) = -\sqrt{\rho/E}\pi {R_{SPH}}^2 \vec{v_i}.\vec{n} \tag{2.1}$$

2.1.3 Mesh

The SPH method is used to mesh the most deformable part, or both parts if those are of similar hardness. The lattice is hexagonal compact and the SPH particle radius is R_{SPH}, fixed throughout the computation and the same for all SPH elements due to current software limitations. A basic artificial viscosity described in [MON 09] is used to stabilize the dynamic response of the impact load, with a linear coefficient $C_{LINE} = 0.8$ and a quadratic coefficient $C_{QUAD} = 4$. The kernel function used is the common cubic spline M_4 kernel (see figure 1.11 in Chapter 1 section 1.3.2.2) , with an search radius of four times the SPH particle radius and a number of neighbors limited to 50. The time step value is limited by the formula of Lattanzio (2.2) with a stability coefficient C_{stab} of 0.5 (even though a value of 0.05 was found to be necessary for the material algorithm to get more than one step in the elastic regime at the beginning of impact, which would be better in terms of accuracy but is not a problem here), and v being the element speed and c the local sound speed.

$$\Delta t_{max} = 0.3 C_{stab}(2R_{SPH}/\sqrt{v+c^2}) \tag{2.2}$$

Because solids are simulated, the SPH method used is Total Lagrangian to avoid tensile instability, with a search for neighbors only at the initial step. To ensure consistency, a normalization matrix from [BEL 00] is used to get first-order completeness.

Due to the computational cost of the Finite Element method being a lot lower than the SPH method, whenever possible the hardest and less deformed part is meshed with FE, especially the substrate due to its large size and contribution to simulation time consumption compared to the particle, with cubic elements containing one Gauss point of size L_{FE}.

For more details, a description of the model can also be found in [PRO 16] and more explanations on the SPH method for solids can be found in [PRO 16, LIU 10, MAU 12].

2.1.4 Material

All material parameters found in this section are summarized in Appendix B.

Table 2.1: Material parameters used for aluminum

Properties	Parameter	Value	Unit
General	Density, ρ	2710	$kg.m^{-3}$
	Specific heat, k	904	$J.kg^{-1}.K^{-1}$
	Melting temperature, T_{melt}	916	K
	Inelastic heat fraction	0.9	
Elastic	Elastic modulus	70.9	GPa
	Poisson's ratio	0.3	
Plastic (Johnson-Cook plasticity model)	A, B, C, n, M	148.4, 345.5, 0.001, 0.183, 0.895	MPa, MPa
	Ref. strain rate, $\dot{\varepsilon}^p_{ref}$	1	s^{-1}
	Ref. temperature, T_{ref}	300	K

2.1.4.1 Johnson-Cook law

The material law used for both parts is the common Johnson-Cook law (1.26), which gives the yield stress (σ_Y) by taking into account equivalent plastic strain (ε^p) hardening, equivalent plastic strain-rate ($\dot{\varepsilon}^p$) hardening and thermal softening. Here adiabatic heating is considered with 90% of plastic work converted in heat using , with T the temperature, W^{plast} the plastic work, and k the thermal capacity. This ratio is commonly chosen because a portion of the plastic work is consumed in mechanisms other than temperature increase, but other ratios can be used.

The Johnson-Cook material parameters used in the simulations for aluminum and copper are shown in Table 2.1 and Table 2.2.

Once the thermal softening was implemented, the first high speed impact tests showed that the initial radial-return algorithm in the software was often not able to converge on a solution. To remedy to this problem, another algorithm was coded which would be used in the case of a material with thermal softening, one which converges less quickly but simpler and more robust, that is a simple dichotomy method (or bisection method, or interval halving method, or binary search method).

The dichotomy method consists in halving the predicted solution domain and finding in which half the solution lies. This half is then cut in two again and the same process is repeated until the size of the solution domain is within the desired error margin. In our case, one starts with the plastic strain increment predicted by the elastic equations, then first test a lower increment value and a higher increment value to know which direction to go. Boundaries are thus obtain between which the true increment solution has to be. This domain is then cut in half and the same process is repeated, narrowing the domain boundaries at each step, and eventually getting the boundaries within the desired error margin where the middle value is used as solution.

Table 2.2: Material parameters used for copper

Properties	Parameter	Value	Unit
General	Density, ρ	8960	$kg.m^{-3}$
	Specific heat, k	1356	$J.kg^{-1}.K^{-1}$
	Melting temperature, T_{melt}	385	K
	Inelastic heat fraction	0.9	
Elastic	Elastic modulus	124	GPa
	Poisson's ratio	0.34	
Plastic (Johnson-Cook plasticity model)	A, B, C, n, M	90, 292, 0.025, 0.31, 1.09	MPa, MPa
	Ref. strain rate, $\dot{\varepsilon}^{p}_{ref}$	1	s^{-1}
	Ref. temperature, T_{ref}	300	K

2.1.4.2 Damage law in the bulk

Damage softening is added by multiplying equation (1.26) by $(1-D)$, where D is a local material damage parameter, so as to get better localization at the interface and account for element erosion, which has been shown to improve general behavior [YIL 11]. This damage parameter also influences the stiffness of the material by degrading the Young modulus.

An initial random damage value of up to 0.001 is first distributed throughout the materials to ease localization.

For stability purposes, a maximum allowed damage softening coefficient D_{max} is set to 90% with element erosion for finite elements, but no element deletion for SPH elements. Indeed, since the SPH algorithm is total Lagrangian, deleting elements proved to make the normalization matrix computation unstable. The choice was thus made to account for erosion only for finite elements. This choice can be seen as non logical since the point of using SPH is usually to easily account for high deformations and element deletion, but actually deleting surface SPH elements while they are undergoing adhesive forces and studying its influence on the final result and the instabilities it creates due to the use of a total Lagrangian method has so far been postponed to future improvements which will probably first include the change for an updated Lagrangian method. Instead, damage has an influence on the adhesion by implementing an adhesion erosion criterion, as described in a following section.

A shear failure criterion based on shear band localization is used for damage initiation in aluminum, based on the definition and the parameters given in the "Progressive failure analysis of thin-wall aluminum extrusion under quasi-static and dynamic loads" example available on the online Abaqus manual (link in Appendix B). These parameters, obtained from series of experiments, are used to compute equivalent plastic strains for which shear instability occurs, as a function of strain and strain-rate.

This shear failure criterion was implemented in the following manner, with values used for aluminum:

First, the Shear stress ratio θ_S is computed using equation 2.3, with a maximum possible

value $\theta_S^+ = 2.2$ and a minimum possible value $\theta_S^- = 1.42$, where $K_S = 0.3$ is a material constant, P is the pressure, σ_{eq} is the equivalent Von Mises stress, and σ_{12}, etc are the shear stresses.

$$\theta_S = \frac{K_S P + \sigma_{eq}}{Max(\sigma_{12}, \sigma_{13}, \sigma_{23})} \tag{2.3}$$

Then, using this ratio, we can compute the shear failure strains for defined strain rate limits. At the lowest defined strain rate $\dot{\varepsilon}_S^- = 0.001 s^{-1}$, the corresponding shear failure strain ε_S^- is computed with the third order polynomial equation 2.4, with $A^- = 4.391$, $B^- = -19.66$, $C^- = 29.38$ and $D^- = -14.39$, values found by fitting the data from Abaqus with a third order polynomial equation. The same process is used to find ε_S^+ at $\dot{\varepsilon}_S^+ = 250 s^{-1}$, with parameters $A^+ = 0.0$, $B^+ = 0.951$, $C^+ = -2.848$ and $D^+ = 2.466$.

$$\varepsilon_S^- = A^- {\theta_S}^3 + B^- {\theta_S}^2 + C^- \theta_S + D^- \tag{2.4}$$

From these two boundaries we can now compute the shear failure strain for the actual strain rate $\dot{\varepsilon}$, if the latter is contained in the strain rate interval used, using equation 2.5.

$$\varepsilon_S = \varepsilon_S^- + (\varepsilon_S^+ - \varepsilon_S^-)(\frac{\dot{\varepsilon} - \dot{\varepsilon}_S^-}{\dot{\varepsilon}_S^+ - \dot{\varepsilon}_S^-}) \tag{2.5}$$

For copper, because no available shear failure parameters were found, the Johnson-Cook ductile failure initiation criterion (equation 2.6 giving the failure initiation strain ε_f) is used, with values first taken from [YIL 11] but fitted to better represent the material used in the experiments (see Appendix B).

$$\varepsilon_f = (D_1 + D_2 exp(D_3 \frac{\sigma_{mean}}{\sigma_{eq}}))(1 + D_4 ln\left[\frac{\dot{\varepsilon}_p}{\dot{\varepsilon}_0}\right])\left[1 + D_5(\frac{T - T_0}{T_{melt} - T_0})^M\right] \tag{2.6}$$

The evolution of the damage parameter D once failure has been initiated is defined by a damage evolution law. That law can be a function of equivalent plastic strain (or deformation to limit the mesh dependency), implemented during this work using equation 2.7, where $\dot{\varepsilon}^p$ is the plastic strain evolution, ε_D^p is the failure initiation plastic strain, and ${\varepsilon^p}_{max} = 2.0$ is the chosen maximum plastic strain where maximum damage occurs.

$$\dot{D} = \frac{\dot{\varepsilon}^p}{\varepsilon_{max}^p - \varepsilon_D^p} \quad \text{if} \quad \dot{\varepsilon}^p > 0 \tag{2.7}$$

A fracture energy dissipation law was also implemented where the damage evolution $\dot{D}$ is given as a function (equation 2.8) of the plastic work $\dot{W}_p = \sigma_Y \dot{\varepsilon}_p$, with σ_Y the current yield stress, $\dot{\varepsilon}_p$ the plastic strain evolution, D_{max} the maximum reachable damage, and G_f the fracture energy.

$$\dot{D} = \frac{\dot{W}_p}{G_f} D_{max} \tag{2.8}$$

Only one damage initiation criterion can be used for each material, further software development being required to make several available at the same time.

Discussion on the choice of the damage model and post-failure behavior is not of interest for this specific short paper as it serves more as a proof of concept, but its influence on the results should not be forgotten.

2.1.5 Contact

The contact detection method used is a sliding surfaces, slave and master method when the model is SPH on FE, with the SPH nodes declared as slaves and the finite elements declared as masters. This method is the most accurate available in the software Europlexus.

In the case of SPH on SPH, the Pinball method is used since no element surface is available. The pinball radius associated to the SPH element is equal to the SPH radius R_{SPH}.

In either case, the system of equations for the contact forces is solved using Lagrange multipliers.

An important point which has not been addressed yet is the friction between the particle and the substrate, which is now inexistent and could have a considerable influence on the behavior of the elements in contact, especially reduce their tendency to jet, and give more stable computations.

2.2 The adhesion model for the interface

2.2.1 Adhesion exhaustion criterion

A cohesive/attractive stress is applied between two elements if they have been in contact, have both met the activation criterion if one is declared, and if they are currently separating. The Lagrange multiplier given by the contact algorithm is used for the cohesive stress value. A maximum value for the cohesive stress, σ_c, can be declared. It has been shown in [PRO 16] to have a considerable influence on the dynamics of the impact and this point will be fully developed in the next chapter, section 3.5.1. The work associated with this stress is updated at every step and compared to the maximum work allowed, defined by the product of an adhesive surface energy G_c and the surface associated with an SPH particle, $S_{SPH} = \pi * {R_{SPH}}^2$, which is thus for now mesh dependent. When this limit is reached, the bond is broken and the cohesive stress is no longer applied. The obtained interaction law can be seen in Fig. 2.2.

This model in itself is not a novelty but differs from the one used in [YIL 14] where the criterion for stopping the adhesion is the cohesive stress reaching the maximum cohesive stress. It has no notion of energy dissipation, even though estimates on the necessary surface energy for adhesion at critical speed is inferred from the results obtained. The new model is less mesh dependent and hence more robust, because it introduces a surface energy to predict failure of the adhesion.

In the experiments the adhesion is successful only between a minimum impact velocity and a maximum one. The goal is to try to give an explanation of the two limits by adhesion modeling. The following process will be used: There must be enough shear at the interface to activate the adhesion; If the impact velocity is too large, the material on one side of the interface damages and the adhesion is then broken. We will now explain how these two ideas are implemented.

2.2.2 Adhesion activation

The main point of this study was to introduce a new concept in the adhesive model used for particle-substrate interaction, that is an activation criterion. Indeed in [YIL 14] and other impact models containing cohesive forces, those are applied locally as soon as contact occurs, resulting in an adhesive surface equal to the surface in contact. Here however, an activation criterion is introduced which will, if declared, use different routines, depending on the criterion

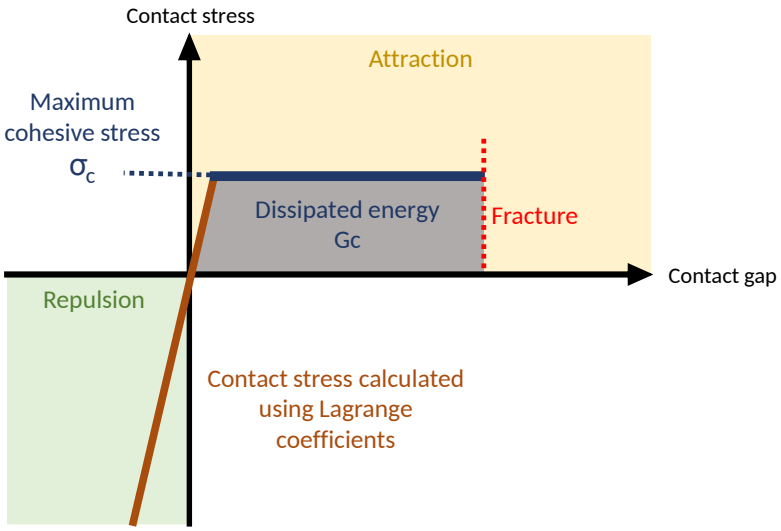

Figure 2.2: Schematic of the adhesive interaction law

chosen, to monitor variations of some internal variables in both contacting elements and switch the adhesive part of the interaction on if a defined pattern was observed, resulting in an adhesive surface different from the contacting surface.

The idea is thus to monitor the occurrence of a shear instability on either or both of the contacting elements, since it is thought to be the main driving force behind adhesion of metallic particles in Cold Spray.

Several definitions of a shear instability exist in the literature in terms of variations of internal variables, but for the sake of simplicity it has been decided here to detect shear instability as a given percentage drop in the local yield stress value σ_Y, starting from the maximum yield stress witnessed. A drop in yield stress can be the result of thermal softening and/or damage in the material, which is the reason for using when possible a shear failure model, designed to model shear stress instability and its critical effect in yield stress variation compared to only thermal softening. Shear instability can occur with only thermal softening, it requires however a mesh fine enough for two or three elements to be the same size as the width of a typical shear band, and some initial small inhomogeneities in the material. So as to get that instability with relatively coarse meshes, use of the shear failure model is the best option available.

The localization detection mechanism is shown in Fig. 2.3, and an example of the obtained activated contacting elements can be seen in Fig. 2.4 with a cut view of a test impact simulation. The activated nodes do not have to be directly in the contact region, which can also give an idea of the width of the ”shear band” obtained using this criterion, which is useful for fitting the damage law parameters in other shear banding models such as compression of a tilted cylinder, without necessarily using the adhesion model.

2.2.3 Adhesion erosion criterion

In the Cold Spray process has a critical velocity above which adhesion occurs, but also a maximum velocity, above which the particles start to erode the substrate instead of sticking to it. The introduction of a damage law in the materials and of erosion should in theory, if

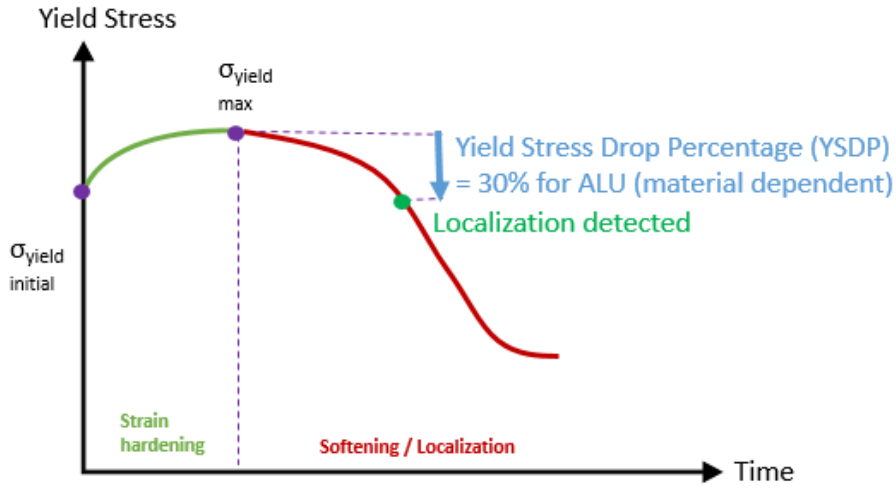

Figure 2.3: Schematic of the localization detection process

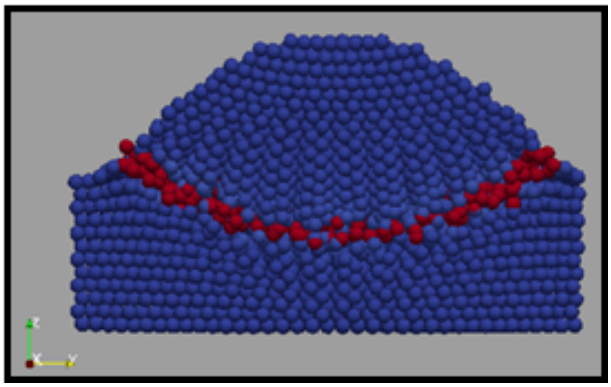

Figure 2.4: Cross section view of an impacted particle with the adhesive zone activated by the localization detection criterion in red

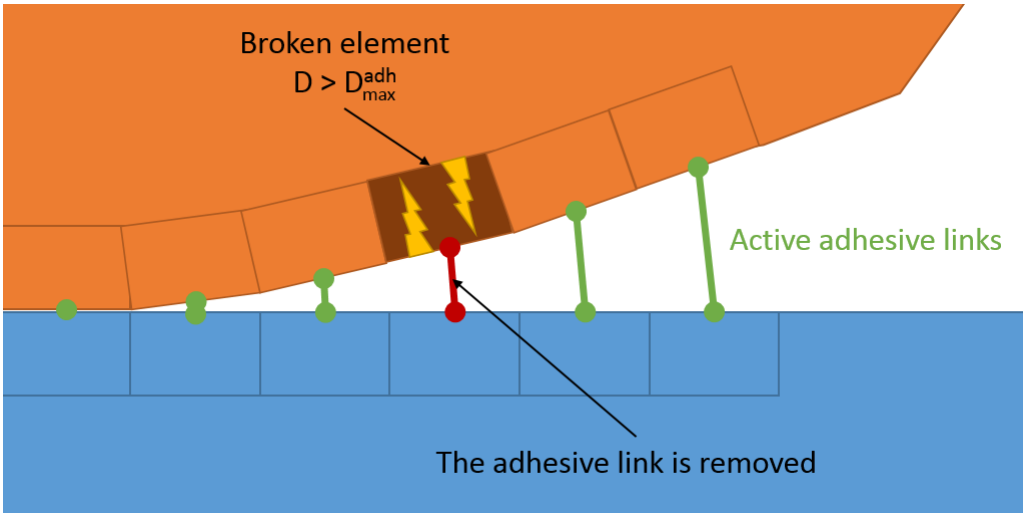

Figure 2.5: Illustration of the removal of an adhesive link due to a damaged supporting element

correctly tuned, result in such a phenomenon. The SPH method is however not stable enough in this work, possibly due to its total Lagrangian nature, to account easily for erosion, meaning that no erosion was put for SPH. The damage law is nonetheless kept, giving the option of adding a criterion to retrieve te erosion behavior. Thus a local adhesive bond is broken if one of the elements in the link has reached a maximum allowed damage value for adhesion D^{adh}_{max} as illustrated in Figure 2.5.

2.2.4 Defining the local adhesive surface

For SPH on SPH, the surface under adhesion is defined as π*R^2 with R the average radius of the two contacting Pinballs.

For SPH on EF, the surface under adhesion is defined as the smallest between the master surface of the FE and the surface π*R^2 with R the SPH radius of the slave node.

For EF on EF, that surface is difficult to define, which is one of the main reasons why this tool is not made available for EF on EF contact models. One idea would be to do the same as for SPH on EF, but with the surface for the slave node defined as: FE face surface of the slave node divided by the number of nodes of this surface. The difficulty is to find the right slave FE, since only the node number is stored, and the node can (actually should) belong to several different contacting surfaces.

2.3 Summary

Due to the mesh size involved, a correct representation of the material movement in the shear band is neither required nor beneficial. The models involved in simulation behavior of shear bands are complex and yet new. The model developed here thus only detects the beginning of a localization as a rapid drop in yield stress, and is not meant to simulate with great details the material behavior after instability has occurred.

Chapter 3

Numerical validation of the model

In this chapter the different numerical validations made to ensure the numerical tools give the desired results will be presented. First the viability of the solid SPH method with the Johnson-Cook material law is assessed with simulated Hopkinson bar tests. In a second time traction tests are simulated and the results compared with results from the same model in Abaqus. Then the effect of the failure law on localization dynamics is investigated by Shear Banding simulations. Finally the model of the impact of a single particle without adhesion is created and briefly studied, before adding the adhesion model for validation.

Contents

3.1 Solid SPH and Johnson-Cook validation by Hopkinson bar simulation

The first validation test is carried out just after making the Johnson-Cook material law available for solid SPH. The aim is to check the viability of the use of the SPH method by looking at the level of difference between FE and SPH results in fast dynamics impact problems, and the effect of the different SPH parameters on these results.

3.1.1 The compression Hopkinson bar model

The choice is made to simulate compression Hopkinson bar experiments, which are commonly used to get experimental data on the behavior of materials at high strain rates. The model is the numerical model described in [LEC 09], a technical note for Europlexus users on how o model a Hopkinson bar.

Figure 3.1 shows the principle of the ELSA compression Hopkinson bar, which uses a hydraulic actuator and a breaking link to load a part of the input bar until a desired tensile stress is reached due to an unilateral constraint preventing the movement (and thus the deformation and stress) to propagate to the rest of the input bar. The breaking link is then broken, unloading the pre-tensioned bar, resulting in a short intense compressive wave rushing through the input bar and from then into the specimen and out in the output bar.

Figure 3.2 shows the geometry of the parts involved and the positions of the different strain gauges monitoring the load in the bars. The specimen used has a length of $L_s = 5mm$ and a diameter of $D_s = 5mm$. The pre-tensioned, input and output bars are all made of steel and modeled with an elastic law only with a density $\rho = 7800kg/m^3$, a Poisson ratio $\nu = 0.3$ and a Young modulus $E = 2e^{11}Pa$. The specimen is modeled with the Johnson-Cook law using the values in Table 3.1, with a conversion coefficient for temperature increase, when used, of 80% of the plastic work. The study of the influence of the numerical methods used to simulate this experiment is made in the report cited above. The model used here is already optimized, thus we will only focus on relative differences between the output signal obtained in gauge g6 when using the modified Johnson-Cook material law, when using SPH, and when evaluating the effects of the different SPH parameters to try and optimize the method in terms of mesh size and time-consumption (neighborhood search).

3.1.2 Validation of implemented thermal softening

The first verification is made after adding thermal softening to the Johnson-Cook law, to check that the implementation gives a correct effect of softening. A computation with finite elements and a Johnson-Cook material law is used as reference, with the test case being the same (mesh, material parameters... etc), only with the addition of thermal softening. Since no reference is directly available with thermal softening, it is seen as sufficient to check the implementation only qualitatively. The result of the comparison can be seen in Figure 3.3, where a small but observable softening is obtained for the stress variation in the output bar on gauge 6, stress variation which corresponds to the response of the material the the compressive wave coming from the input bar.

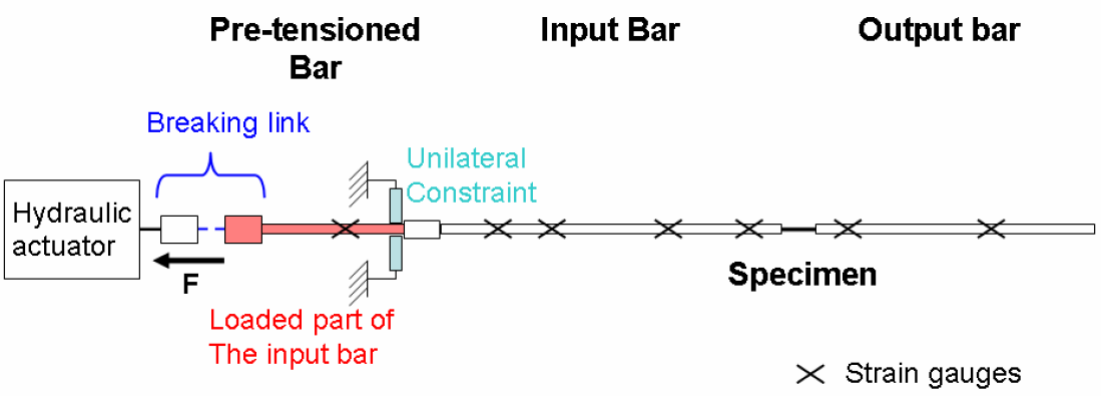

Figure 3.1: Principle of ELSA compression Hopkinson bars

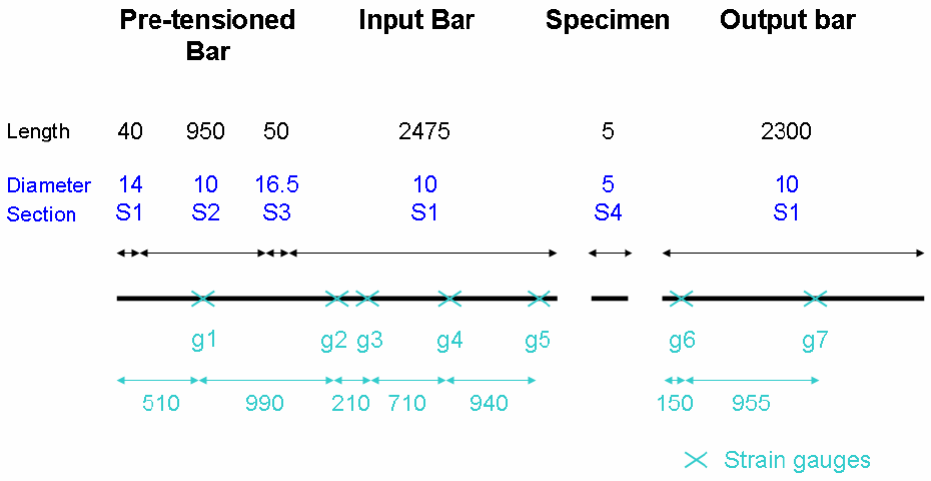

Figure 3.2: Geometrical properties of the compression Hopkinson bars (mm)

Table 3.1: Material properties used for steel in the Hopkinson sample

Properties	Parameter	Value	Unit
General	Density, ρ	7800	$kg.m^{-3}$
	Specific heat, k	480	$J.kg^{-1}.K^{-1}$
	Melting temperature, T_{melt}	1800	K
	Inelastic heat fraction	0.8	
Elastic	Elastic modulus	200	GPa
	Poisson's ratio	0.3	
Plastic (Johnson-Cook plasticity model)	A, B, C, N, M	266, 229, 0.0294, 0.3, 1.0	MPa, MPa
	Ref. strain rate, $\dot{\varepsilon}^p_{ref}$	1	s^{-1}
	Ref. temperature, T_{ref}	293.15	K

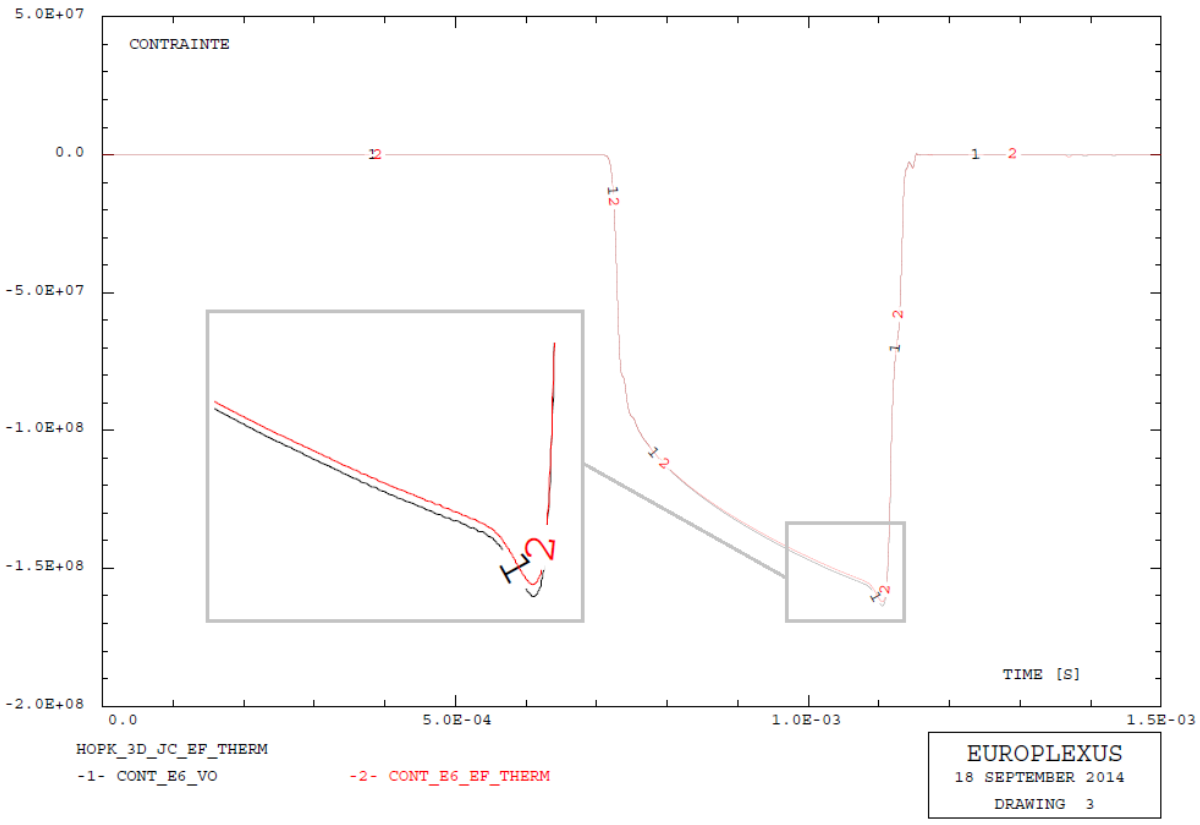

Figure 3.3: Effect of the developed thermal softening for Johnson-Cook

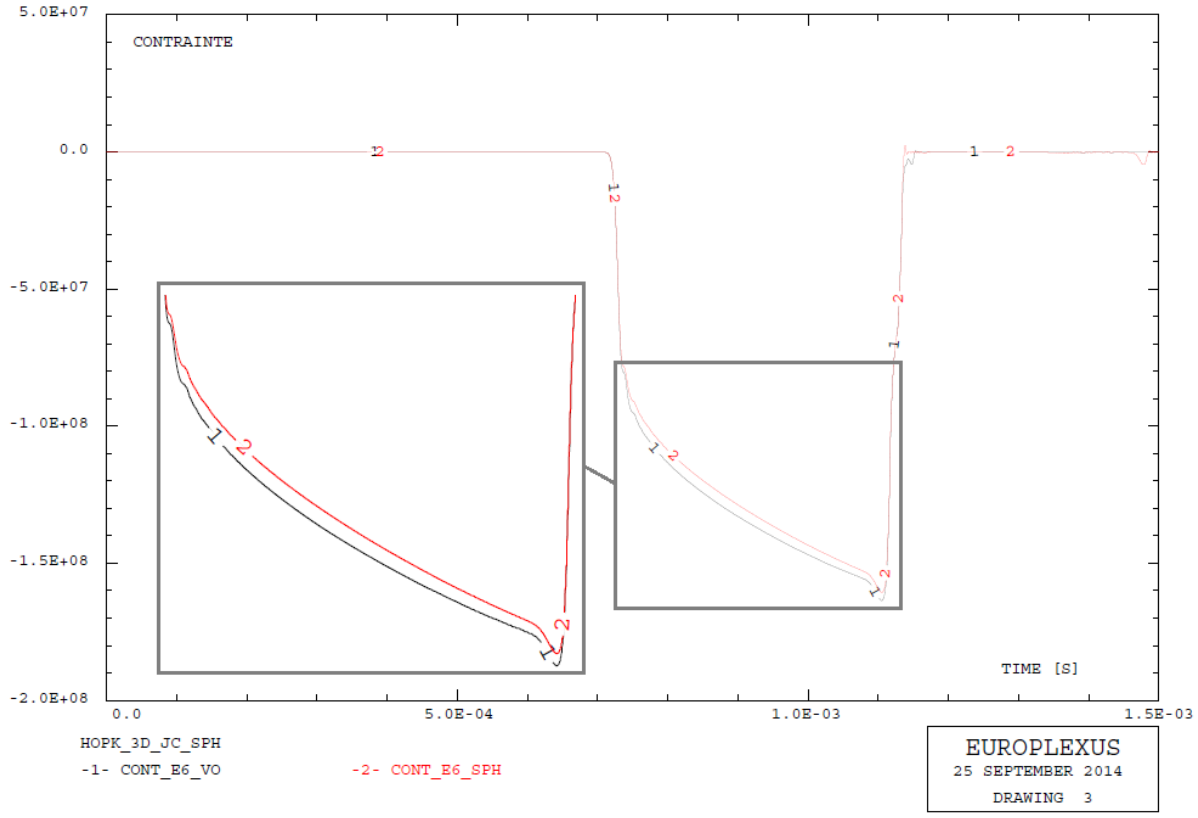

Figure 3.4: Effect of using a SPH mesh

3.1.3 Validation of the implementation of Johnson-Cook with the SPH method

The next step is to make the Johnson-Cook law available for use with the SPH method. The reference used is the finite elements model, and the test case is the same, only with the specimen meshed with SPH instead of finite elements. This first SPH mesh has an SPH particle radius $R_b = 125\mu m$, a very high search radius of four times the SPH kernel radius (the SPH kernel radius or influence radius being twice the SPH particle radius), a maximum number of neighbors of one hundred and it contains 8880 elements (hence 8880 nodes and 8880 Gauss points), whereas the FE mesh contains 1520 prism elements with 6 Gauss points each, giving 1067 nodes and 9120 Gauss points, so the number of Gauss points is similar for the two meshes.

Figure 3.4 shows the effect using this SPH mesh has on the material response. As can be seen, the global response of the specimen is very similar and can be considered correct (only a few percents in maximum load difference), even though the SPH mesh is a little softer than the FE mesh, which as we will see depends on the mesh parameters used. These indeed not only do have an effect on the stiffness of the mesh and quality of the interpolation due to the number of Gauss points, but the SPH method also involves a packing method (a cubic lattice or, as in all the computations in this work, a hexagonal compact lattice) which means that the mesh size has an influence on the quality of the spatial discretization in terms of obtained global shapes. Hence the actual specimen diameter D_s depends on the meshing technique and SPH particle

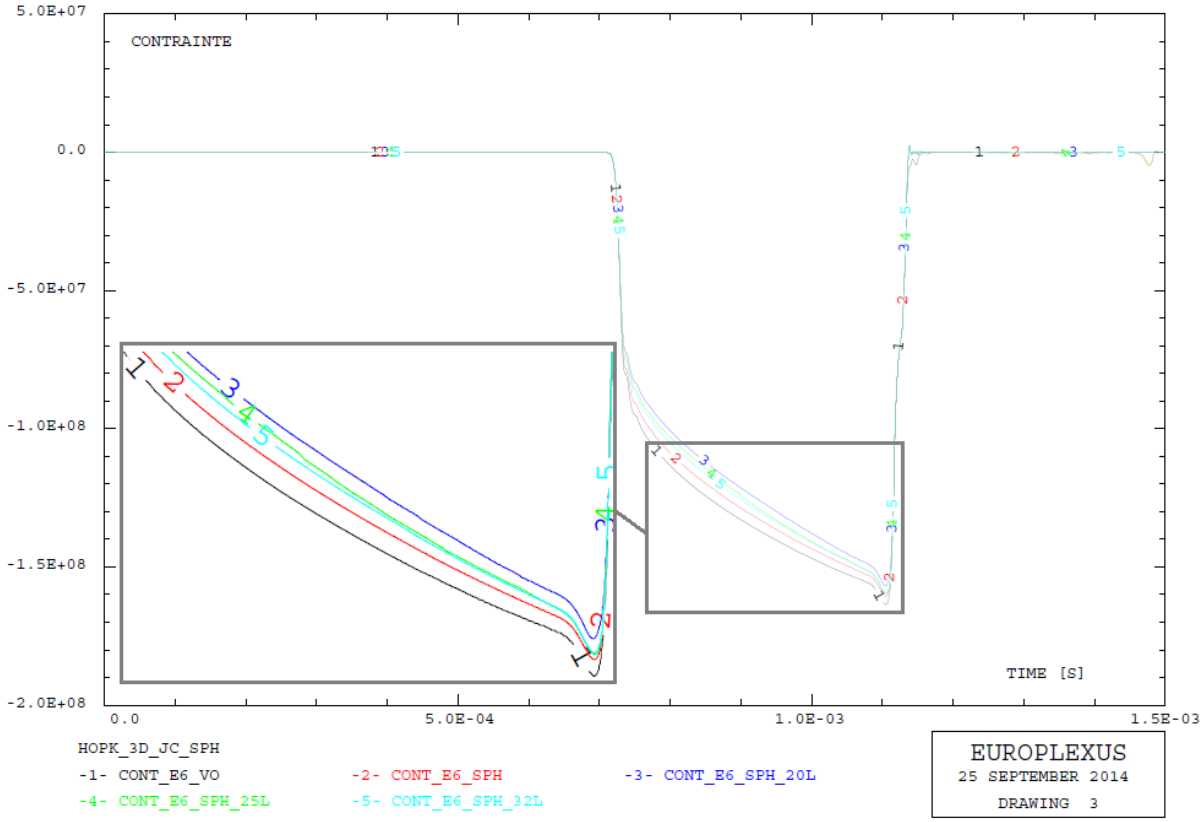

Figure 3.5: Effect of SPH spatial discretization refinement

size, which could explain part of the difference observed in terms of specimen response to the load.

3.1.3.1 Effect of SPH particle size

To further assess the effect of the choice of mesh refinement, three other SPH meshes with larger SPH particle radii are used. The specimen length to SPH particle radius ratio $\frac{L_s}{R_b}$ is used for comparison.

In Figure 3.5 are shown the response of the reference FE mesh in black, of the previous SPH mesh with $\frac{L_s}{R_b} = 40$ in red, of an SPH mesh with $\frac{L_s}{R_b} = 20$ in blue, of an SPH mesh with $\frac{L_s}{R_b} = 25$ in green, and of an SPH mesh with $\frac{L_s}{R_b} = 32$ in light blue.

Even when dividing the SPH particle size by two, the global response of the specimen stays within a few percents difference of the reference curve, which can indicate that the first mesh used was indeed already fine enough, and that degrading the spatial discretization this much did not yet have a dramatic effect.

3.1.3.2 Effect of SPH search radius

When using SPH one should keep in mind that there is an intrinsic difference between refining the spatial discretization by using more SPH particles, and refining the kernel interpolation by putting more particles in the influence zone of the SPH kernel.

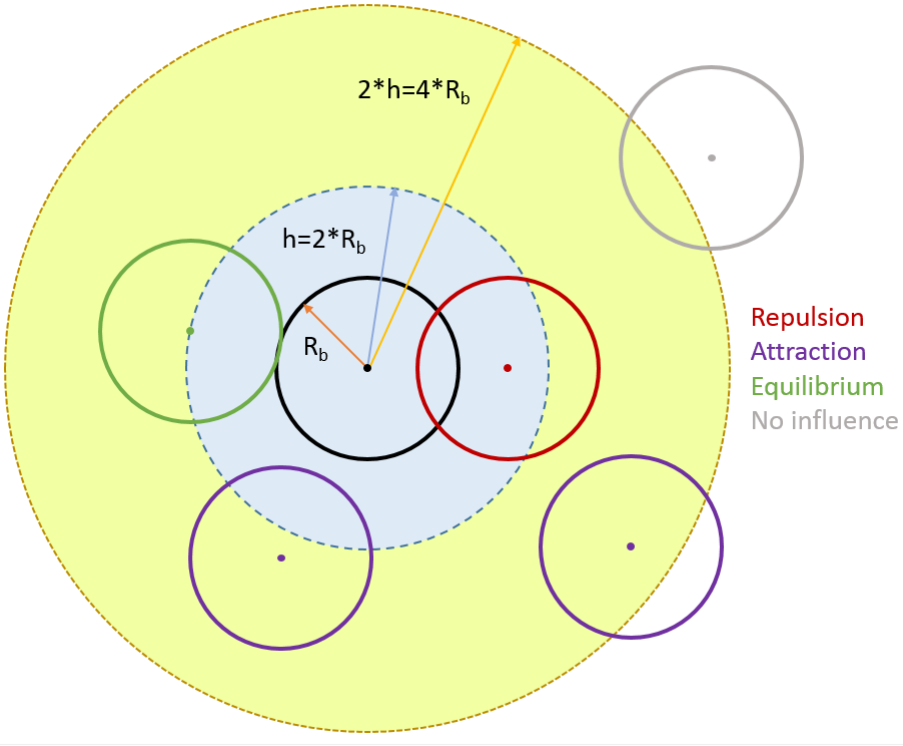

Figure 3.6: Typical interaction of an SPH particle with its surroundings

The influence of the input parameter defining the radius of the zone for potential neighbor around a particle is shown in Figure 3.7, where the reference FE curve is in black, the original SPH computation with a search radius of 16 times the particle radius is in red, a search radius of 5 times the particle radius is in blue, 4 times in green, and finally 2 times in light blue.

This parameter can be useful in situations where the particle radius varies across the mesh and along the computation. However here, since all particles have the same unchanging radius, the kernel or influence radius will always be the same everywhere, hence a minimal search radius corresponding directly to this kernel radius is enough. Since here the kernel radius is twice the particle radius, and its influence extends to twice that value, the curves obtained are the same for a search radius of 4 times the particle radius or more. A good depiction of the distances involved is presented in Figure 3.6.

This verification can seem trivial, but the point is to minimize the search radius to limit the time-consumption of the algorithm, and also to make sure that the limited number of neighbors the algorithm looks for are actually the ones in the sphere of influence (which, as previously said, depends on the kernel used). The neighbor search algorithm indeed looks for potential neighbors by increments in coordinates, which means that the maximum number of neighbors allowed for one point can be reached while only the particles on one side of the one of interest have been screened, resulting in an imbalance of the interpolation scheme.

3.1.3.3 Effect of SPH maximum number of neighbors

As seen previously, the parameters for the neighborhood search algorithm were investigated, with an optimum search radius found to be quite logically the radius of the sphere of influence

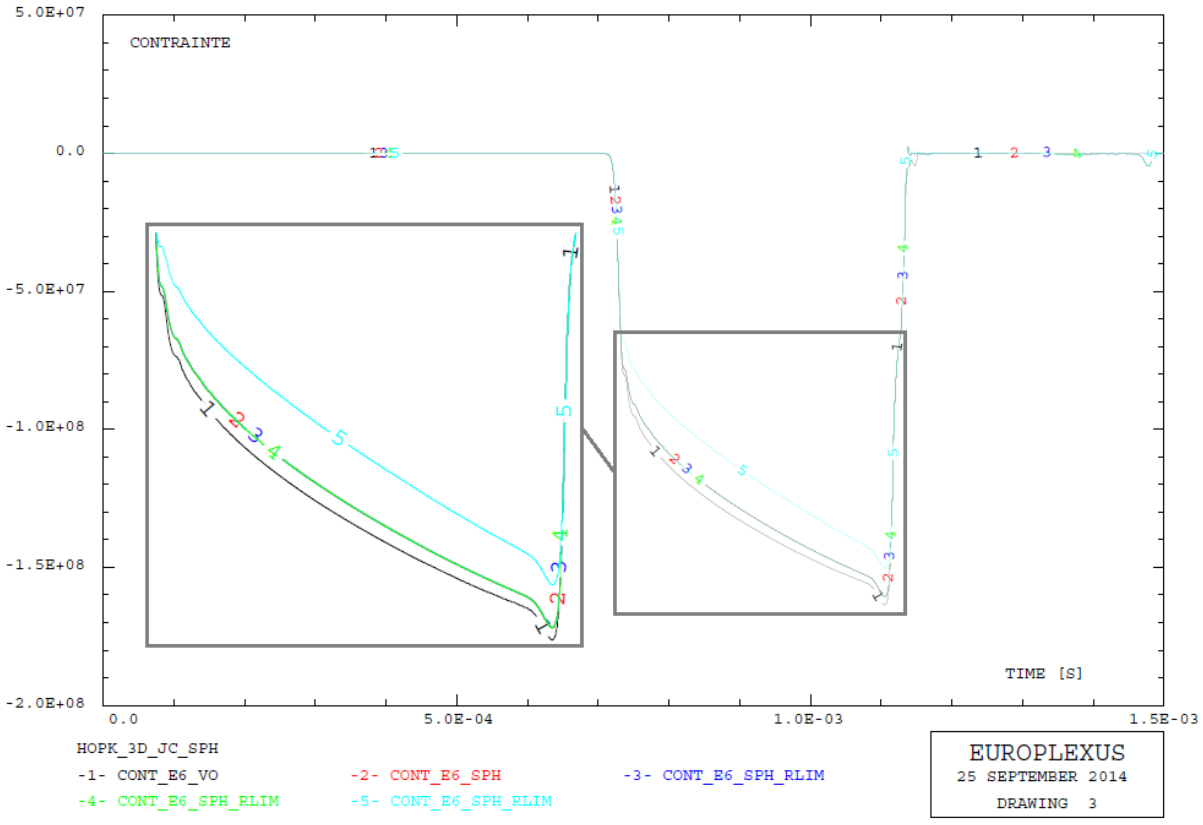

Figure 3.7: Effect of SPH neighbor search radius

of the SPH kernel (which is programmed as twice the kernel radius). The next step was to find the maximum number of neighbors the algorithm should look for which can actually fit in that sphere with the packing used. To assess this, the software Paraview was used to view the mesh generated by the software Europlexus with a given particle size in its original configuration, and a node was chosen randomly in the center of the specimen. The part of the mesh contained in a sphere of radius four times the particle radius centered around that particular node was extracted, and the number of nodes contained in that selection was measured. Hence for the search radius previously found, the average number of nodes contained in the selection made, for a hexagonal compact lattice, was found to be of 50. The corresponding parameter was thus chosen as 50 for the rest of the computations.

3.1.4 Discussion on the results

In conclusion, the compression Hopkinson bar model from official guidelines for Europlexus was used to study the behavior of the newly developed thermal softening for Johnson-Cook, and the viability of the solid SPH method to simulate fast dynamics problems, as well as the influence of the different meshing parameters. The reference used was the curve given by the initial model using the FEM. Results showed that while different, the results given by the SPH method fall well within a comfortable certitude zone of less than 10% difference with the typical FEM mesh with an equivalent number of Gauss points. As expected, refining the SPH mesh brings the results always closer to the FEM results, be it because of the increase in the number of Gauss points but also from the increase in quality of spatial representation of the shape of the specimen. Guidelines should thus be to use a mesh as fine as available time and resources allow, but the SPH method used with Johnson-Cook and thermal softening seemed to converge quite quickly to a solution.

3.2 Material law and SPH quantitative validation by traction test simulation

The first effort made towards validating quantitatively the material law is a comparison of results given by Abaqus simulations of a traction test with the results given by Europlexus for the same model and with the same material laws and parameters. First the material softening is investigated, then the influence of the SPH method.

3.2.1 Traction test model

The material is pure aluminum, with the same material laws and coefficients used in both softwares. A cylinder is used as specimen, with a diameter of 40 mm and a length of 120 mm. The traction in both softwares is simulated by an imposed displacement on the nodes at one of the extremity of the cylinder, and an imposed null displacement on the other end. An example of temperature distribution for such a cylinder under traction is shown in Figure 3.8.

3.2.2 Thermal softening

To be able to validate quantitatively the effect of the thermal softening implementation for the Johnson-Cook material law, a traction test is simulated with Finite Elements on both Abaqus

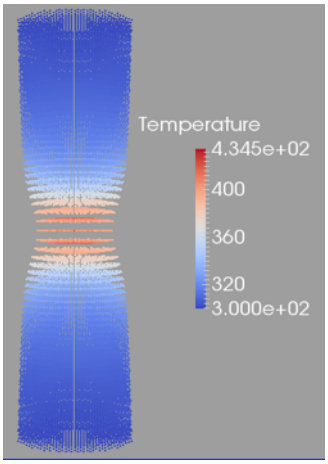

Figure 3.8: An example of traction test cylinder for SPH with Europlexus visualized using Paraview

and Europlexus.

The Europlexus mesh is made of 12000 cubic elements with one Gauss point each, and 13161 nodes, giving 40 elements in the length of the cylinder. The Abaqus mesh is made of 12800 C3D8R 8-node linear cubic elements, to give a similar mesh density and the same 40 elements in the length of the cylinder. The traction test is carried out at a strain rate of 20 s^{-1} with an imposed displacement of 2.4 m in 1 s. Figure 3.9 shows the force (force applied by the imposed displacement, in Newtons) versus strain curve for Abaqus and Europlexus, both with and without thermal softening taken into account. The results are nearly identical, and the softening due to temperature is also nearly identical, hence the thermal softening effect implemented in Europlexus was considered as quantitatively validated.

3.2.3 SPH mesh convergence

The influence of the mesh refinement on the results using SPH was assessed by comparing the results for the same traction tests on aluminum but at 200 $s.^{-1}$. Figure 3.10 shows the results obtained in force (force applied by the imposed displacement, in Newtons) versus strain for a FE mesh identical the one used in the previous section and three SPH meshes, with element sizes R_b of 2, 1.5, 1 and 0.5 mm. The SPH meshes are hexagonal compact, with a search radius of 4 times the particle radius and a maximum number of neighbors of 50. For R_b= 2 mm, the mesh contains 3009 SPH elements, nodes and Gauss points, for R_b= 1.5 mm it goes up to 7314, for R_b= 1 mm up to 25593, and for R_b= 0.5 mm up to 207288. For SPH meshes, the imposed displacements are imposed on three layers of elements for the SPH smoothing function to correctly represent the condition, but the resulting force of only one layer is monitored. The SPH mesh is thus made a little longer than the FEM mesh, since the two top element layers on each sides are what can be called ”ghost elements”, meaning they are here to ensure the limit condition is modeled properly, but are not considered part of the specimen under investigation.

As can be seen, the SPH result is always lower than the FE result, in the same manner as results from the Hopkinson bar simulations. However in terms of maximum force attained, they are lower by 11%, 8%, 5% and 3.6% when refining the SPH mesh. This can be considered within normal error margins for numerical simulations.

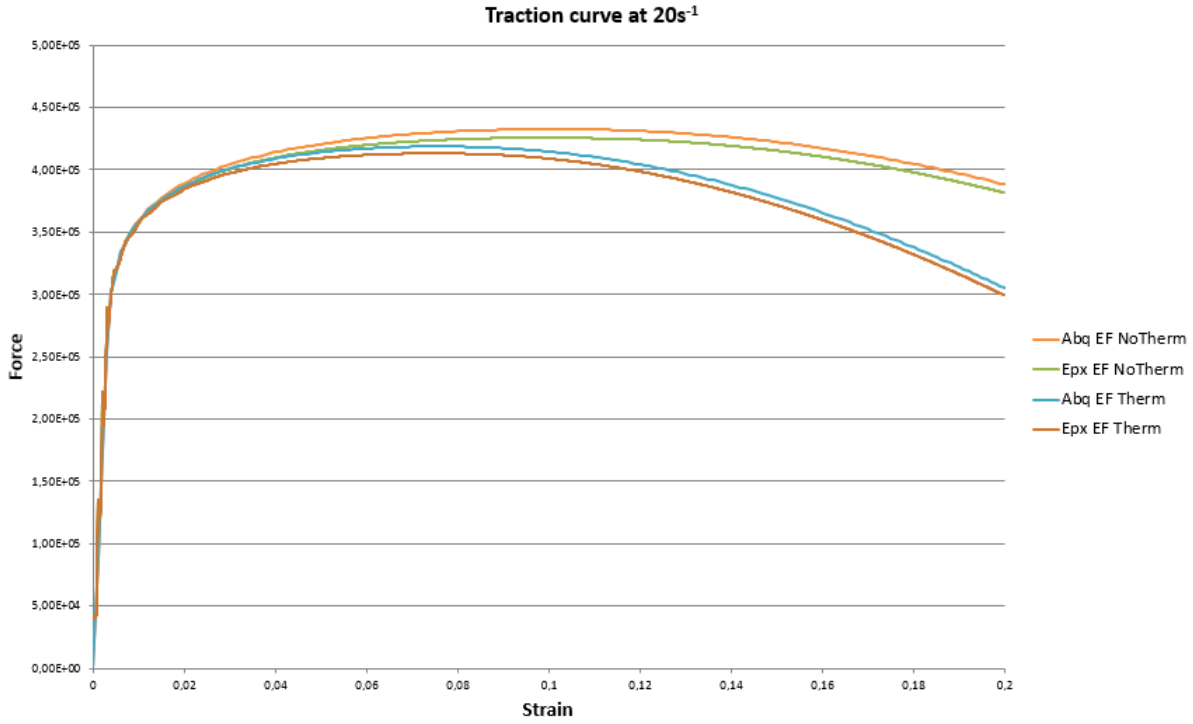

Figure 3.9: Comparison of results from Abaqus and Europlexus with FE, with and without thermal softening

3.2.4 Discussion on the results

The comparison of the results given by the new developed material law and SPH mesh to results given by a FE mesh from Abaqus for a simple case of a traction test at a relatively low strain rate of 250 s^{-1} clearly shows that the behavior is quantitatively similar: within 1-2% for a FE mesh, and within 11% or less for even very coarse SPH meshes, down to under 5% for finer SPH meshes for the maximum load value. The conclusion is that the Johnson-Cook model with thermal softening used with SPH is suitable to simulate high strain-rate behaviors such as in Cold Spray, but it should be kept in mind that an SPH mesh seems to be softer than an FE mesh, and the relative element size required to obtain results within 5% of similarity can be twice smaller, resulting in a lot more elements and a higher time-cost for SPH models. This drawback is known, but it should be counterbalanced by capacity of SPH meshes to sustain higher deformations and strains.

3.3 Failure laws validation by Shear Banding simulation

The next step in the validation of the numerical model was to study the influence of and validate the behavior of the failure laws implemented.

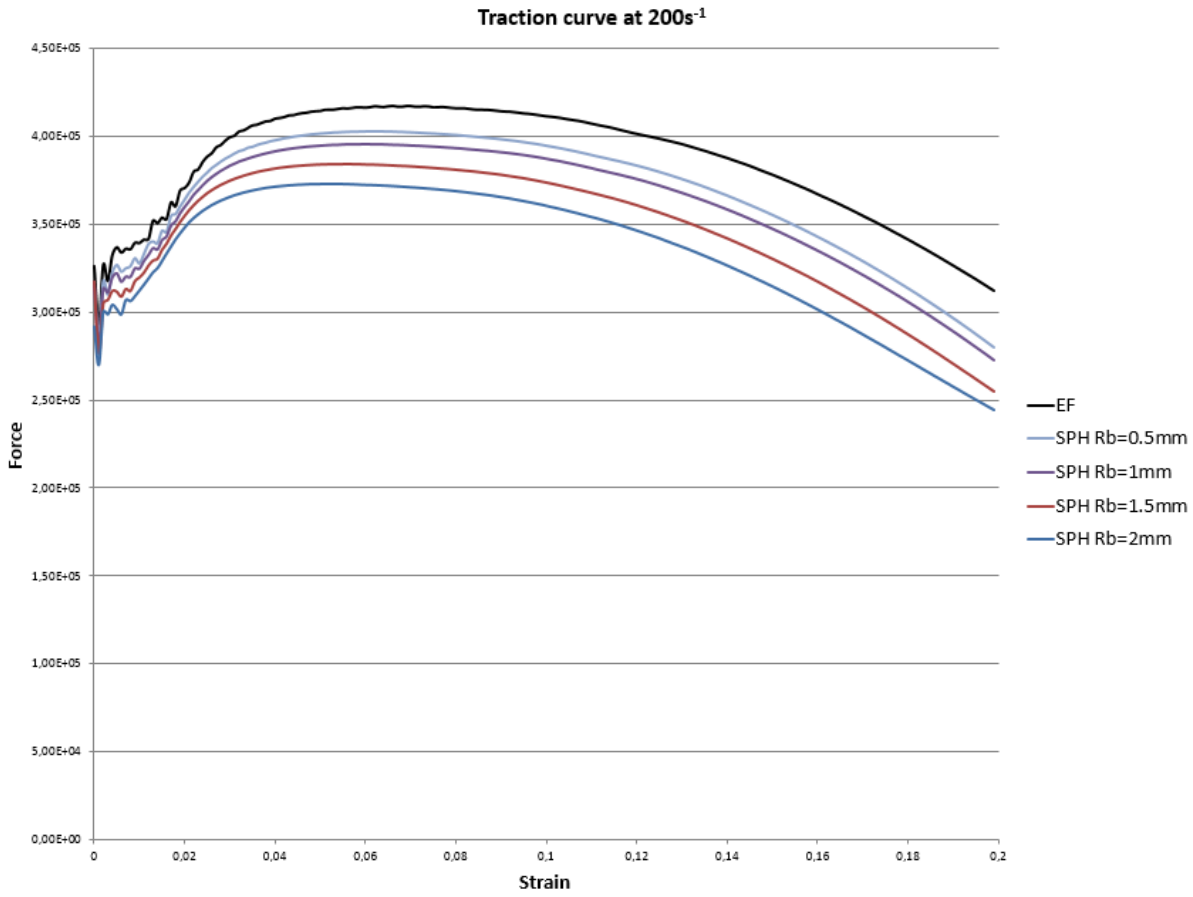

Figure 3.10: Comparison of results from Europlexus with FE and from Europlexus with SPH and several mesh sizes

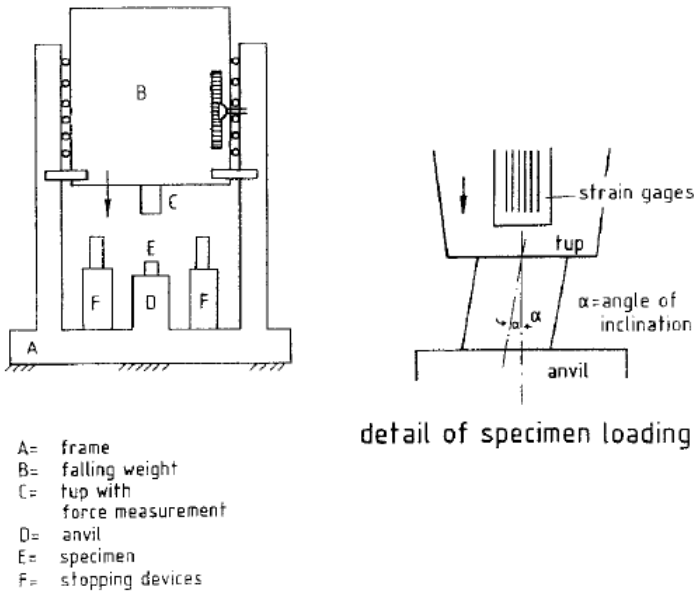

Figure 3.11: Diagram of the biaxial dynamic loading system [MEY 94]

3.3.1 The Shear Banding model

The global aim of introducing a failure law was to ease occurrence and onset of a shear instability, but not to simulate the precise dynamics of the evolution of a shear band. The experimental case of adiabatic shear failure in a Ti6Al4V tilted cylinder under biaxial dynamic compression/shear loading found in [MEY 94] was used as reference. As discussed in 2.1.4.2, numerical models and simulations have already been performed to study initiation and propagation of adiabatic shear bands, however they often rely on geometrical discontinuities such as a notch or a strong angle in the shape of the specimen to force initiation of the shear band. These approaches have the benefit of knowing where the shear band will develop, with mesh refinement efforts concentrated on that area. They also always use Finite Elements, so the capacity of SPH to show the same kind of behavior had to be validated. In our case, the impact of a particle on a substrate, there is no initial geometrical discontinuity to speak of, except for the discontinuity the contact creates, and furthermore the adhesive model being macroscopic, simulating the complete shear band with a fine mesh is exactly what we are trying to avoid. So, to study the effect of the failure law on the initiation of an adiabatic shear failure in a material (i.e. the effect of the material law on the induced propensity of the material to undergo shear banding), the case of a tilted cylinder under biaxial dynamic compression, where localization occurs only due to a material instability and failure susceptibility without requiring an artificial initiation site, is deemed to be the best choice in terms of testing the numerical model.

Figure 3.11 shows the apparatus used in [MEY 94] to load the tilted cylinder specimen in a dynamic biaxial manner, with a weight dropped on the specimen and stoppers to limit the compression to a defined value. Figure 3.12 gives a typical response from the specimen in terms of stress, with a first elastic loading, a plastic deformation zone with strain hardening and a localization with rapid subsequent failure due to an adiabatic shear band initiating and propagating through the diagonal of the specimen.

The numerical model built is shown in Figure 3.13 and consists of two supports in cubic

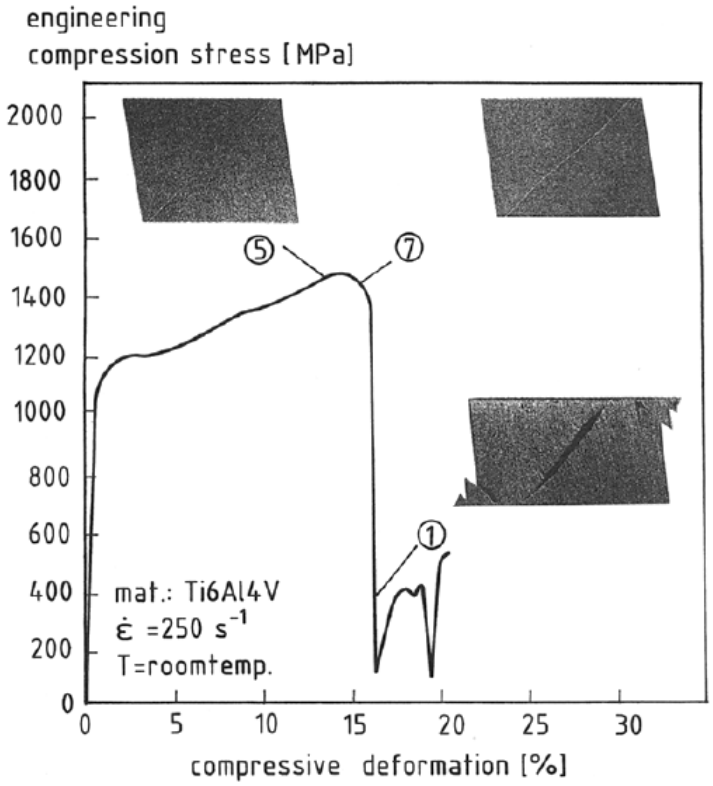

Figure 3.12: Loading curve for a specimen tilted by 6°at room temperature [MEY 94]

Finite Elements with 192 elements each and a material defined by an extremely rigid linear elastic material law with a Young modulus of $2e^6$ GPa. The cylinder of diameter and height equal to 6 mm and inclination of 6°is modeled with SPH elements and the Johnson-Cook law, with parameters given in Table 3.2 found on the ASM website and in [CHE 11] except for the second Johnson-Cook coefficient for strain-hardening, which is changed to fit the plastic loading part of the experimental curve. The contact between supports and cylinder uses the sliding surfaces master-slave method from Europlexus with Lagrange multipliers. The compression is induced by an imposed displacement on the top layer of the top support of 1.5 m in 1 s, giving a strain rate of 250 s^{-1}. Final simulated time is chosen as 1 ms, which gives a final compression ratio of 25%. If not told otherwise, the SPH particle size used is $R_b = 200\mu m$, giving a mesh with 3676 SPH elements.

3.3.2 With adiabatic thermal softening only

First, the capacity of the model to localize is investigated without any damage law, that is the propensity of the thermal softening only to lead to localization.

3.3.2.1 Influence of material inhomogeneities

In theory, under a homogeneous loading, a perfectly homogeneous material should not localize. In reality of course the material is never perfectly homogeneous, thus the idea of artificially introducing a random initial field of damage, which will not evolve during the loading, is first

Table 3.2: Material parameters used for Ti6Al4V

Properties	Parameter	Value	Unit
General	Density, ρ	4430	$kg.m^{-3}$
	Specific heat, k	526.3	$J.kg^{-1}.K^{-1}$
	Melting temperature, T_{melt}	1604	K
	Inelastic heat fraction	0.9	
Elastic	Elastic modulus	113.8	GPa
	Poisson's ratio	0.342	
Plastic (Johnson-Cook plasticity model)	A, B, C, N, M	860, 900, 0.035, 0.47, 1.0	MPa, MPa
	Ref. strain rate, $\dot{\varepsilon}^{p}_{ref}$	1	s^{-1}
	Ref. temperature, T_{ref}	300	K

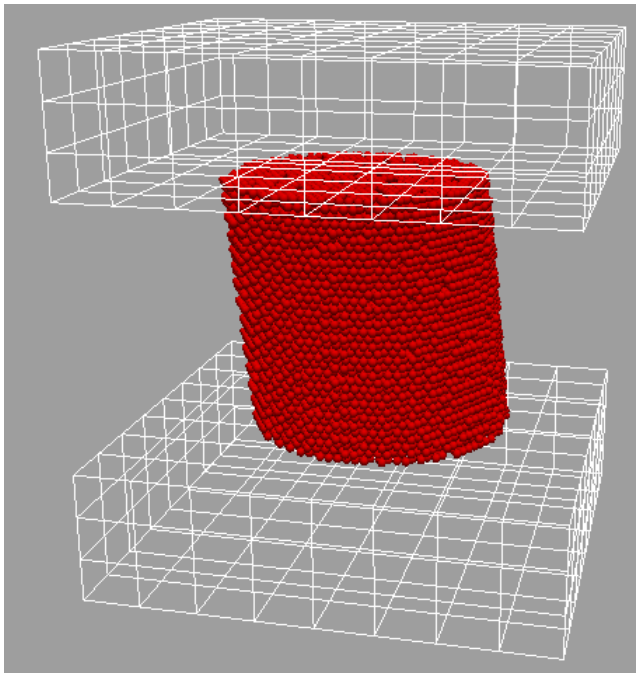

Figure 3.13: View of the Shear Banding compression cylinder model used in Europlexus (fine mesh)

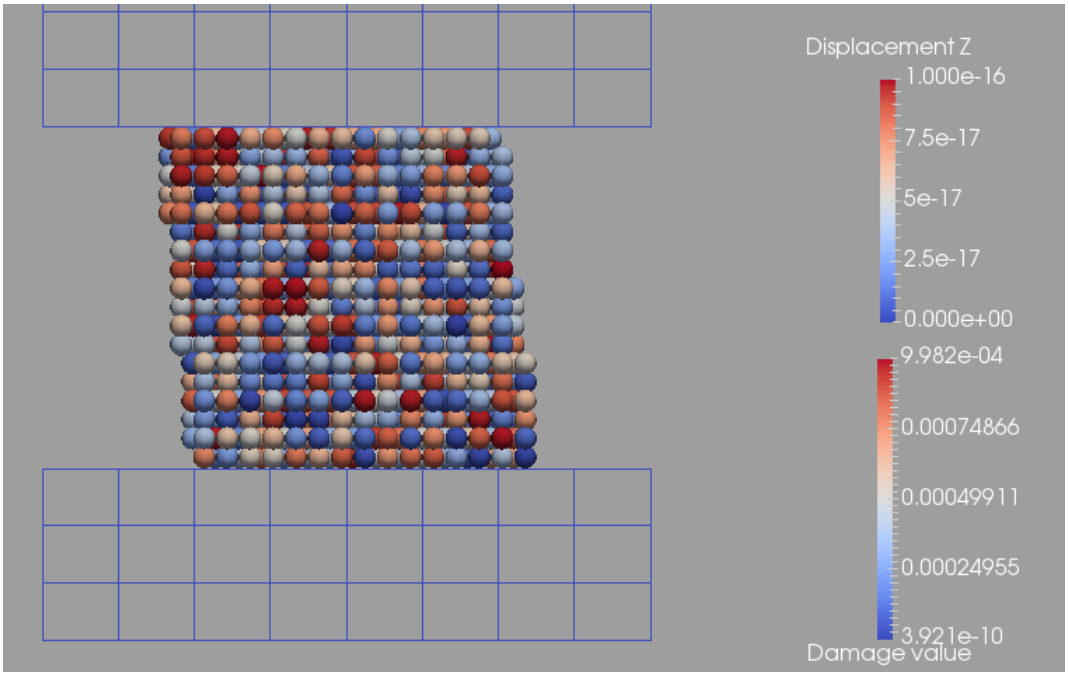

Figure 3.14: Cut view of the tilted cylinder with the random initial damage field

studied to see if it allows the adiabatic thermal softening to localize. Figure 3.14 shows an example of a damage field initialized with random values ranging from 0 to $1e^{-3}$, resulting in an inhomogeneous initial yield stress field with variations of 0.1% in value shown in Figure 3.15, with an equal effect on the initial Young modulus value and thus sound speed value throughout the material.

Figure 3.16 shows the stress-strain curve obtained with five different values of the parameter RAND, the parameter giving the maximum random damage value attainable. The first curve with RAND=0.0 thus corresponds to an homogeneous material, which does not localize for the strains and strain rate considered with thermal softening alone. Then, the parameter is increased to 0.01%, 0.1% and 1% without any clearly visible effect on the response of the material. Finally with initial inhomogeneities of 10% in the yield stress, Young modulus and sound speed fields, we can observe a drop in the global strength of the specimen, without however seeing any change in the overall behavior, and especially still no localization for the strains considered.

As a conclusion it is confirmed that artificial initial inhomogeneities in the material properties are not sufficient to create a localization process due to solely adiabatic thermal softening.

3.3.2.2 Influence of mesh size

Localization is also a phenomenon that is known to be mesh dependent, thus a finer mesh is tested with initial random inhomogeneities. The SPH particle radius is $R_b = 100\mu m$, giving a mesh with 29357 elements. The parameter RAND is given a value of 0.01%.

As can be seen in Figure 3.17, even with a finer mesh the adiabatic thermal softening alone does not lead to localization. Even finer meshes should of course be tested, however in the scope of this work the goal is to create a model which does not require extremely fine meshes, hence the addition of a damage law is considered the best option for a macroscale shear band simulation.

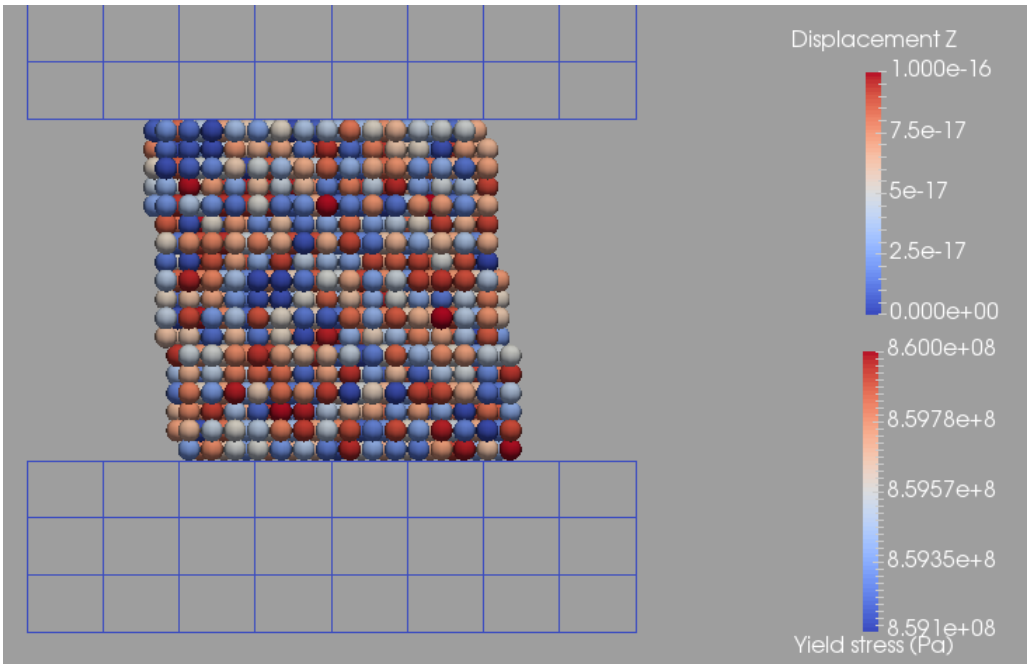

Figure 3.15: Cut view of the tilted cylinder with the initial inhomogeneous yield stress field

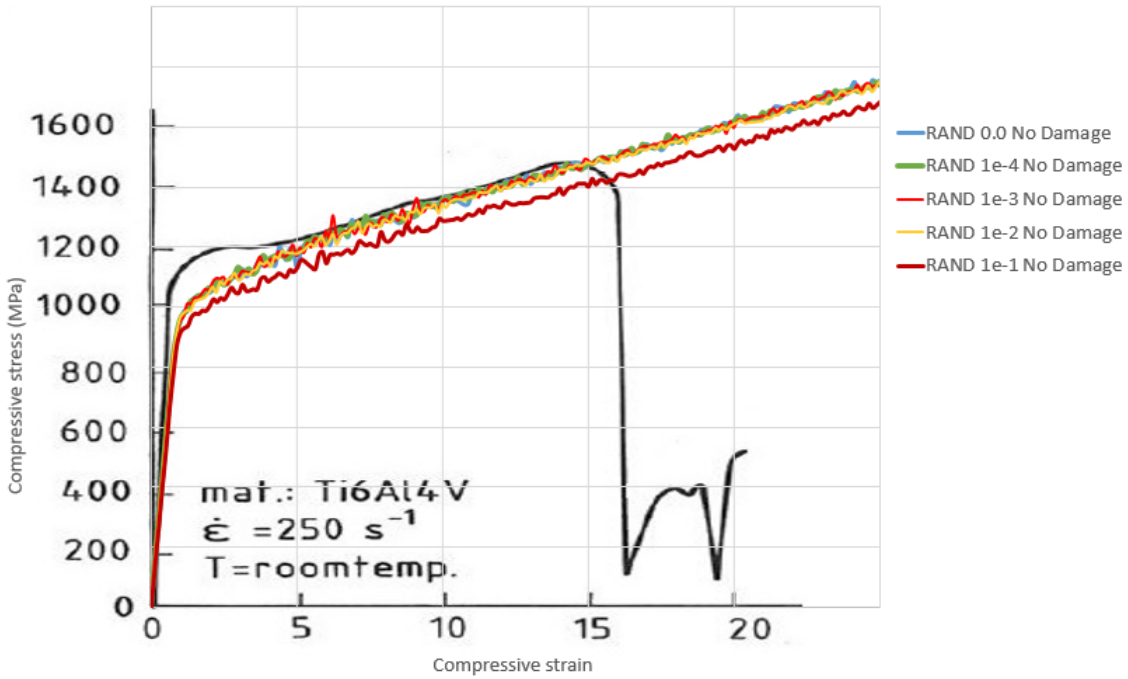

Figure 3.16: Effect of adding random initial material inhomogeneities on localization with thermal softening only in the Shear Banding model

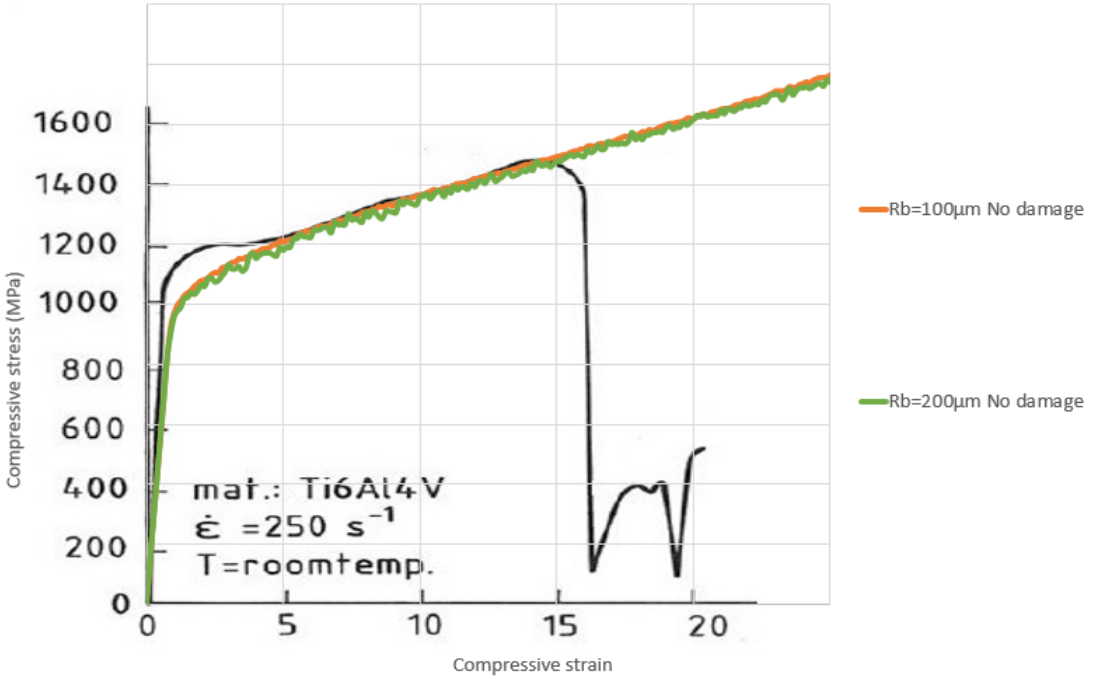

Figure 3.17: Effect of mesh size on adding random initial material inhomogeneities with thermal softening only in the Shear Banding model

3.3.2.3 Conclusion

One will now let the damage increase to search if this can help localization and Shear Band initiation.

3.3.3 The Johnson-Cook damage initiation criterion

The first damage law which was implemented and tested is a law using the Johnson-Cook damage initiation criterion, as seen in 2.1.4.2. The parameters, found in [CHE 11, SUN 08] are shown in Table 3.3. The second parameter, for strain-hardening, is once again changed to fit more or less the localization strain from the experiments. At first the damage evolution law is chosen as full instant maximum damage, which is chosen as D_{max}=0.9. No erosion is put on the SPH elements, meaning that once the initiation criterion is met, damage will instantly increase to 0.9 and stay there.

Figure 3.18 shows the localization induced by the Johnson-Cook ductile failure model in the stress-strain curve. The effect can be seen on Figures 3.19 and 3.20, showing the yield stress field at final time with and without the influence of damage. It can be clearly seen that a shear band formed in the diagonal of the sample in the case of damage softening being present. Figures 3.21 and 3.22 shows where the Johnson-Cook ductile failure was met in both cases (without however actually activating any damage in the first case). As expected, damage initiated in the corners of the sample, and then propagated throughout the sample in the manner of a shear band. The ability of the criterion to simulate a shear band was thus confirmed qualitatively. In terms of stress-strain curve, the first slow drop in stress after around 17% compression is actually due to the damage in the corners, with the shear band finally propagating at around

Table 3.3: Johnson-Cook failure parameters used for Ti6Al4V

Properties	Parameter	Value	Unit
Ductile Failure (Johnson-Cook failure model)	d_1, d_2, d_3, d_4, d_5	-0.09, 0.45, -0.5, 0.014, 3.87	
Damage evolution	Maximum Initial Damage	0.001	
	Plastic strain at failure	2.0	

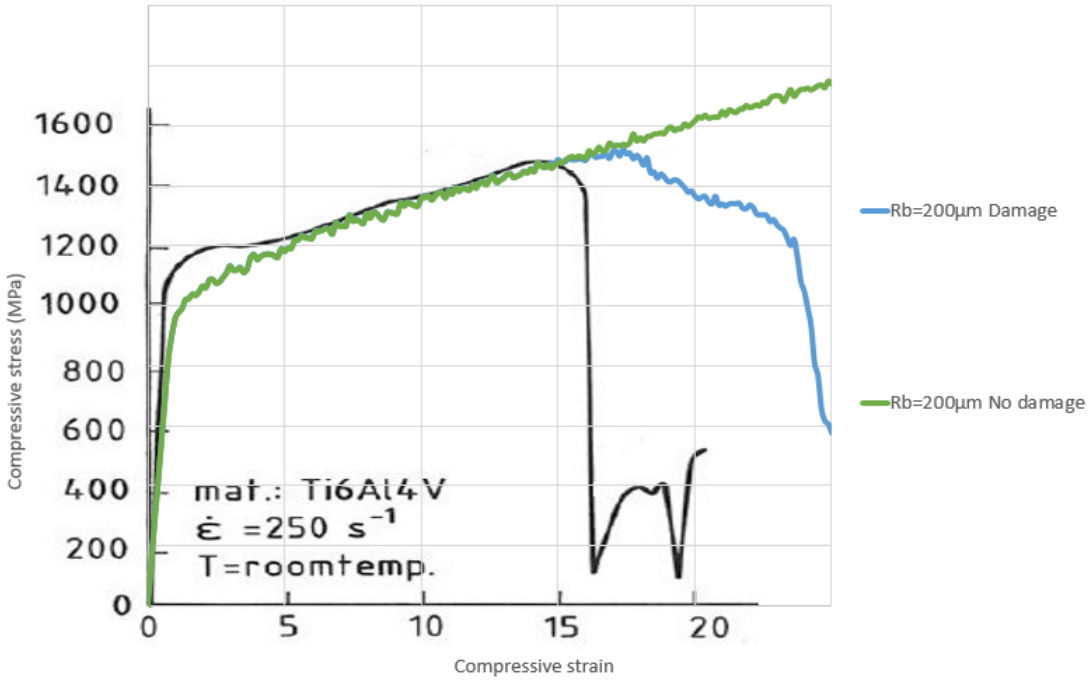

Figure 3.18: Effect of the J-C failure model on the localization in the Shear Banding model

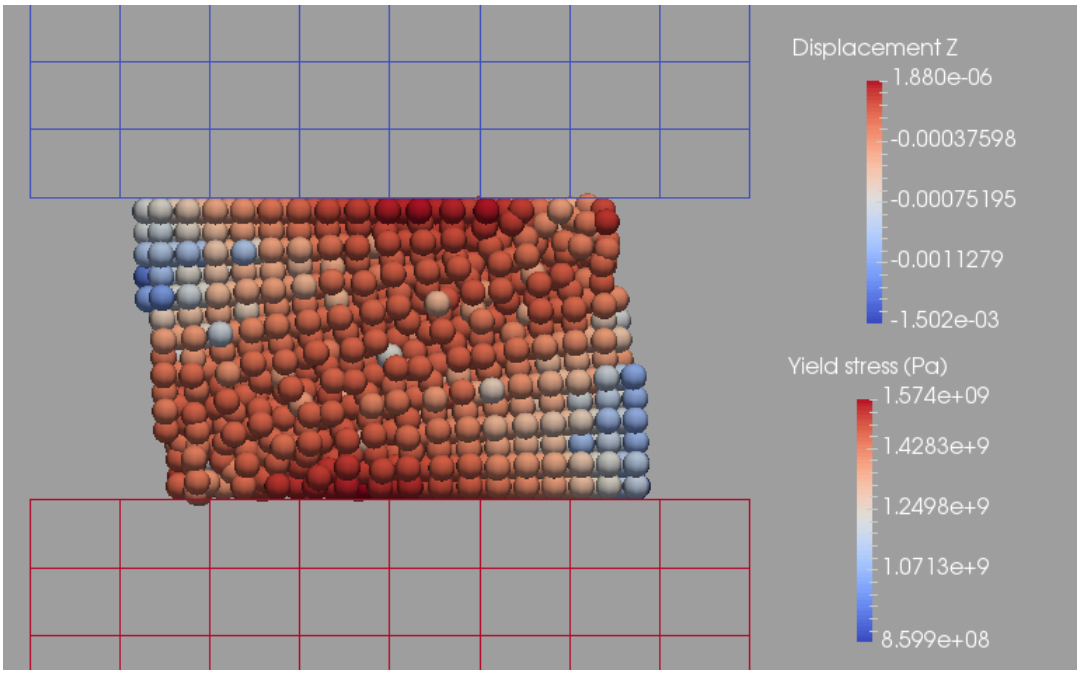

Figure 3.19: Final yield stress field without the J-C failure model

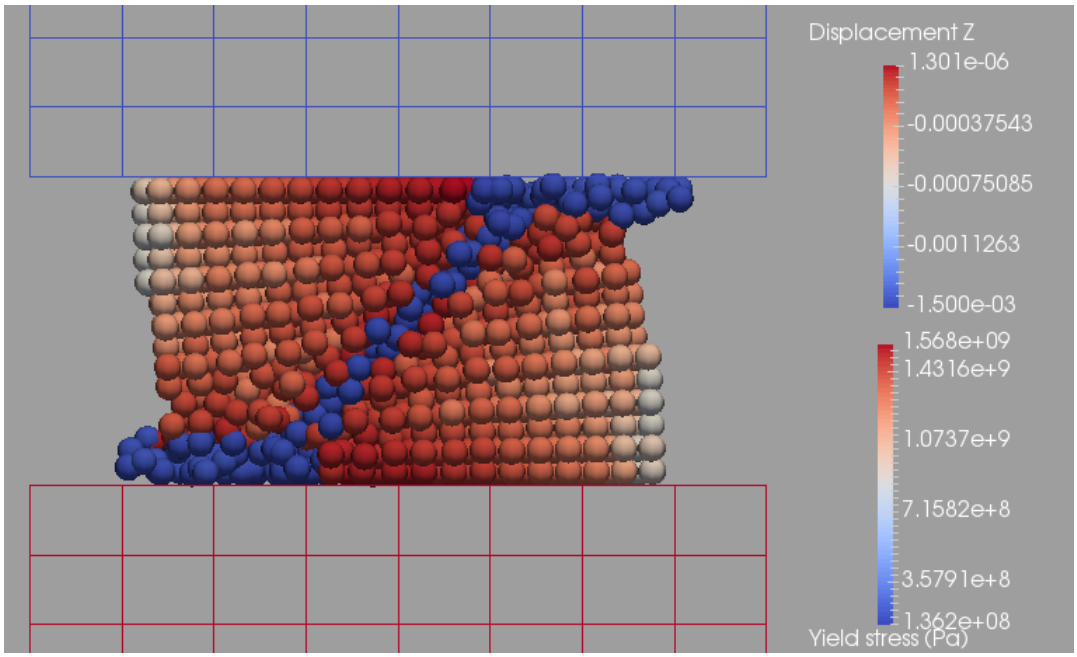

Figure 3.20: Final yield stress field with the J-C failure model

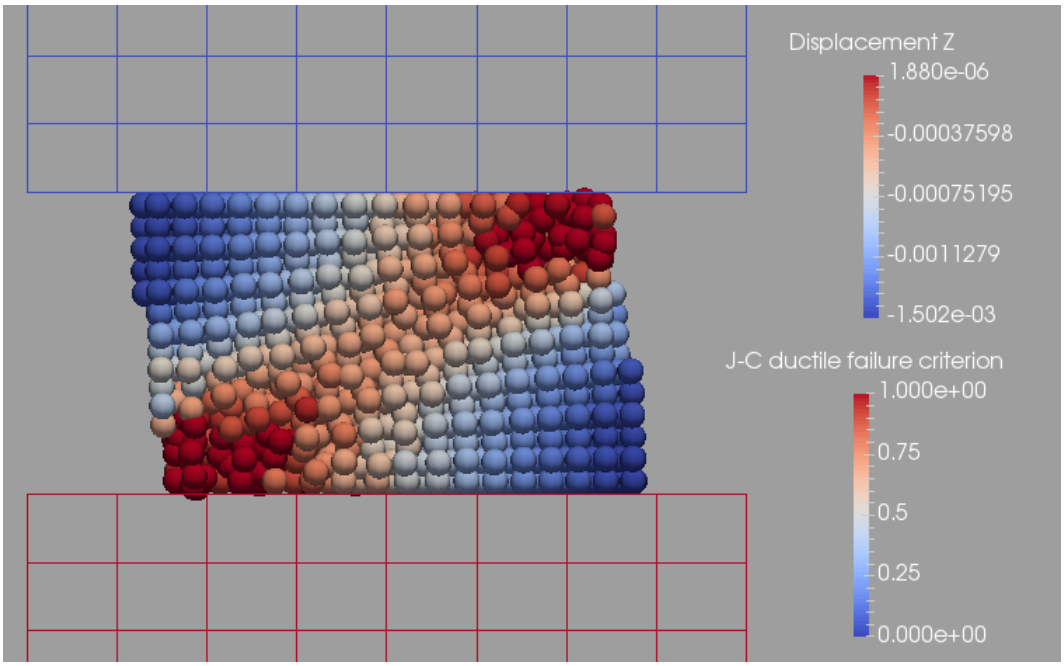

Figure 3.21: J-C failure criterion field, without activating damage

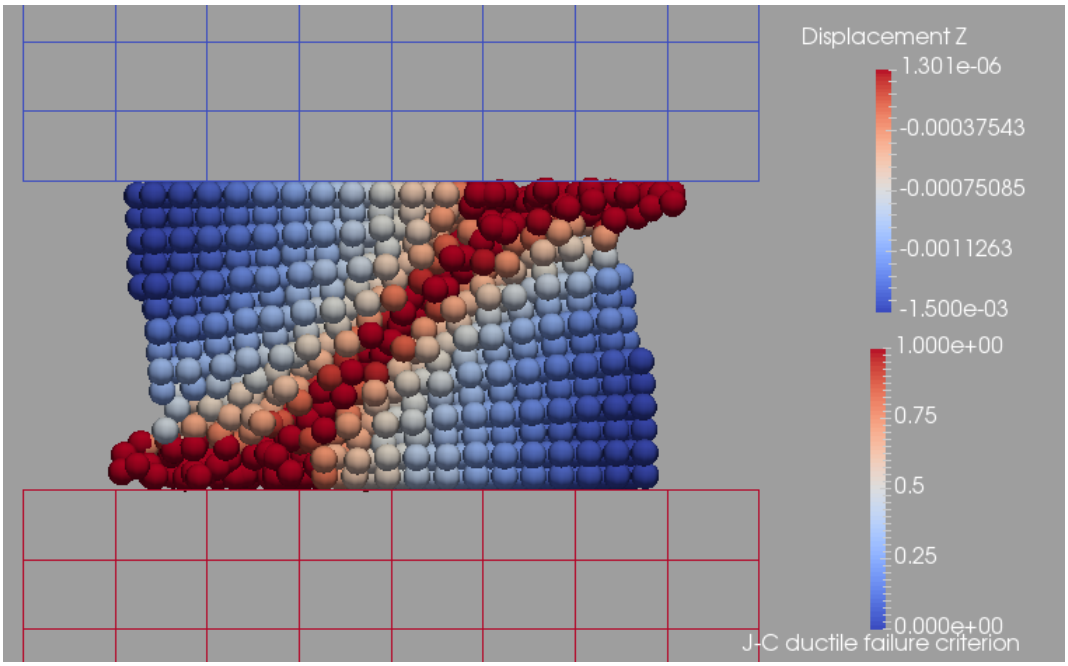

Figure 3.22: J-C failure criterion field, activating damage

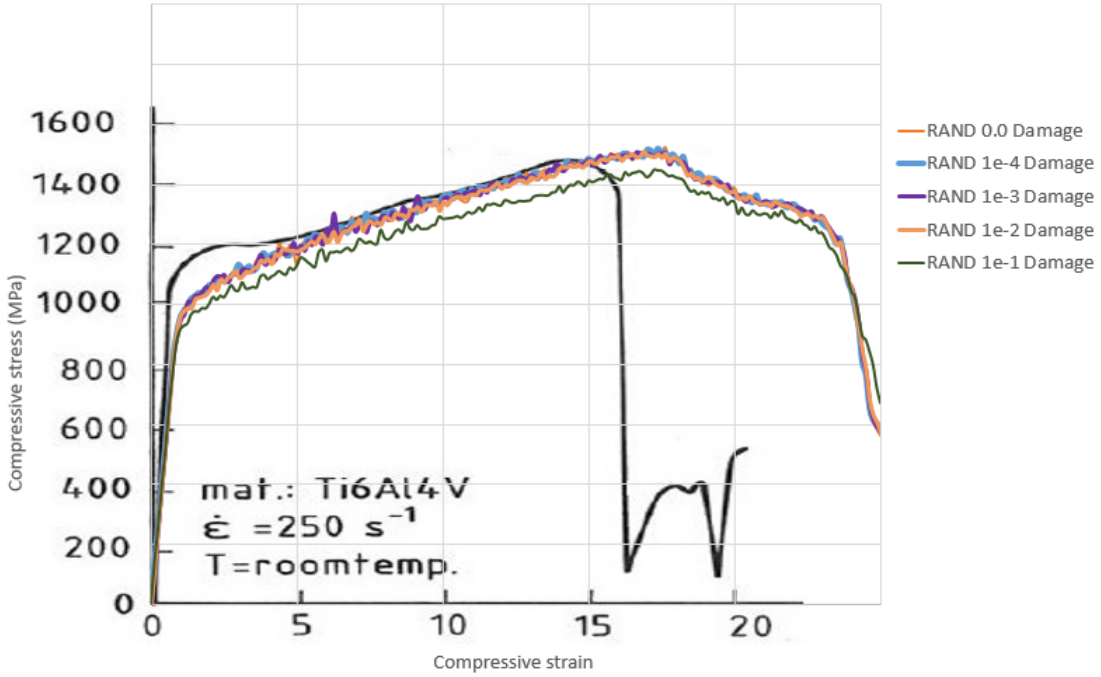

Figure 3.23: Cut view of the tilted cylinder with the random initial damage field

23% compression with a sudden drop in strength of the sample.

3.3.3.1 Influence of material inhomogeneities

Next the influence on initial inhomogeneities in the material is once again assessed, this time with damage softening taken into account. In the same manner as previously, as can be seen in Figure 3.23, the parameter has no effect at 0.01%, 0.1% and 1%, giving the same response as for 0%, but at 10% in maximum random material strength variation, the global strength is decreased during all compression. The localization strain however is still the same. Hence even with damage taken into account, initial material inhomogeneities do not have a critical or helpful effect on shear banding and localization.

3.3.3.2 Influence of mesh size

The effect of the mesh size on the localization strain is investigated by comparing the results given with damage for the initial mesh with an SPH radius $R_b = 200\mu m$ giving 3676 elements, and the finer mesh with $R_b = 100\mu m$ consisting of 29357 elements. The computational time required for these simulations is of 0.9h and 30.5h respectively.

As can be seen in Figure 3.24, refining the mesh seems to primarily improve the behavior at the corners, that is the first loss in strength from 17 to 23% compression. The corners being modeled with more elements, it sounds reasonable to assume that they would not be so quick to fail, swifting upwards the value of the stress before shear band propagation at 23%. It can be assumed that refining the mesh a lot more would give a behavior similar to the experiments, with the slow drop in strength seen between 14 and 16% compression before the dramatic loss in strength, which would then be situated at around 22-23% in our numerical case for the

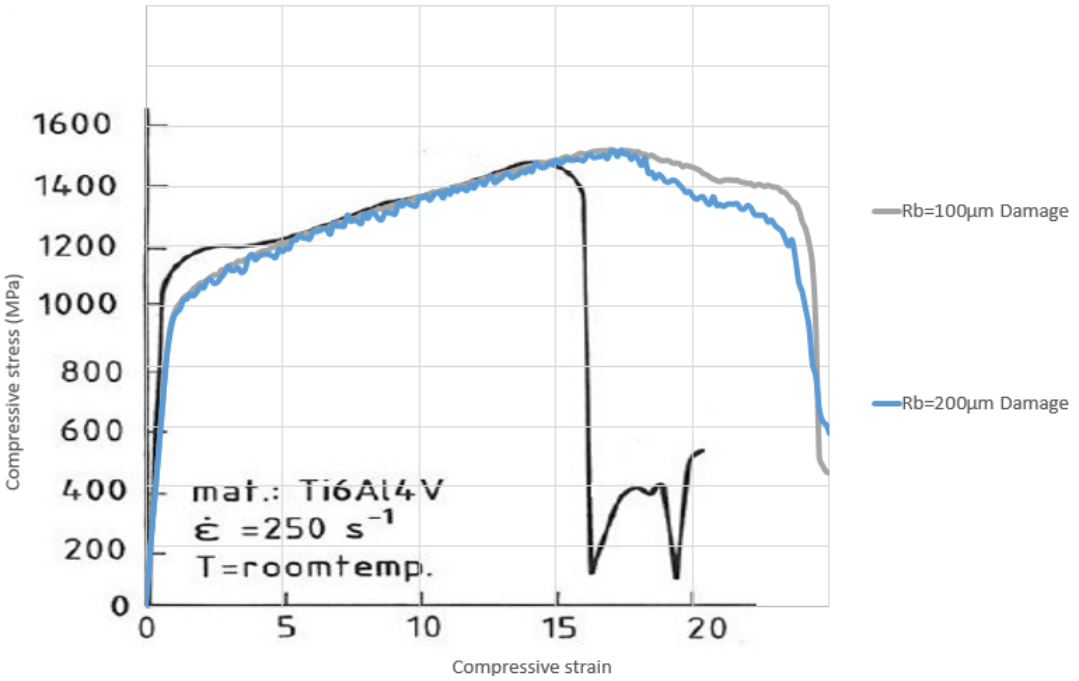

Figure 3.24: Effect of the mesh size on the response of the tilted cylinder

parameters used here. It is worth mentioning also that the strength at final computation time drops lower with the finer mesh, meaning that lower values similar to the experimental case might be achieved.

3.3.3.3 Influence of erosion

The possibility of eroding the SPH particles once then attain the maximum damage D_{max} is also studied. The idea is that to create an actual fracture in the material, SPH nodes have o be eroded, or at least their interaction with surrounding particles has to be canceled. The latter is done here. The effect on the response of the material is shown in Figure 3.27. At first one could think that the trend observed of a steeper drop in material strength is exactly what is desired. However when looking at the actual deformations and material properties fields obtained, shown in Figures 3.28 an 3.29, we can see that the behavior obtained is not that of a propagating shear band, but rather of the continuous eroding of the top and bottom of the cylinder. In conclusion the use of erosion for SPH is not a good tool to simulate shear band initiation and propagation with the corresponding loss of material strength and will not be used in further computations. Also, a lot of numerical instabilities appeared because of the change in SPH neighborhood, especially for the normalizing matrix B. This might once again be adressed by switching to Updated Lagrangian.

3.3.4 Failure evolution laws

Until then no damage evolution law was used. Direct full damage was put on the element as soon as the criterion for damage was met. Here this issue is addressed with the study of the influence of the two failure evolution laws newly implemented for Johnson-Cook in Europlexus:

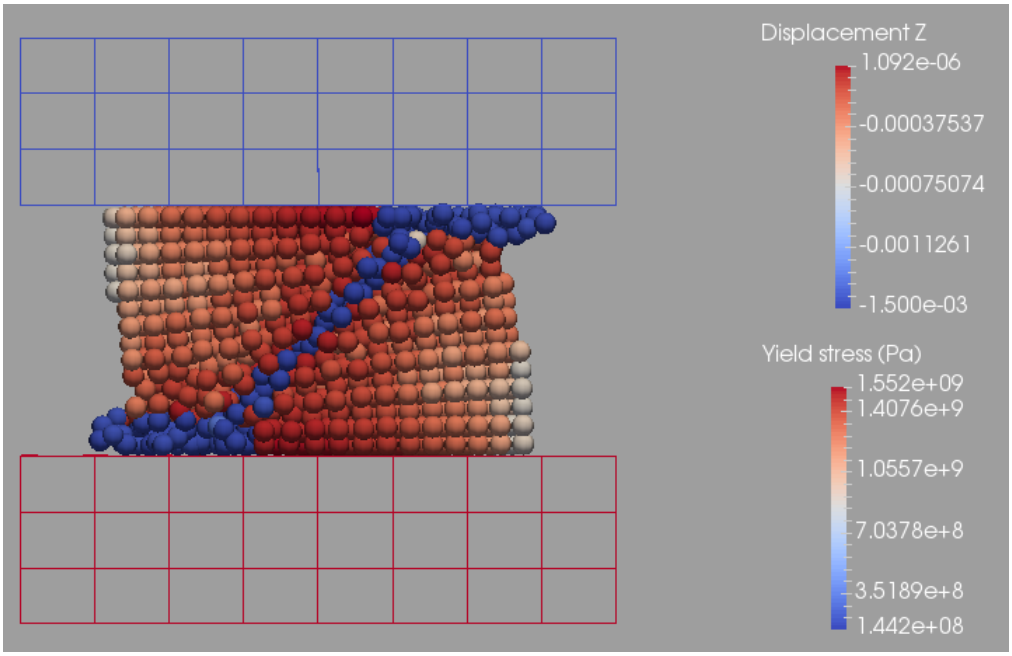

Figure 3.25: Yield stress field in the coarse mesh at final time

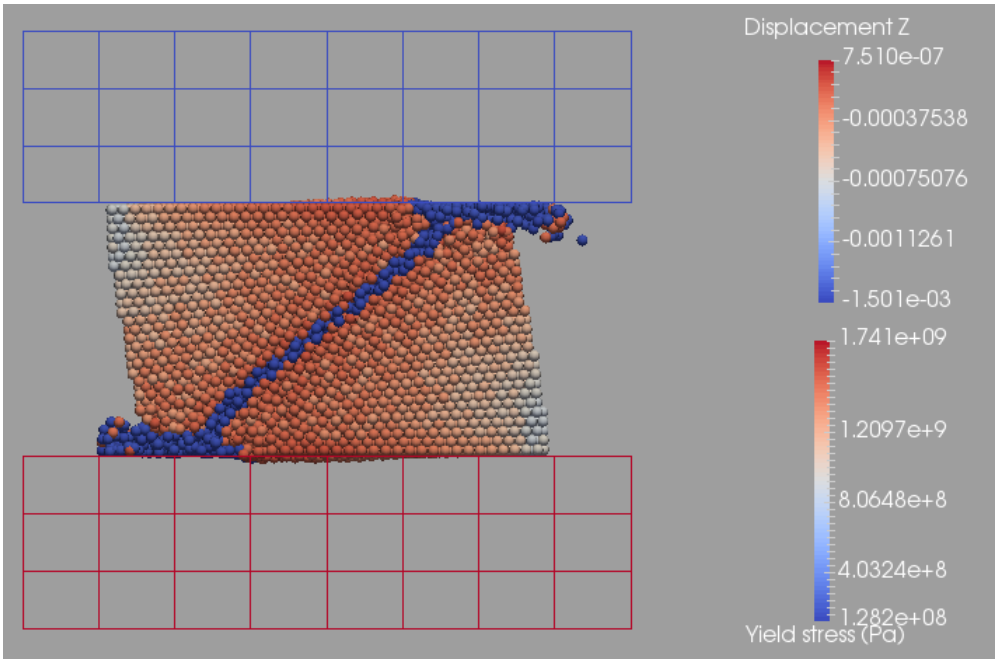

Figure 3.26: Yield stress field in the fine mesh at final time

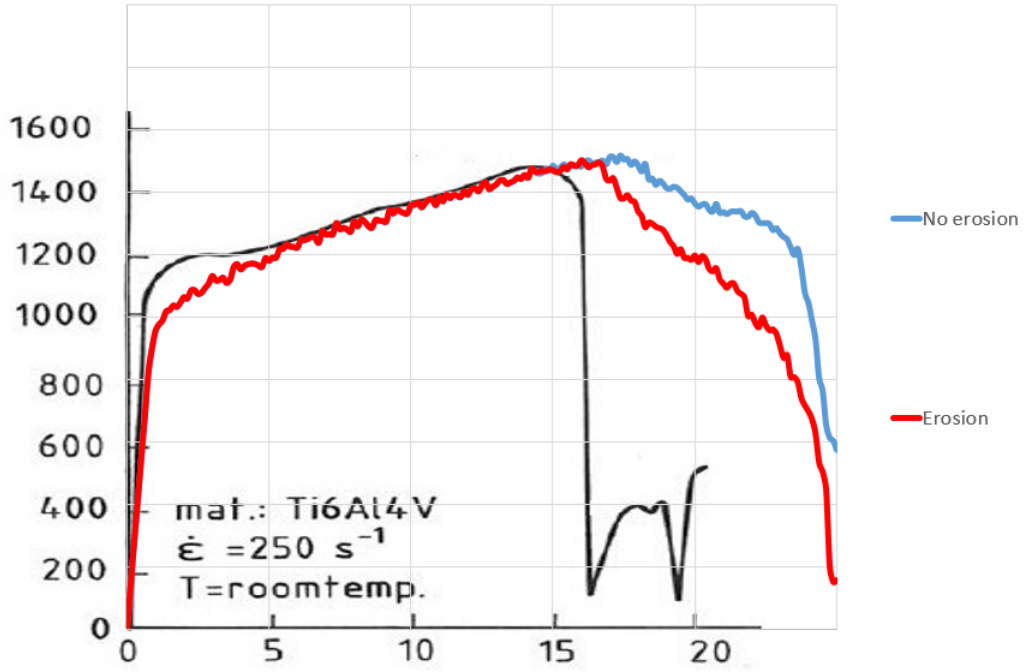

Figure 3.27: Effect of erosion on the response of the tilted cylinder

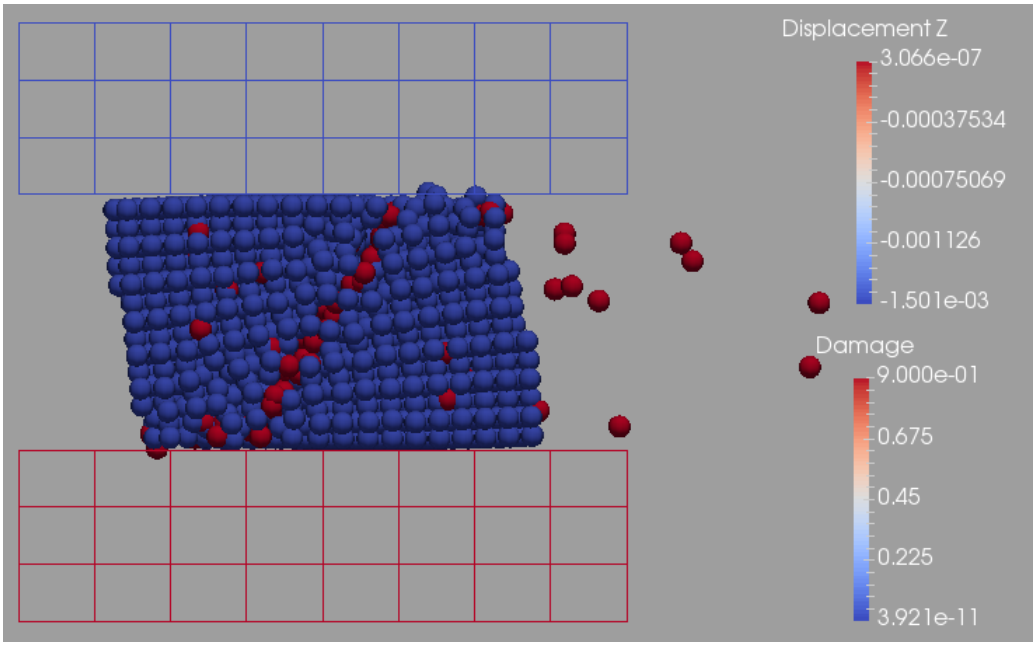

Figure 3.28: Damage field at final time in the case of erosion

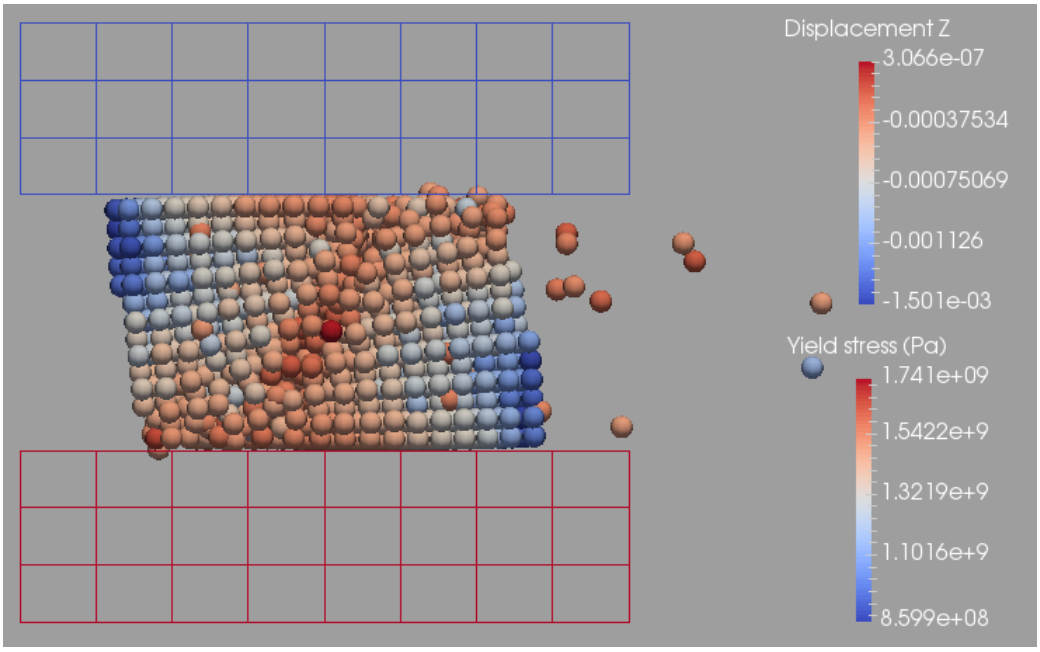

Figure 3.29: Yield stress field at final time in the case of erosion

the fracture energy dissipation law, and the maximum equivalent plastic strain law.

3.3.4.1 Fracture energy

The first law implemented because thought to be the most physically grounded is the fracture energy dissipative law, explained in 1.3.4.2. Figure 3.30 shows the effect of the value of WFRA on the material response. Three values are tested: WFRA = 0.0 J/m corresponds to no fracture energy and the same response as the material without the evolution law, giving a reference for comparison. WFRA = 1000 GJ/m gives the response of the material for an enormous amount of energy to dissipate, meaning the local damage value will actually nearly never increase, and gives back the response for the material without damage. WFRA = 36.13 MJ/m gives the curve for a physically plausible value of the fracture energy for Ti6Al4V per typical element size (the SPH diameter). This value was found for Ti6Al4V using the equation explained in 1.3.4.2 for fracture energy evaluation, given in [CHE 11] and first developed by [MAB 08] for aluminum. As seen in Figure 3.30 however, the change in material overall response for this energy value is found to be negligible. Logically, adding a fracture energy will give a higher localization compressive strain.

3.3.4.2 Maximum equivalent plastic strain

The second law implemented is the maximum equivalent plastic strain law, which, as described in 1.3.4.2, gives the evolution of damage by comparing current local equivalent plastic strain with the equivalent plastic strain at damage initiation and the maximum equivalent plastic strain for damage, for which the material is considered to have completely failed, or at least attained the maximum damage value possible.

Figure 3.31 shows the effect of increasing this maximum equivalent plastic strain to values of 1, 2 and 3. The overall effect is to increase the localization strain to values not contained in

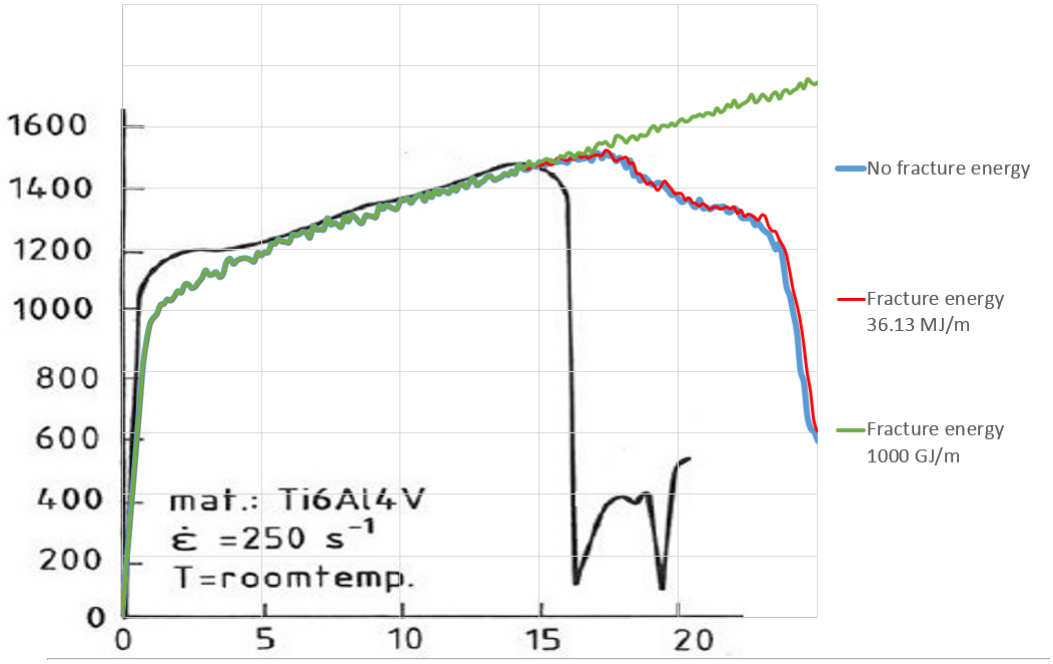

Figure 3.30: Stress-strain curves for different values of the fracture energy in the damage evolution law

the graph, even with only a value of 1. For 2 and 3, virtually the same response as the material with no damage is obtained on the compressive strains considered.

3.3.5 The Shear damage initiation criterion

The previous work was done entirely with the Johnson-Cook ductile failure initiation criterion, but a second one is also used in this work, allegedly more capable of simulating shear bands but also more complicated: the shear failure initiation criterion. This small section presents briefly an example of its use and the effect on the response of the material compared with the Johnson-Cook ductile failure criterion in Figure 3.32. The parameters used are complicated and not the subject of this work, suffice to know that the ones available for aluminum in the Abaqus documentation on Shear Failure is used, once again however fitted to obtain a localization in the compressive strains of interest. The behavior obtained is overall very similar to the case of the Johnson-Cook ductile failure criterion, as can also be seen on Figures 3.33, 3.34 and 3.35, with only some more flattened corners to be seen. Thus the Shear failure model is validated as also able to simulated a shear band and a localization.

3.3.6 Discussion on the results

The model is thus not yet completely satisfactory in terms of post-initiation and shear band propagation behavior, and more work is required to improve the model to better predict shear bands, especially since other materials like aluminum and copper with their own sets of parameters to fit to experimental values will be used in the next simulations.

This was however not the point of this small study, it being more about concept and implementation validation, and the need for a localization realistic enough to connect with the

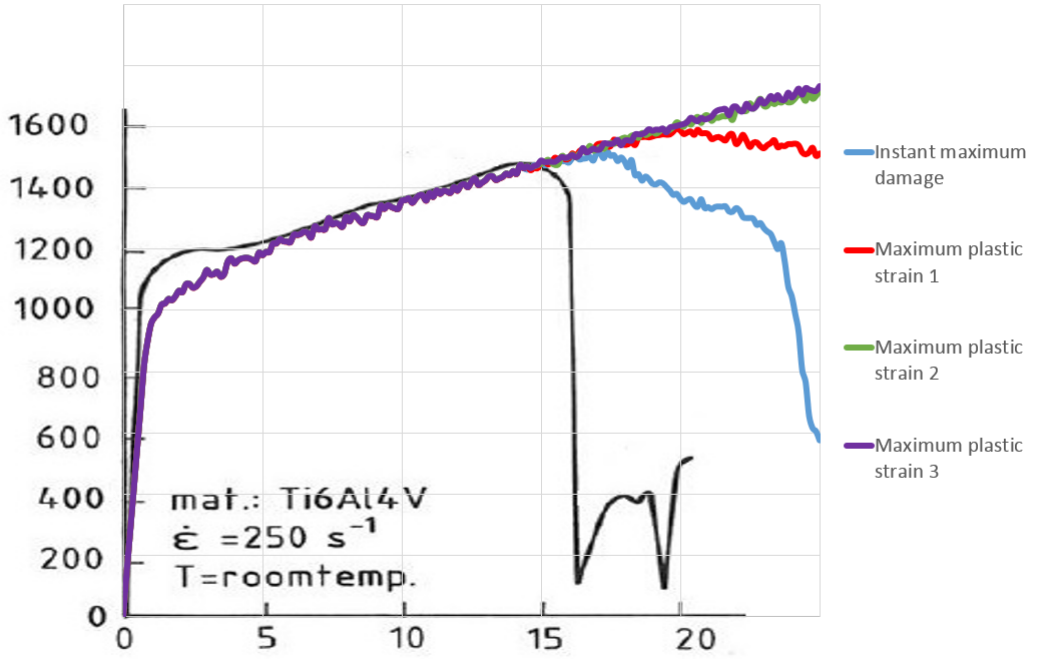

Figure 3.31: Stress-strain curves for different values of the maximum equivalent plastic strain in the damage evolution law

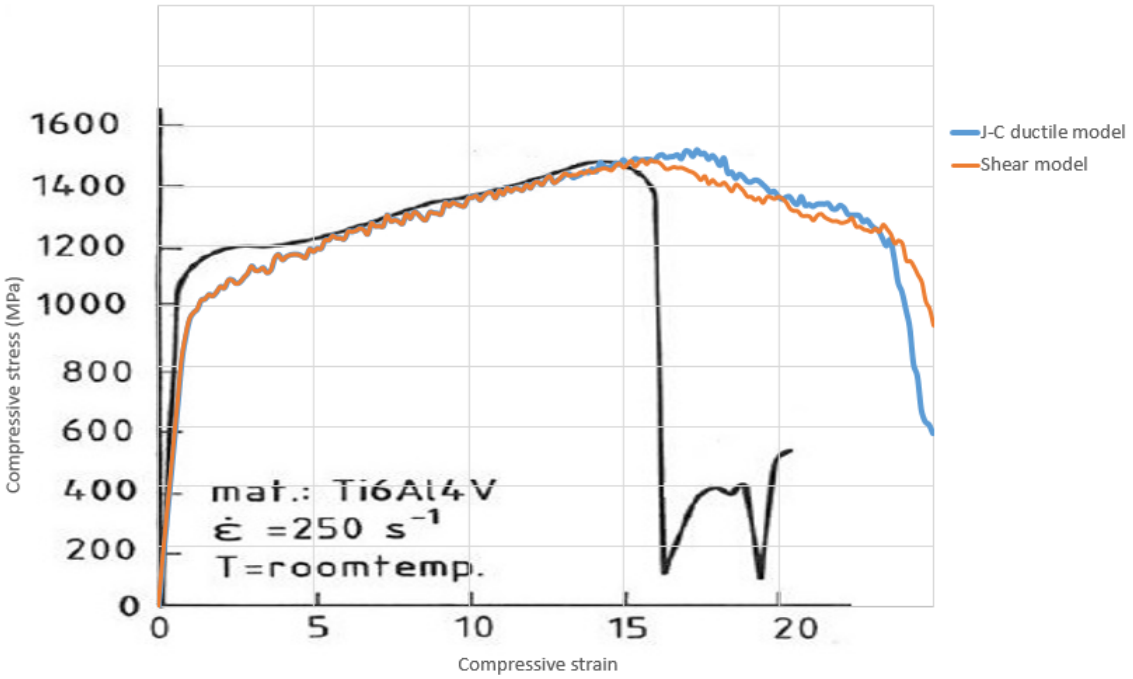

Figure 3.32: Stress-strain curve for the Shear failure model

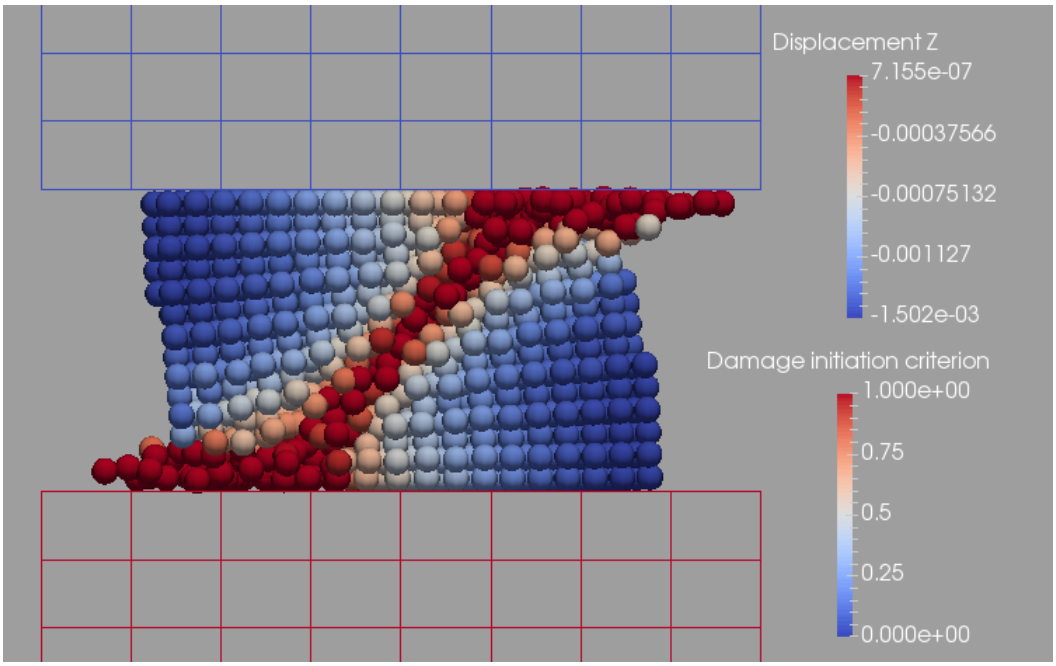

Figure 3.33: Damage initiation criterion field at final time in the case of a Shear failure criterion

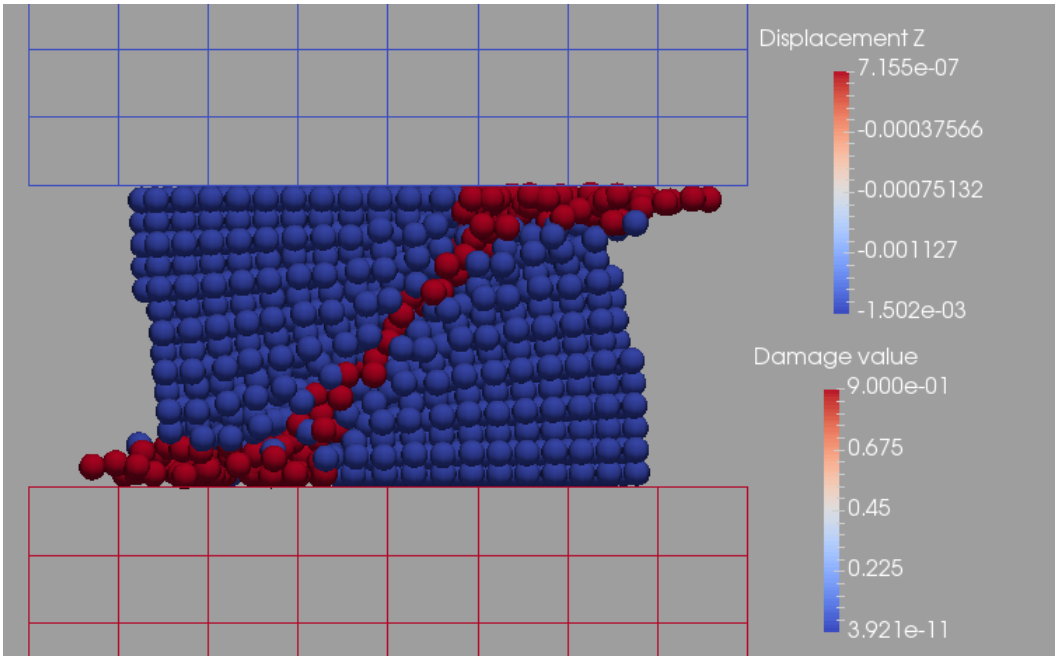

Figure 3.34: Damage field at final time in the case of a Shear failure criterion

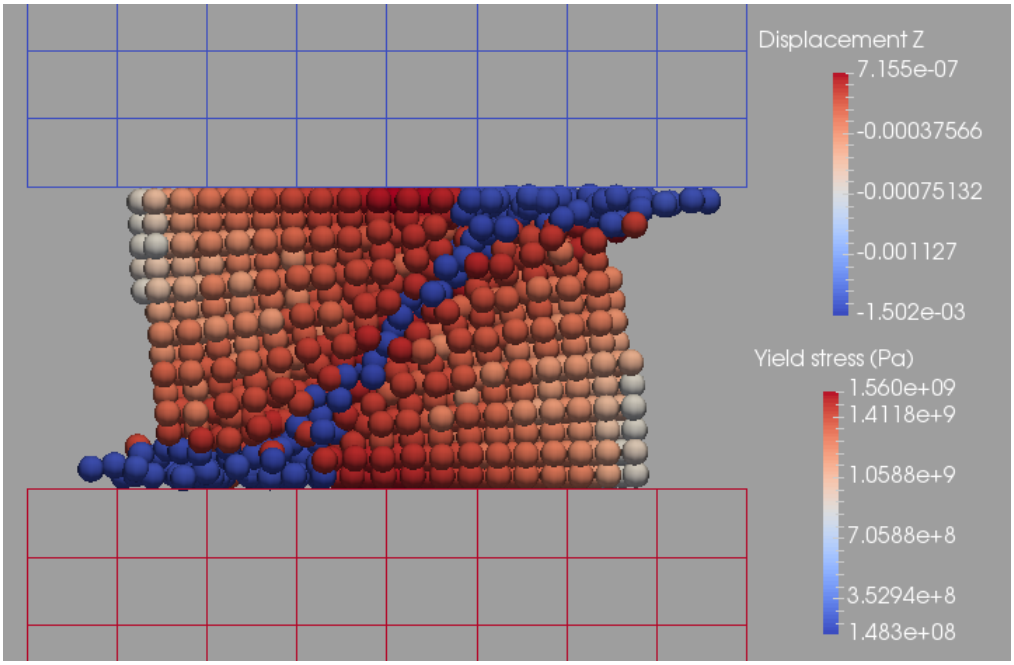

Figure 3.35: Yield stress field at final time in the case of a Shear failure criterion

adhesion model.
In the rest of this work only parameter values and failure laws already used in other papers will be directly used for the simulations of particle impacts with copper and/or aluminum.

3.4 Study of a particle impact without adhesion

The next step is then to apply the tools previously validated in an actual particle impact situation. The goal is to perform a convergence study which would take into account all the elements which would be present in the final model (except for now the adhesion interaction model).

The convergence of the model is evaluated in the case of the impact of an aluminum particle on a copper substrate without adhesion, using SPH elements for the particle and Finite elements for the substrate since the latter is harder. The parameters used for each material in the Johnson-Cook equation can be found back in the second chapter in Table 2.1 for aluminum and Table 2.2 for copper. Four different meshes are used, with SPH particle radii R_{SPH} of 1.25μm, 1.00μm, 0.75μm and 0.5μm. Each time, the FE mesh for the substrate is also refined so as to keep the element size similar to the SPH particle diameter, giving for the first mesh 737 SPH particles and 3703 FE. The second mesh contains 1443 SPH particles and 9000 FE. The third mesh contains 3422 SPH particles and 33135 FE. Finally the fourth mesh contains 11534 SPH particles and 72000 FE. Final computation time is chosen as 0.2 μs. In these simulations, a particle of radius $R_b = 12.5\ \mu m$ impacts a substrate of lengths $L_s = 60.0\ \mu m$ and height $H_s = 20.0\ \mu m$ at initial velocities ranging from 100 m.s^{-1} to 1000 m.s^{-1}.

For copper, because no direct shear failure parameters were found, the Johnson-Cook ductile failure initiation criterion is used, with values taken from [YIL 11] and shown in Table 3.4. The author also describes a method to obtain shear failure parameters, but this method actually gives

Table 3.4: Johnson-Cook failure parameters used for copper(modified [YIL 11])

Properties	Parameter	Value	Unit
Ductile Failure (Johnson-Cook failure model)	d_1, d_2, d_3, d_4, d_5	0.3, 0.28, 3.03, 0.014, 1.12	
Damage evolution	Maximum Initial Damage	0.001	
	Plastic strain at failure	2.0	

the strain at the maximum stress on Johnson-Cook yield stress curves for different strain rates, which is actually somewhat different from the actual localization strain at which the material undergoes a severe loss in strength. The method given thus only gives the strains at which thermal softening overtakes strain hardening. For aluminum, the shear failure parameters found in the input files for the "Progressive failure analysis of thin-wall aluminum extrusion under quasi-static and dynamic loads" example available on the online Abaqus Example Problems Manual [SIM 14] were used to compute equivalent plastic strains for which shear instability occurs, as a function of strain, strain-rate and temperature. These parameters originally come from [HOO 04] (access requires payment).

The results are shown in Figure 3.36. Figure 3.36(a) represents the change in height of the particle, Figure 3.36(b) is the particle penetration in the substrate (as a percentage of its initial height), and Figure 3.36(c) shows the final rebound velocity of the particle. The first observation to be made is that results for the finer meshes are not available for high initial impact speeds, with 900 m.s^{-1}, 800 m.s^{-1} and 600 m.s^{-1} as maximal impact speeds for which the meshes manage to finish the simulation. Figure 3.37 shows the result of the yield stress field in the particle and vertical displacement for the substrate in the case of a 500 m.s^{-1} impact. The local drop in yield stress near the interface is clearly visible as well as some form of jetting of the particles.

The main limitation at higher speeds is the sudden drop in stable time increment due to the intense localization of SPH particles, "fleeing" the contact zone. Erosion of these particles could solve this problem but result in its own instabilities and are not always the best method as seen in the previous section. A solution to make these computations with finer meshes stable is currently investigated. An example of a particle impacted at 900 m.s^{-1} is shown in Figure 3.38, where we can clearly see the problem of the SPH particles not behaving correctly.

Until then however, the model is already very consistent in its predictions in terms of deformations, and in terms of rebound speed for impact speeds under 700 m.s^{-1}, which is usually enough to get a realistic critical speed. The goal is not anyway to get a complete clear convergence of results with mesh refinement since the model includes a localization process, known to be intrinsically mesh dependent.

3.5 Adhesion model validation

In this section the numerical tests used to validate the adhesion model presented in 2.2 are discussed and the ability of this model to recreate a critical and maximum velocity as in Cold

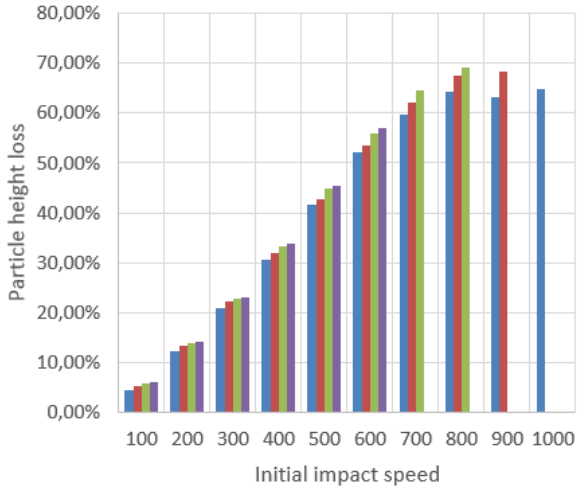

(a)

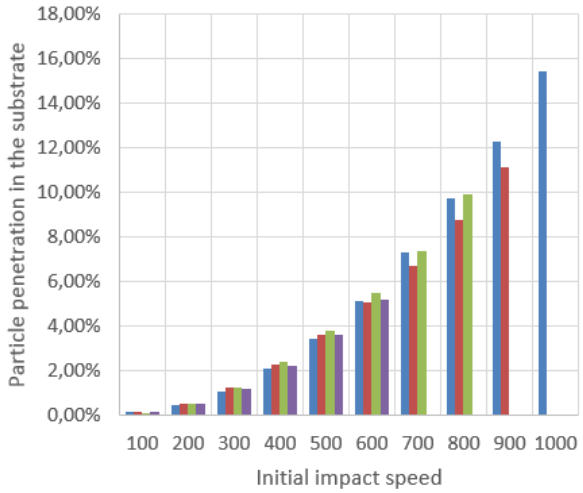

(b)

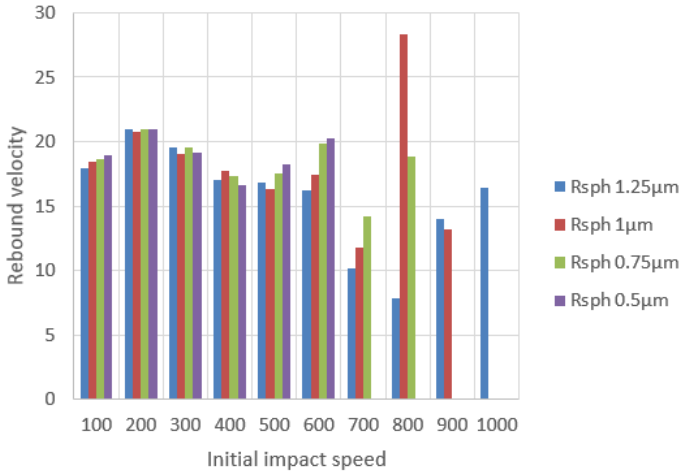

(c)

Figure 3.36: Convergence with SPH particle radius for Al on Cu, SPH on FE impacts

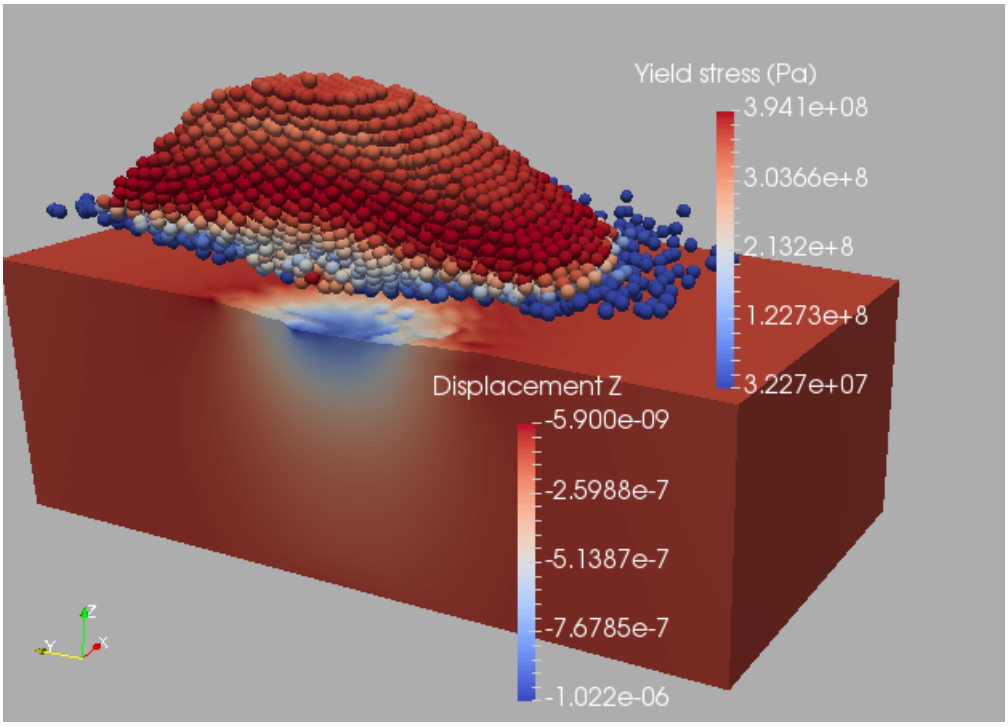

Figure 3.37: Yield stress field at final time in the case of 25 μm SPH copper particle impacting an FE aluminum substrate at 500 m.s^{-1}

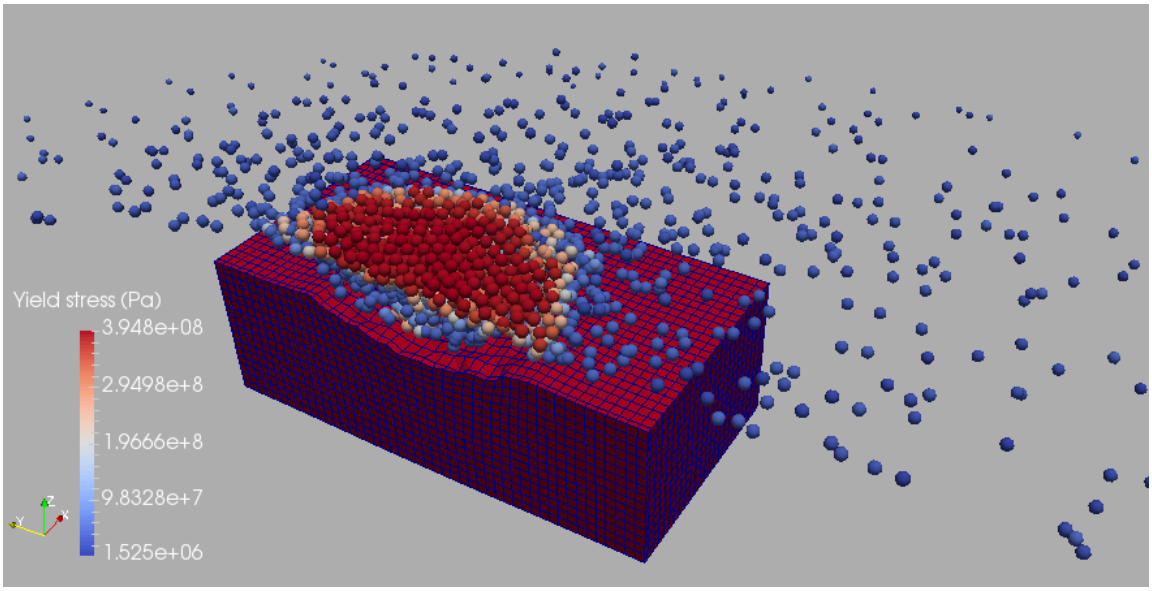

Figure 3.38: Yield stress field at final time in the case of 25 μm SPH copper particle impacting an FE aluminum substrate at 900 m.s^{-1}

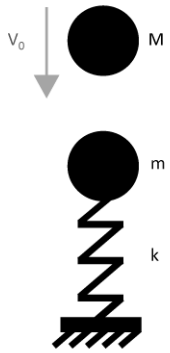

Figure 3.39: The basic impact model

Spray is demonstrated.

3.5.1 Basic models validations

First basic models are used as demonstration tools because of the complexity of the final particle impact model and te energy exchanges and variations involved in it. The complexity will thus be incrementally increased.

3.5.1.1 Adhesion elementary problem and its quasi-analytic solution

First, let us consider the very simple case of the impact of a rigid sphere of mass M projected vertically downward with a negative velocity V_0 onto another rigid sphere of mass m, initially at rest, supported by a spring of stiffness k (Figure 3.39).

In the case of a spring with zero stiffness, one has simply two masses in contact. We shall show that in this case, and in this case alone, the final velocities of the spheres depend only on the cohesive energy G_C, and not on the magnitude of the cohesive load F_c which exists during the adhesion phase. The velocities after the rebound can be easily calculated by expressing the conservation of the momentum and kinetic energy through the impact. The velocities of masses M and m immediately after the impact are:

$$\begin{aligned} V_1 &= \frac{M-m}{M+m} V_0 \\ v_1 &= \frac{2M}{M+m} V_0 \end{aligned} \tag{3.1}$$

Immediately after the impact, the gap opens with the opening velocity $-V_0$. One can calculate the movement of the two masses by solving the momentum conservation equation for each mass. Let (A, V, U) and (a, v, u) be the acceleration, velocity and displacement of masses M and m respectively, and let F_c be the cohesive force which resists the movement. If $V_1 > 0$, one has:

$$\begin{aligned} M\,A &= -F_c \\ m\,a &= F_c \end{aligned} \tag{3.2}$$

which leads to the equations of the velocities and displacements of the two masses as functions of time:

$$\begin{aligned} V(t) &= V_0\frac{M-m}{M+m} - \frac{F_c}{M}t \\ v(t) &= V_0\frac{2M}{M+m} + \frac{F_c}{m}t \end{aligned} \tag{3.3}$$

$$\begin{aligned} U(t) &= V_0\frac{M-m}{M+m}t - \frac{F_c}{M}\frac{t^2}{2} \\ u(t) &= V_0\frac{2M}{M+m}t + \frac{F_c}{m}\frac{t^2}{2} \end{aligned} \tag{3.4}$$

Then, one can calculate the evolution of the gap over time. The cohesive forces cease to be active when the gap reaches the value gap_c. Thus, one can calculate the time at which the gap opens, which is the solution of the second-degree equation:

$$0.5\frac{F_c^2}{2}\frac{m+M}{mM}t^2 + V_0F_ct + G_C = 0 \tag{3.5}$$

The initial velocity must be sufficient for the mass to separate ($V_0 > \sqrt{2.G_C\frac{m+M}{mM}}$). This separation occurs at time:

$$t_c = \frac{-V_0 + \sqrt{V_0^2 - 2.G_C\frac{m+M}{mM}}}{F_c\frac{m+M}{mM}} \tag{3.6}$$

One can immediately see, by substituting t_c for t in Equation (3.3), that the final velocities of the masses depend only on G_C. Now, if one considers that mass m is supported by a spring of stiffness k, Equation (3.2) becomes:

$$\begin{aligned} MA &= -F_c \\ ma + ku &= F_c \end{aligned} \tag{3.7}$$

The evolution of the gap as a function of time in the absence of cohesive forces is given by the following equation:

$$Gap(t) = V_1t - \frac{v_1}{\omega}sin(\omega t) - F_c(\frac{1}{M} + \frac{1-cos(\omega t)}{k})\frac{t2}{2} \tag{3.8}$$

with $\omega = \sqrt{\frac{k}{m}}$. There is no simple solution giving the time of separation, but one can solve the equation numerically (e.g. using Mathematica) for specific values of the constants. Table 3.5 compares, for a particular case, the separation velocities of mass M obtained with several values of F_c for the same cohesive energy G_C. Here, we chose a mass M equal to 1, a mass m equal to 2 and a stiffness k equal to 0 or 0.5. The initial velocity was -1. We chose $G_C = 0.2$. One can observe that the separation velocity of mass M is independent of the choice of F_c if k=0, but not if k=0.5.

Table 3.5: The effect of the choice of the cohesive stress on the particle's rebound velocity: elastic rebound with $G_C = 0.2$ J.m^{-2}

F_c	k=0.0	k=0.5
0.05	0.0898	0.000
0.5	0.0898	0.086
5	0.0898	0.091

Thus, contrary to the quasi-static case, the choice of the magnitude of the cohesive stress has an essential influence on the rebound velocity when the elasticity of the bodies in contact is taken into account.
If ωt_c is small, one can carry out an expansion of the sine function in $Gap(t_c)$, which leads to the same solution as when there is no elastic support. In this case, the magnitude of the cohesive force has no influence on the separation velocity of mass M.

3.5.1.2 SPH cylinder impact with adhesion and size effect

In this section, our goal is to show that taking adhesion into account induces a size effect. This effect is predictable. The strain and kinetic energies are proportional to the volume, whereas the adhesion energy is proportional to the area. Consequently, if one does not take the adhesion effects into account, the cylinder's rebound effects are the same regardless of the size of the particle impacting the substrate. Conversely, if these forces are taken into account, the smaller the particles, the lower the rebound velocities.

Elastic impact of an aluminum cylinder of radius 12.5 μm and height 16.67 μm (so its initial kinetic energy is the same as that of a sphere of similar radius) which is projected at 20 ms^{-1} onto a cylindrical target of radius 25 μm with the same height (16.67μm). The cylindrical target is built-in at its base. The Young's modulus is 70,000 MPa, the Poisson's coefficient is 0.3 and the density is 2.7. We assumed a surface density of adhesion energy $G_C = 0.02$ J/m^2. The SPH mesh was compact hexagonal with 618 SPH in the impactor and 2,526 SPH in the support. The radius of each SPH was 1.25 μm. Therefore, there were 20 SPH along a diameter. We chose not to set a maximum cohesive stress. The calculations were carried out with 7 10^{-12} s time steps. Then, the same calculations were repeated after multiplying the time steps and the dimensions by 10, and then by 100, keeping the same material constants and the same adhesion surface energy. The calculations without and with adhesive forces were compared. The calculations without adhesive forces, which are dimensionless with respect to time, all lead to the same time history of the velocity of the impactor: in all cases, the particle rebounds with a velocity of $12ms^{-1}$. Figure 3.40 shows the evolution of the total adhesion energy available in the contact for the 3 calculations.

One can observe that the impact of the largest specimen quickly consumed all the available adhesion energy and the impactor bounced back. The two other cases show that only 5.5% (for the smallest particle) and 55% (for the medium-size particle) of the adhesion energy were consumed after 20,000 calculation steps. The two smallest particles remained stuck to the substrate. The observation of the time history of the average gap (Figure 3.41) shows that after a first major rebound the gap oscillates and regresses progressively for the smallest two particles. These small oscillations about the motionless "stuck" state actually dissipate very little energy,

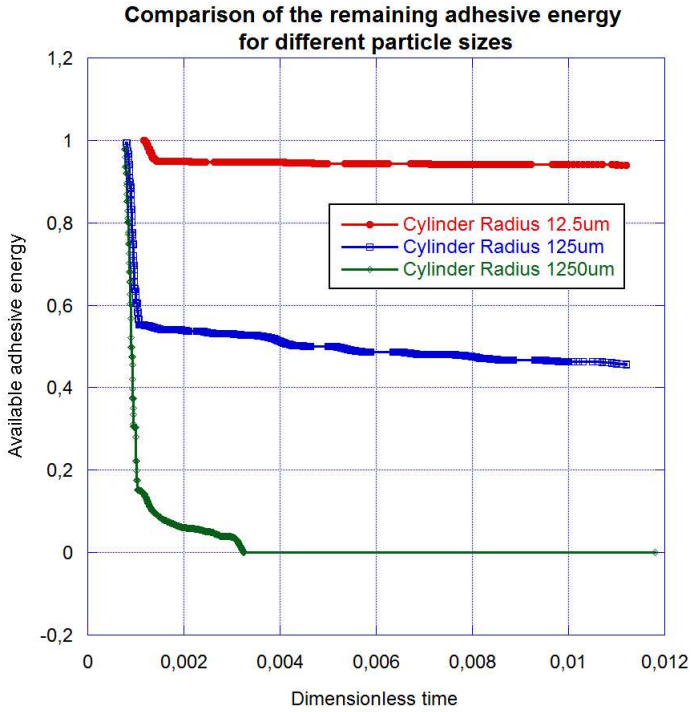

Figure 3.40: The adhesion energy dissipation for the 12.5μm, 125μm and 1,250μm cylinders

which enables us to conclude that the sticking would continue even over longer calculations. For the largest specimen, the gap does not follow the same trend and tends toward infinity upon complete separation near t=3.5ms. The rebound velocity is much lower than in the free case ($1.64ms^{-1}$ *vs.* $12ms^{-1}$).

As anticipated, there is, indeed, a size effect.

3.5.1.3 Discussion

We clearly showed the importance of scale effects in this problem. With the SPH model, we arrive at the same conclusions as with the quasi-analytic model: in the absence of adhesion, there is no scale effect. If there is adhesion, the smaller the particle, the better it adheres. It might seem surprising that the particle would stick even though the adhesion energy is very small compared to the initial kinetic energy. The observation of the time history of the energies of the various subsets shows that the two objects start vibrating at very high frequency during the contact. The activation of the cohesive forces leaves enough time for these high-frequency energy exchanges to take place and, thus, to borrow from the initial kinetic energy.
Figure 3.42 shows the evolution of the various energies involved during the impact, with and without adhesion, for the largest-diameter cylinder and for the intermediate-diameter cylinder. One can see that the main difference between the larger cylinder which separates and the smaller cylinder which sticks lies in the distribution of the strain energy (internal energy) between the substrate and the particle. The longer sticking time in the case of the medium-sized cylinder allows more strain energy to move from the particle to the substrate, which hampers the separation of the particle.

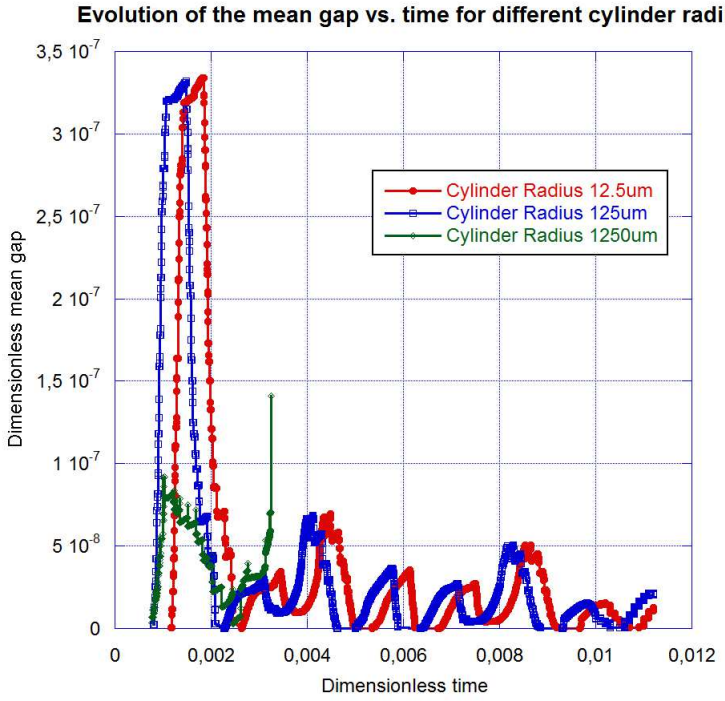

Figure 3.41: Evolution of the gap for the 12.5μm, 125μm and 1,250μm cylinders

3.5.2 Impact of a spherical projectile onto a substrate

Now, let us consider the impact of a spherical particle of radius 12.5μm onto a parallelepipedic substrate of length 75μm and height 33.4μm. The particle and the substrate were meshed using respectively 737 and 15,776 SPH. First, we will study an elastic impact and focus on the effect of the choice of the adhesion model's maximum cohesive stress on the rebound velocity. Then, we will study how the boundary condition chosen at the base of the substrate affects the rebound. Finally, we will address the elastic-plastic case, which gives a more realistic representation of the behavior of the particle's and substrate's material, using the Johnson Cook elastic-plastic model with adiabatic thermal softening.

3.5.2.1 Impact in elasticity: effect of the adhesive stress

Here, we compare the results of the rebound velocities with various adhesion parameters for a $-20ms^{-1}$ velocity of the spherical impactor. The adhesion surface energy is still $G_C = 0.02J/m^2$. First, let the parallelepiped be built-in at its base. The Griffith adhesion model uses the Lagrange coefficient given by the contact algorithm directly. The Dugdale model requires a maximum cohesive stress σ_c, whose magnitude was incremented from 100 to 1,600 MPa. Because of this choice, the largest allowable gap prior to the rupture of a cohesive link was 0.2 nm, which remains very small compared to the size of the objects being considered and the radius of the SPH spheres. Figure 3.43 shows the variation of the particle's velocity during impact as a function of the maximum adhesive stress.

One can see that the choice of the maximum adhesive stress has a significant influence on the time history of the velocities, and that the final rebound velocity is highly dependent on the adhesive stress level chosen (Figure 3.44).

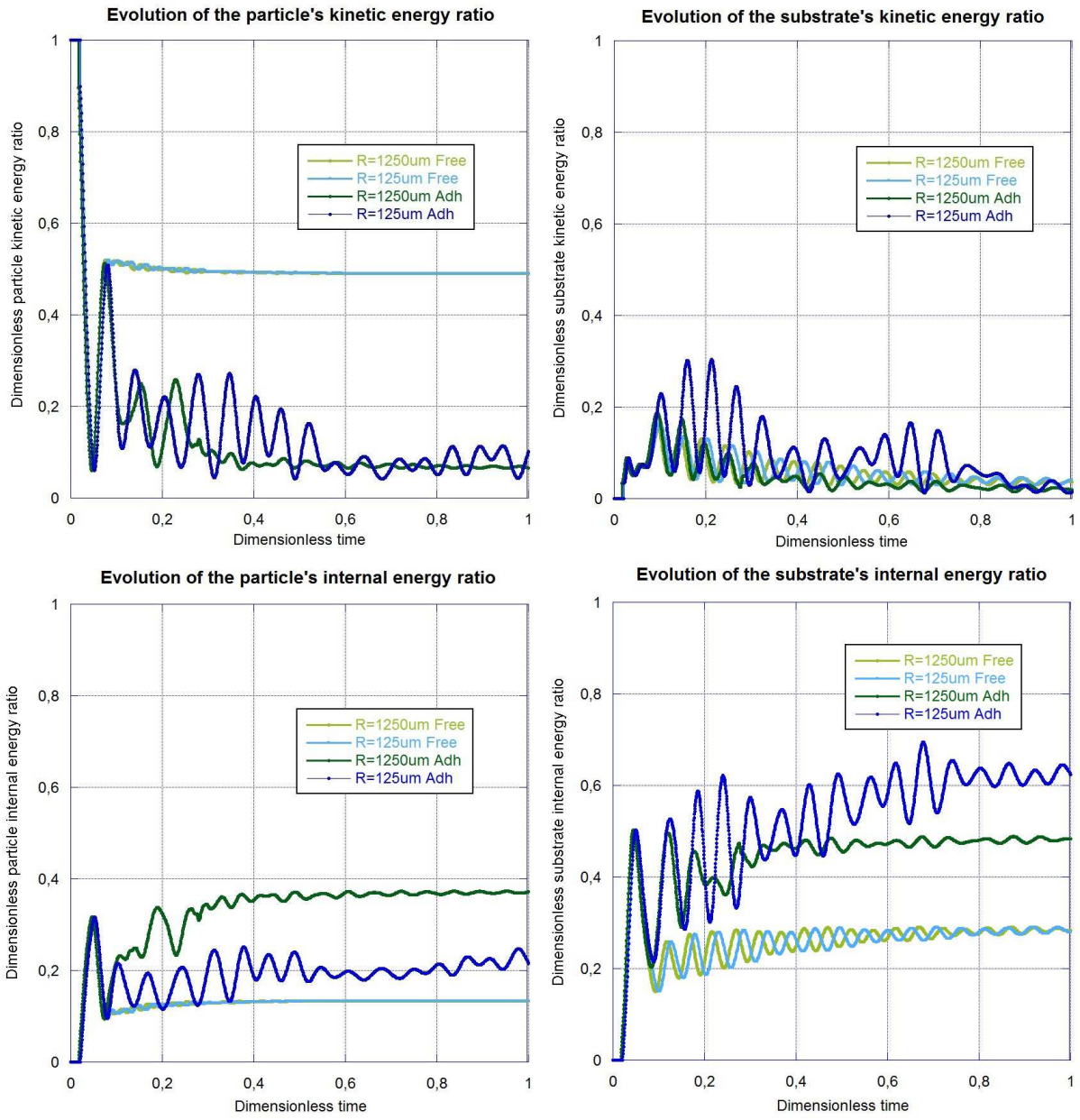

Figure 3.42: Energy distribution during the cylinder impacts

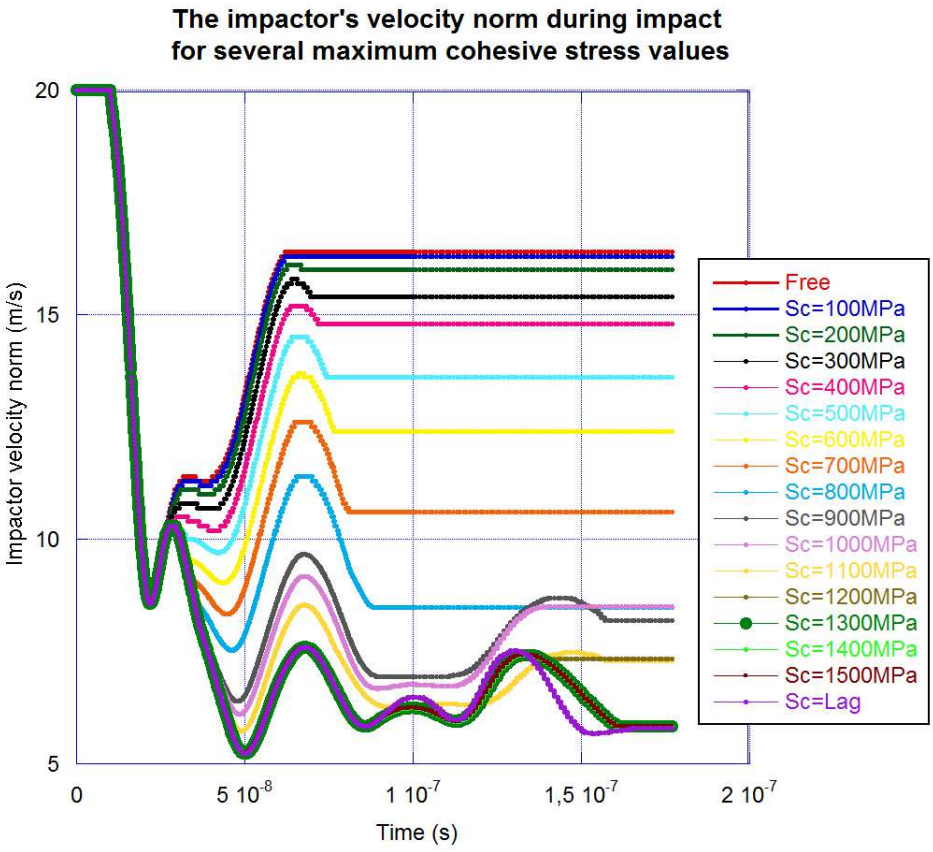

Figure 3.43: Evolution of the velocity norm during impact for several values of the maximum cohesive stress

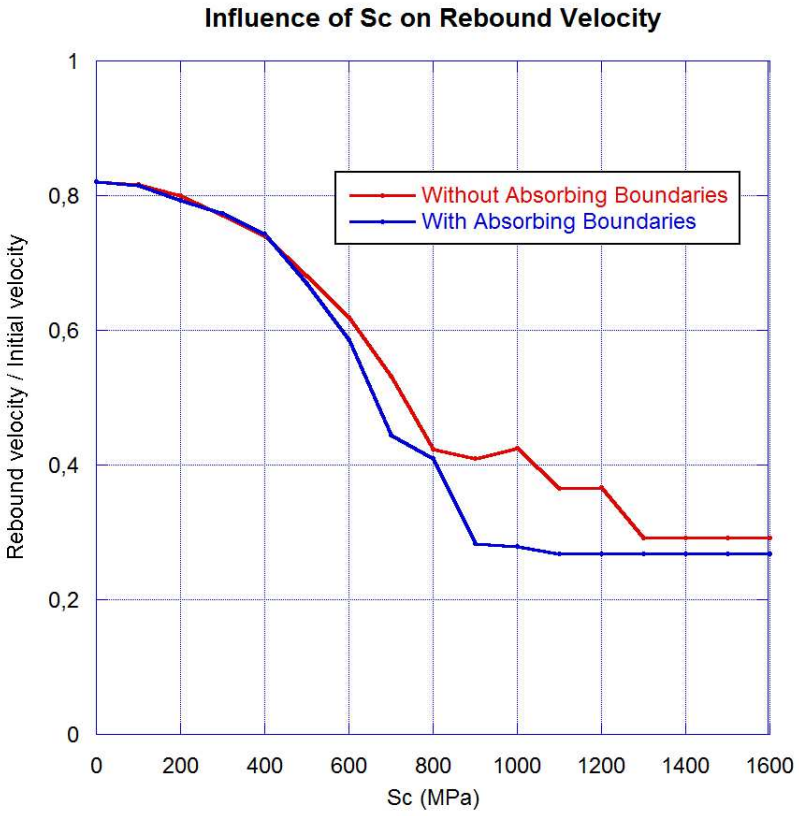

Figure 3.44: Evolution of the rebound velocity norm during impact for several values of the maximum cohesive stress

When the maximum cohesive stress increases, the rebound velocity decreases to reach a stable value of 30% of the initial velocity. The irregularities between 800 and 1,300 MPa are due to the occurrence of additional rebounds in the impact history due to an increase in the cohesive recovery load on the particle. The calculation was carried out in elastoplasticity by multiplying the initial yield stress of the material by 1,000. This result is important because it proves that for a dynamic impact, contrary to the static case, the choice of the plateau stress of the cohesive model is significant. This influence will be even greater in the plastic case.

3.5.2.2 Impact in elasticity: effect of the modeling of the substrate's absorbing boundaries

Next, absorbing boundaries were added to the model in order to simulate a semi-infinite substrate. An elastic impedance was applied over the bottom and the vertical sides of the parallelepipedic substrate. At each SPH node of the boundary, the impedance condition can be expressed as:

$$\mathbf{F_{SPH}} = -\mathbf{V}\sqrt{\rho\, E} S_{SPH} \tag{3.9}$$

This is a force which is directed opposite to the point's velocity and is proportional to that velocity and to the square root of the product E ρ.
Figure 3.44 shows the influence of these absorbing boundaries on the rebound velocity as a function of the maximum adhesive stress σ_c. One can observe a decrease in the rebound velocity compared to the case without absorbing boundaries. This difference increases as the value of σ_c increases until, again, it reaches a plateau.
Thus, as anticipated, the presence of these boundaries results in an energy loss in the system leading to a slight decrease in the rebound velocity and a change in impact behavior (in terms of the number of rebounds prior to separation), which should facilitate the adhesion of the particles.
The two cases presented here (built-in substrate and semi-infinite substrate) are the bounds of the actual case of a substrate whose size is finite, but usually much greater than the size of the particle.

3.5.2.3 Impact in the case of material nonlinearities

Here, we address a more realistic impact model which takes into account the elastic-plastic behavior of the material, which is represented by a Johnson-Cook law (see 1.3.4.1). The parameters chosen to represent the behavior of aluminum were taken from the literature and are given in Table 3.6.

The specific heat was set at $904 J/kg/^oK$

Experiments have shown that for particles of a given diameter adhesion occurs only in a specific velocity range. Therefore, our objective is to reproduce this observation numerically. The cohesion energy is unknown. Let us try, through calculations, to identify a value of the adhesion energy which matches the experimental observation, and then to study the influence of the associated cohesive stress. Here, we present, for several values of the impact velocity between 100 and $1,000 ms^{-1}$, the results of a series of calculations of the cohesive energy G_C and of the cohesive stress σ_c. The calculations were carried out with a fixed maximum time step equal to $7\ 10^{-12} s$.

Table 3.6: The Johnson-Cook material parameters for aluminum

Properties	Parameter	Value	Unit
Plastic (Johnson-Cook plasticity model)	A, B, C, N, M	148.4, 345.5, 0.001, 0.183, 0.895	MPa, MPa
	Ref. strain rate, $\dot{\varepsilon}^p_{ref}$	1	s^{-1}
	Ref. temperature, T_{ref}	300	K

3.5.2.4 Effect of the impact velocity in the elastic-plastic case

First, let us consider the calculations in which no limit was set on the cohesive stress and we allowed the adhesion energy G_C to vary. It is relatively difficult to tell what really happened in the calculations because they always stopped after a certain simulation time (typically, 5,000 time steps). In general, the transfers of energy among the particle, the substrate and the infinite medium had not been completed, although the adhesion energy was practically stable. Besides, this consumed adhesion energy represented only a very small portion of the initial kinetic energy. Therefore, it is difficult to distinguish between rebound or sticking based on energy balances and comparing the particle's kinetic energy and the unused adhesion energy.
We chose to decide about adhesion based on the percentage of the nodes that stuck. Thus, we counted the number of nodes in the particle which were stuck at the end of the calculation and compared that number with the maximum number of nodes which were stuck during the calculation. This was used as the sticking criterion: we decided that if more than 1% of the nodes remained stuck at the end of the calculation that meant that the particle had stuck. Of course, this value is completely arbitrary and can be debated. The duration of the calculations was chosen in order to allow this number to become stable over a period equivalent to or double the transition period. Table 3.7 summarizes these results for a range of values of G_C between 0.002 and 0.05.

The conclusion from this table is that if G_C is too high sticking occurs regardless of the impact velocity. Once G_C becomes equal to or less than 0.02, there is no sticking if the impact velocity is small and sticking if the velocity is in a range which depends on the value of G_C. The minimum velocity is between 300 and $500 ms^{-1}$. The particle bounces when the impact velocity exceeds $600 ms^{-1}$. This result comes close to the experimental results for this type of aluminum/aluminum impact. The maximum plastic strains are in the order of 1.5. There is a second sticking range, associated with impact velocities greater than $900 ms^{-1}$, which does not correspond to experimental observations. The accumulated plastic strains given by the calculations exceed 5 in the vicinity of the interfaces. At this strain level, damage most certainly occurs in the material and generates a third body which prevents sticking. Therefore, these calculation results are not very realistic. Figure 3.45 shows, for $G_C = 0.02$, the deformed shapes of the particle and the substrate along with the isovalues of the accumulated plastic strains for the three impact velocities (300, 600 and $700 ms^{-1}$) at final simulated time ($0.35 \mu s$ in every case). The faster the impact, the more the particle flattens out and penetrates the substrate. One can observe an accumulated plastic strain which culminates at 1.47 for a relatively coarse mesh. These strains are concentrated near the interfaces, which is a sign of significant shearing in these

Table 3.7: The effect of G_C on the percentage of stuck SPH at computation end, in the absence of a maximum cohesive stress

Impact velocity (ms^{-1})	G_C ($J.m^{-2}$)							
	0.002	0.01	0.015	0.017	0.018	0.019	0.020	0.05
100	0%	0%	0%	0%	0%	0%	0%	5%
200	0%	0%	0%	0%	0%	0%	0%	19%
300	0%	0%	0%	0%	0%	0%	0%	19%
400	0%	0%	0%	4%	1%	7%	12%	47%
500	0%	0%	1%	1%	3%	3%	6%	37%
600	0%	1%	6%	14%	19%	20%	24%	51%
700	0%	0%	0%	0%	0%	0%	0%	48%
800	0%	0%	0%	0%	0%	9%	9%	40%
900	0%	11%	21%	21%	21%	22%	22%	36%
1,000	18%	23%	31%	31%	31%	31%	31%	38%

regions.

Figure 3.46 shows, for the same cases, the isocurves of Von Mises' stresses. These stresses are quasi-uniform in the sphere and localized beneath the impact in the substrate.

Figure 3.47 shows the final temperatures for the case which corresponds to the highest velocity. The maximum temperature is almost 500°K. The particle does not melt.

Finally, we studied the model with the addition of a maximum cohesive stress σ_c. The same calculations were carried out with stress values equal to 100, 200, 300 and 500 MPa. The results did not change significantly. The sticking velocity range is relatively unaffected by the value of σ_c.

3.5.2.5 Discussion

The adhesion energy alone is insufficient to assess what happens in dynamics when the material behavior is elastic. If one simulates plastic behavior, there is not much difference between the models with a maximum cohesive stress and those without if one is interested only in whether the particle sticks to its substrate or not. This is an interesting result because it makes setting the parameters of the problem easier. The proposed model is unrealistic when the impact velocities are too high because it predicts sticking at very high impact velocities, which is not observed experimentally. This is due to an excessive flattening of the particle which leads to huge plastic strains. In such conditions, damage probably occurs in the material and generates a third body in the contact, which hampers sticking. This cannot be reproduced by the model proposed in this work. For very large strains, the error in the calculations of the sticking area for each point should also be taken into account and the method improved in order to achieve more physically realistic results at high speed.

3.5.3 Adhesion criteria validation by Cold Spray simulation

The influence of the adhesion activation and erosion criteria on the behavior of the model is now evaluated.

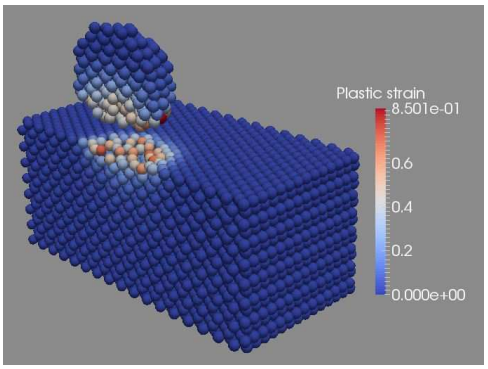

(a) Impact at $300ms^{-1}$

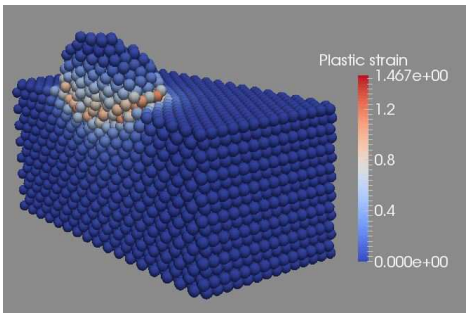

(b) Impact at $600ms^{-1}$

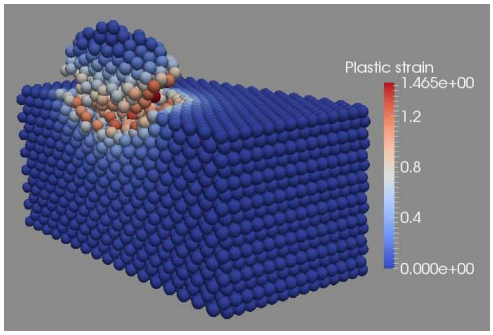

(c) Impact at $700ms^{-1}$

Figure 3.45: The deformed bodies along with the accumulated plastic strains

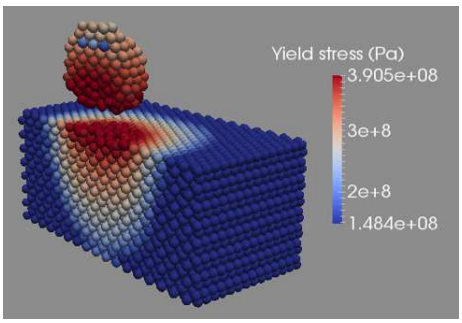

(a) Impact at $300ms^{-1}$

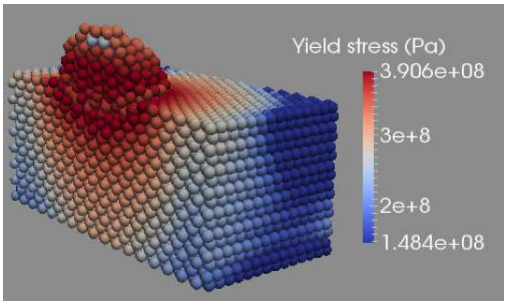

(b) Impact at $600ms^{-1}$

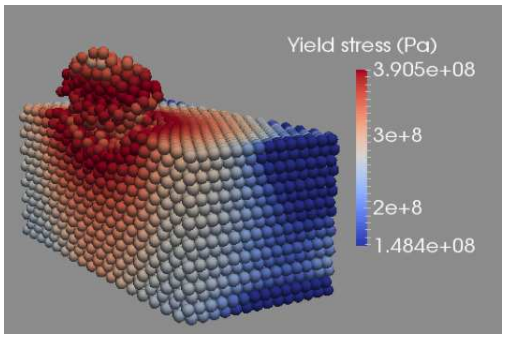

(c) Impact at $700ms^{-1}$

Figure 3.46: The deformed bodies along with the Von Mises stresses

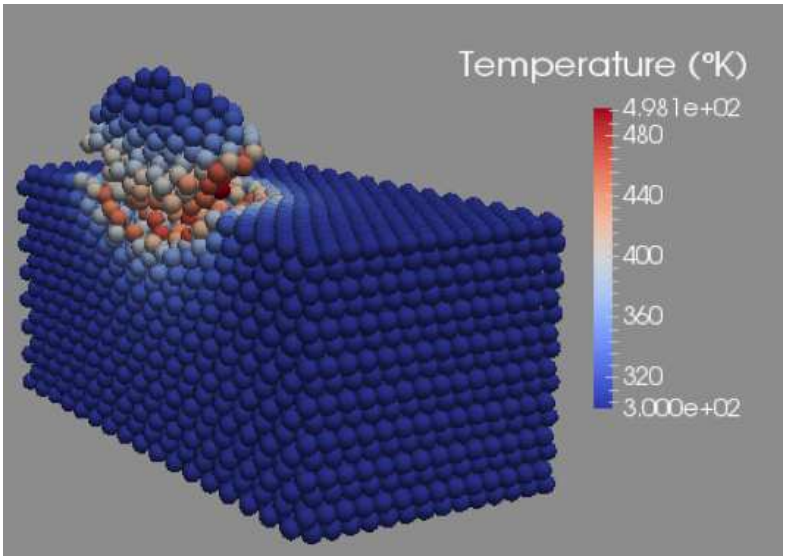

Figure 3.47: The deformed bodies at $700 ms^{-1}$ along with the temperatures in°K

Three sets of computations are carried out, all with a final simulated time of around $0.177\ \mu s$ found to be high enough for energy variations to settle down. For each set are observed: the number of elements having been in contact, the number of adhesive couples having been activated, the number of adhesive couples having dissipated all of their assigned energy, the number of adhesive couples broken by damage, and the number of adhesive couples still active. In these simulations, a particle of radius $R_b = 12.5\ \mu m$ impacts a substrate of lengths $L_s = 73.7\ \mu m$ and height $H_s = 33.1\ \mu m$ (approximate values due to the SPH packing method and homemade mesh generation algorithm) at initial velocities ranging from 100 m.s^{-1} to 1900 m.s^{-1}.

Both parts are aluminum and meshed using SPH, with an SPH particle radius $R_{SPH} = 1.25\ \mu m$. A very coarse mesh is used, for quick computations, containing 15776 SPH elements in the substrate and 737 SPH elements in the impacting particle. The adhesive parameters used are a surface energy $G_c = 30\ J.m^{-2}$, and no maximum cohesive stress σ_c.

Fig. 3.48 shows for three scenarios the variation of the final state of the computation as a function of impacting speed. In scenario (a) no activation trigger nor erosion trigger is used, so all contacting elements undergo adhesion and some little adhesion is still present at the end of the simulation, even for low speeds of 100 m.s^{-1}, making it difficult to conclude on a critical speed. Scenario (b) shows the effect of the activation criterion based on a drop in local yield stress value of 30%. The activated surface is no longer the same as the contacting surface, resulting in adhesion during the impact only for initial particle speeds of 500 m.s^{-1} and above, which can be interpreted as the critical velocity necessary for adhesion. The surface under adhesion then converges to the surface in contact at higher speeds, meaning that the activation criterion is met on an increasing part of the contacting surface. The number of adhesive links still active at final time however still stabilizes with increasing speed. In scenario (c), the adhesion erosion criterion is used with a value of $D_{max}^{adh} = 0.5$. The behavior at low speeds is the same as in scenario (b), but once above 600 m.s^{-1}, an increasing part of the adhesive couples is broken before they can dissipate all their assigned energy. The presence of the deletion criterion results in a drop in the number of active adhesive links at final time with increasing impact speed, to finally get a maximum impact speed for adhesion at around 1700 m.s^{-1}. The relation between contacting surface and adhesive surface is however unaffected.

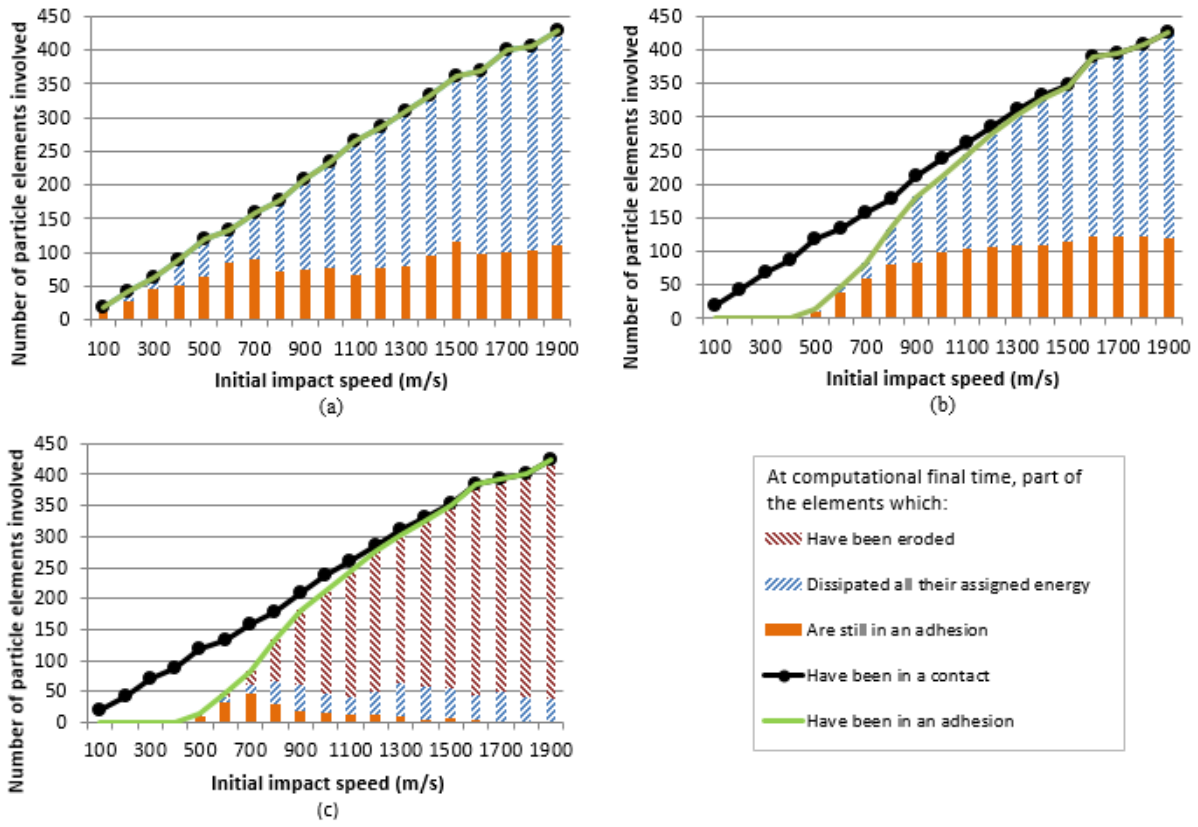

Figure 3.48: Behavior of the model as a function of initial particle speed, without criteria (a), with adhesion initiation criterion (b), and with adhesion initiation and erosion criteria (c), for the test case of Al/Al full SPH model

The notion of final adhesion is here chosen as at least one adhesive couple being still active, but while convenient here for interpretation, this choice is of course not realistic and the notion of a ”minimal final adhesive surface for sufficient particle adhesion strength” should later be investigated and implemented. This notion will further be discussed in 5.2.

Remark: The influence of the simple presence of an adhesion on the deformation was also investigated with an infinite and instantaneous adhesion, but it proved to be negligible compared to other factors such as material parameters and mesh parameters.

3.6 Summary

The conclusions to be made from this chapter are as follows:

- The implementations of the Johnson-Cook law with thermal softening and its application to the SPH method is validated by Hopkinson bar simulations and comparisons with Abaqus for traction tests.
- The implementation of the failure laws and their behavior has been validated by Shear Banding simulations. A quantitative validation was not undertaken as depending on too many parameters and other materials would anyway be used. The choice is thus made to use as much as possible the same laws and parameters as in other studies on shear banding.
- The particle impact model has been defined and its behavior in terms of deformations versus mesh studied without adhesion and found to lack consistency and stability at very high impact speeds mostly due to the total Lagrangian nature of the solid SPH method used. A switch to Updated Lagrangian is to be considered.
- The adhesion model has been validated, in terms of implementation and behavior. Its effect in different cases and the influences of its parameters have been shown. The model is has been proven able to simulate the sticking velocity window of Cold Spray with a minimum impact velocity for adhesion, the critical velocity, and a maximum velocity for adhesion, the erosion velocity.

Chapter 4

Experimental observations for model definition

In this section the experimental observations carried out on impacted SPITS samples are presented. The goal of these observations is first of all to evaluate the change in microstructure after impact to see if the adhesion mechanism for a 1mm particle sprayed by SPITS is similar to the adhesion mechanism for a 25um particle sprayed by Cold Spray, to validate the use of the SPITS apparatus. In a second time, the hardness variation across the impacted sample is checked and its link with the change in grain size near the interface is evaluated, to try and clarify whether the macroscale model used here, Johnson-Cook, is appropriate for simulating solid mechanics at a mesoscale level such as in a Cold Spray particle where the latter may only consist of a few grains, or if a model including grain dynamics would be better suited. The first part presents the sample preparation process, the second part shows the results of hardness tests across a few samples. The third part describes the different first observations made with EBSD and some conclusions on the change in microstructure. The fourth part links grain structure maps and hardness measurements to draw some conclusions on change in grain size and hardness variations.

Contents

4.1 The experimental plan

4.1.1 Aims of the experimental plan

The experimental plan carried out in this work has two main goals:

- Improve the current knowledge on impact dynamics and microstructure change in impacted particles by using samples obtained by the Single Particle Impact Testing System, developed in the laboratory, for Electron Backscatter Diffraction analyses. More precisely, the aim is to find recrystallized grains at the interface, which should be a sign a dynamic recrystallization and thus of an adiabatic shear band. We also want to study the overall change in grain size in the particle and around the interface.
- Compare mechanical properties variations in impacted specimens with predicted mechanical properties variations in simulations, the idea being to clarify whether the material model used is adequate or if another model, typically including grain dynamics, would be preferable. This will be done by performing hardness indentations on the cross-section of the samples, and see if the link between grain size change and hardness change (seen as the variation in mechanical properties) is predominant and should be taken into account.

4.2 Sample preparation

Before indentations or EBSD measurements could be made, the samples had to be prepared: both of these methods indeed require a flat polished surface. Once the particle is impacted thanks to the SPITS apparatus, the obtained sample has to be cut to get a cross section of the particle and substrate at the desired position (as near the center of the particle as possible). This cross section then has to be polished. If only hardness tests were to be performed, a simple quick mechanical polishing would be sufficient. Here however the indented surface will also have to be of sufficient quality for EBSD measurements to be possible. To make the link between hardness measurements and local grain size, the indentations have to be observable by EBSD, hence no polishing between the two steps should be performed.

This meant that a mirror polishing had to be performed before the indentations, and the EBSD measurements would be done directly on the indented sample on the following hours for the surface to oxidize as little as possible.

Both sample were cut using a Struers Accutom-50 machine with an abrasive cutting disk at low force and low feed rate parallel to the impact direction and next to the particle. The obtained cross-sections were then mounted in cold-pressed resin then grinded to get just short of the middle of the particle using a Buehler Automet250 from 80grit up to 1200grit. This was followed by a mechanical polishing up to 1 μm and 0.1 μm colloidal silica until a mirror polish was obtained. Just before the observations, a short Flat Ion Milling was performed using a Hitachi IM4000. The different parameters used (here given for copper) were kept as low (polishing force of 15.7 N (3.5 lbs) per sample, each sample being 25.4 mm (1 inch) in diameter, and rotation speeds of 120 rpm for the base and 40 rpm for the head in opposite directions) and short (around 20 mn of polishing with colloidal silica and 3 mn of ion milling at 5 kV accelerating voltage) as possible to get a good enough polish without damaging the interface more than necessary, as these kinds of processes tend to have a concentrated effect on boundaries. It was indeed observed that a too long ion milling time or colloidal silica polishing time or force resulted in erosion in some parts

of the particle/substrate interface. As the aim of this study is to evaluate the microstructure as close to the interface as possible, this effect was not desirable. It could on the other hand prove useful to evaluate the proportion of the interface undergoing firm adhesion as this erosion made more visible the parts where the particle/substrate boundary was not completely closed, hence where adhesion was likely not to occur at all in the first place. The polishing also made it particularly difficult to observe samples made of two different materials, as their different hardness would mean a different polishing rate for each material. This resulted in cross-sections of aluminum particles impacted on copper substrates where the aluminum particle would end up a few microns lower than the copper substrate, making the EBSD measurements and indentations impossible. Another technique or other sets of parameters would have to be used to observe samples with dissimilar materials.

4.3 Hardness tests

This section presents the hardness indentations performed and different conclusions that can be drawn from them.

4.3.1 Parameters

The microhardness indentations were performed first on a copper particle impacted at 457 m.s^{-1} and stuck on a copper substrate, using a Fischer PICODENTER HM500, under a maximum load of 5 mN, a loading time of 10 s with a constant loading rate, and a hold time of 1 s. As the indents used for calibration had a size of around 3 to 4 μm and the machine positioning precision is of 3 μm, an indent spacing of 15 μm was used, so as to agree with the $indentspacing > 3 * indentsize$ criterion given for copper in the ISO6507.1 norm for hardness testing. The first intent of the author was to follow the procedure described in [ZOU 10b], but the loading rate of 0.2 μN.s^{-1} gave a indenting time per point of around 1 h 45 mn and could not be managed in the time available. The current parameters are thus only used to get an idea of local hardness variations and the results will not be compared to the ones from [ZOU 10b].

In a second time a sample of a copper particle impacted and stuck on a on a copper substrate at 230m.s^{-1} was indented using a Fischerscope HM2000LT, using the same loading parameters and indent spacing as for the previous sample. The change of apparatus was caused by unavailability of the previously used indenter, but is not of great concern here since, once again, only variations across a given sample are observed. The hardness value given by indentations, especially at this size, depending too much on the loading parameters used, the apparatus, but also the surface condition of the sample.

4.3.2 Hardness results

In this section the results from hardness tests are presented for two samples of a copper particle impacted on a substrate, one at 230 m.s^{-1} near the critical speed, and one at 457 m.s^{-1} well above the critical speed.

4.3.2.1 Impact at 230 m.s^{-1}

Figure 4.1 shows the indented surface of the sample, with seven indentation lines of 60 indentations each, 900 μm long and crossing the interface at different positions on the contact

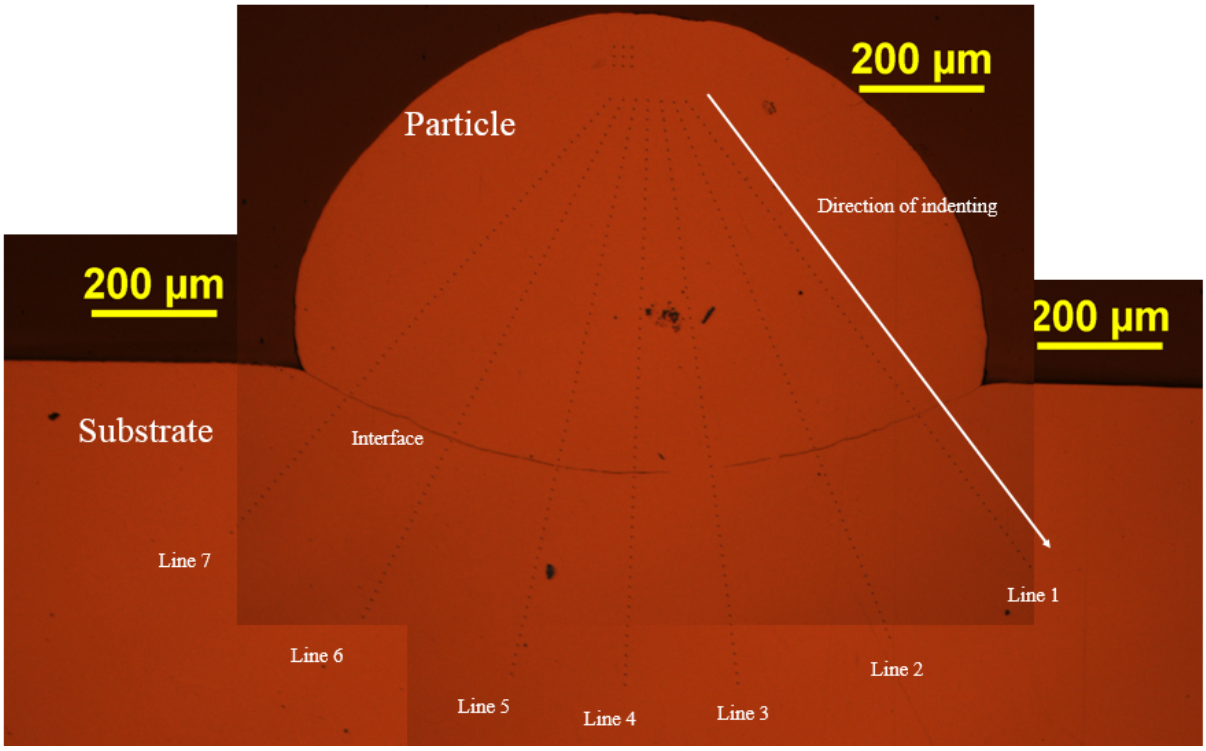

Figure 4.1: Indentations on the sample impacted at 230 m.s^{-1}

zone.

The hardness results obtained using the parameters described in the previous section are given in Figure 4.3 for each line, and the global results are given in Figure 4.2. The Vickers hardness is given as a function of the relative position to the interface, with negative values in the particle and positive values in the substrate. This distance is grossly defined by multiplying the indentation step (15 μm) by the difference between the current indentation number and the indent number closest to the interface for each line. A more accurate approach might be to visually measure the distance from the indentation to the interface with a line perpendicular to the interface.

As can be seen, the particle as well as the substrate undergo hardening, as expected from the plastic deformation involved. It can be noted however that for most of the indentation lines, especially those at an angle with the impact direction, the highest value of hardening is not found at the interface but slightly inside the particle (see trend lines in black on Figure 4.3). Despite the noise in the measurements, probably due to the loading parameters used and specifically the maximum loading of only 5 mn, one can still conclude on a very limited (if present at all) local hardening near the interface, and an overall hardening of the particle compared to the initial value before impact. In the case of the presence of a shear band, one could expect a local loss in strength and thus a very localized drop in local hardness during the impact, however these measurements are made after the particle and substrate have had time to cool down so the thermal softening effect can not be observed.

A remark can be made concerning the position of the indentation lines: there is more hardening for lines 1 and 7 going through the interface on the peripheral region of the impact zone compared to line 4 going through the center of it.

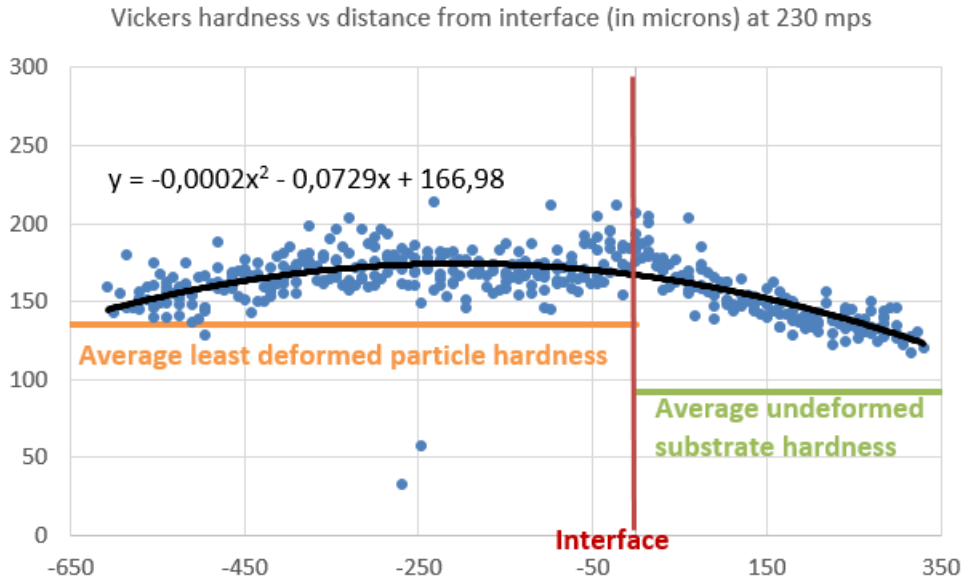

Figure 4.2: Hardness variations on the sample impacted at 230 m.s^{-1}

The ”average least deformed particle hardness” shown in 4.2 is the average hardness value given by a set of 9 indentations made at the top of the particle, supposedly in the least deformed region, to get a basis for comparison throughout the particle. The ”average undeformed substrate hardness” is the average value of another set of 9 indentations, made in the substrate in a region far enough from the impact area to be considered unaffected.

4.3.2.2 Impact at 457 m.s^{-1}

Figure 4.4 shows the indented surface of the sample, with seven indentation lines of 60 indentations each, 900 μm long and crossing the interface at different positions on the contact zone. The particle is a lot more deformed than in the previous case, and the separation between particle and substrate is actually invisible to the eye, and as will be seen later, even difficult to pinpoint with the EBSD measurements.

As Figure 4.6 and 4.5 show us, and as expected from the higher level of deformation of the particle compared to the previous one, the particle undergoes more hardening than at lower speed, and the variation is also more pronounced (although the noise is also higher). A bell shape can clearly be seen especially for indent lines near the impact direction, going through the center of the impact area.

This last observation is apparently in contradiction with what was seen at lower speed, with a hardening more pronounced on the sides of the impact region.

Once again, the ”average least deformed particle hardness” shown in 4.5 is the average hardness value given by a set of 9 indentations made at the top of the particle, supposedly in the least deformed region, to get a basis for comparison throughout the particle. The ”average undeformed substrate hardness” is the average value of another set of 9 indentations, made in the substrate in a region far enough from the impact area to be considered unaffected. Interestingly the value for the particle is lower than at 230 m.s^{-1}, which is counterintuitive but might arise from a difference in initial particle hardness, and is not seen as an important observation since,

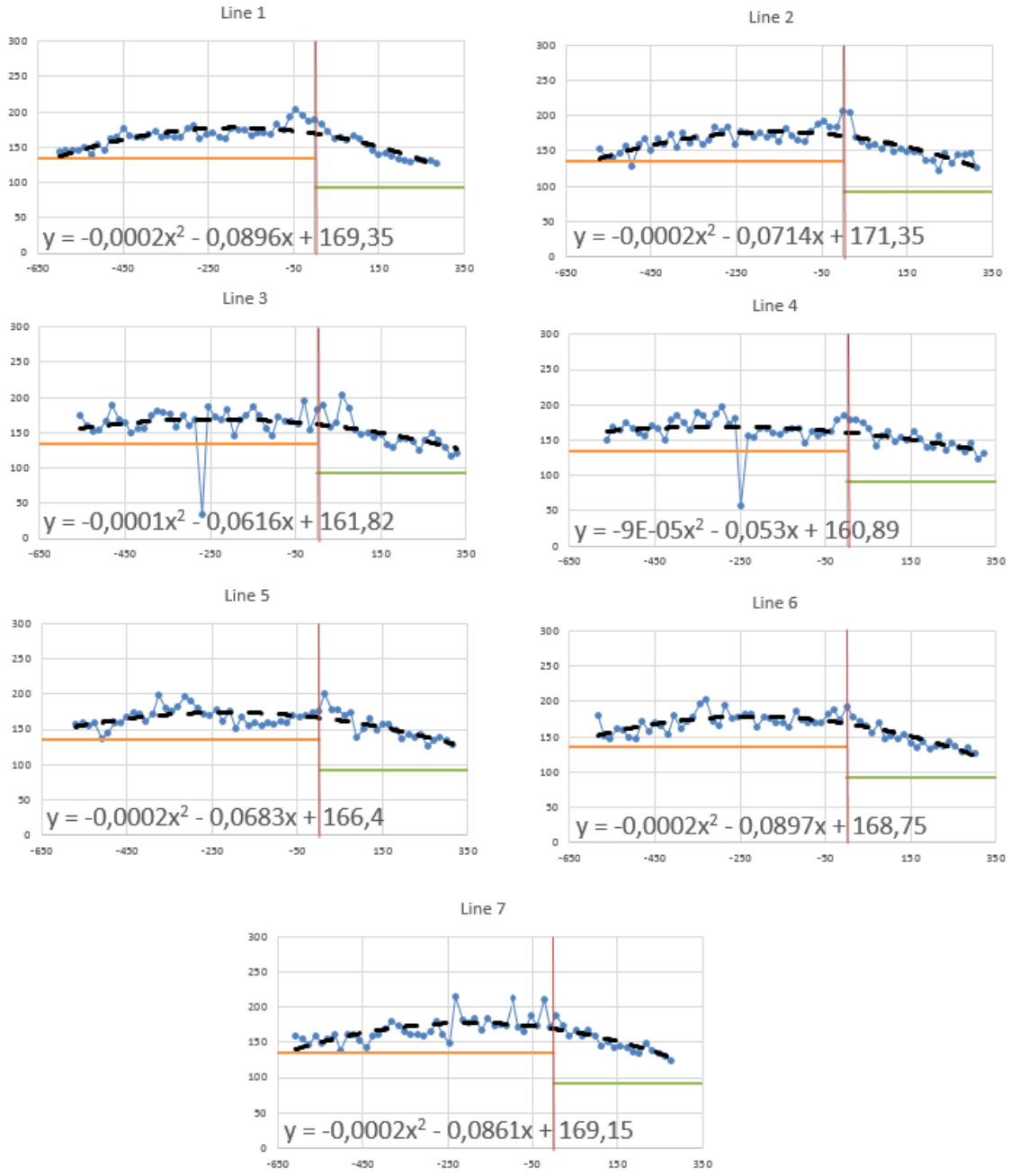

Vickers hardness variation for each indentation line on the 230 m.s^{-1} sample, as a function of distance to the interface (in microns).

Red vertical lines depict the position of the interface.

Black curves are the corresponding trends with their equation displayed.

Orange lines show the average particle hardness at the top of the particle (135HV).

Green lines show the average substrate hardness far from the impact (92HV).

Figure 4.3: Hardness variations on the sample impacted at 230 m.s^{-1} for each indentation line

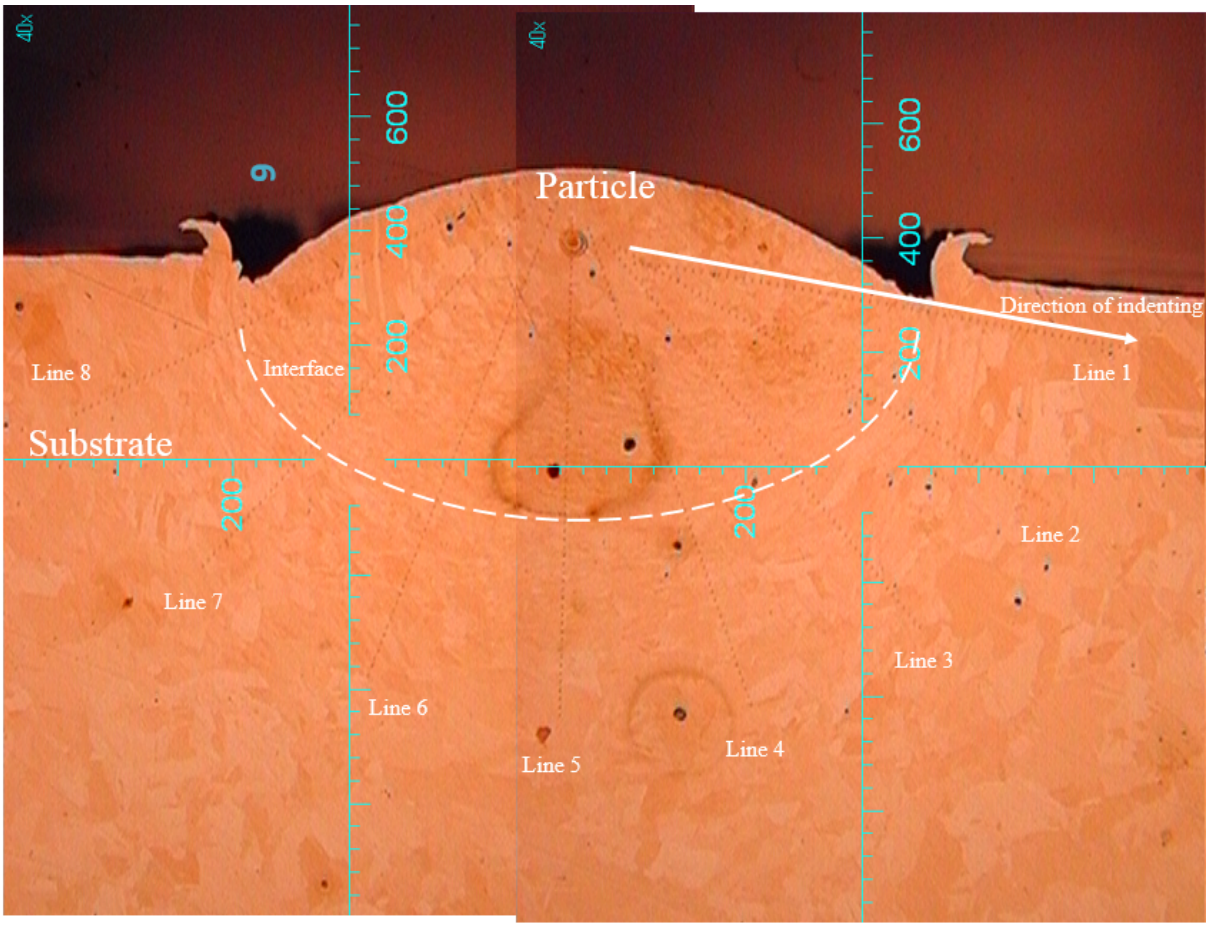

Figure 4.4: Indentations on the sample impacted at 457 m.s^{-1}

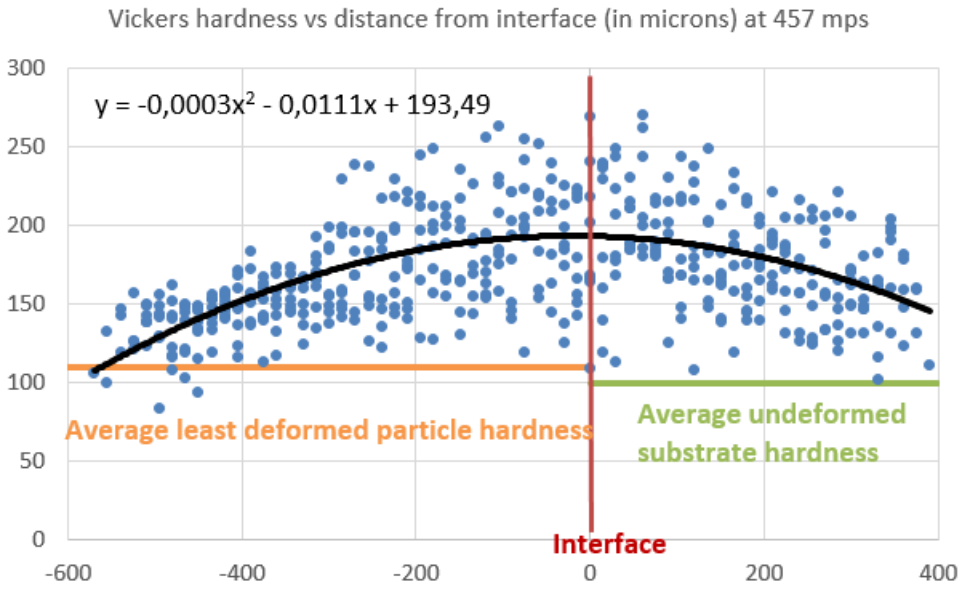

Figure 4.5: Hardness variations on the sample impacted at 457 m.s^{-1}

as explained previously, only the relative variations and trends inside one sample can be seen as relevant, due to the high spread in found values across samples.

Once again however, a clear conclusion on the local behavior near the interface is difficult to make, especially when looking at the global result containing all hardness measurements (Figure 4.5).

4.3.3 Comparison with a simulation

Here we will see what variation in Yield stress value the simulation predicts, and how it can be linked to the hardness and thus to the experimental observations made, to check whether the same trends are observed.

The computations are under way and this section will be written in the following weeks.

4.3.4 Discussion on the hardness results

In conclusion for the hardness measurements, the samples show an overall hardening around the interface, but no local drop in material strength was detected near the interface, possibly due to the distance between each indent, even though several lines were performed which should augment the change of falling on the instability area. These measurements will be put in light of the EBSD microstructure images to better understand this behavior.

4.4 Electron Backscatter Diffraction observations

In this section the observations made with the EBSD technique are presented. First general observations are made on Copper on Copper SPITS samples. These images give indications as to the nature of the microstructure change at the interface leading to adhesion of the particles, and indications as to the general grain size variations. In a second time, the indented samples are observed, and the grain size at indentation sites are extracted to try and link the hardness value with the local grain size.

For a look back at the definitions of the different EBSD maps shown in this section, see Context, section 1.2.1.

4.4.1 Parameters

The EBSD observations were carried out on a Hitachi SU-70 SEM equipped with a TSL SC-200 camera. Acquisition of the EBSD data was made through the EDAX OIM Data Collection software and post-processing via EDAX TSL OIM Analysis 6.2. The acceleration voltage used was 20kV and a global image of the particle embedded in the substrate is first obtained, followed by zooms on areas of interests at step sizes ranging from 0.4 μm to 0.03 μm. This will be specified for each set of figures. For the observations after indentation, again a first global map was obtained with a step size of 2 μm, and then zooms were made on the indentation lines with a step of 0.2 μm.

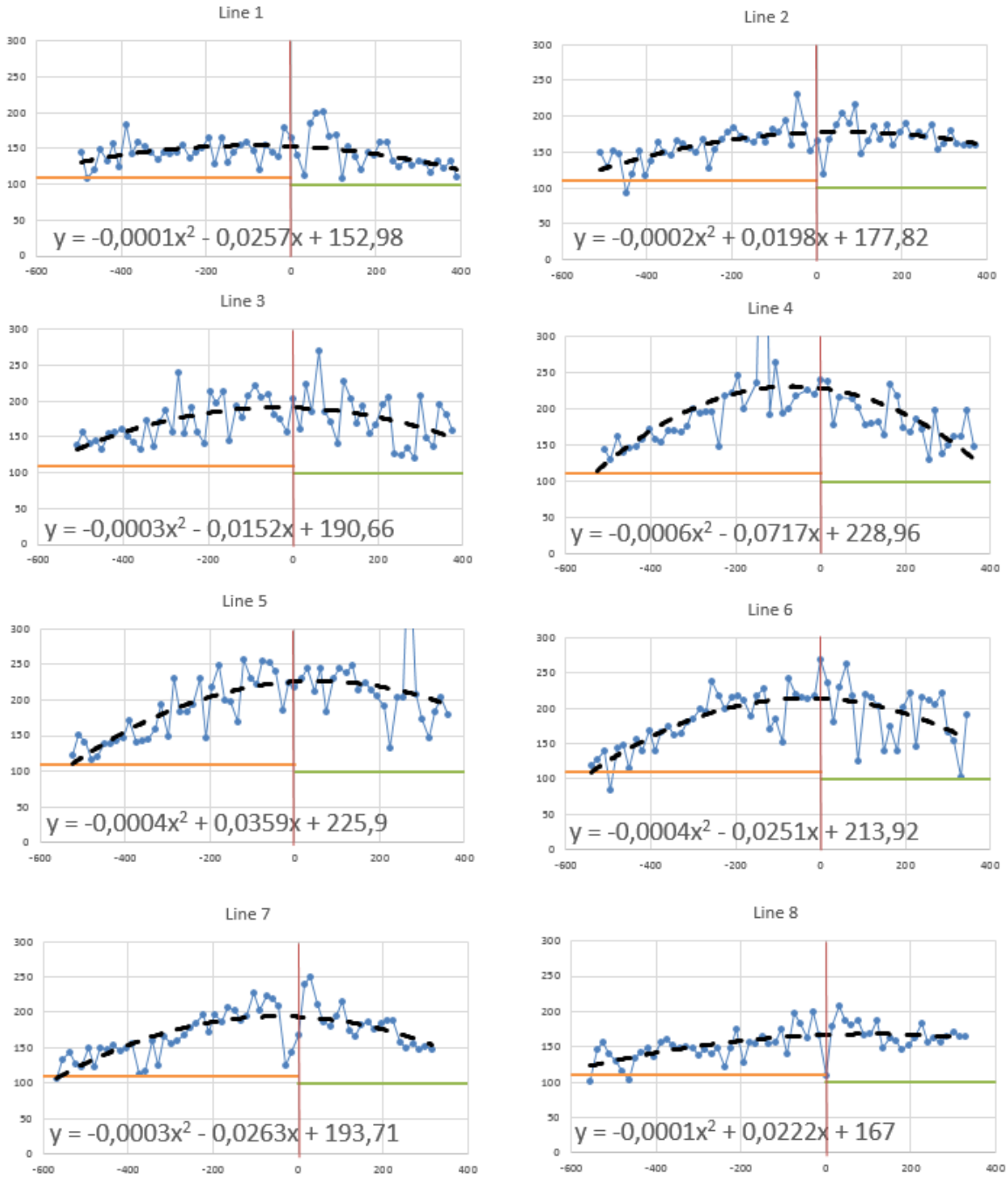

Vickers hardness variation for each indentation line on the 457 m.s^{-1} sample, as a function of distance to the interface (in microns).

Red vertical lines depict the position of the interface.

Black curves are the corresponding trends with their equation displayed.

Orange lines show the average particle hardness at the top of the particle (110HV).

Green lines show the average substrate hardness far from the impact (99.5HV).

Figure 4.6: Hardness variations on the sample impacted at 457 m.s^{-1} for each indentation line

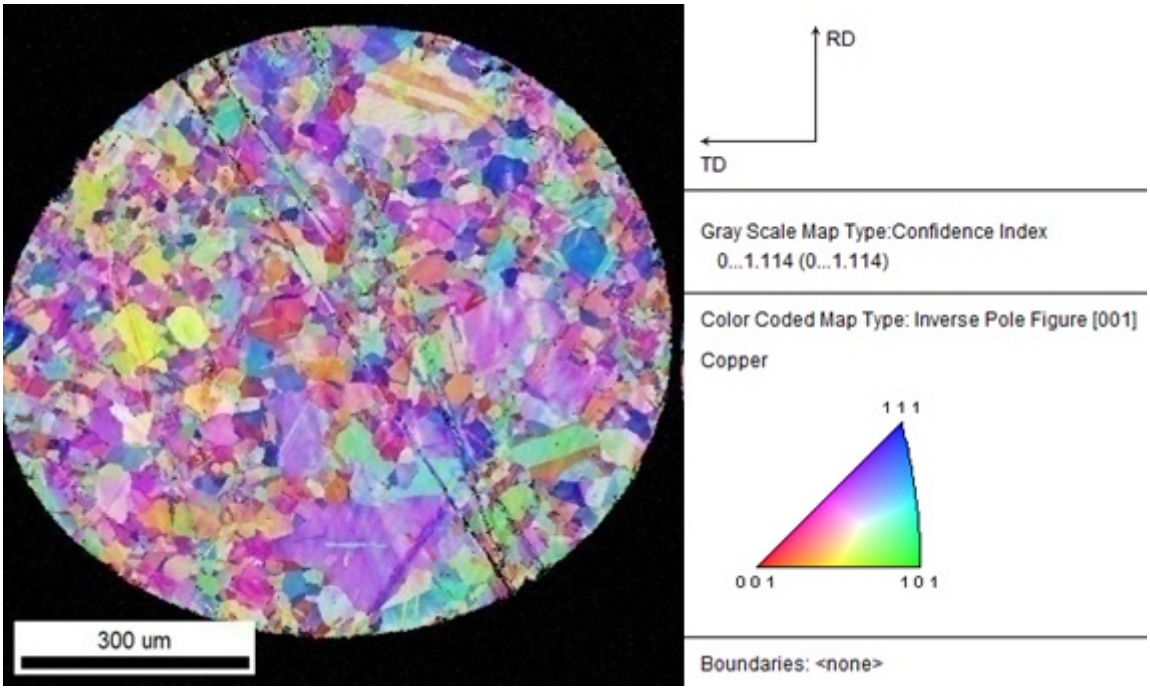

Figure 4.7: Inverse Pole Figure of a typical initial copper particle

4.4.2 General observations

Here the general change in microstructure is observed and described. The recrystallized zone possibly corresponding to the shear band is also studied.

4.4.2.1 Initial copper particle

Figures 4.7, 4.8, 4.9 and 4.10 show the EBSD maps obtained for a typical copper particle used in SPITS using a measurement step of 2 μm. These use a step of 2 μm. On figure 4.8, which shows the Image Quality Figure of this initial copper particle, the particle is mostly white or bright, meaning a high image quality and low deformation levels. In the same manner, figures 4.9 and 4.10 show that despite the remaining scratches from a bad polishing, overall deformation levels are quite low with many grains in figure 4.10 being blue or green, giving orientation spreads lower than 4°.

As for the grain size in the initial particle, we can see in figure 4.11 grains ranging mainly from just under ten to a hundred microns. The image does not however show an abundance of small grains of only a few microns.

4.4.2.2 Initial copper substrate

Next, the copper substrate far from the impact zone (hence still at initial state) is shown in figures 4.12, 4.13, 4.14 and 4.15, with a step of 2 μm.

The first observation is that the grains are in average a lot bigger than for the particle (see figure 4.12), and are mostly around fifty to more than a hundred microns in size. As for the initial deformation levels, figures 4.13, 4.14 and 4.15 show us high image quality values, and very low misorientations and grain spread in orientation (1°or lower). This is because contrary

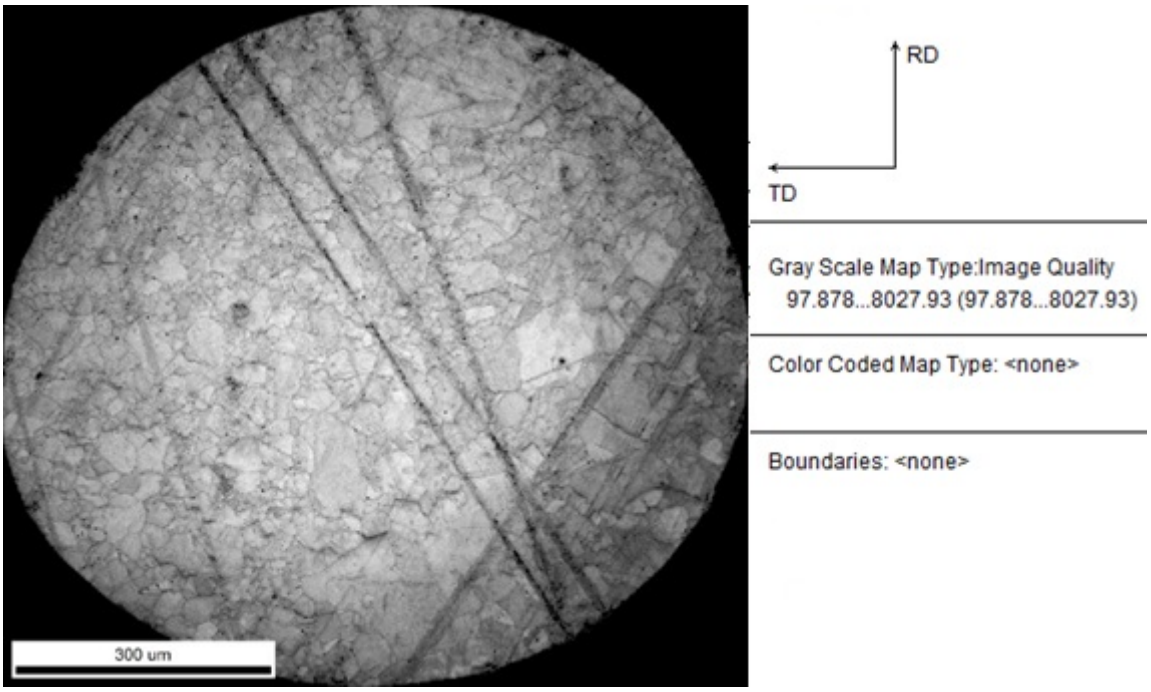

Figure 4.8: Image Quality of a typical initial copper particle

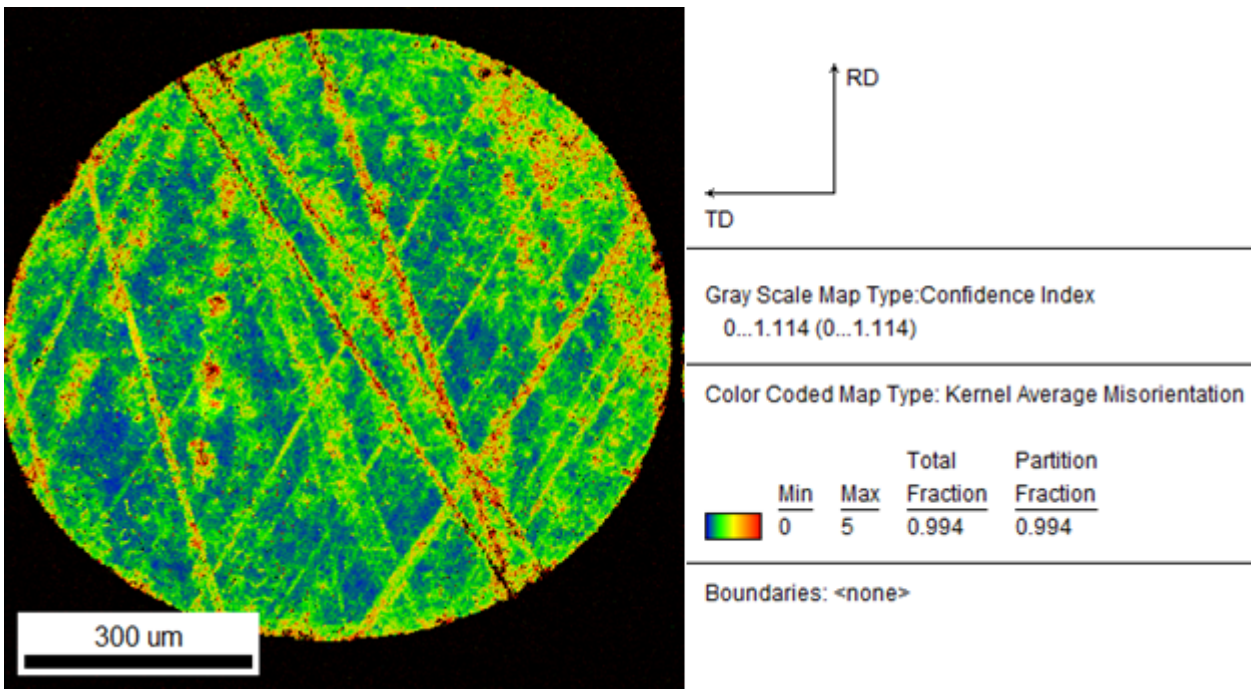

Figure 4.9: Kernel Average Misorientation of a typical initial copper particle

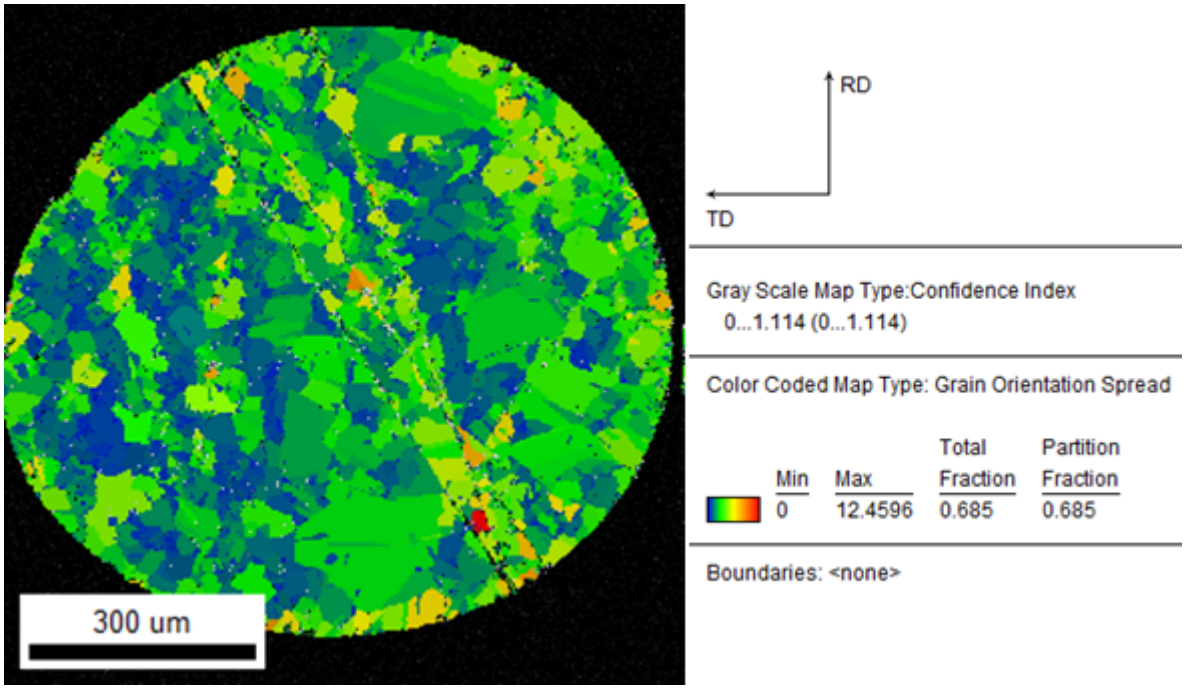

Figure 4.10: Grain Orientation Spread of a typical initial copper particle

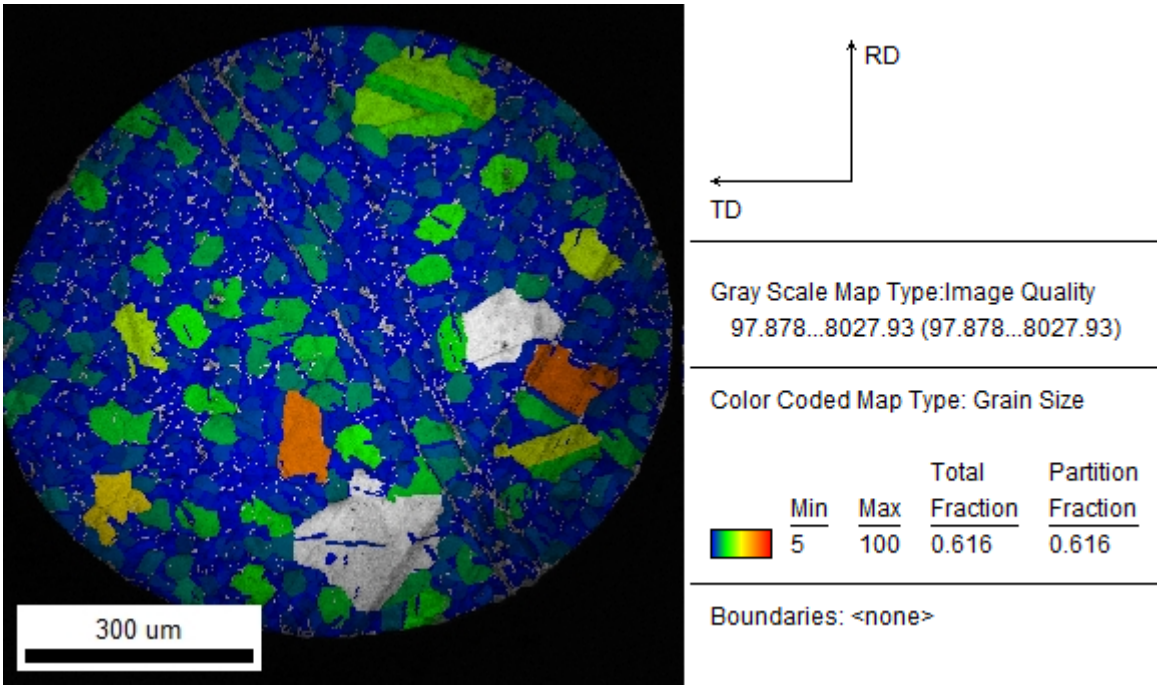

Figure 4.11: Grain size of a typical initial copper particle

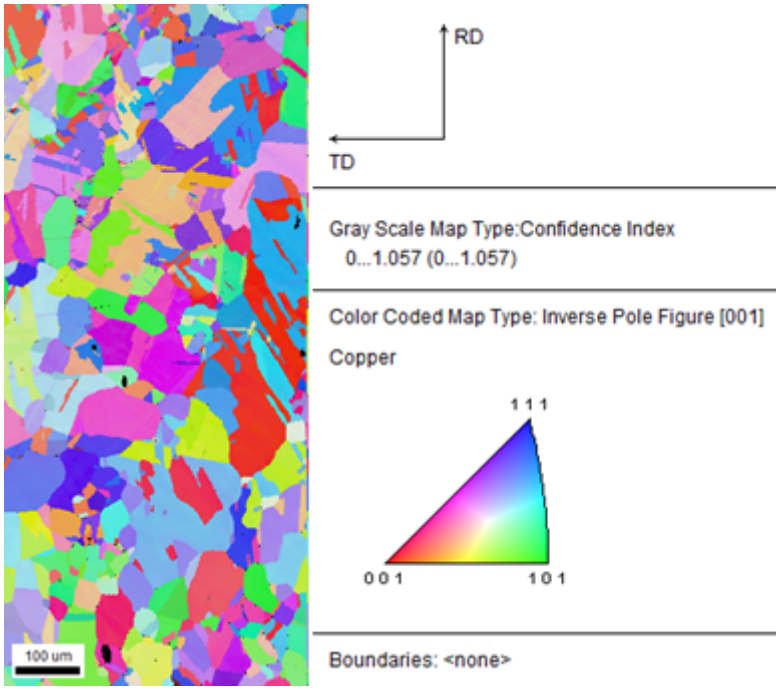

Figure 4.12: Inverse Pole Figure of a typical initial copper substrate

to the particle, the substrate did not undergo the manufacturing process required to obtain balls of a specific diameter. More information on the processing conditions of both the particles and the substrates is given in [ITO 16].

4.4.2.3 Impact at 230 m.s^{-1}

A 1 mm copper particle is impacted by means of SPITS on a copper substrate at 230 m.s^{-1}. Figures 4.16, 4.17, 4.18 and 4.19 show the complete impacted particle with a step of 3 μm.

The first observation is on figure 4.20 with a clear grain refinement of the particle close to the interface, with a zone containing mostly grains under 5 μm in size as shown in **??**hich are not present on that scale in the initial particle (see Figure 4.11).

Second observation, the particle shows lower Image quality values (figure 4.17), and a denser region of misorientations (figure 4.18). These can usually point to more deformation, however the spread levels (figure 4.19) seem to indicate than more than deformation levels of the grains, the differences seen in Image Quality and Kernel Average Misorientation come from the higher grain boundary density near the interface on the particle side.

Figures 4.21, 4.22, 4.23 and 4.24 show a zoom on the left part of the interface with a step of 0.3 μm.

A clear difference can be seen between the particle and the substrate,with very different grain sizes involved (around a few microns on the particle side, and tens of microns in the substrate).

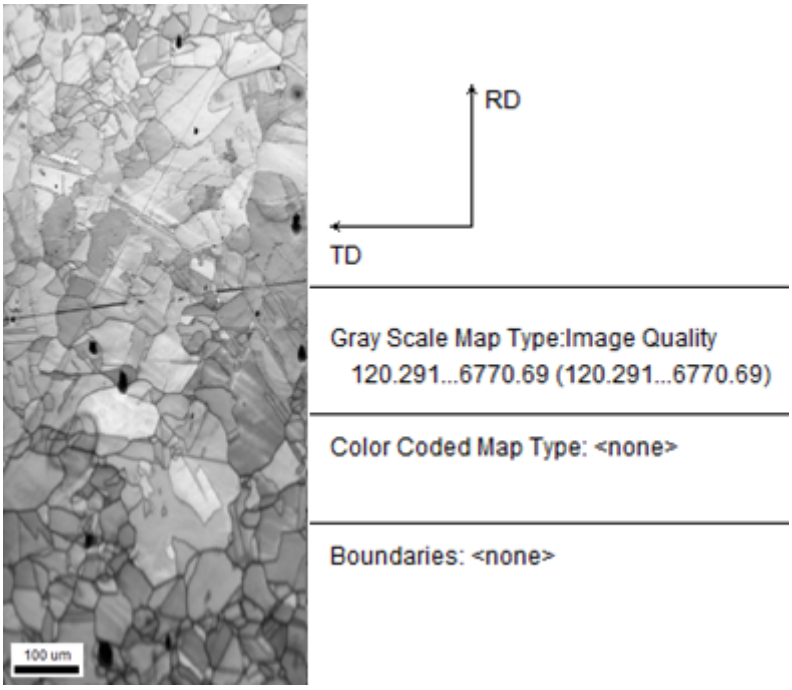

Figure 4.13: Image Quality of a typical initial copper substrate

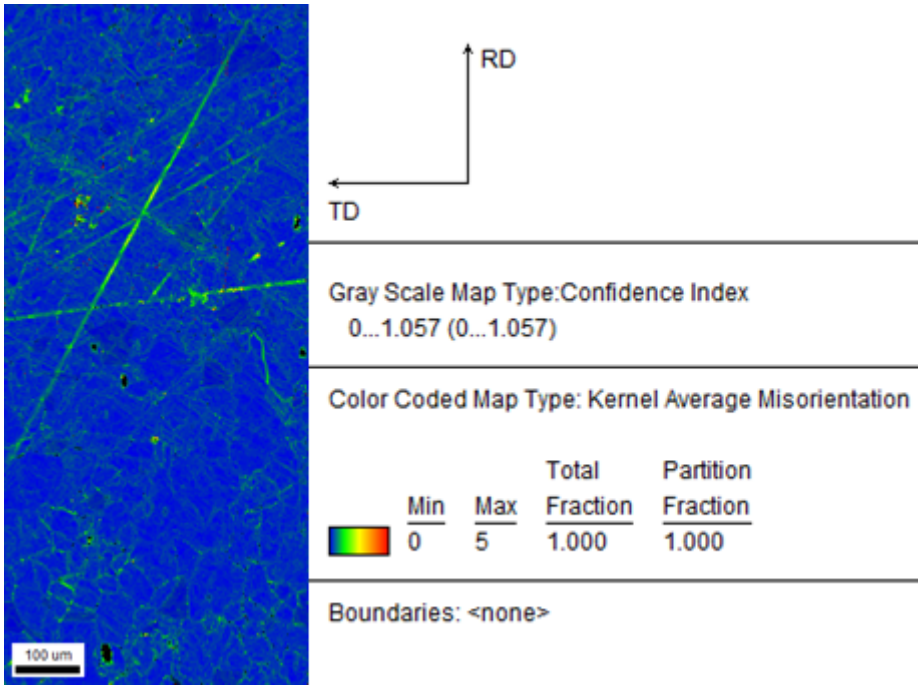

Figure 4.14: Kernel Average Misorientation of a typical initial copper substrate

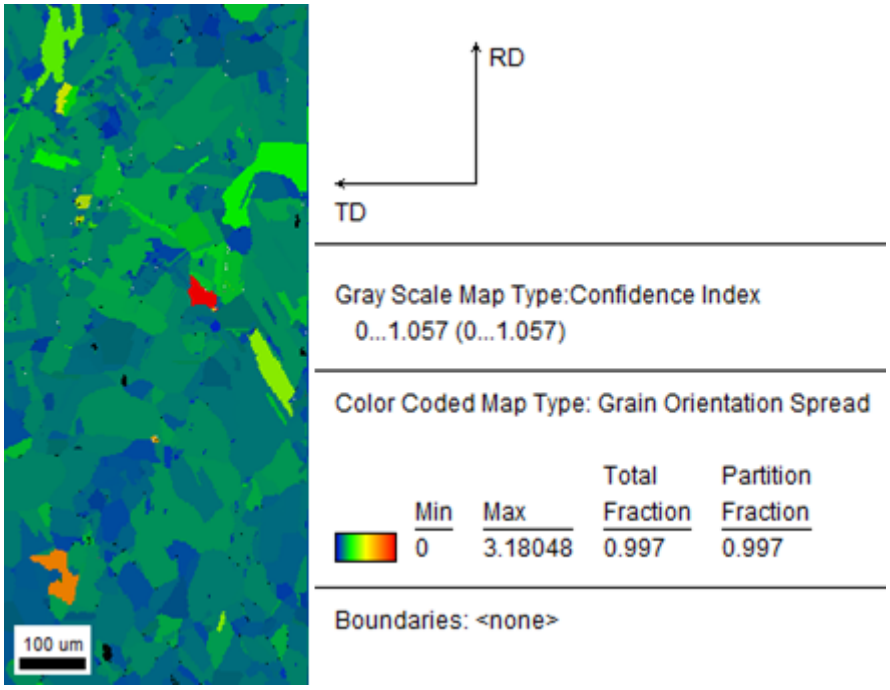

Figure 4.15: Grain Orientation Spread of a typical initial copper substrate

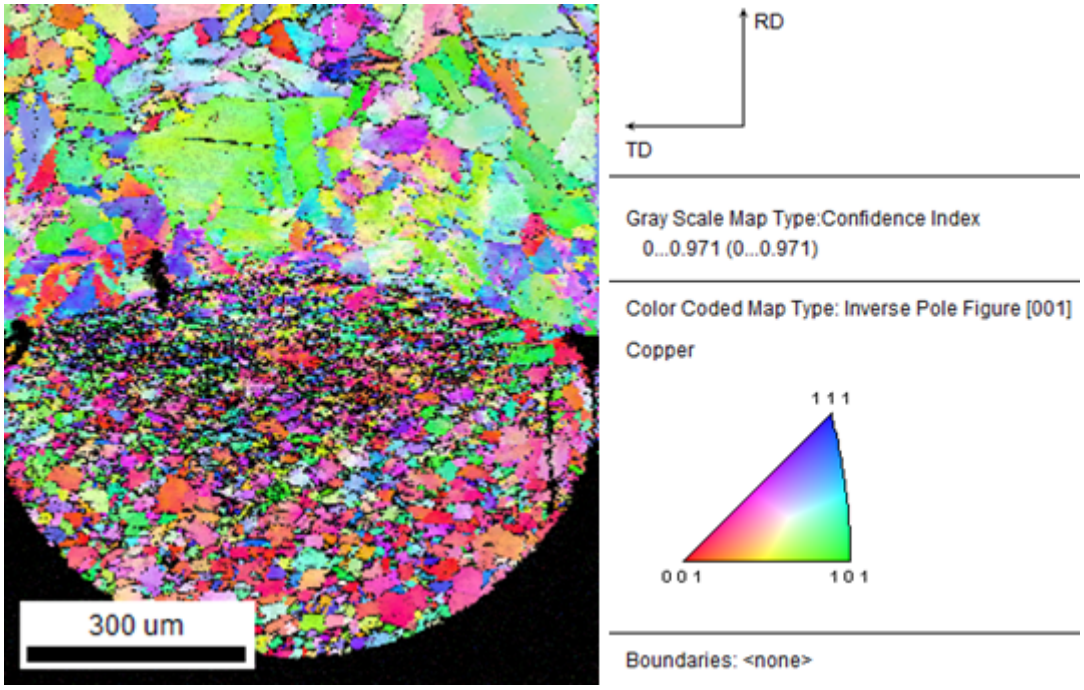

Figure 4.16: Inverse Pole Figure of the sample of impact speed 230 $m.s^{-1}$

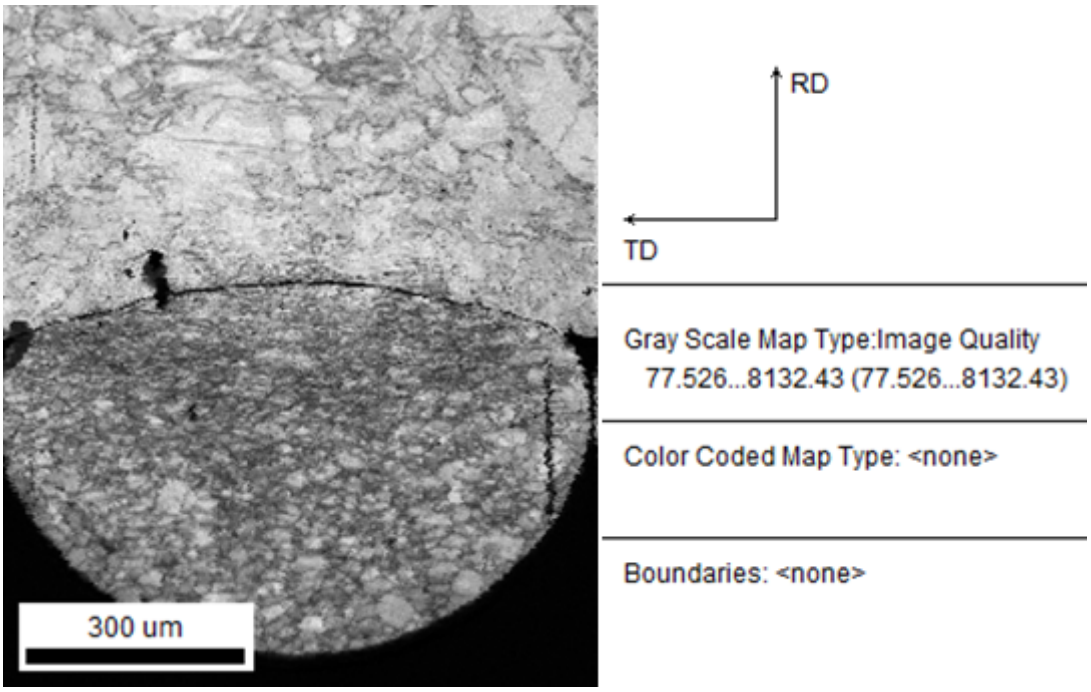

Figure 4.17: Image Quality of the sample of impact speed 230 m.s^{-1}

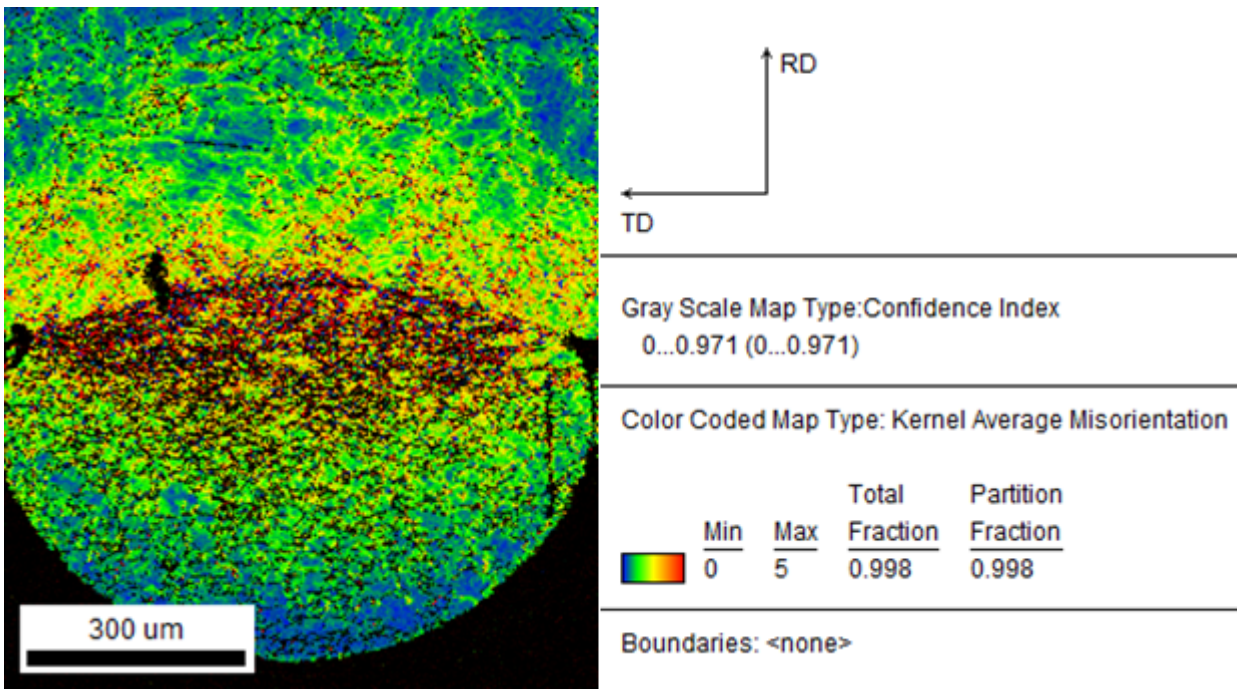

Figure 4.18: Kernel Average Misorientation of the sample of impact speed 230 m.s^{-1}

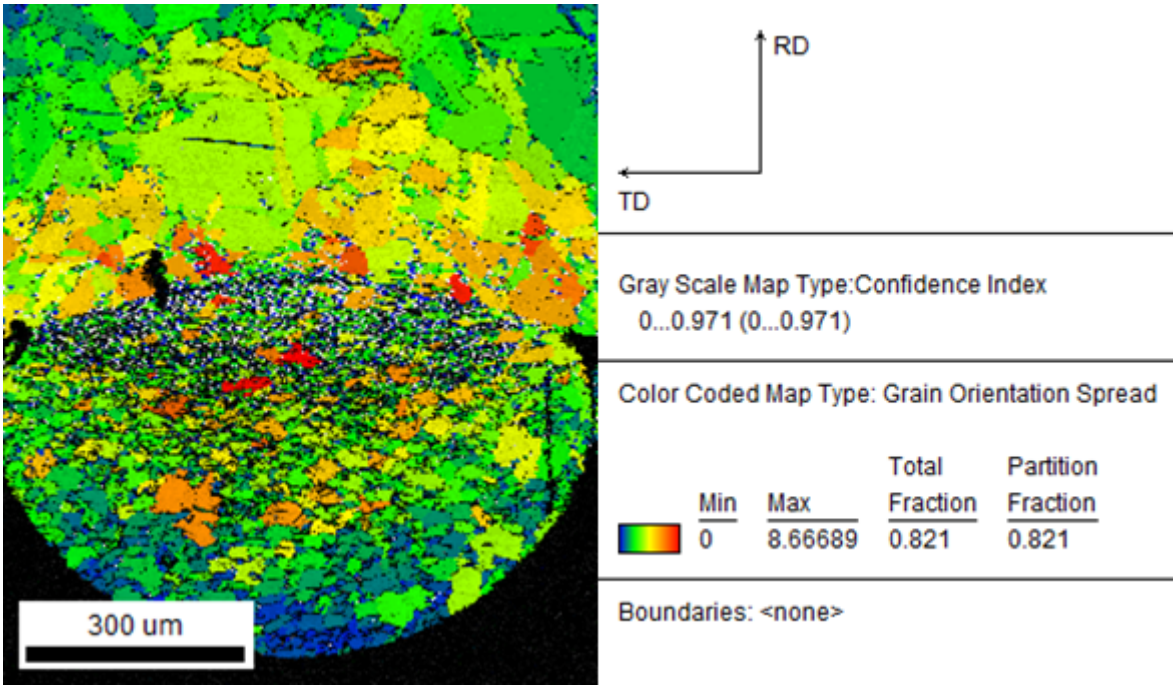

Figure 4.19: Grain Orientation Spread of the sample of impact speed 230 m.s^{-1}

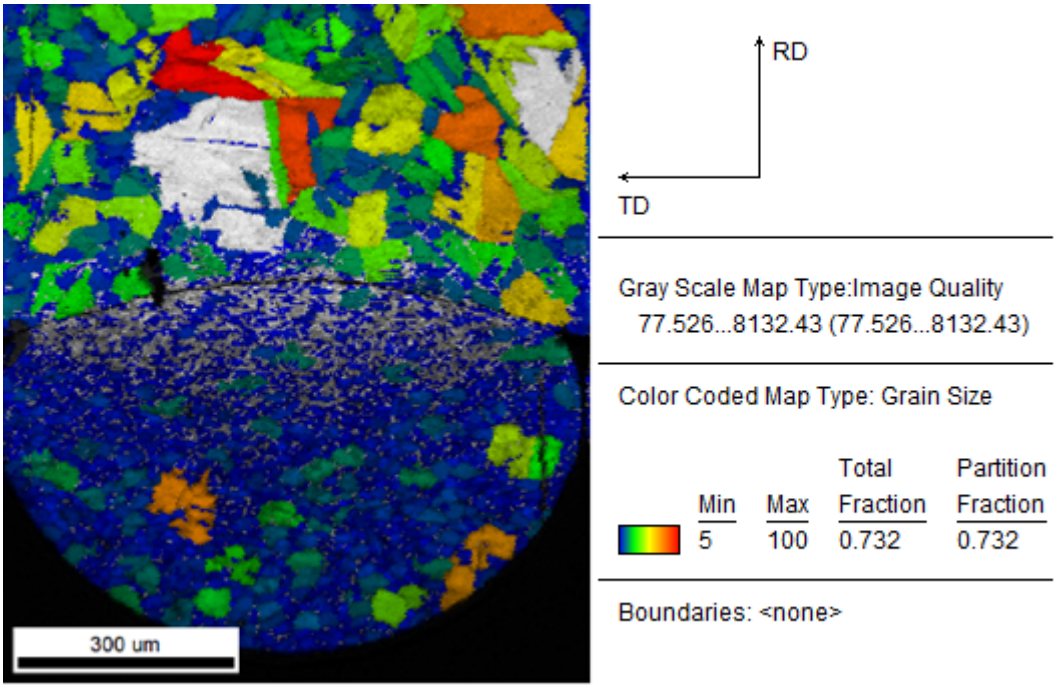

Figure 4.20: Grain size of the sample of impact speed 230 m.s^{-1}

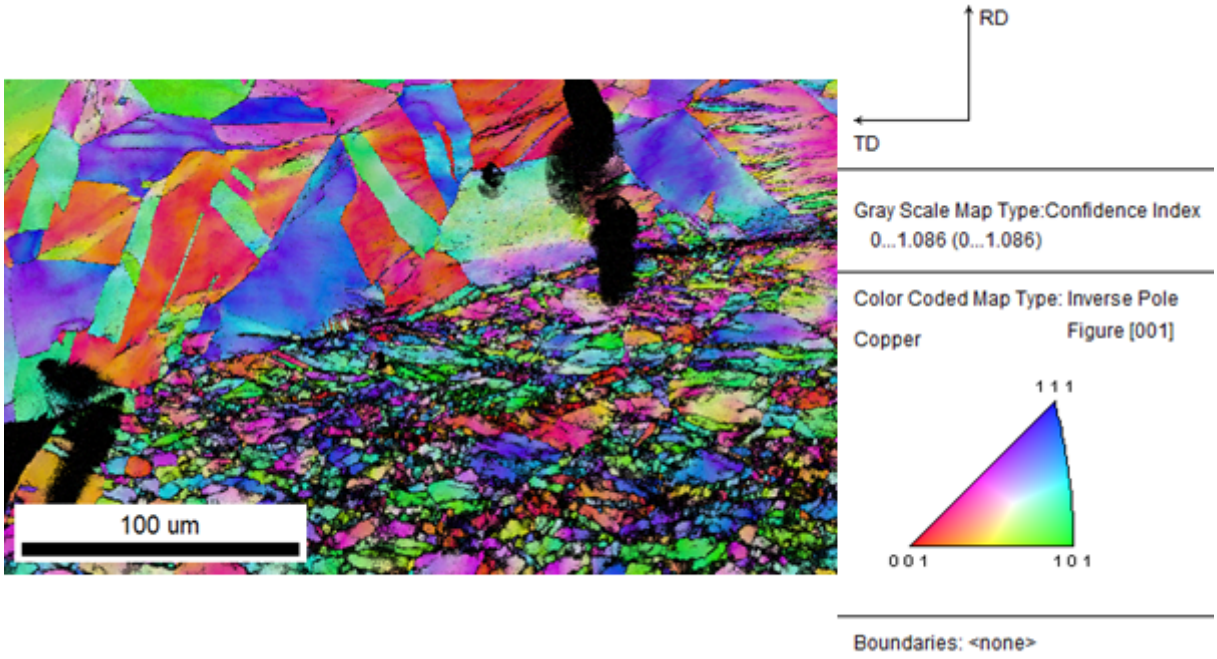

Figure 4.21: Inverse Pole Figure of the sample of impact speed 230 m.s^{-1}

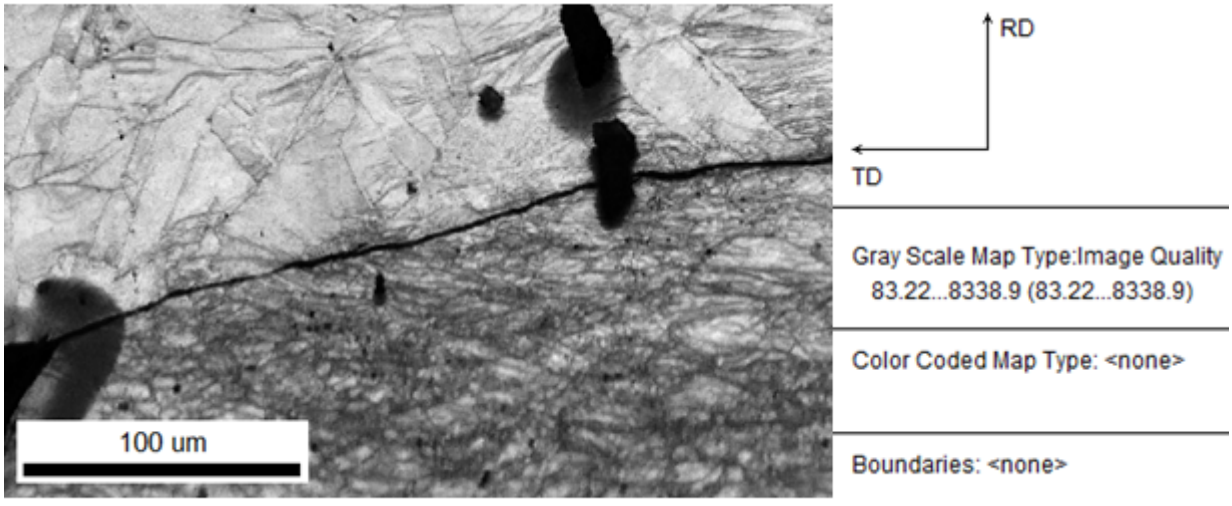

Figure 4.22: Image Quality of the sample of impact speed 230 m.s^{-1}

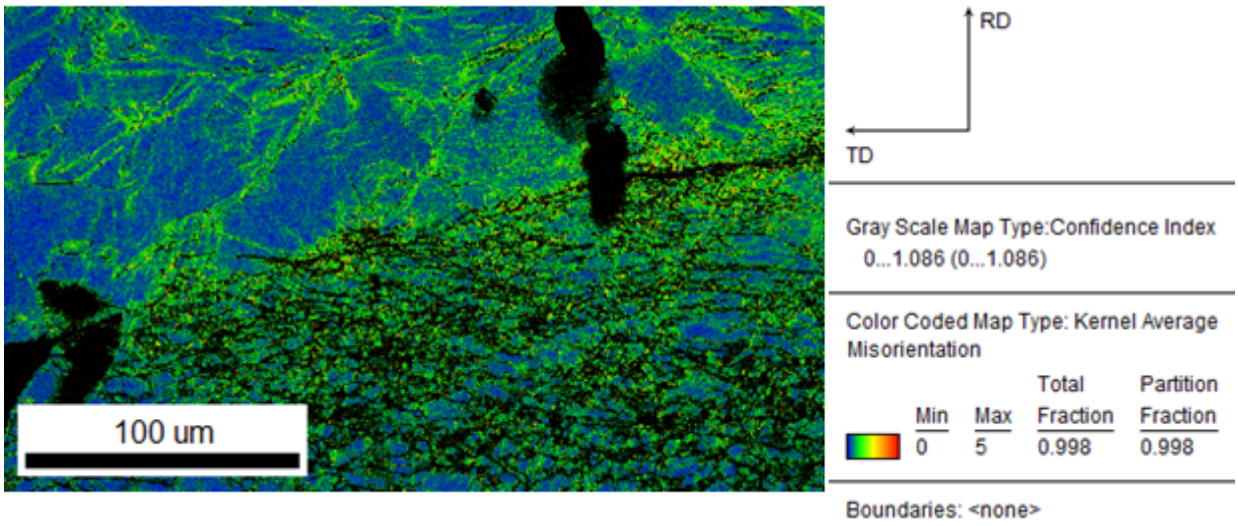

Figure 4.23: Kernel Average Misorientation of the sample of impact speed 230 m.s^{-1}

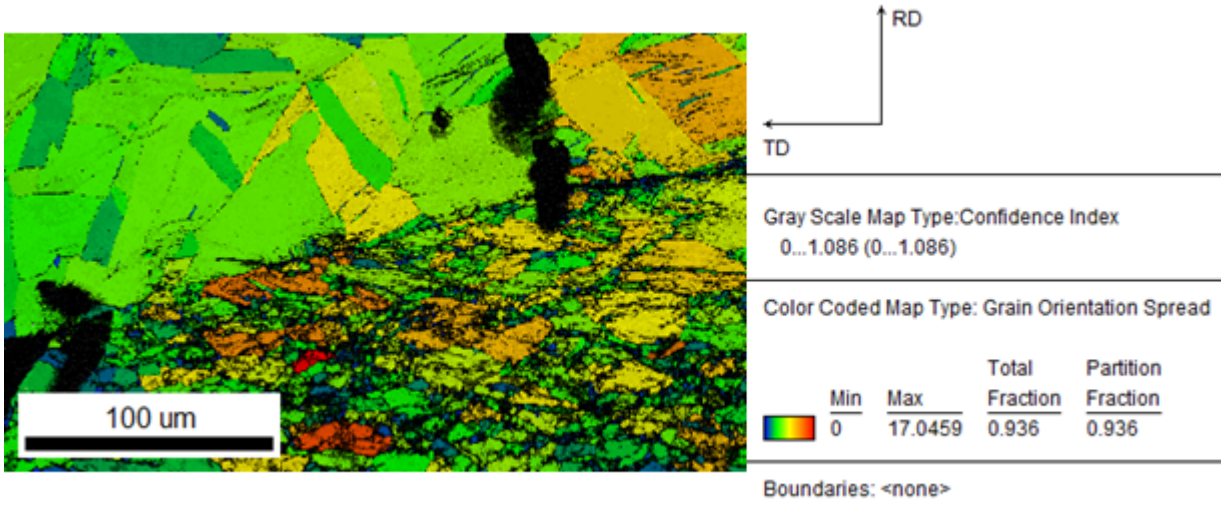

Figure 4.24: Grain Orientation Spread of the sample of impact speed 230 m.s^{-1}

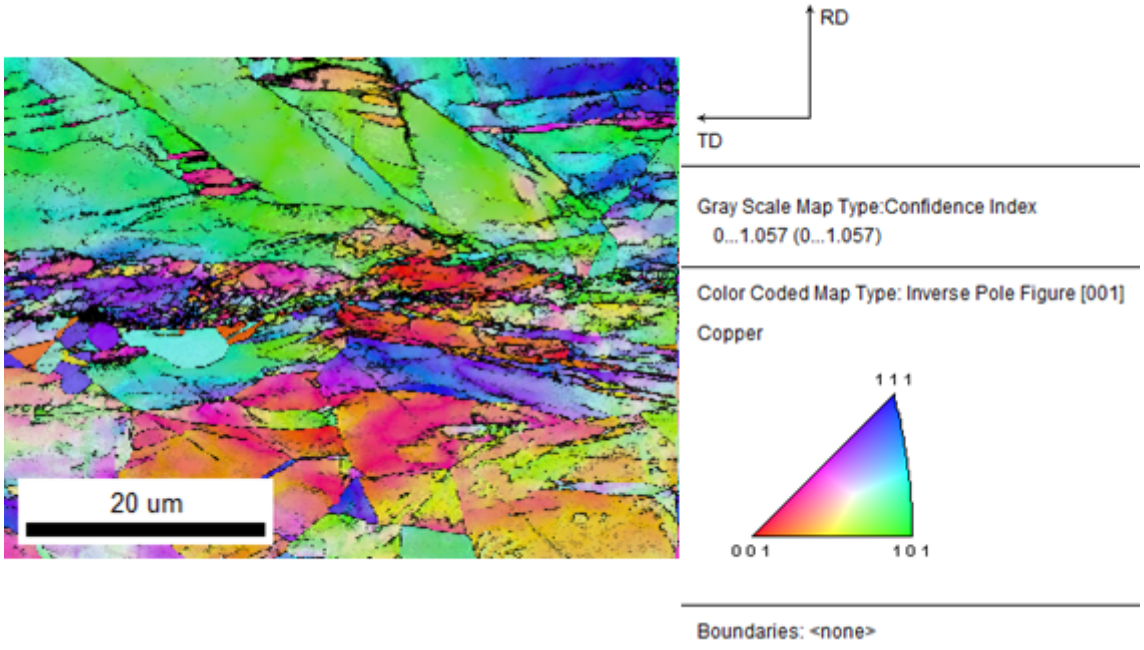

Figure 4.25: Inverse Pole Figure of the sample of impact speed 230 m.s^{-1}

Figures 4.25, 4.26, 4.27 and 4.28 show another zoom, on the interface in the center region of the impact zone, with a step of 0.1 μm.

Here a strain free region can be seen on the particle side of the interface (agglomerate of blue grains above the red one in 4.28, also blue with no green (aka strain) in 4.27). This is interpreted as a strain release due to recrystallization, and particularly dynamic recrystallization during shear banding.

This phenomenon of strain free grains near the interface is however not much observed at 230 m.s^{-1}, as can be seen in figure a global zoom on the interface with a step of 0.3 μm.

The same can also be seen at another position, on figures , again with a step of 0.1 μm. Here however the recrystallized zone is positioned were the substrate and particle seem to be in direct contact. This means that these strain-free zones do not seem to have a direct link with the contact gap, which is counterintuitive and does not agree with the present interpretation of a shear band.

Another zoom was performed on the same region, this time with a step of 0.05 μm. Figure 4.32 shows the local microstructure, with what looks like sheared, elongated grains of a few micrometers between the substrate and the recrystallized region.

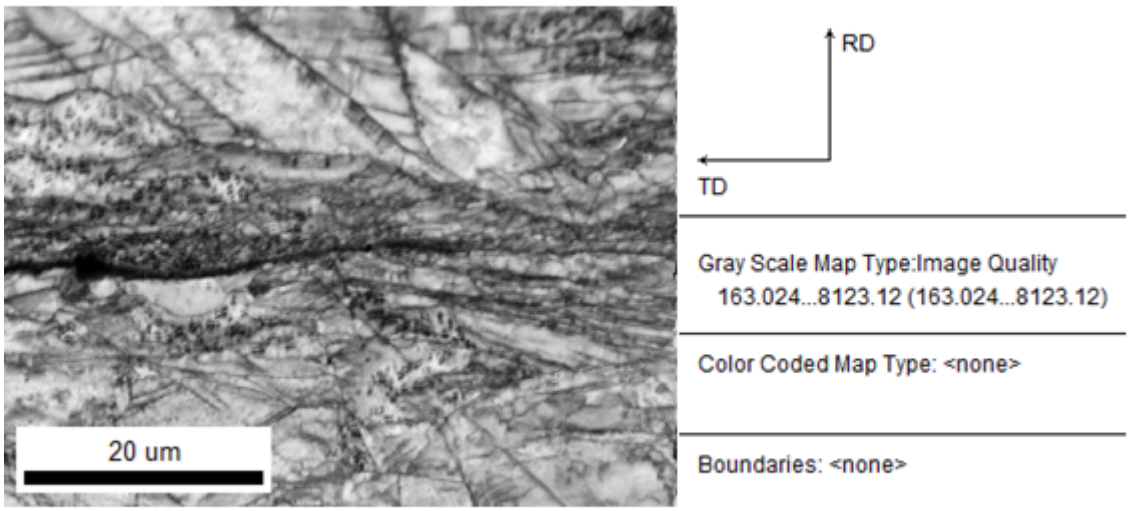

Figure 4.26: Image Quality of the sample of impact speed 230 m.s^{-1}

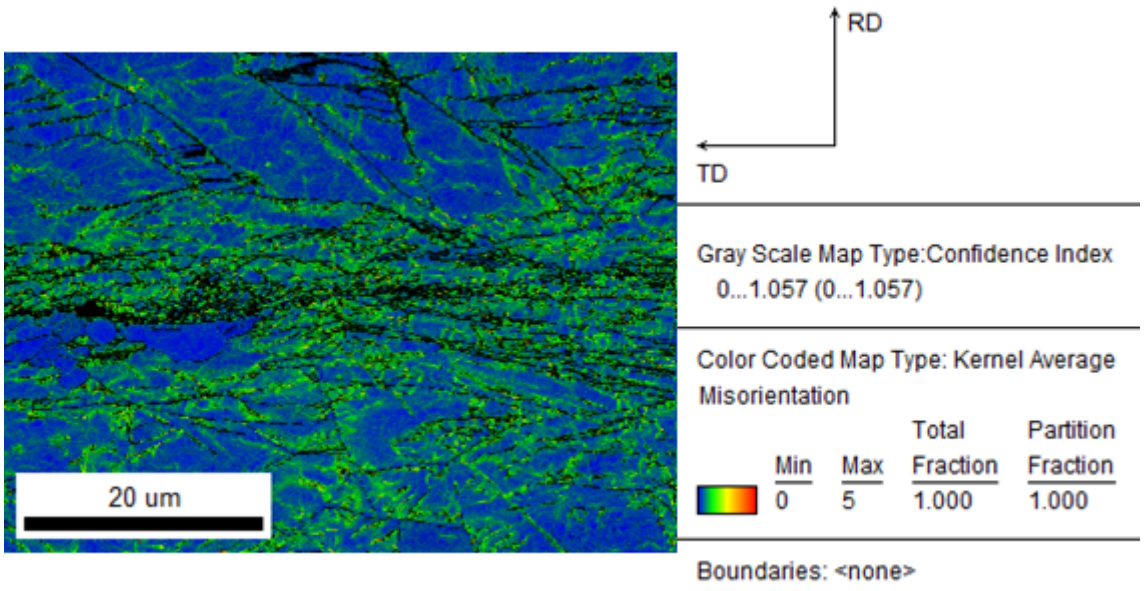

Figure 4.27: Kernel Average Misorientation of the sample of impact speed 230 m.s^{-1}

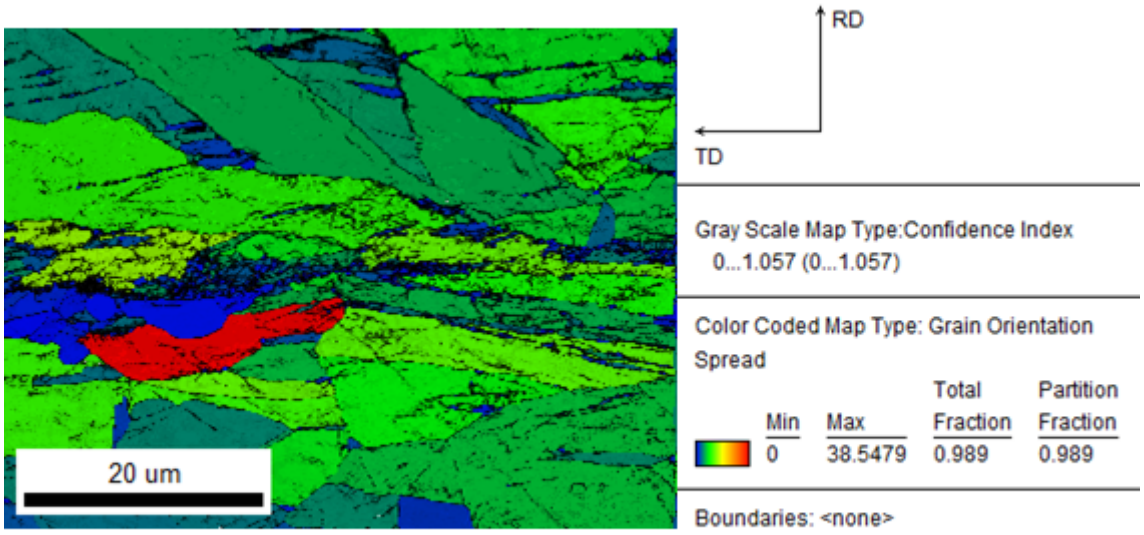

Figure 4.28: Grain Orientation Spread of the sample of impact speed 230 m.s^{-1}

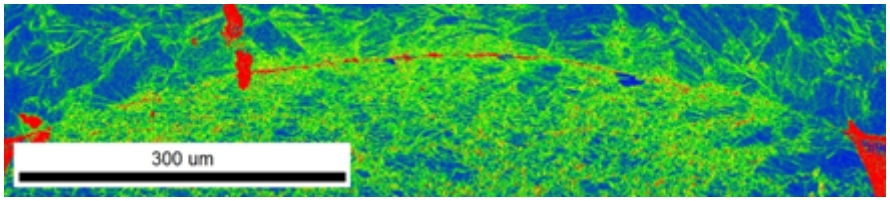

Figure 4.29: Kernel Average Misorientation of the sample of impact speed 230 m.s^{-1}

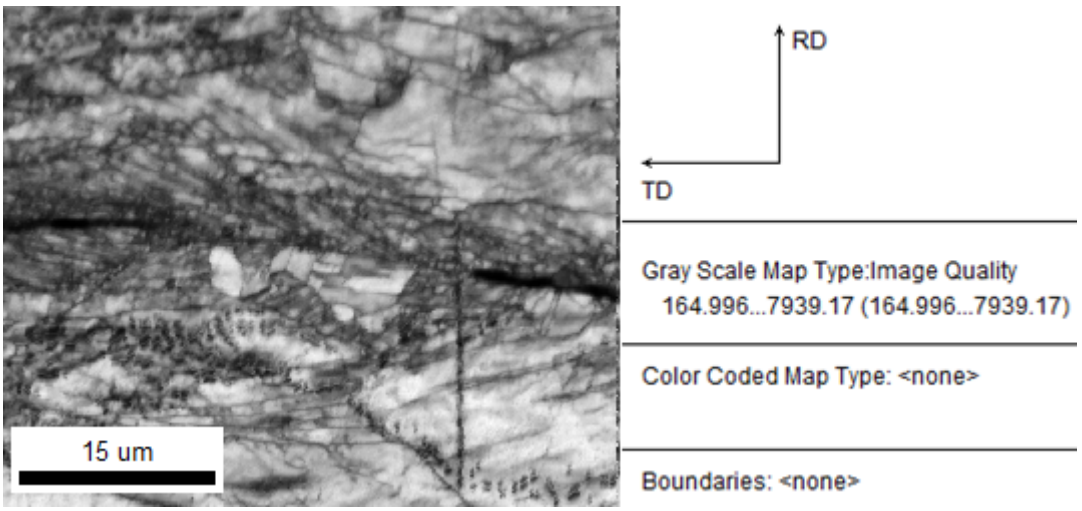

Figure 4.30: Image Quality of the sample of impact speed 230 m.s^{-1}

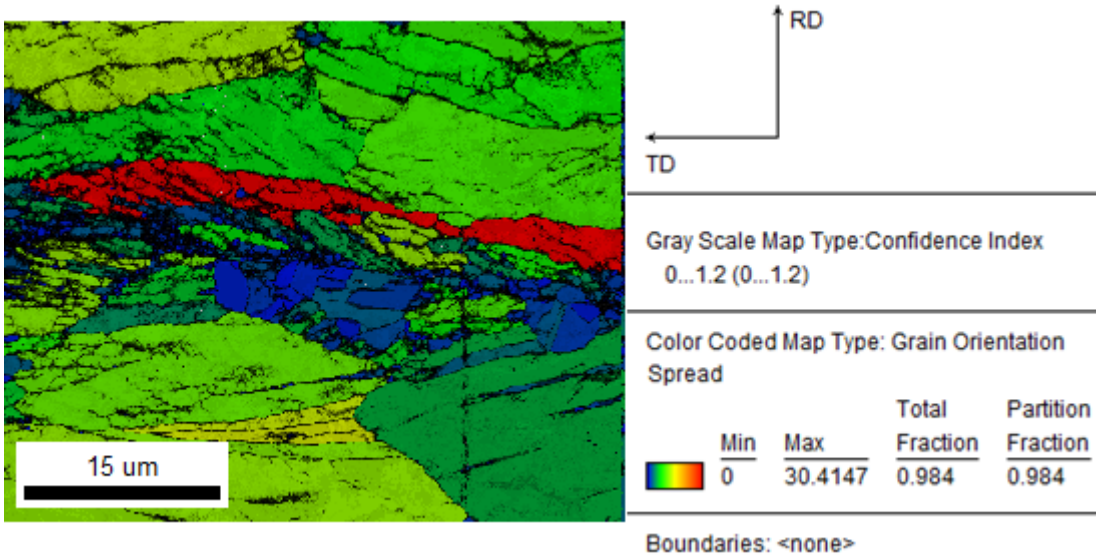

Figure 4.31: Grain Orientation Spread of the sample of impact speed 230 m.s^{-1}

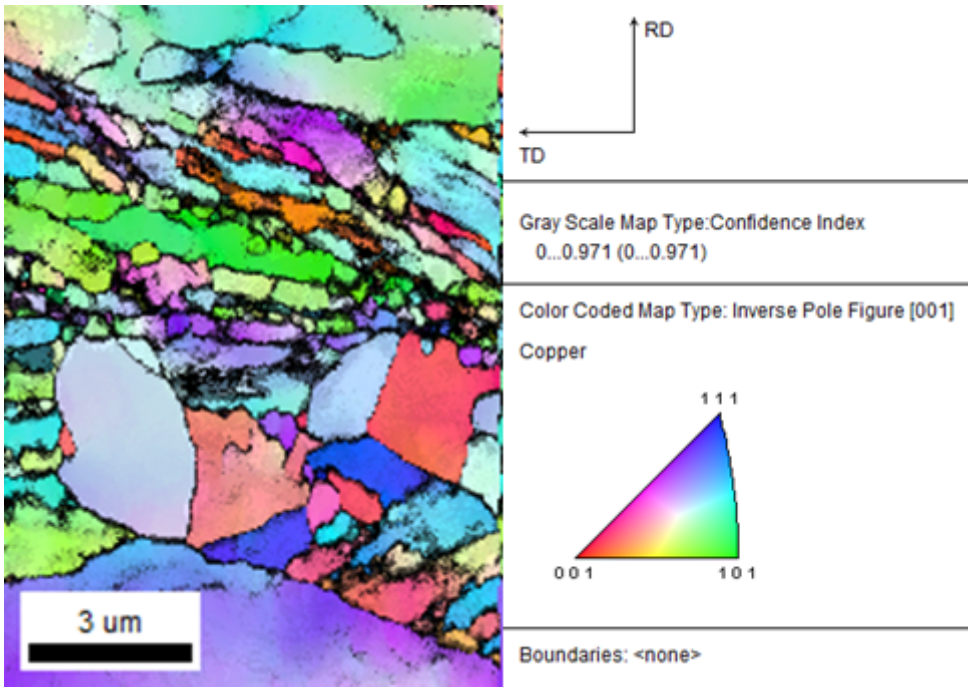

Figure 4.32: Inverse Pole Figure of the sample of impact speed 230 m.s^{-1}

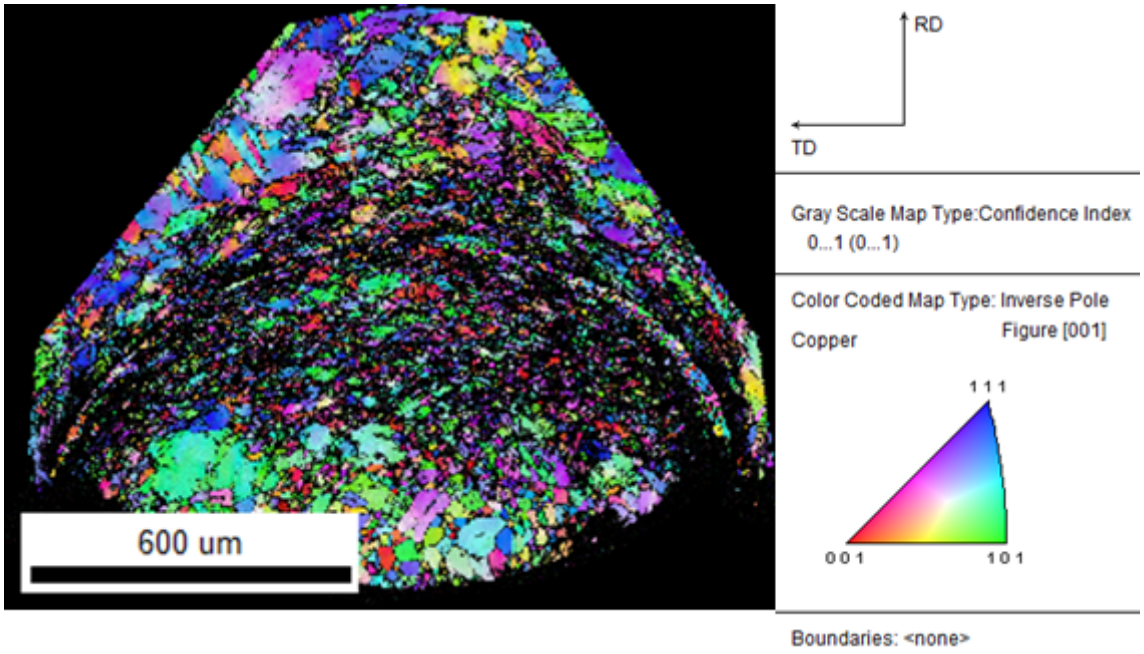

Figure 4.33: Inverse Pole Figure of the sample of impact speed 457 m.s^{-1}

4.4.2.4 Impact at 457 m.s^{-1}

A 1 mm copper particle is then impacted by means of SPITS on a copper substrate at 457 m.s^{-1}. Figures 4.33, 4.34, 4.35 and 4.36 show the complete impacted particle with a step of 0.4 μm. Figure 4.33 shows that this time grain refinement also occurred on the substrate side, and both sides underwent large deformations. The most interesting observations however is on figures 4.35 and 4.36, where we can see large strain-free zones on the left and right sides of the contact zone.

Then a zoom on this same map (step 0.4 μm) is shown, of the extreme left of the interface, near the material jet. Figure 4.37 shows the local microstructure, with the strain-free grains following the interface. These range in size from a few to ten microns. The other grains however seem to go as low as under 1 micron, especially in what appears to be a shear band in the substrate going up from the bottom left corner. The strain-free zone appears to be around ten microns thick.

Another zoom with a step of 0.2 μm shows the strain-free zone on the right of the interface. Here the strain-free region appears to be larger, around 20 to 50 microns large, and contains grains of 5 to 10 microns in size.

4.4.2.5 Discussion on the general EBSD observations

In conclusion to these general observations, a strain-free zone was detected, especially at high impact speed, but also on some parts of the interface for the low impact speed. This strain-free zone is positioned on both sides of the impact surface, which correlates with the highly sheared region in an impact. This is seen as a sign of presence of an instability region.

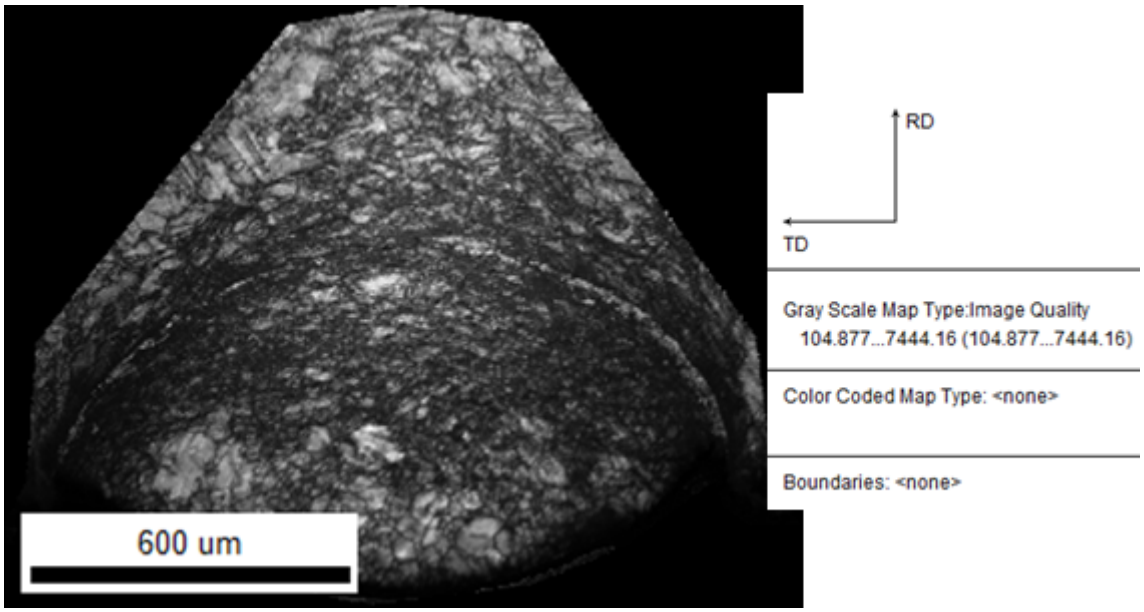

Figure 4.34: Image Quality of the sample of impact speed 457 m.s^{-1}

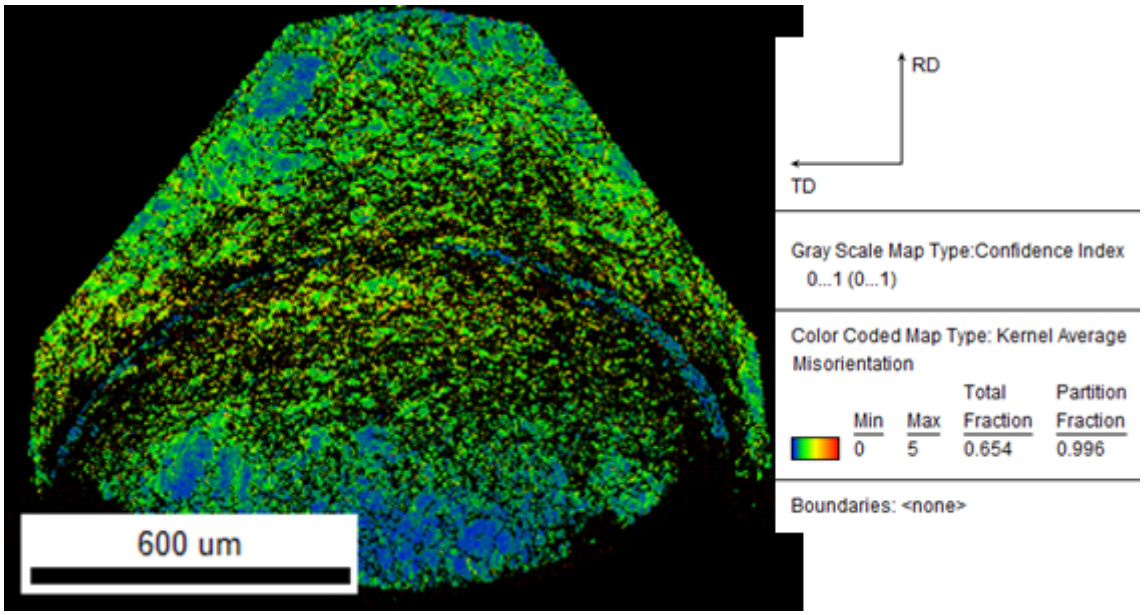

Figure 4.35: Kernel Average Misorientation of the sample of impact speed 457 m.s^{-1}

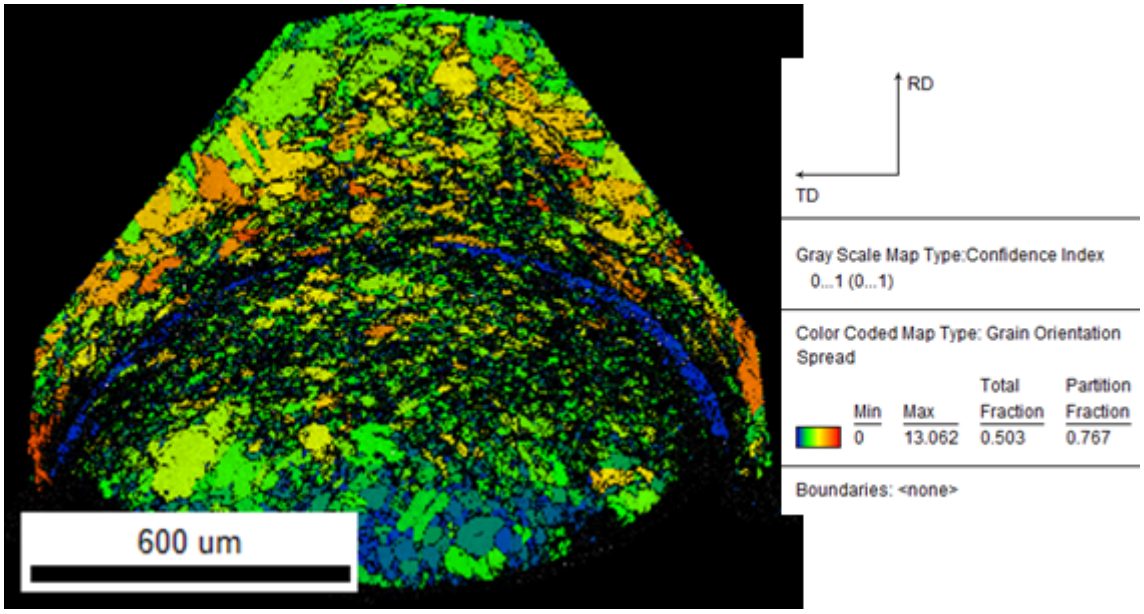

Figure 4.36: Grain Orientation Spread of the sample of impact speed 457 m.s^{-1}

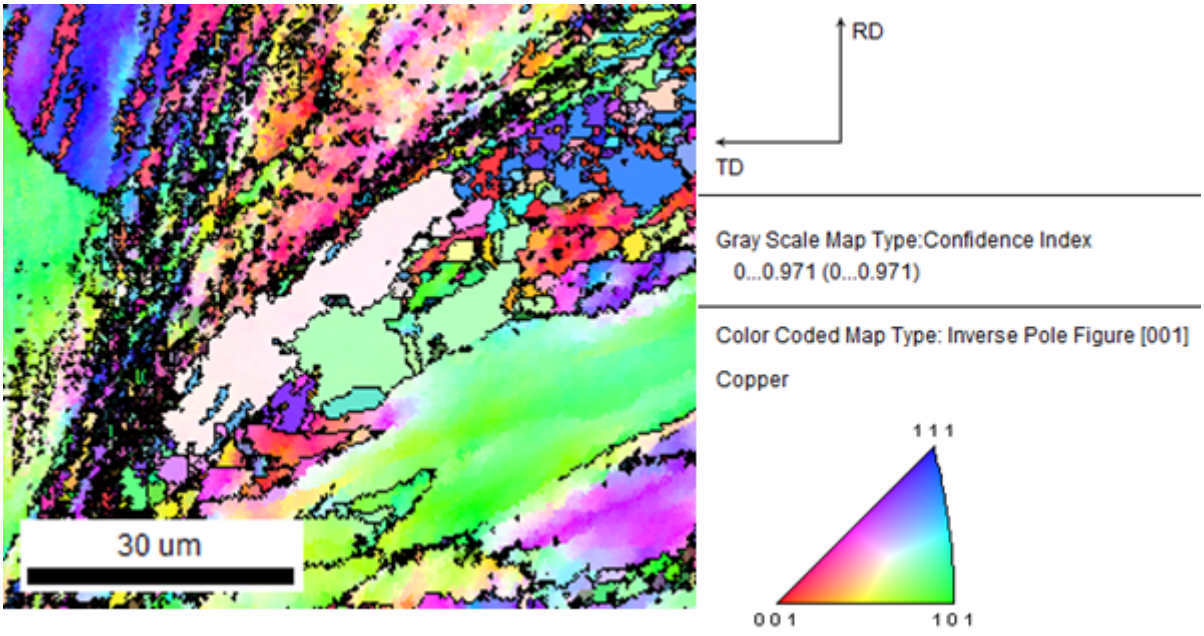

Figure 4.37: Inverse Pole Figure of the sample of impact speed 457 m.s^{-1}

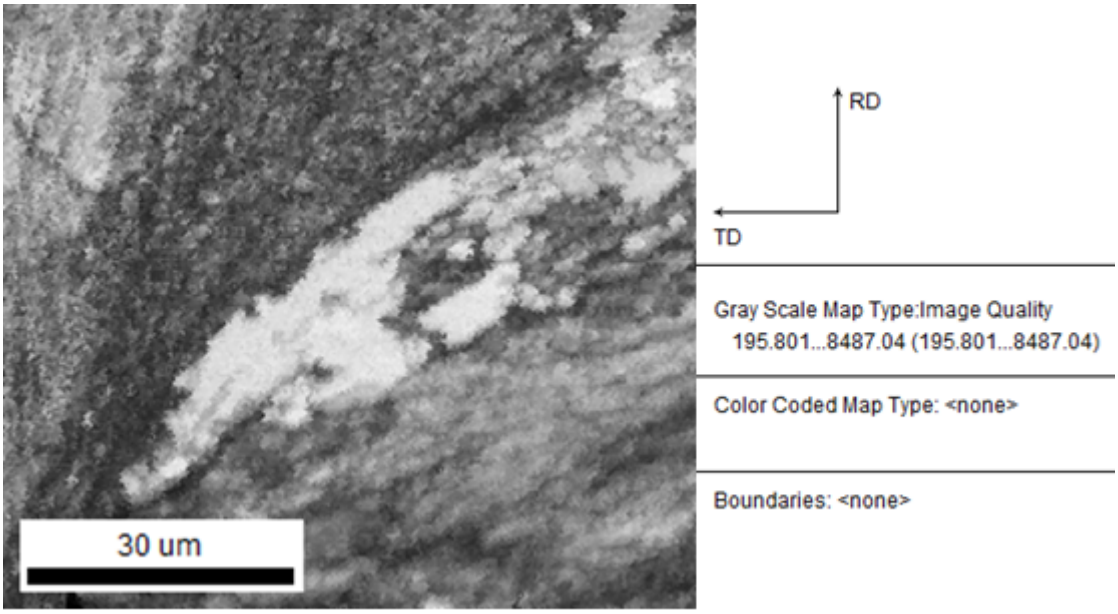

Figure 4.38: Image Quality of the sample of impact speed 457 m.s^{-1}

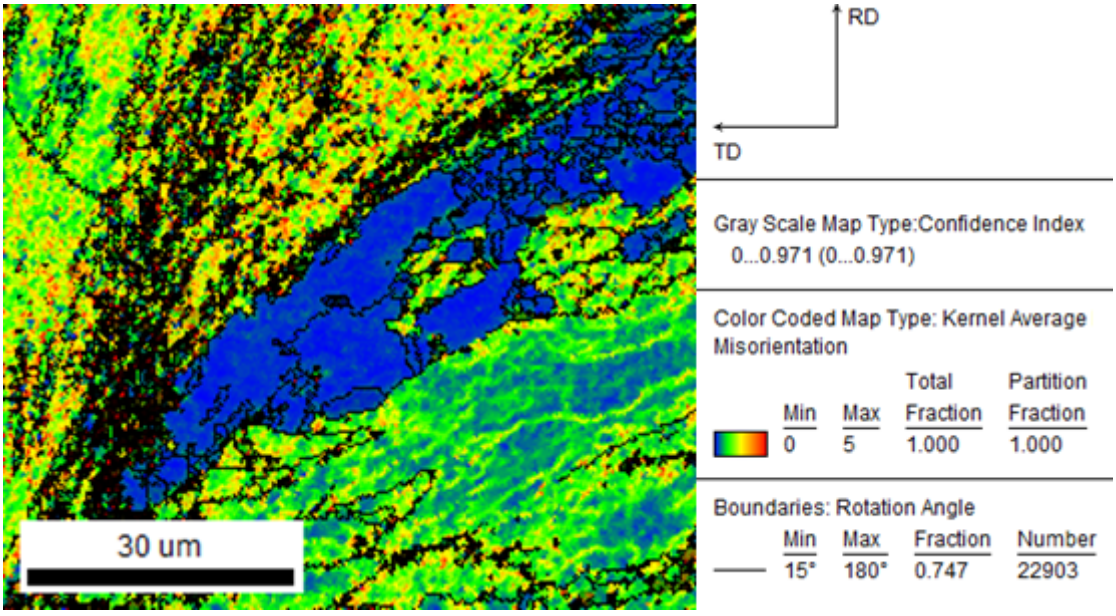

Figure 4.39: Kernel Average Misorientation of the sample of impact speed 457 m.s^{-1}

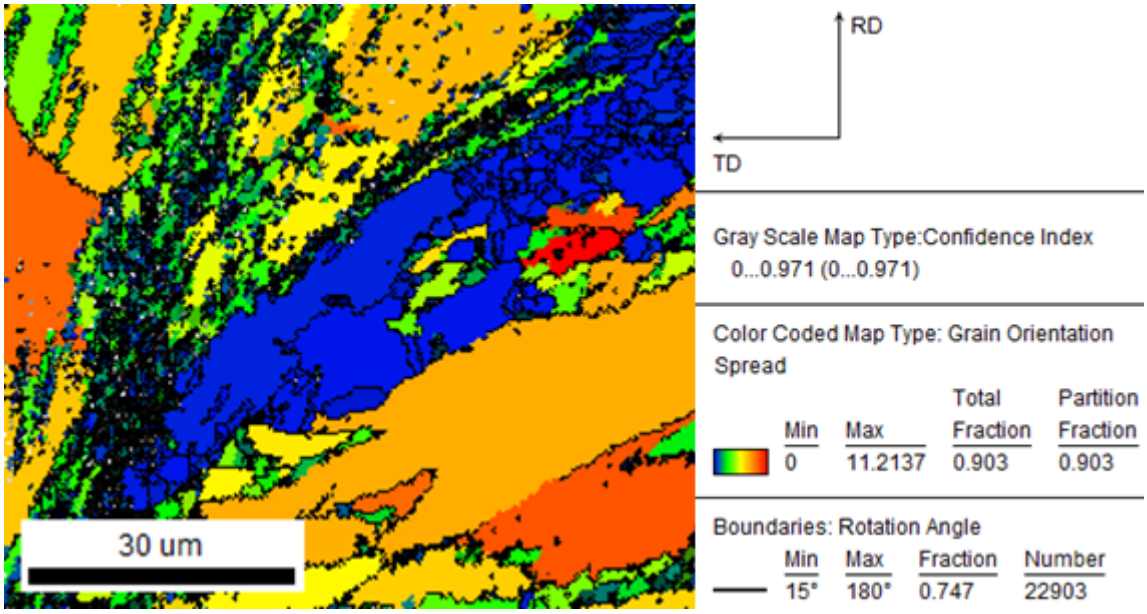

Figure 4.40: Grain Orientation Spread of the sample of impact speed 457 m.s^{-1}

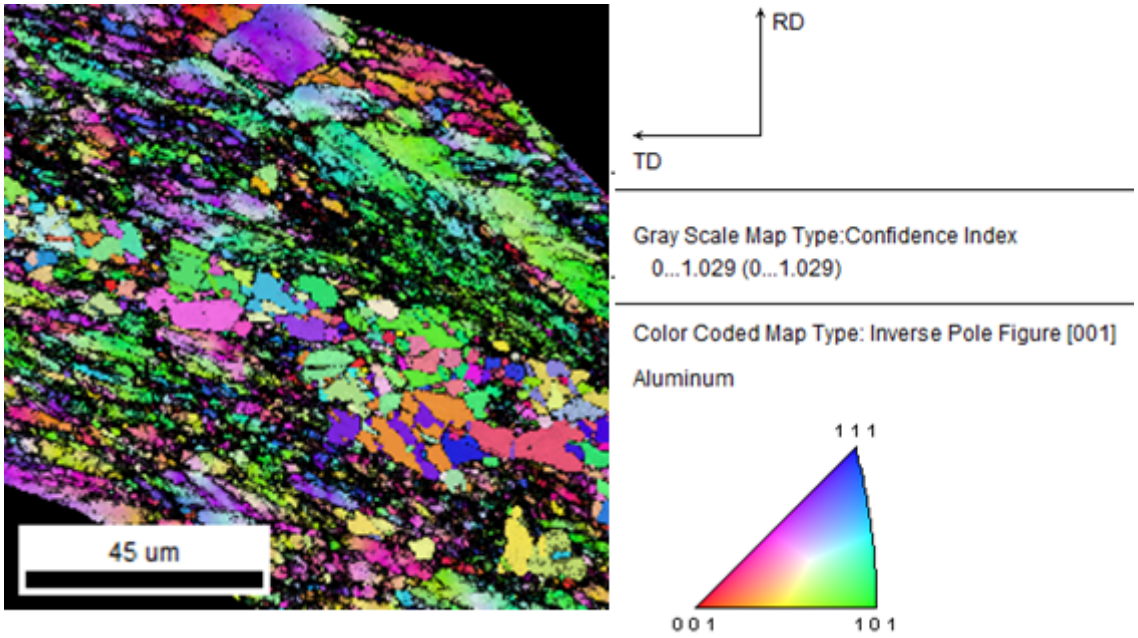

Figure 4.41: Inverse Pole Figure of the sample of impact speed 457 m.s^{-1}

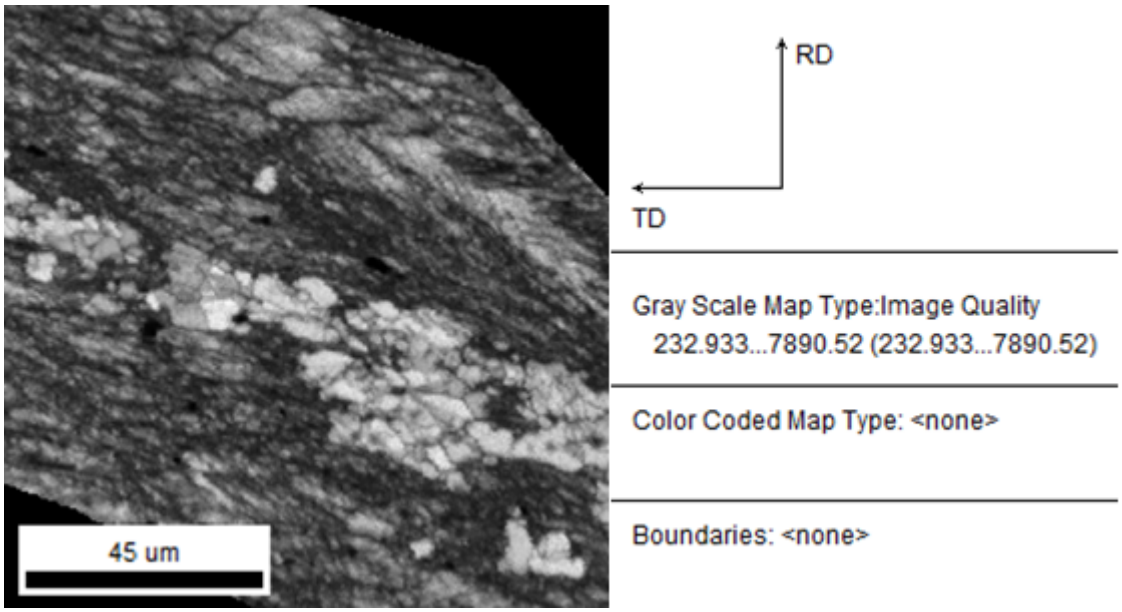

Figure 4.42: Image Quality of the sample of impact speed 457 m.s^{-1}

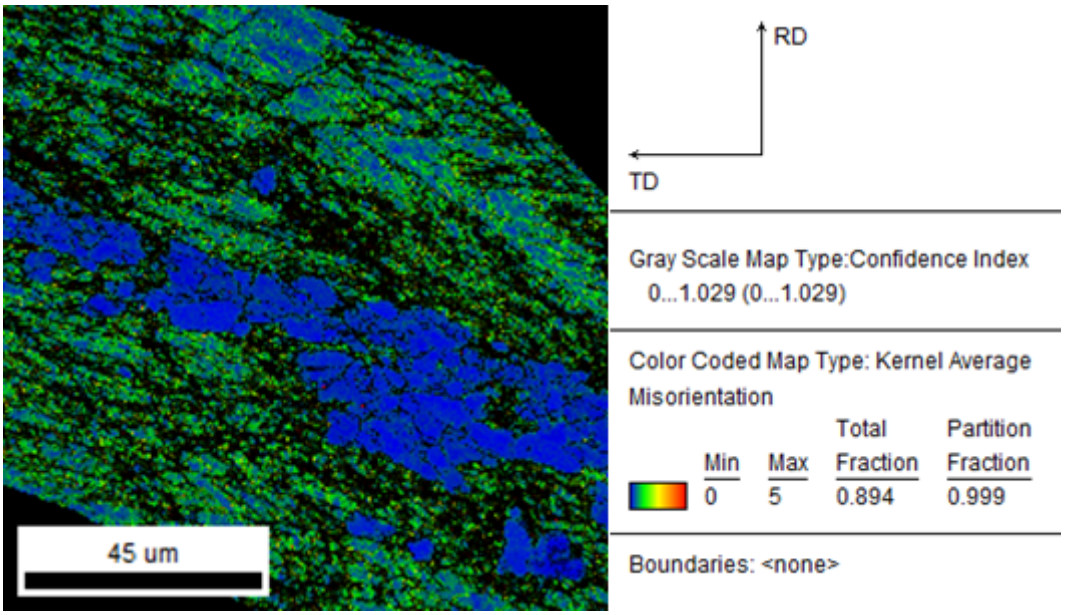

Figure 4.43: Kernel Average Misorientation of the sample of impact speed 457 m.s^{-1}

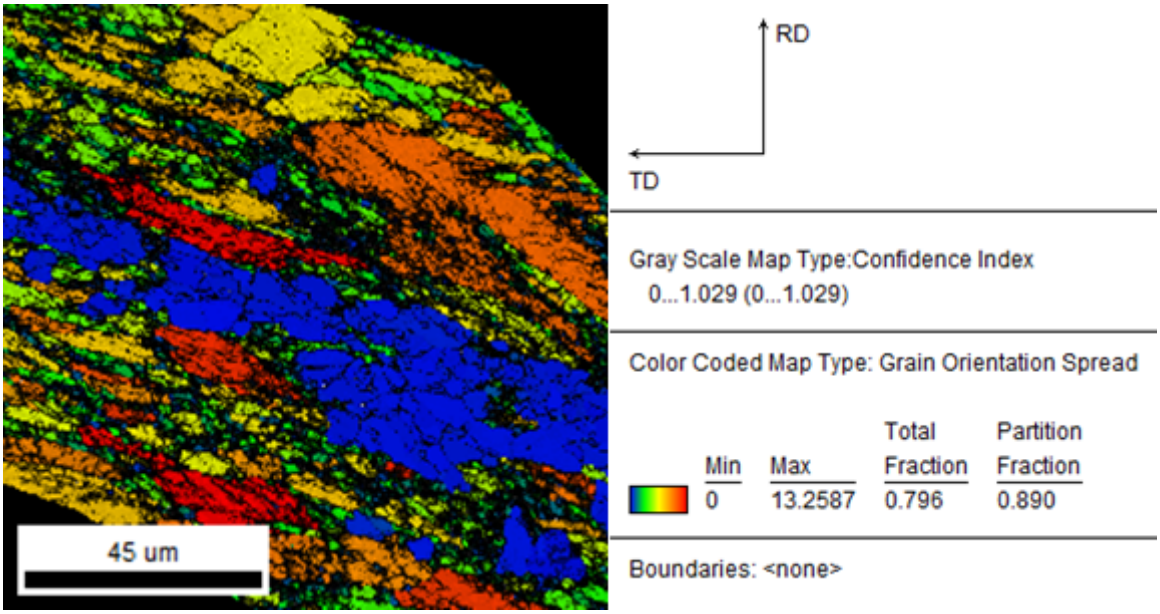

Figure 4.44: Grain Orientation Spread of the sample of impact speed 457 m.s^{-1}

This instability thus seems to be sporadicly present at low speed, despite the fact that the particle is stuck to the substrate after impact. However the measurements being made on a cross-section, more strain-free regions might appear in other parts of the complete contact surface, and end up being enough for adhesion. Another possibility is that this strain-free region is not the first sign of instability and adhesion, but only appears for higher loads and pressures.

At higher speed this strain-free region spreads nearly on the complete contact zone, except at the center.

The link between adhesion and grain refinement and recrystallization is thus not completely clear, but these observations are a first step toward a more complete and thorough investigation.

4.4.3 Grain size evaluation

The measurements of local grain size at indentation sites is presented here. For each sample, first a global EBSD map is performed with a measurement step of 2 μm, giving a general view of the impacted sample and a general idea of the size of the coarsest grains involved. Indeed with a step of 2 μm, grains of a width as low as 4 or 6 μm can theoretically be detected and indexed by the analysis software. In a second time, more precise zooms were made with a measurement step of 0.2 μm on each indentation line. As for the grain size evaluation process, the coarse image is used to highlight the grain on which an indentation has fallen, and then the software performs a grain size evaluation described first as the number of data points contained in a grain. The grain area is then calculated by summing up the number of points in a grain multiplied by the product of the square of the step size and a factor depending on the type of scanning grid. Here a hexagonal grid is used, so the factor is half the square root of 3. The grain size can then be defined as a diameter. This diameter is determined by assuming the grain is round, and is equal to twice the square root of the area divided by π.

This diameter value is the one used in this work. Since this evaluation was made in order to link hardness and grain size, only grains where an indentation was made are considered. This

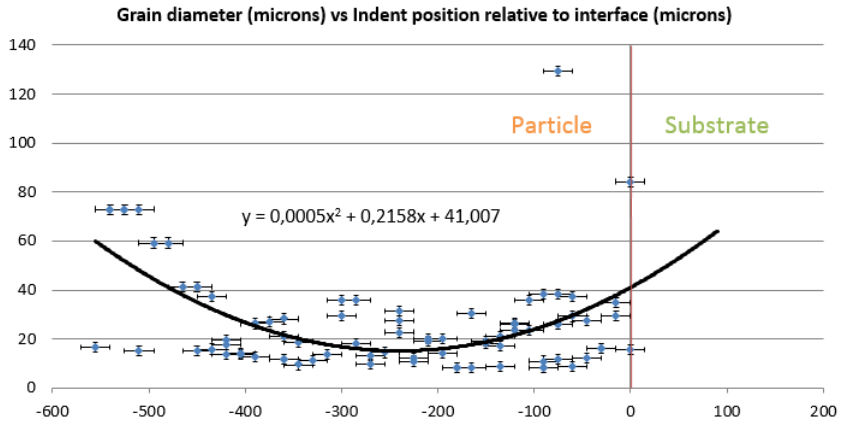

Figure 4.45: Grain size variation with the relative position to the interface at 230 m.s^{-1}

can be a bias as smaller grains would thus have a lesser chance of being recorded. It is however quite obvious from the EBSD images that this bias is limited as the grains are usually never under 1 μm in size, at least for the sample impacted at 230 m.s^{-1}.

4.4.3.1 Impact at 230 m.s^{-1}

First the grain diameter for the particle impacted at 230 m.s^{-1} is evaluated. The result on all obtained EBSD scans is shown in Figure 4.45 where the local grain size is given as a function of the relative position to the interface, determined in the same manner as in section 4.3.2.

The EBSD maps used for these measurements are shown in Figure 4.46 and 4.47, with the red rectangle showing the zoomed in region.

We can see that the grain size is indeed refined near the interface, at least on the particle side. The trend curve shows us that the most refined region is not near the interface but rather 250 μm away from it in the particle. This however takes into account the substrate grains which have already been shown to start bigger and experience less refining. It also takes into account to extreme values near the interface on the particle side. If those are not taken into account we can see that the trend actually stabilizes between 400 and 0 μm inside the particle.

The conclusion here is that looking at the EBSD images and grain size measurements, the particle experiences refining due to the extreme loading and deformations. A localized effect near the interface is however not observed at 230 m.s^{-1}.

4.4.3.2 Impact at 457 m.s^{-1}

The indentations on the sample impacted at 457 m.s^{-1} were also investigated by EBSD to find the local grain size. The results are shown in Figure 4.48. The EBSD maps used for these measurements are shown in Figure 4.49 and 4.50, with the red rectangle showing an example of a zoomed in region.

The results obtained with the global EBSD map with a step of 2 μm were far too coarse to have any capability of finding local grain sizes, due to the higher deformations undergone by the particle. The local zooms on indentations, although helpful, are too precise and narrow to contain most of the full grains. Therefore a third EBSD map of intermediate precision of 1 μm was also used.

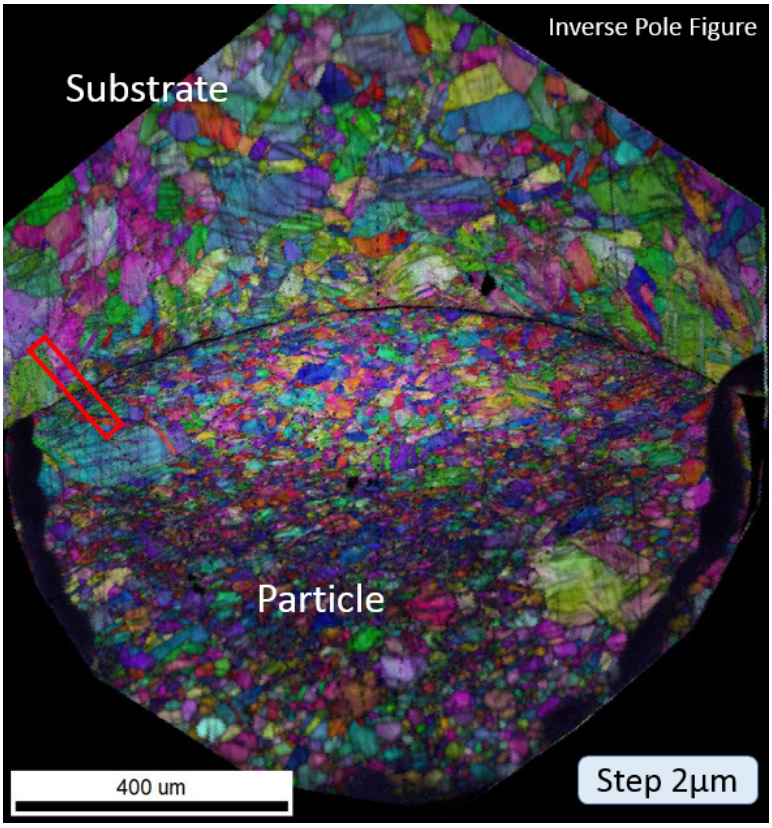

Figure 4.46: Inverse Pole Figure of the global map used for grain size measurement of the sample impacted at 230 m.s^{-1}

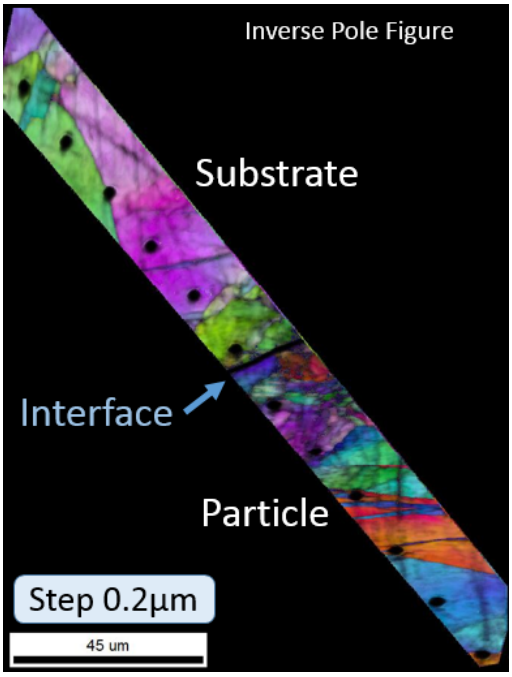

Figure 4.47: Example of Inverse Pole Figure of a zoom on indentations used for grain size measurement of the sample impacted at 230 m.s^{-1}

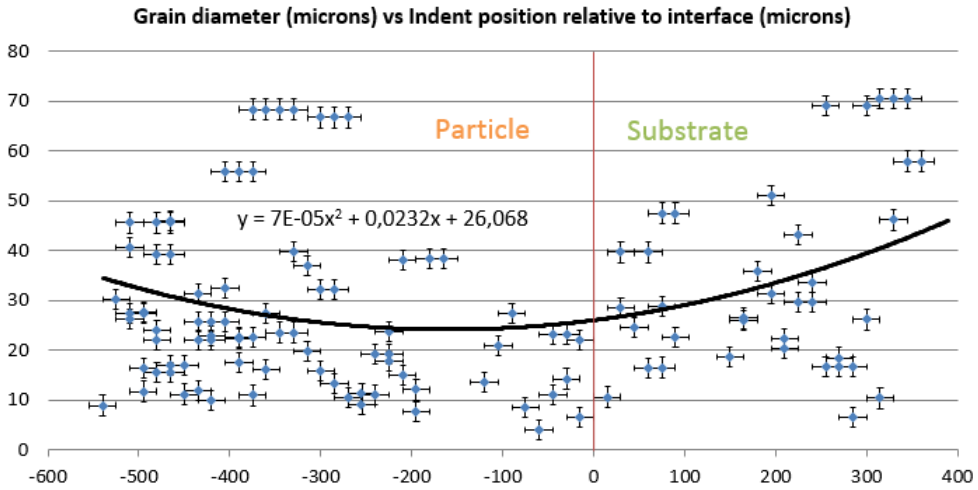

Figure 4.48: Grain size variation with the relative position to the interface at 457 m.s^{-1}

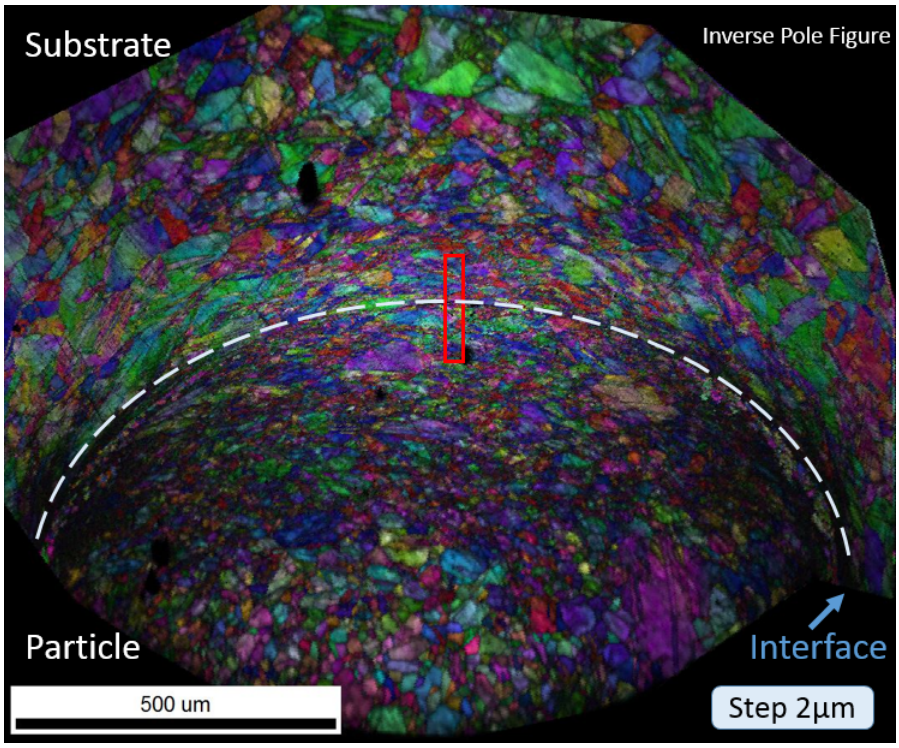

Figure 4.49: Inverse Pole Figure of the global map used for grain size measurement of the sample impacted at 457 m.s^{-1}

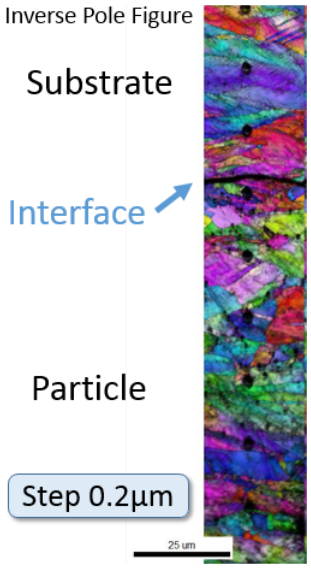

Figure 4.50: Example of Inverse Pole Figure of a zoom on indentations used for grain size measurement of the sample impacted at 457 m.s^{-1}

Once again, the particle as well as the substrate seem to experience a change in grain size near the interface. The trend is however not so clear this time and the spread in values is high. It should be noted that once again the step between indentations is probably too large to correctly capture the finest grains, even though by looking at the EBSD maps one can confirm that the smallest grains are always at least 1 μm in size. The range of grain sizes measured is also lower than at the lower speed, which is consistent with the grain refinement increasing with initial kinetic energy and possibly contact pressures.

4.5 Link between grain size and hardness

A tentative is made to link grain size change and hardness change to conclude on the viability of the macroscopic Johnson-Cook material law to predict mesoscopic behaviors.

4.5.1 Impact at 230 m.s^{-1}

As can be seen in Figure 4.51, where the local hardness value is plotted as a function of the local grain size at the indentation site, no clear trend is observed for the particle impacted at 230 m.s^{-1}.

The same figure with a logarithmic scale for the grain size is shown in Figure 4.52. Once again no clear effect of the grain size on the hardness value can be derived from these results at 230 m.s^{-1}.

4.5.2 Impact at 457 m.s^{-1}

The local hardness value is plotted as a function of the local grain size at the indentation site for the sample impacted at 457 m.s^{-1} in Figure 4.53, and again no clear trend is observed.

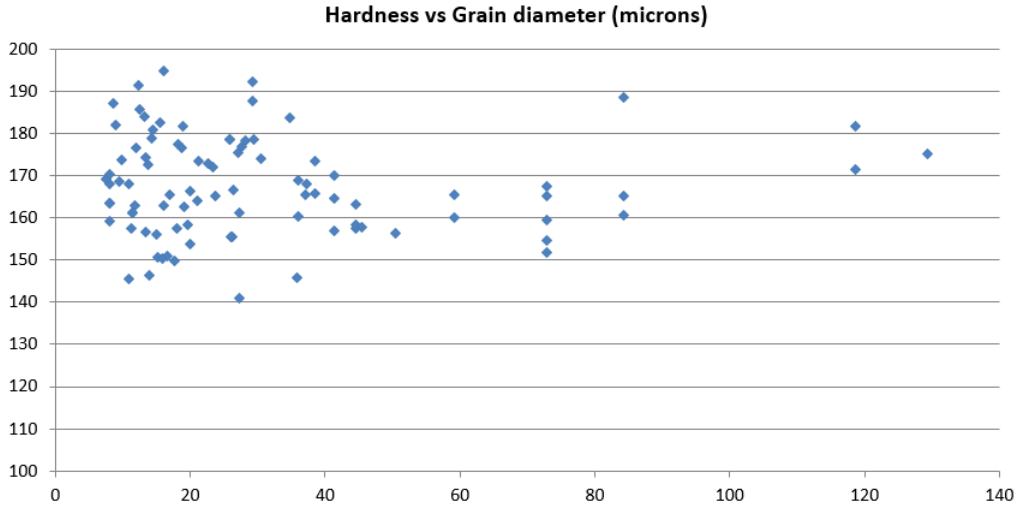

Figure 4.51: Hardness variation as a function of local grain diameter at 230 m.s^{-1}

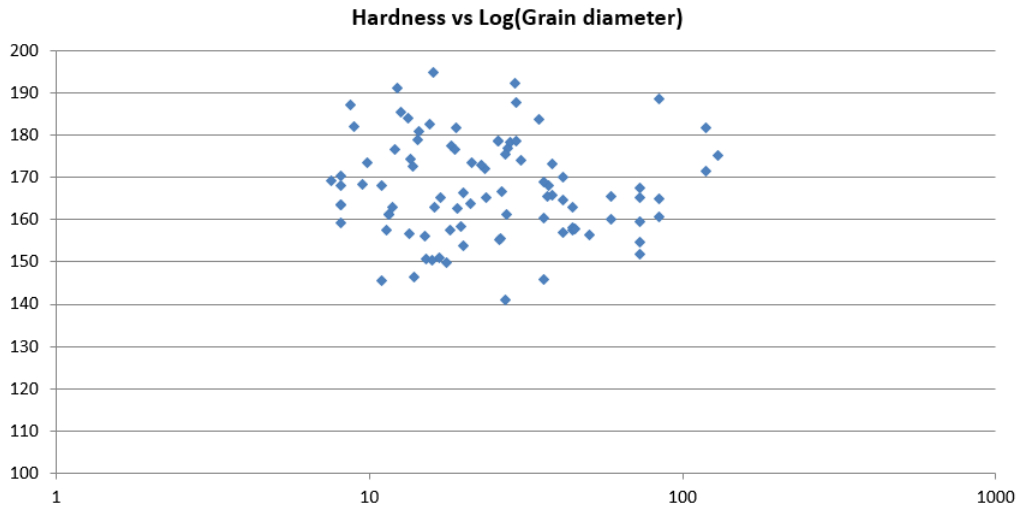

Figure 4.52: Hardness variation as a function of the logarithm of the local grain diameter at 230 m.s^{-1}

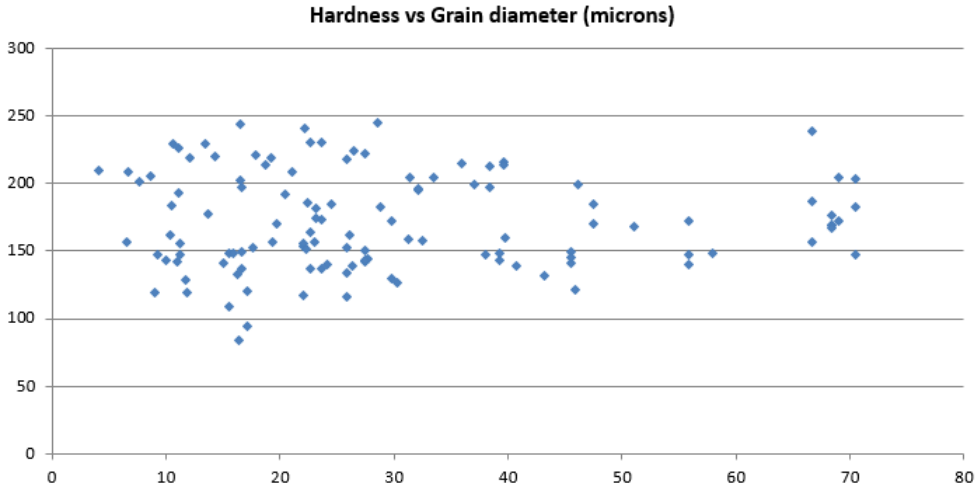

Figure 4.53: Hardness variation as a function of local grain diameter at 457 m.s^{-1}

The same figure with a logarithmic scale for the grain size is shown in Figure 4.54. Once again no clear effect of the grain size on the hardness value can be derived from these results at 457 m.s^{-1}.

4.5.3 Discussion on the results

It is thus concluded that for 1 mm copper particles impacted on a copper substrate with the SPITS system at 230 and 457 m.s^{-1}, the simulation of grain dynamics and specifically the change in grain size is not required and the usual Johnson-Cook macroscopic law is sufficient for the model, as a strong dependence between material properties and grain size is not observed.

4.6 Comparison with simulated deformed shapes

In this section a brief comparison of simulated deformations with the shapes obtained experimentally is made, with conclusions on the validity of the model.

4.6.1 Impact at 230 m.s^{-1}

Several sets of simulations are carried out of the impact of a 1 mm copper particle on a copper substrate at 230 m.s^{-1} as in the experimental case. The best results obtained involve: using a mesh size of 30 μm as SPH radius, using a FE substrate with the same element size (more on the possible reasons why later), and fitting the copper material properties associated with both parts to the hardness results previously obtained on the substrate in a region far from the impact site. The initial yield strength (coefficient A in the Johnson-Cook law) is changed to a value of 3 times the $HV_{0.1}$ value, a way of getting a coarse approximation, found in the manual for the Fischer indentation machine.

The result obtained is given in Figure 4.55 where the final vertical size of the particle and the vertical displacement of the substrate are shown, giving a decrease in particle height of 23.5%

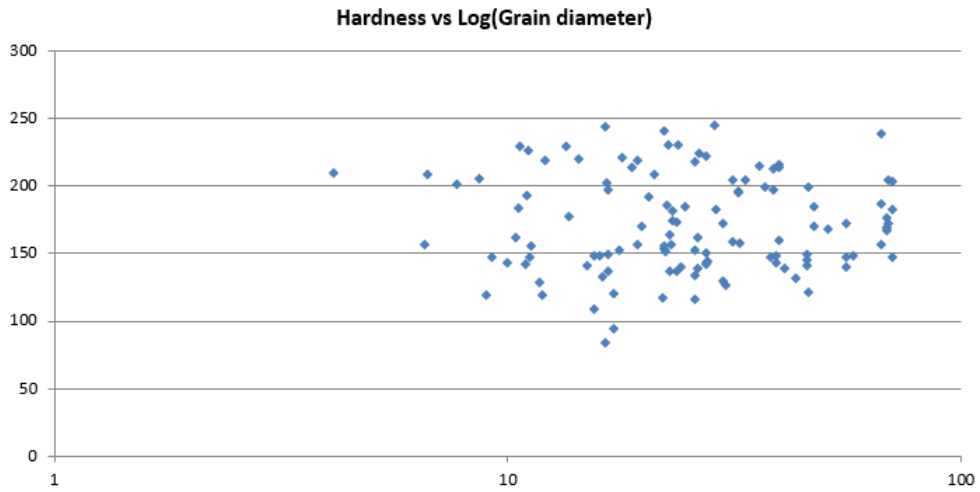

Figure 4.54: Hardness variation as a function of the logarithm of the local grain diameter at 457 m.s^{-1}

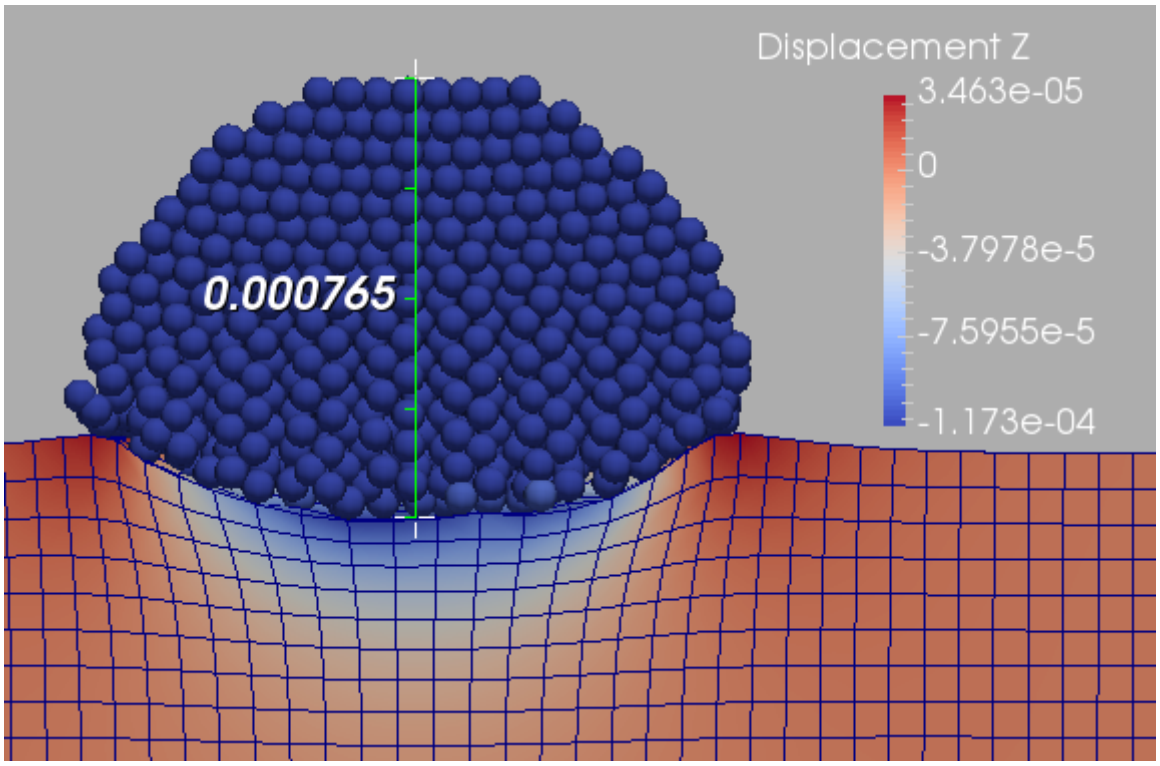

Figure 4.55: Cut view of the simulated copper on copper SPSS impact at 230 m.$^{-1}$ with vertical displacements

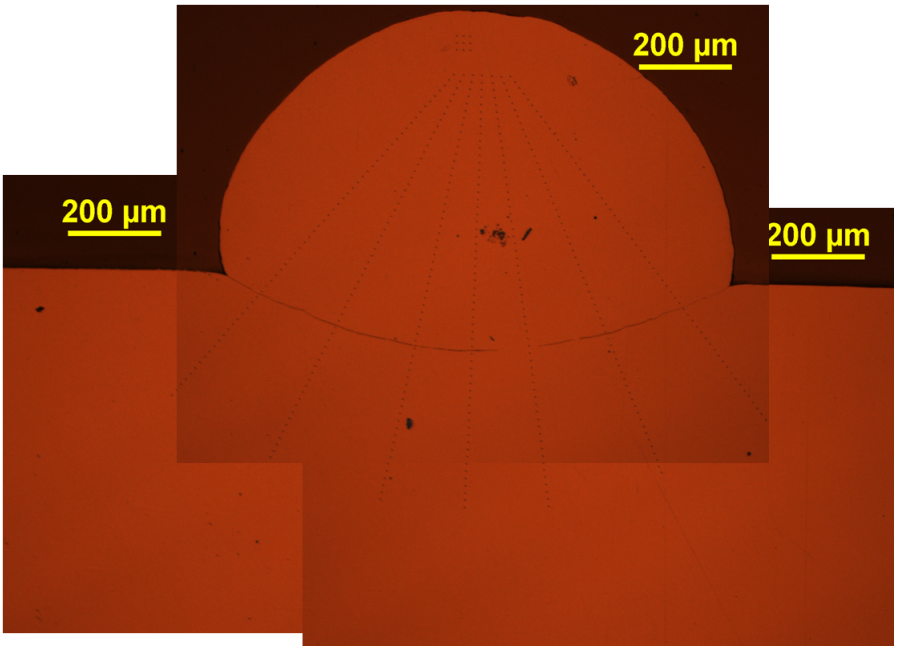

Figure 4.56: Cross-section view of the copper on copper SPSS impact at 230 m.$^{-1}$

and a penetration of 15.2% (both relative to the initial particle diameter of 1 mm). The measured increase in particle diameter, not shown here, is of 16%.

For comparison, the same variables found on the experimental specimen shown again in Figure 4.56 are of 30% decrease in particle height, 7.5% substrate penetration, and 10% increase in particle diameter. These values, measured using the scale on the image, are to be considered carefully as everything indicates that the particle was not cut at its perfect center or even in a plane perfectly parallel to the impact direction.

These few values however show that the difference is within 5 to 10% for particle deformation, which is considered good in terms of numerical simulation. The substrate penetration is however not considered satisfactory, but once again should be considered with caution as the sample might not have been cut at the position of maximum penetration. Overall the global deformed shape is thus considered similar and valid.

4.6.2 Impact at 457 m.s^{-1}

The same numerical setup is used to simulate the impact at 457 m.$^{-1}$, only this time using a mesh size of 40 μm due to stability issues at the time of the simulation.

The deformed shape obtained is given in Figure 4.57, where the final diameter of the particle and the vertical displacement of the substrate are shown. The decrease in height is of 31.5%, the penetration is of around 46% if considering the jetted material, or 33.5% when considering the initial substrate surface position (the way the experimental values are recorded), and the increase in diameter is of 38%.

Using Figure 4.58, one can see a decrease in height of around 40%, a penetration of around 36%, and an increase in particle diameter of only 20%, which is a lot less than what could be expected, and is probably mostly due to the cut not being at the center of the particle, meaning that all these values are in reality higher at the center and thus closer to the simulation values.

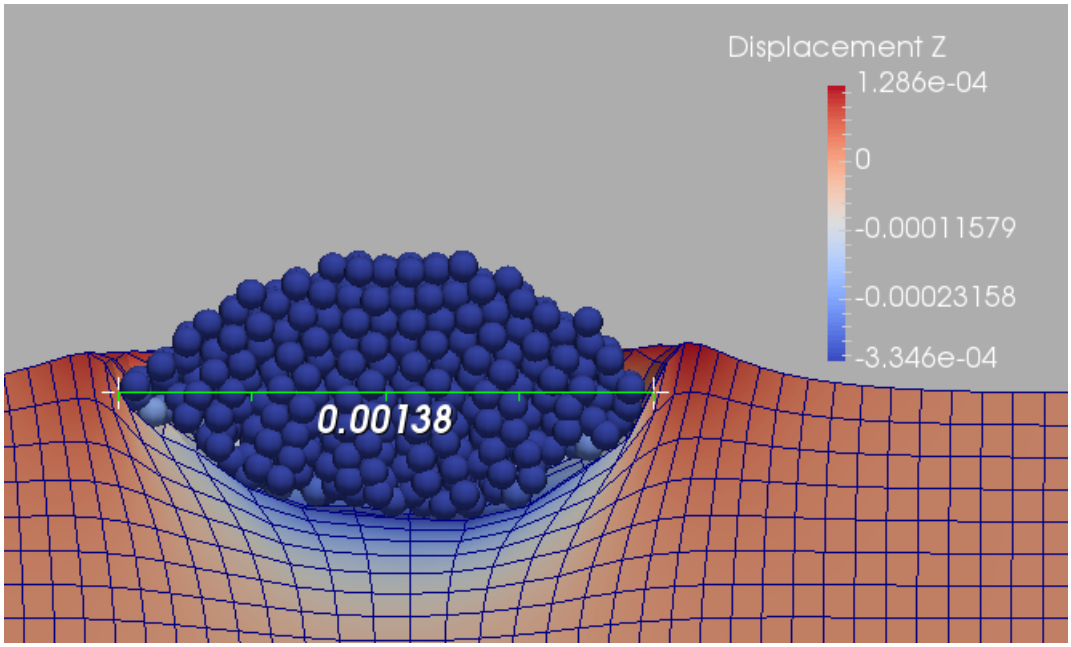

Figure 4.57: Cut view of the simulated copper on copper SPSS impact at 457 m.$^{-1}$ with vertical displacements

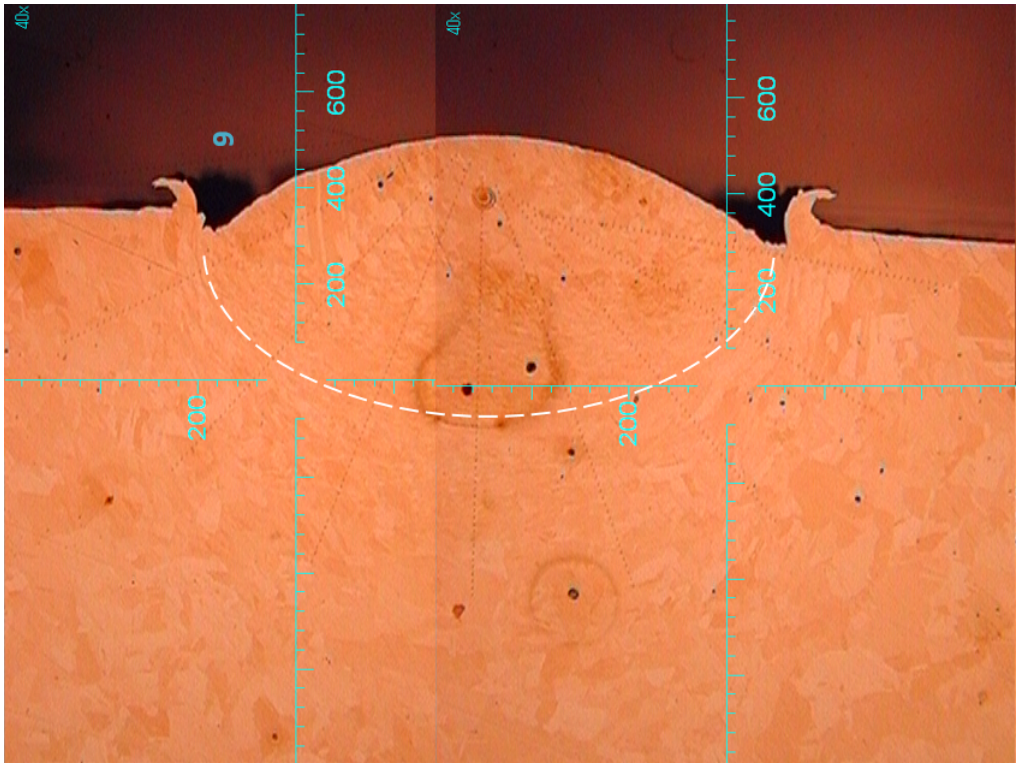

Figure 4.58: Cross-section view of the copper on copper SPSS impact at 457 m.$^{-1}$

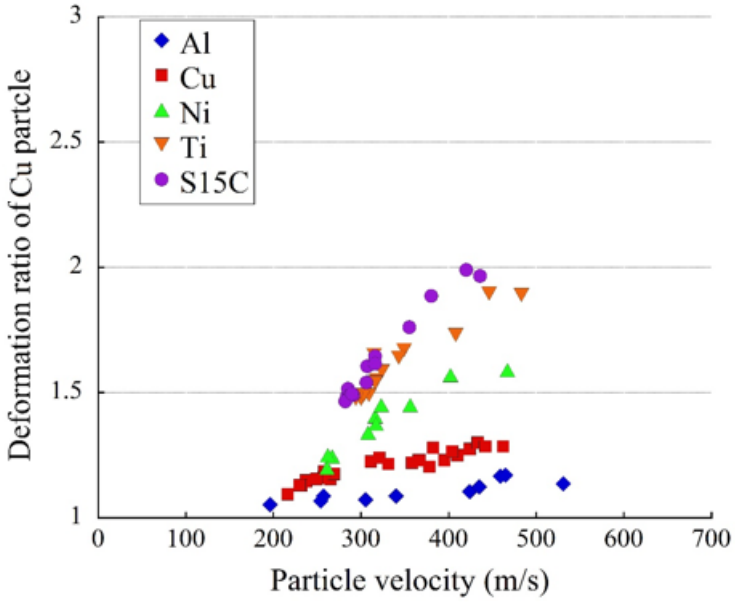

Figure 4.59: Deformation ratio of a 1 mm Cu particle on different substrates impacted by SPSS [ITO 16]

Once again, the overall shape and deformation values point to a similarity between experimental and numerical deformed shape, and the results are considered acceptable.

Remark: If the cross-section is moved away from the center in the simulation results, for example to match the experimental increase in diameter of 20%, one can find new values for height decrease and penetration respectively 44% and 30%. The mesh size used here gives however sudden variations as particular elements are taken out of the cross-section, but this method can prove useful on finer meshes to effectively compare experimental and simulated results. A finer mesh would also make a better representation of the jetting material, even though the need for it to get a better overall deformation is not clear.

4.6.3 Discussion on the results

In conclusion it is shown that the obtained shapes are similar, considering the uncertainties involved, be it the usual numerical 10% uncertainty or the expected experimental spread in obtained shapes which according to previous results from [ITO 16] can be as high as 10% to 15%, as showed in Figure 4.59 where the red points depict the deformation ratio of a copper particle impacted on a copper substrate by SPITS, results containing the samples studied. It can be seen that the spread in results is not negligible, especially around 400 $m.s^{-1}$ impacts. This would be even more observable if several impacts had been done at one same speed.

The difference between computational results and experimental results for the final shape of the particles can thus be considered within the range of current uncertainties, validating the model once more in terms of obtained deformations for these two cases.

The problem of the penetration value might be solved be using two different sets of parameters for the particle and the substrate, this time using approximates given by the hardness values found in [ITO 16], the particle being found to be initially harder than the substrate, probably due to the shaping process involved in getting the particles to the desired size. This could also

explain the need for the use of FE for the substrate, which give the mesh a different stiffness than an SPH mesh.

More work should thus be done, both experimentally with a more statistically relevant set of deformation data for each impact speed, and numerically in the definition of the differences in initial material parameters and influence of the choice of mesh size and numerical method.

4.7 Summary

The goal of these experimental measurements was twofold: to study the microstructural change in the particle for different impact speeds, and its link with adhesion; to get hardness variations across the samples and its link with grain size, to conclude on the necessity for a model including grain dynamics. These were performed on copper particles impacted on a copper substrate, at 230 and 457 $m.s^{-1}$.

In terms of change in microstructure, it is clear that the particle undergoes grain refinement, but not only near the interface. Near the interface however strain-free grain regions develop with higher impact speeds, most likely by recrystallization, possibly dynamic recrystallization and adiabatic shear banding. These regions are tens of micrometers thick and mostly situated in the highly sheared regions of the contact surface, which are on the sides. The link between these strain-free regions and local adhesion is however not clear and deserves more investigations. The link between local impact loading and grain refinement will be made thanks to future numerical results.

The hardness variation measurements made show that the particle and substrate undergo hardening, so grain refinement and hardening are most likely linked. It does however not show a local change near the interface, or then it is lost in the noise or lost in the indentation step. The strain-free regions seen in the EBSD measurements are however tens of microns thick, so some indentations must have fallen on it, but it does not seem the lead to a drastic change in hardness, be it hardening or softening. The impact simulations show a local drop in Yield Stress near the interface, which if we link Yield stress and hardness, is not seen in the hardness curves. However the simulation considers the case where the particle has not cooled down yet, so the link between simulated hardness variation and real sample hardness variation is not direct and a post-processing phase taking into account cooling should be used. Despite this, the dependence of hardness with grain size can be seen as low or inexistent, which concludes on the Johnson-Cook material law being sufficient for this type of simulations. The damage laws however might need some more tuning to get the same variations in material properties as in the experiments.

Chapter 5

Application of the model to experiments

In this short last chapter the methodology is described for using the model, as currently implemented in Europlexus, to study Cold Spray adhesion. Then comments are made on how to interpret the results, and how to link the model with experimental results from adhesion tests.

Contents

5.1 Using the model

5.1.1 Methodology

The methodology presented is the one used in this work to get simulated critical speeds for a defined set of adhesive parameters and material parameters. By doing several of these tests with different adhesive parameters, one can get their influence on the result and conclude on the likely value necessary to fit an experimental case.

Methodology for finding the critical speed:

Create an impact model and corresponding input file with the desired material laws, and give the adhesion law a surface energy, possibly a maximum stress, an initiation criterion, and possibly an erosion criterion.

Then a set of computations can be done for a range of impact speeds thought to include the critical speed (and the maximum speed if desired). The final computation time should be the same for all these simulations, and taken long enough to enable the distinction between a stuck particle and a rebounding particle to be clear (by looking at the variation in average particle speed for example, and the surface area under adhesion). The energies involved should be given sufficient time to oscillate down to a near equilibrium.

The different obtained final states can then be post-processed using a criterion for final adhesion, it currently being for at least one adhesive link to be active between two elements at final time. The variation of average particle speed across the different initial speeds at final computational time can also give a quick and easy visualization of what can be considered as the ”adhesion efficiency” commonly used in Cold Spray studies, albeit only for one particle in this case. This again might be tricky as this average velocity will never really fall down to an exact zero, and this gives absolutely no information as to the surface area under adhesion at final time.

This process can then be repeated with other adhesion parameters and criteria, or new material parameters. The combined results of all the computations can then be used to investigate the influence on the critical speed of all these parameters, especially the activation criterion developed for the material studied.

5.1.2 Creating an impact case

First the mesh should be generated, using Cast3m or other meshing tools. Europlexus having automatic SPH generation capabilities, the Cold Spray particle is usually generated in Europlexus, whereas the substrate, for which boundaries have to be defined, is usually meshed in Cast3m. An example of an Europlexus input file for the impact model is shown with comments in Appendix A.

An oblique impact could easily be simulated by changing the initial position of the particle relative to the substrate, enlarging the substrate, and giving the particle an initial speed along the desired impact direction.

A multiple impact case can also be easily defined by adding Cold Spray particles using the automatic SPH meshing tool of Europlexus, and defining an additional adhesive interaction between the newly created particle and the other parts of the model (particles and substrate). The adhesive interaction tool is indeed built to accept several declarations.

5.1.3 Extracting and visualizing the results

The information on the adhesive link, the energy dissipated... etc, is for now stored in the ".listing" file. An Excel file with a homemade code was used to read and extract these results and display them in the same manner as in 3.5.3.

The software Paraview was used to get animated sequences of the results in terms of deformations and variations of material properties with time.

5.2 Interpreting the results

Care should be taken in the choice of the final time, by making sure the impact is finished (the remaining vibrations are negligible). A good estimate is given by the variation of adhesive energy dissipated, which should come to a plateau at the end of the simulation as in the cylinder impact case in 3.5.1.2.

As mentioned previously, some work is still required during post-treatment of the results to translate them from numerical predictions to an actual engineering statement concerning the adhesion of the particle. Three points should be assessed:

- Translate the number of elements in adhesion at the end of computation in an physical surface area value. This value can then be compared to the particle total surface or the contact surface to conclude on final sticking. If only 1% of the contact surface is under adhesion, this should be considered insufficient for a real adhesion able to sustain the further loading conditions it will undergo in real conditions.
- A surface value criterion for the final area under adhesion should also be defined considering the bonding strength it induces. The adhesive stress must be considered. The question of its value is debatable and should be approximated using experiments described in the next section. The total strength criterion, required for the particle to be manipulated or processed without risk of breaking the bond, should also be evaluated.
- Once the area and hence strength required for a clear and realistic bonding are present, the problem of the remaining adhesive energy associated with these bonds should also be investigated. It could be for example that the whole adhesive surface remained unbroken at the end of computation, hence giving a high surface area and a high equivalent adhesive strength, while each bond has dissipated near to all its allocated adhesive energy. Due to the definition of the problem in terms of energy dissipation, this means that while the surface area and adhesive stress give a high bonding strength, this would quickly break under any sustained loading. The available energy could then be considered as reseted after the end of impact, or it could also be considered a criterion for the effective bonding of the particle.

5.3 Required experimental results

5.3.1 Adhesive parameters

Several useful experiments can be performed to get the parameters for the adhesive interaction. The cohesive stress and remaining adhesive energy after impact can for example be found with scratching and peeling tests, as in [GOL 12]. Indeed, using the force-displacement curve obtained with these experiments, one can approximate the energy under the curve as well

as the adhesive stress from the maximum force.

Another novel experiment done in Ogawa laboratory involves cutting by Focused Ion Beam a local piece of the interface of a cross-section of an impacted sample, such as the ones used in this work. A traction test is then performed in the FIB machine, and a traction curve is obtained. This way one can study the very local strength of the interface between the stuck particle and the substrate. The values found for the interface strength can then be used as input parameters for the adhesion model.

The parameters used for the adhesion model should in the end be justified by the following process: Mesh the adhesion experiments with the same mesh size as the impact computation, compute the experiments, and fit the parameters to have the same behavior as the traction or scratching tests. The values found can then be used for the impact simulations.

A parametric study to find the influence of a variation around these parameter values can then be performed to conclude on the sensibility of the whole system to the precision of the measurements.

5.3.2 Adhesion initiation criterion

The adhesion initiation criterion is probably the most novel tool developed during this thesis. Since the direct application of the model was in the context of Cold Sprayed metals, a specific criterion was developed, for metals, based on the detection of a loss in yield strength.
New criteria can however be easily implemented for other materials and other physical phenomena, such as a specific change in temperature, or contact pressure, or any other material variable available in Europlexus.
The model is thus highly adaptable to the study of adhesion of other materials for Cold Spray or other processes. New theories on physical phenomena inducing adhesion can thus easily be simulated and tested, and their validity can be assessed.
In the present case, the validity of the simple criterion of a loss of local yield stress was not fully investigated, and the idea was at first to link the yield stress loss parameter to experimental values found by hardness testing. These proved however not to show the behavior expected and could thus not be used in this manner. Consequently this criterion should be viewed with skepticism and should be improved or even changed.

The ideal case would then be to have defined experimental based values for the rest of the model, leaving only the activation criterion as subject to development and research.

5.3.3 Material parameters

One of the most important things to keep in mind is the influence of the choice of the material parameters. These should be investigated thoroughly, especially since the Cold Spray particles undergo different processing methods before being sprayed, and these processes all have more or less an influence on the initial material characteristics during spraying.

Hopkinson bar experiments are a good tool to get the material behavior at high strain rates and even as a function of temperature. They can however not reach the high strain rates achieved during a particle impact at 1000 $m.s^{-1}$. The limits of such models as the Johnson-Cook should be kept in mind and several researchers are actively looking to improve it. The use of other models, best suited for a given material, or with more available parameters should be actively considered when creating a new impact model.

The damage law parameters are maybe the most sensitive ones, not so much for the dynamics of the impact, but especially for the adhesive behavior when using criteria based on damage in the material. Fitting of these parameters to experimental results such as traction tests with fracture or shear banding tests should be considered.

5.4 Summary

The model created is on conclusion highly versatile and has a lot of potential as a tool for studies of adhesion in fast dynamics as in Cold Spray. The objective in this sense has been met. It requires however several groups of input parameters, each of which should be carefully considered and linked to experimental results as much as possible:

- The numerical parameters for the FE or SPH methods have a direct influence on the results. Care should be taken in performing convergence studies before using a set of parameters for a parametric set of computations. The influence of these parameters might also depend on the type of material law used: for example here adding a damage law and localization process reinforces the effect of the mesh size on the results. It would be for example useful to test the numerical parameters on simple models to try and reproduce traction test results.
- The material parameters, here for the Johnson-Cook law and the damage law, should be chosen carefully and linked to experiments made if possible on the exact materials used in the experimental impact tests.

Chapter 6

Conclusions

In this work, a novel adhesive interaction model has been developed and integrated in a computational model of the impact of a metallic particle on a metallic substrate as in Cold Spray.

This cohesive model and its implementation have been validated with benchmark tests, and shown to exhibit a novel behavior. This model uses a surface energy to define the local adhesive energy that can be dissipated by the adhesive stresses, as in a Griffith model. A limit can be put on these adhesive stresses to prevent them from getting too high (while keeping the adhesion active), as in a Dugdale-Barenblatt model, and it has been shown to have a direct effect on the dynamics of the rebound in the elastic and elasto-plastic dynamic simulations of impacts, which is a new result, as usually these adhesive impacts are studied in quasi-statics or at low speeds. Thus the rebound of the particle has been shown to depend on the cohesive model in fast dynamics.

The second result of this work is with the addition of physical criteria to the adhesion model:

- An activation criterion, which dictates when local adhesion can occur, based on variations in the material properties on both sides of the contact.
- An erosion criterion, which monitors the damage on each side of the contact, and breaks off the local adhesion when a given damage value is reached.

The activation criterion was here based on the presence of an adiabatic localization and a loss of local yield strength, which is seen as a sign of an adiabatic shear band, the main mechanism behind adhesion in Cold Spray for metals. Using this criterion proved to create a critical velocity for adhesion, just like in the real Cold Spray process, below which the particle does not have enough kinetic energy to start a localization at the interface and thus start the adhesion. This gives a simulated critical velocity based on a physical mechanism.

The erosion criterion, when used, put a limit for adhesion at high speeds. At these very high speeds, due to the localization process and the damage law used, the material is highly damaged and can no longer sustain adhesion, leading to a loss in adhesive surface and finally a rebound. This created a maximum speed for adhesion, just like in the real Cold Spray process, based on a physical mechanism.

In conclusion a numerical model for the simulation of fast impacts of particles with adhesion was thus created, exhibiting a Cold Spray-like behavior with a critical and a maximum speed, both based on physical mechanisms. This model can easily be used with other materials

like polymers or ceramics, and new adhesion criteria can be defined and tested for these materials.

The third result concerns experimental observations of the change in microstructure for impacts of 1 mm copper particles on a copper substrate with the Cold Spray-like SPITS system. It showed that recrystallization occurs at the interface and is probably linked to adhesion. The link between the grain refinement and the hardness variations was made and no clear effect was observed. The conclusion was that simulation of the grain dynamics on a mesoscale is not necessary, and the use of the Johnson-Cook macroscale material model was validated for the simulations.

Bibliography

[AJA 04] AJAJA J., GOLDBAUM D., CHROMIK R. R., YUE S., REZAEIAN A., IRISSOU E.
Mechanical Properties and Indentation Size Effect of Ti Cold Spray Coatings. *Journal of Materials*, , n° Imi, 2004, Page 981.

[ALA 54] ALAM M. N., BLACKMAN M., PASHLEY D. W.
High-Angle Kikuchi Patterns. *Proceedings of the Royal Society A: Mathematical, Physical and Engineering Sciences*, vol. 221, n° 1145, 1954, p. 224–242.

[ALK 98] ALKHIMOV A. P., KOSAREV V. F., PAPYRIN A. N.
Gas-dynamic spraying. An experimental study of the spraying process. *Journal of Applied Mechanics and Technical Physics*, vol. 39, n° 2, 1998, p. 318–323.

[AND 94] ANDRADE U., MEYERS M. A., VECCHIO K. S., CHOKSHI A. H.
Dynamic recrystallization in high-strain, high-strain-rate plastic deformation of copper. *Acta Metallurgica et Materialia*, vol. 42, n° 9, 1994, p. 3183–3195.

[ASS 03] ASSADI H., GÄRTNER F., STOLTENHOFF T., KREYE H.
Bonding mechanism in cold gas spraying. *Acta Materialia*, vol. 51, n° 15, 2003, p. 4379–4394.

[BEL 91] BELYTSCHKO T., NEAL M. O.
Contact-impact by the pinball algorithm with penalty and Lagrangian methods. *International Journal for Numerical Methods in Engineering*, vol. 31, n° 3, 1991, p. 547–572.

[BEL 00] BELYTSCHKO T., GUO Y., KAM LIU W., PING XIAO S.
A unified stability analysis of meshless particle methods. *International Journal for Numerical Methods in Engineering*, vol. 48, n° 9, 2000, p. 1359–1400, John Wiley {&} Sons, Ltd.

[BEL 13] BELYTSCHKO T., LIU W. K., MORAN B., ELKHODARY K.
Nonlinear Finite Elements for Continua and Structures. Wiley, 2013.

[BEN 90] BENSON D. J., HALLQUIST J. O.
A single surface contact algorithm for the post-buckling analysis of shell structures. *Computer Methods in Applied Mechanics and Engineering*, vol. 78, n° 2, 1990, p. 141–163.

[BOR 03] BORCHERS C., GARTNER F., STOLTENHOFF T., ASSADI H., KREYE H.
Microstructural and macroscopic properties of cold sprayed copper coatings. *Journal of Applied Physics*, vol. 93, n° 12, 2003, Page 10064, AIP Publishing.

[CAL 11] CALEYRON F.
Simulation numérique par la méthode SPH de fuites de fluide consécutives à la déchirure d'un réservoir sous impact. Thse de doctorat, oct 2011.

[CAL 13] CALEYRON F., COMBESCURE A., FAUCHER V., POTAPOV S.
SPH modeling of fluid-solid interaction for dynamic failure analysis of fluid-filled thin shells. *Journal of Fluids and Structures*, vol. 39, 2013, p. 126–153, Elsevier.

[CHA 99] CHANDLER H.
Hardness Testing, 2nd Edition. N° January 1999 ASM International, 1999.

[CHA 02] CHANDRA N., LI H., SHET C., GHONEM H.
Some issues in the application of cohesive zone models for metal-ceramic interfaces. *International Journal of Solids and Structures*, vol. 39, n° 10, 2002, p. 2827–2855.

[CHA 05] CHAMPAGNE V. K., HELFRITCH D., LEYMAN P., GRENDAHL S., KLOTZ B.
Interface Material Mixing Formed by the Deposition of Copper on Aluminum by Means of the Cold Spray Process. *Journal of Thermal Spray Technology*, vol. 14, n° 3, 2005, p. 330–334.

[CHA 07] CHAMPAGNE V. K.
The cold spray materials deposition process Fundamentals and applications. 2007.

[CHE 11] CHEN G., REN C., YANG X., JIN X., GUO T.
Finite element simulation of high-speed machining of titanium alloy (Ti-6Al-4V) based on ductile failure model. *International Journal of Advanced Manufacturing Technology*, vol. 56, n° 9-12, 2011, p. 1027–1038.

[DIN 92] DINGLEY D. J., RANDLE V.
Microtexture determination by electron back-scatter diffraction. *Journal of Materials Science*, vol. 27, n° 17, 1992, p. 4545–4566.

[GIN 77] GINGOLD R. A. M. J. J.
Smoothed particle hydrodynamics: theory and application to non-spherical stars. *Mon. Not. R. astr. Soc*, vol. 181, 1977.

[GOL 11a] GOLDBAUM D., AJAJA J., CHROMIK R. R., WONG W., YUE S., IRISSOU E., LEGOUX J. G.
Mechanical behavior of Ti cold spray coatings determined by a multi-scale indentation method. *Materials Science and Engineering A*, vol. 530, n° 1, 2011, p. 253–265, Elsevier B.V.

[GOL 11b] GOLDBAUM D., CHROMIK R., YUE S., IRISSOU E., LEGOUX J.-G.
Mechanical Property Mapping of Cold Sprayed Ti Splats and Coatings. *Journal of Thermal Spray Technology*, vol. 20, n° 3, 2011, p. 486–496.

[GOL 12] GOLDBAUM D., SHOCKLEY J. M., CHROMIK R. R., REZAEIAN A., YUE S., LEGOUX J. G., IRISSOU E.
The effect of deposition conditions on adhesion strength of Ti and Ti6Al4V cold spray splats. *Journal of Thermal Spray Technology*, vol. 21, n° March, 2012, p. 288–303.

[GRU 03] GRUJICIC M., SAYLOR J. R., BEASLEY D. E., DEROSSET W. S., HELFRITCH D.
Computational analysis of the interfacial bonding between feed-powder particles and the substrate in the cold-gas dynamic-spray process. *Applied Surface Science*, vol. 219, n° 3-4, 2003, p. 211–227.

[GRU 04] GRUJICIC M., ZHAO C. L., DEROSSET W. S., HELFRITCH D.
Adiabatic shear instability based mechanism for particles/substrate bonding in the cold-gas dynamic-spray process. *Materials {&} Design*, vol. 25, n° 8, 2004, p. 681–688.

[HAB 12] HABOUSSA D., ELGUEDJ T., LEBLÉ B., COMBESCURE A.
Failure mode transition at high rates of shear loading. *International Journal of fracture*, vol. 178, n° 1, 2012, p. 195–213, Springer.

[HAL 85] HALLQUIST J. O., GOUDREAU G. L., BENSON D. J.
Sliding interfaces with contact-impact in large-scale Lagrangian computations. *Computer Methods in Applied Mechanics and Engineering*, vol. 51, n° 1-3, 1985, p. 107–137.

[HER 11] HERMAN H., SAMPATH S., MCCUNE R.
Thermal Spray: Current Status and Future Trends. *MRS Bulletin*, vol. 25, n° 07, 2011, p. 17–25, Cambridge University Press.

[HOO 04] HOOPUTRA H., GESE H., DELL H., WERNER H.
A comprehensive failure model for crashworthiness simulation of aluminium extrusions. *International Journal of Crashworthiness*, vol. 9, n° 5, 2004, p. 449–464, WoodHead Publishing.

[HUG 12] HUGHES T. J. R.
The Finite Element Method: Linear Static and Dynamic Finite Element Analysis. 2012.

[HUM 04] HUMPHREYS F. J.
Characterisation of fine-scale microstructures by electron backscatter diffraction (EBSD). *Scripta Materialia*, vol. 51, n° 8, 2004, p. 771–776.

[IDE 03] IDELSOHN S. R., ONATE E., CALVALO N., DEL PIN F.
The meshless finite element method. *International Journal of Numerical Methods in Engineering*, vol. 58, 2003, p. 893–912, Wiley.

[ITO 16] ITOU K.
Thesis Kiyouhiro Itou. Thse de doctorat, Tohoku University, 2016.

[JAK 15] JAKUPI P., KEECH P. G., BARKER I., RAMAMURTHY S., JACKLIN R. L., SHOESMITH D. W., MOSER D. E.
Characterization of commercially cold sprayed copper coatings and determination of the effects of impacting copper powder velocities. *Journal of Nuclear Materials*, vol. 466, 2015, p. 1–11, Elsevier B.V.

[JOH 96] JOHNSON G. R. STRYCK R. A. B. S. R.
SPH for high velocity impact. *Computer methods in applied mechanics and engineering*, vol. 139, 1996, p. 347–373.

[JOH 02] JOHNSON G. R.
An improved generalized particle algorithm that includes boundaries and interfaces. *International journal for numerical methods in engineering*, vol. 53, 2002, p. 875–904.

[KAL 87] KALTHOFF J. F., WINKLER S.
Failure mode transition at high rates of loading. *Impact loading and dynamic behavior of materials*, vol. 1, 1987, p. 185–195.

[KAM 06] KAMAYA M., WILKINSON A. J., TITCHMARSH J. M.
Quantification of plastic strain of stainless steel and nickel alloy by electron backscatter diffraction. *Acta Materialia*, vol. 54, n° 2, 2006, p. 539–548.

[KIM 05] KIM H.-J., LEE C.-H., HWANG S.-Y.
Fabrication of WCCo coatings by cold spray deposition. *Surface and Coatings Technology*, vol. 191, n° 2-3, 2005, p. 335–340.

[KLI 05] KLINKOV S. V., KOSAREV V. F., REIN M.
Cold spray deposition: Significance of particle impact phenomena. *Aerospace Science and Technology*, vol. 9, n° 7, 2005, p. 582–591.

[LEC 09] LECONTE N.
Numerical modelling of the compression Hopkinson bar of ELSA. 2009.

[LEM 90] LEMAITRE J., CHABOCHE J.-L.
Mechanics of materials. Cambridge university press, 1990.

[LEM 06] LEMAITRE J., DESMORAT R.
Engineering Damage Mechanics. Springer, 2006.

[LI 07] LI W. Y., LIAO H., LI C. J., BANG H. S., CODDET C.
Numerical simulation of deformation behavior of Al particles impacting on Al substrate and effect of surface oxide films on interfacial bonding in cold spraying. *Applied Surface Science*, vol. 253, n° 11, 2007, p. 5084–5091.

[LI 09] LI W. Y., ZHANG C., LI C. J., LIAO H.
Modeling aspects of high velocity impact of particles in cold spraying by explicit finite element analysis. *Journal of Thermal Spray Technology*, vol. 18, n° December, 2009, p. 921–933.

[LI 10] LI W. Y., YIN S., WANG X. F.
Numerical investigations of the effect of oblique impact on particle deformation in cold spraying by the SPH method. *Applied Surface Science*, vol. 256, n° 2010, 2010, p. 3725–3734.

[LIN 07] LINS J. F. C., SANDIM H. R. Z., KESTENBACH H. J., RAABE D., VECCHIO K. S.
A microstructural investigation of adiabatic shear bands in an interstitial free steel. *Materials Science and Engineering A*, vol. 457, 2007, p. 205–218.

[LIU 05] LIU G., GU Y.
An Introduction to Meshfree Methods And Their Programming. Springer, 2005.

[LIU 10] LIU M. B., LIU G. R.
Smoothed Particle Hydrodynamics (SPH): an Overview and Recent Developments, vol. 17. 2010.

[LIU 15] LIU Y., WANG Y., SUO X., GONG Y., LI C.-J., LI H.
Impact-induced bonding and boundary amorphization of TiN ceramic particles during room temperature vacuum cold spray deposition. *Ceramics International*, , 2015, Elsevier.

[LUO 14] LUO X.-T., LI C.-X., SHANG F.-L., YANG G.-J., WANG Y.-Y., LI C.-J.
High velocity impact induced microstructure evolution during deposition of cold spray coatings: A review. *Surface and Coatings Technology*, vol. 254, 2014, p. 11–20, Elsevier B.V.

[MAB 08] MABROUKI T., GIRARDIN F., ASAD M., RIGAL J.-F.
Numerical and experimental study of dry cutting for an aeronautic aluminium alloy (A2024-T351). *International Journal of Machine Tools and Manufacture*, vol. 48, n° 11, 2008, p. 1187–1197.

[MAN 11] MANAP A., OKABE T., OGAWA K.
Computer simulation of cold sprayed deposition using smoothed particle hydrodynamics. *Procedia Engineering*, vol. 10, 2011, p. 1145–1150.

[MAU 06] MAUREL B., COMBESCURE A., POTAPOV S.
A robust SPH formulation for solids. *European Journal of Computational Mechanics*, vol. 15, n° 5, 2006, p. 495–512.

[MAU 08] MAUREL B., COMBESCURE A.
An SPH shell formulation for plasticity and fracture analysis in explicit dynamics. *International Journal for Numerical Methods in Engineering*, vol. 76, n° 7, 2008, p. 949–971.

[MAU 12] MAUREL B., COMBESCURE A., POTAPOV S.
A robust SPH formulation for solids. *European Journal of Computational Mechanics/Revue Européenne de Mécanique Numérique*, , 2012, Taylor & Francis Group.

[MEY 94] MEYER L. W., STASKEWITSCH E., BURBLIES A.
Adiabatic shear failure under biaxial dynamic compression/shear loading. *Mechanics of materials*, vol. 17, 1994, p. 203–214.

[MIK 15] MIKAMI Y., ODA K., KAMAYA M., MOCHIZUKI M.
Effect of reference point selection on microscopic stress measurement using EBSD. *Materials Science and Engineering: A*, vol. 647, 2015, p. 256–264, Elsevier.

[MIS 08] MISHRA A., MARTIN M., THADHANI N. N., KAD B. K., KENIK E. A., MEYERS M. A.
High-strain-rate response of ultra-fine-grained copper. *Acta Materialia*, vol. 56, n° 12, 2008, p. 2770–2783.

[MON 09] MONAGHAN J. J.
Smoothed particle hydrodynamics. *Reports on Progress in Physics*, vol. 68, n° 8, 2009, p. 1–34.

[OLI 11] OLIVER W. C., PHARR G. M.
Measurement of hardness and elastic modulus by instrumented indentation: Advances in understanding and refinements to methodology. *Journal of Materials Research*, vol. 19, n° 01, 2011, p. 3–20, Cambridge University Press.

[P. 01] P. G. J., J. M. J.
SPH elastic dynamics. *Computer methods in applied mechanics and engineering*, vol. 190, 2001, p. 6641–6662.

[PAP 07] PAPYRIN A. N., KOSAREV V. F., KLINKOV S., ALKHIMOV A. P., FOMIN V.
Cold Spray Technology. 2007.

[PRO 16] PROFIZI P., COMBESCURE A., OGAWA K.
SPH modeling of adhesion in fast dynamics : application to the Cold Spray process. *Comptes Rendus Mecanique*, , 2016.

[ROK 15] ROKNI M. R., WIDENER C. A., CRAWFORD G. A., WEST M. K.
An investigation into microstructure and mechanical properties of cold sprayed 7075 Al deposition. *Materials Science and Engineering A*, vol. 625, 2015, p. 19–27.

[SCH 09] SCHMIDT T., ASSADI H., GÄRTNER F., RICHTER H., STOLTENHOFF T., KREYE H., KLASSEN T.
From Particle Acceleration to Impact and Bonding in Cold Spraying. *Journal of Thermal Spray Technology*, vol. 18, n° 5-6, 2009, p. 794–808.

[SIM 14] SIMULIA D. S.
ABAQUS Analysis User's Manual, Volume III: Materials. *Providence, Stand*, , 2014.

[SUN 08] SUN J., GUO Y. B.
Material flow stress and failure in multiscale machining titanium alloy Ti-6Al-4V. *The International Journal of Advanced Manufacturing Technology*, vol. 41, n° 7-8, 2008, p. 651–659.

[TIL 06] TILLMANN W., VOGLI E.
Selecting Surface-treatment Technologies. *Modern Surface Technology*, , 2006, p. 1–10.

[VID 07] VIDAL Y., BONET J., HUERTA A.
Stabilized updated Lagrangian corrected SPH for explicit dynamic problems. *International Journal for Numerical Methods in Engineering*, vol. 69, n° 13, 2007, p. 2687–2710, Wiley and Sons.

[VIG 09] VIGNJEVIC R., CAMPBELL J.
Review of Development of the Smooth Particle Hydrodynamics (SPH) Method. HIERMAIER S., Ed., *Predictive Modeling of Dynamic Processes*, p. 367–396 Springer US, 2009.

[WIL 06] WILKINSON A. J., MEADEN G., DINGLEY D. J.
High-resolution elastic strain measurement from electron backscatter diffraction patterns: New levels of sensitivity. *Ultramicroscopy*, vol. 106, n° 4-5, 2006, p. 307–313.

[WRI 03] WRIGHT T., PERZYNA P.
Physics and Mathematics of Adiabatic Shear Bands. *Applied Mechanics Reviews*, vol. 56, n° 3, 2003, Page B41.

[XIE 14] XIE J.
Simulation of the Cold Spray Particle Deposition Process. *INSA de Lyon*, , n° English, 2014.

[XIE 15] XIE J., NÉLIAS D., WALTER-LE BERRE H., OGAWA K., ICHIKAWA Y.
Simulation of the Cold Spray Particle Deposition Process. *Journal of Tribology*, vol. 137, n° 4, 2015, Page 41101.

[XUE 08] XUE Q., BINGERT J. F., HENRIE B. L., GRAY G. T.
EBSD characterization of dynamic shear band regions in pre-shocked and as-received 304 stainless steels. *Materials Science and Engineering: A*, vol. 473, n° 1-2, 2008, p. 279–289.

[YIL 11] YILDIRIM B., MUFTU S., GOULDSTONE A.
Modeling of high velocity impact of spherical particles. *Wear*, vol. 270, n° 9-10, 2011, p. 703–713.

[YIL 14] YILDIRIM B., FUKANUMA H., ANDO T., GOULDSTONE A., MÜFTÜ S.
A Numerical Investigation Into Cold Spray Bonding Processes. *Journal of Tribology*, vol. 137, n° 1, 2014, Page 11102.

[YOD 10] YODA R., YOKOMAKU T., TSUJI N.
Plastic deformation and creep damage evaluations of type 316 austenitic stainless steels by EBSD. *Materials Characterization*, vol. 61, n° 10, 2010, p. 913–922, Elsevier Inc.

[ZOU 09] ZOU Y., QIN W., IRISSOU E., LEGOUX J. G., YUE S., SZPUNAR J. A.
Dynamic recrystallization in the particle/particle interfacial region of cold-sprayed nickel coating: Electron backscatter diffraction characterization. *Scripta Materialia*, vol. 61, n° 9, 2009, p. 899–902, Acta Materialia Inc.

[ZOU 10a] ZOU Y.
Microstructural Studies of Cold Sprayed Pure Nickel , Copper and Aluminum Coatings. , n° February, 2010.

[ZOU 10b] ZOU Y., GOLDBAUM D., SZPUNAR J. A., YUE S.
Microstructure and nanohardness of cold-sprayed coatings: Electron backscattered diffraction and nanoindentation studies. *Scripta Materialia*, vol. 62, n° 6, 2010, p. 395–398, Acta Materialia Inc.

Appendix A

The following part shows a typical input file used to describe the impact model for Europlexus.

```
******
! Name of the user
!
NAME OF THE SIMULATION - DESCRIPTION
!
! LAGC = Use Lagrangian method
LAGC
! TRID = three dimensions problem
TRID
! EROS = erosion for finite elements
EROS
! CROI = erosion of crossed elements
CROI
!
! get the Cast3m mesh
CASTEM FORM
! address of the Cast3m mesh
' /mesh.msh'
! name of the mesh object to load
mesh
!
! activate echo option
OPTI echo
!
! declare dimensioning of the problem
DIME
! Number of SPH elements
BILL 32880
! Number of cube (EF) elements
CUBE 100000
! Number of absorbing boundaries elements
CL3D 10000
! Number of "particle-structure" couples
NPEF 2
! Total number of nodes defining these
! "particle-structure" couples
NPTS 440811
! Maximum number of mesh points
NPOI 440811
! Number of degrees of freedom
NDDL 440811
TERM
!
! Parameters
! Impacting particle radius
%rays = 0.5e-3
! Initial distance from the substrate
%decal= 1e-6
! Sum of the two previous parameters
%haus = 0.501e-3
! Top of the impacting particle
%topZ = 1.001e-3
! Negative impacting particle radius
%minusRays = -0.5e-3
!
! SPH particle radius
%rayb = 40e-6
! SPH particle diameter
%diam = 80e-6
!
OPTI NOPR PMESH PLINK
!
! Affect element types to the cast3m geometry
GEOM
CUBE substrate
CL3D impe
TERM
!
! Geometrical complements
COMPLEMENT
! Creation of the SPH sphere
GBIL 1 RBIL %rayb RESE 0
INSI SPHE XC 0.0 YC 0.0 ZC %haus R %rays
!
```

```
! Declaration of the SPH parameters
CBILLE RAYON %rayb LINE 0.8 QUAD 4 RESEAU 0 VOISIN 50 RLIM 2
!
! Declaration of groups for output purposes
! Groups of elements
! Top layer of elements of the substrate
GROU 1 'TOPS' LECT substrate TERM COND ZB GT -160e-6
!
! Groups of nodes
NGRO 5
! Node at the top of the particle
'NTOP' LECT _gbil001 TERM
COND NEAR POIN 0 0 %topZ
! Node at the bottom of the particle
'NBOT' LECT _gbil001 TERM
COND NEAR POIN 0 0 %decal
! Node at the left of the particle
'NLEF' LECT _gbil001 TERM
COND NEAR POIN %minusRays 0 %haus
! Node at the right of the particle
'NRIG' LECT _gbil001 TERM
COND NEAR POIN %rays 0 %haus
! Node at the center of impact of the substrate
'NSUB' LECT substrate TERM
COND NEAR POIN 0 0 0
!
! Definition of the materials
MATE
!
! Johnson-Cook law parameters for ALUMINUM
! RO: density in kg.m-3
! YOUN: Young modulus in Pa
! NU: Poisson coefficient
VMJC RO 2710 YOUN 70.2e9 NU 0.3
! COA1: first J-C parameter (A) in Pa
! COA2: second J-C parameter (B) in Pa
! CLB1: J-C strain-rate parameter (C)
! CLB2: J-C strain hardening power (n)
! SRRF: reference strain-rate in s-1
COA1 60e6 COA2 140e6 CLB1 0.001 CLB2 0.183 SRRF 1
! Thermal properties
! RT: reference temperature in °K
! MT: melting temperature in °K
! COEM: J-C thermal coefficient (m)
THER RT 300.0 MT 916.0 COEM 0.895
! ITMP: Initial temperature in °K
! KK: heat capacity in J/kg/°K
! COET: plastic work to temperature conversion coefficient
ITMP 300.0 KK 904.0 COET 0.9
! Failure law definition
! RAND: Maximum initial random damage
FAIL RAND 0.0001
! SHEA: shear failure law definition
! KS: triaxiality coefficient
! EPRL: strain rate lower boundary
! EPRH: strain rate higher boundary
! SSRL: triaxiality lower boundary
! SSRH: triaxiality higher boundary
SHEA KS 0.3 EPRL 1e-3 EPRH 2.5e2 SSRL 1.42 SSRH 2.2
! SCAL, SCBL, SCCL, SCDL: polynomial lower curve coefficients
SCAL 4.391 SCBL -19.66 SCCL 29.38 SCDL -14.39
! SCAH, SCBH, SCCH, SCDH: polynomial higher curve coefficients
SCAH 0.0 SCBH 0.951 SCCH -2.848 SCDH 2.466
! Damage evolution law
! EPLS: Maximum plastic strain
EVOF EPLS 2.0
! DMAX: Maximum damage
DMAX 0.9
! NOFA: No failure at highest damage
NOFA
! Shear instability detection
! YSDP: Yield strength drop percentage
SSI YSDP 0.3
! Apply the material to the particle
LECT _gbil001 TERM
!
! Johnson-Cook for OHFC COPPER
VMJC RO 8960 YOUN 124e9 NU 0.34
COA1 160.e6 COA2 150e6 CLB1 0.025 CLB2 0.31 SRRF 1
THER RT 300.0 MT 1356.0 COEM 1.09
ITMP 300.0 KK 385.0 COET 0.9
FAIL RAND 0.0001
! JOCO: J-C ductile failure criterion
! COD1, COD2, COD3, COD4, COD5: J-C failure parameters
JOCO COD1 0.3 COD2 0.28 COD3 3.03 COD4 0.014 COD5 1.12
EVOF EPLS 2.0
DMAX 0.9
NOFA
SSI YSDP 0.05
```

```
LECT substrate TERM
!
! Absorbing boundaries (using values of the substrate)
! RO: density in kg.m^-3
! C=sqrt(YOUN/RO): sound speed
IMPE ABSO RO 8960 C 3720
LECT impe TERM
!
! Definition of the initial conditions
INIT
! Vertical impact speed definition
VITE 3 -311.0
LECT _gbil001 TERM
!
! Interactions and links definition
LINK
COUP
!========================= PINB ====
! Pinball method definition
!  PINB BODY DIAM %diam LECT _gbil001 TERM
! BODY DIAM %diam LECT tops TERM
!
!========================= GLIS ====
! Sliding surface method definition
GLIS 1 PGAP 1.e-12
MAIT LECT tops TERM
PESC LECT _gbil001 TERM
!
!========================= ADHW ====
! Adhesive interaction definition
! ADHW "X": Number of adhesive interactions
! WADH: Surface adhesive energy
ADHW 1 WADH 100000000.0
! TRIG: Adhesion activation criterion
! SSI: Shear stress instability
! TRIG SSI
! MAXD: Adhesion erosion criterion
! MAXD 0.5
! ADHS: Adhesive stress limit in Pa
! ADHS 400e6
GRO1 LECT _gbil001 TERM
GRO2 LECT tops TERM
!
! SPH method declaration
! SPHY "X": Number of SPH bodies or interactions
SPHY 1 BILL LECT _gbil001 TERM
!
! Definition of loads/boundary conditions
! CHARGE
! FACTO
! ABDI: Directional SPH absorbing boundaries !
ABDI 3
! 1 LECT absX TERM
! 2 LECT absY TERM
! 3 LECT botZ2 TERM
!
! Regions definition
REGION
! Give a name to the particle region and define
! internal variables and average speed as outputs
'bil_1' ECRG VMOY
LECT _gbil001 TERM
!
! Give a name to the substrate region and define
! internal variables as outputs
'substrate' ECRG
LECT substrate TERM
!
! Change the minimal precision of parameters
OPTI TION 2e-13
!
! Output definition on the screen
ECRIT ECRO TFRE 1.6e-7
NOPO
NOEL
!
! Definition of the Alice file for curves
FICH ALIC TEMP
'/local/users/pprofizi/Param/param.alt'
TFRE 3e-9
POIN LECT tous TERM
ELEM LECT tous TERM
!
! Definition of the Paraview output
FICHIER PVTK
TFRE 0.75e-7
GROUPE 2 OBJET _gbil001 TERM OBJET substrate TERM
PINB
VARI DEPL VITE ACCE ECRO
!
! Computation parameters
! PAS AUTOMATIQUE: Automatic time step
! CSTAB: stability coefficient
OPTI PAS AUTOMATIQUE CSTAB 0.05
! Options relative to the GLIS interaction
```

```
GLIS NORM ELEM GAP ELEM REPE
! TINI: Initial time in s
! TFIN: End time in s
! DTMI: Minimal time step in s
! NMAX: Maximum number of steps
CALCUL TINI 0.0 TFIN 3e-6 DTMI 1e-12
NMAX 24000000
!
! Post-treatment definition
!========== POST ==========
SUIT
Post-treatment (time curves from alice temps file)
ECHO
! Open the Alice file
OPNF 11
'/local/users/pprofizi/Param/param.alt'
RESU ALIC TEMP GARD PSCR
*
OPTI PRIN
SORT GRAP
PERFO
*
AXTE 1.0 'Time [s]'
*
! Curves definitions
COURBE 1 'WSYS'
WSYS
*
COURBE 2 'ECIN 1'
ECIN NORME
REGION 1
*
COURBE 3 'ECIN 2'
ECIN NORME
REGION 2
*
COURBE 4 'EINT 1'
EINT
REGION 1
*
COURBE 5 'EINT 2'
EINT
REGION 2
*
COURBE 6 'FCONT'
RESU NORME
REGION 1
*
COURBE 7 'FCONTZ'
RESU COMP 3
REGION 1
*
COURBE 8 'VZ'
VMOY COMP 3
REGION 1
*
COURBE 9 'VN'
VMOY NORME
REGION 1
*
COURBE 10 'DISTANCEVERT'
DISTANCE LECT NTOP NBOT TERM
*
COURBE 100 'MAXVERT'
MAX 10
*
COURBE 101 'DIV1'
DIV 10 100
*
COURBE 102 'MOIN'
SUBC 101 1.0
*
COURBE 12 'ECRASEMENTTIME'
MULC 102 -1.0
*
COURBE 11 'DISTANCEHORI'
DISTANCE LECT NLEF NRIG TERM
*
COURBE 110 'MINHORI'
MIN 11
*
COURBE 111 'DIV2'
DIV 11 110
*
COURBE 13 'ELONGATIONTIME'
SUBC 111 1.0
*
COURBE 14 'ENFONCEMENTTIME'
DEPL COMP 3
NOEU LECT NSUB TERM
*
*
SCOURBE 15 'LASTCOORX'
SAXE 1.0 'bouh' INIT LECT _gbil001 TERM
COOR COMP 1
*
SCOURBE 16 'INITCOORX'
T 0.0
SAXE 1.0 'bouh' INIT LECT _gbil001 TERM
COOR COMP 1
```

```
*
COURBE 17 'MAXINITX'
MAX 16
*
COURBE 18 'MININITX'
MIN 16
*
COURBE 19 'INITSIZE'
SUB 17 18
*
COURBE 20 'MAXFINALX'
MAX 15
*
COURBE 21 'MINFINALX'
MIN 15
*
COURBE 22 'FINALSIZE'
SUB 20 21
*
COURBE 23 'DIV3'
DIV 22 19
*
COURBE 24 'ELONGATION'
SUBC 23 1.0
*
COURBE 25 'DT'
DT1
*
! Curves to plot
TRAC 1 axes 1.0 'WSYS' ! System energy
TRAC 2 axes 1.0 'ECIN 1' ! Particle kinetic energy
TRAC 3 axes 1.0 'ECIN 2' ! Substrate kinetic energy
TRAC 4 axes 1.0 'EINT 1' ! Particle internal energy
TRAC 5 axes 1.0 'EINT 2' ! Substrate internal energy
TRAC 6 axes 1.0 'FCONT' ! Contact force
TRAC 7 axes 1.0 'FCONTZ'! Vertical component
TRAC 8 axes 1.0 'VZ' ! Vertical particle average speed
TRAC 9 axes 1.0 'VN' ! Norm of particle average speed
TRAC 12 axes 1.0 'ECRASEMENT' ! Crushing of the particle
TRAC 13 axes 1.0 'ELONGATIONMID' ! Enlarging of the particle
TRAC 14 axes 1.0 'ENFONCEMENT' ! Depth of the crater
TRAC 24 axes 1.0 'ELONGATIONMAX' ! Enlarging of the particle
TRAC 25 axes 1.0 'DT' ! Time step
*
! Curves to store
LIST 1 axes 1.0 'WSYS'
LIST 2 axes 1.0 'ECIN 1'
LIST 3 axes 1.0 'ECIN 2'
LIST 4 axes 1.0 'EINT 1'
LIST 5 axes 1.0 'EINT 2'
LIST 6 axes 1.0 'FCONT'
LIST 7 axes 1.0 'FCONTZ'
LIST 8 axes 1.0 'VZ'
LIST 9 axes 1.0 'VN'
LIST 12 axes 1.0 'ECRASEMENTTIME'
LIST 13 axes 1.0 'ELONGATIONTIME'
LIST 14 axes 1.0 'ENFONCEMENTTIME'
LIST 24 axes 1.0 'ELONGATIONMAX'
LIST 25 axes 1.0 'DT'
*
FIN
```

Appendix B

This part is a quick summary of all material parameters used in this work.

The general and Johnson-Cook parameters for copper and aluminum come from common values found in the literature, however, since the particles to be impacted had undergone a heat treatment, hardness tests results were used to fit the hardening parameters.

Shear failure parameters for aluminum are based on the online Abaqus Example Manual: "Progressive failure analysis of thin-wall aluminum extrusion under quasi-static and dynamic loads"
(https://things.maths.cam.ac.uk/computing/software/abaqus_docs/docs/v6.12/books/exa/default.htm).
These were however modified to ease fracture for quicker tests purposes.

The Johnson-Cook ductile failure parameter values for copper were first taken from [YIL 11] but again fitted to better represent the material used in the experiments.

The general and Johnson-Cook parameters for steel in the Hopkinson simulations are taken from the reference used to model the Hopkinson bar [LEC 09].
The general and Johnson-Cook parameters for Ti6Al4V were found on the ASM website and in [CHE 11] except for the second Johnson-Cook coefficient for strain-hardening, which is changed to fit the plastic loading part of the experimental curve in [MEY 94].
The Johnson-Cook ductile failure parameter values for Ti6Al4V are found in [CHE 11, SUN 08]. The second parameter, for strain-hardening, is once again changed to fit more or less the localization strain from the experimental curve in [MEY 94].

For all materials an adiabatic heating of 90% of plastic work is used (inelastic heat fraction), except for the steel in the Hopkinson bar simulations (same value as in the reference).

A maximum initial random damage of $1e^{-3}$ is put for all materials with damage (based on the study on the influence of initial random damage in 3.3.2.1).

For damage evolution, $\varepsilon^p{}_{max} = 2.0$ is the chosen maximum plastic strain, where maximum damage occurs.

Table 6.1: Material properties for aluminum

Properties	Parameter	Value	Unit
General	Density, ρ	2710	$kg.m^{-3}$
	Specific heat, k	904	$J.kg^{-1}.K^{-1}$
	Melting temperature, T_{melt}	916	K
	Inelastic heat fraction	0.9	
Elastic	Elastic modulus	70.9	GPa
	Poisson's ratio	0.3	
Plastic (Johnson-Cook plasticity model)	A, B, C, N, M	148.4, 345.5, 0.001, 0.183, 0.895	MPa, MPa
	Ref. strain rate, $\dot{\varepsilon}^{p}_{ref}$	1	s^{-1}
	Ref. temperature, T_{ref}	300	K
Shear Failure	K_S, θ^{+}_{S}, θ^{-}_{S}	0.3, 2.2, 1.42	
	$\dot{\varepsilon}^{+}_{S}$, $\dot{\varepsilon}^{-}_{S}$	250, 0.001	s^{-1}
	A^{+}, B^{+}, C^{+}, D^{+}	0.0, 0.951, -2.848, 2.466	
	A^{-}, B^{-}, C^{-}, D^{-}	4.391, -19.66, 29.38, -14.39	
Damage evolution	Maximum Initial Damage	0.001	
	Plastic strain at failure	2.0	

Table 6.2: Material properties for copper

Properties	Parameter	Value	Unit
General	Density, ρ	8960	$kg.m^{-3}$
	Specific heat, k	1356	$J.kg^{-1}.K^{-1}$
	Melting temperature, T_{melt}	385	K
	Inelastic heat fraction	0.9	
Elastic	Elastic modulus	124	GPa
	Poisson's ratio	0.34	
Plastic (Johnson-Cook plasticity model)	A, B, C, N, M	90, 292, 0.025, 0.31, 1.09	MPa, MPa
	Ref. strain rate, $\dot{\varepsilon}^{p}_{ref}$	1	s^{-1}
	Ref. temperature, T_{ref}	300	K
Ductile Failure (Johnson-Cook failure model)	d_1, d_2, d_3, d_4, d_5	0.3, 0.28, 3.03, 0.014, 1.12	
Damage evolution	Maximum Initial Damage	0.001	
	Plastic strain at failure	2.0	

Table 6.3: Material properties for steel

Properties	Parameter	Value	Unit
General	Density, ρ	7800	$kg.m^{-3}$
	Specific heat, k	480	$J.kg^{-1}.K^{-1}$
	Melting temperature, T_{melt}	1800	K
	Inelastic heat fraction	0.8	
Elastic	Elastic modulus	200	GPa
	Poisson's ratio	0.3	
Plastic (Johnson-Cook plasticity model)	A, B, C, N, M	266, 229, 0.0294, 0.3, 1.0	MPa, MPa
	Ref. strain rate, $\dot{\varepsilon}^{p}_{ref}$	1	s^{-1}
	Ref. temperature, T_{ref}	293.15	K

Table 6.4: Material properties for Ti6Al4V

Properties	Parameter	Value	Unit
General	Density, ρ	4430	$kg.m^{-3}$
	Specific heat, k	526.3	$J.kg^{-1}.K^{-1}$
	Melting temperature, T_{melt}	1604	K
	Inelastic heat fraction	0.9	
Elastic	Elastic modulus	113.8	GPa
	Poisson's ratio	0.342	
Plastic (Johnson-Cook plasticity model)	A, B, C, N, M	860, 900, 0.035, 0.47, 1.0	MPa, MPa
	Ref. strain rate, $\dot{\varepsilon}^{p}_{ref}$	1	s^{-1}
	Ref. temperature, T_{ref}	300	K
Ductile Failure (Johnson-Cook failure model)	d_1, d_2, d_3, d_4, d_5	-0.09, 0.45, -0.5, 0.014, 3.87	
Damage evolution	Maximum Initial Damage	0.001	
	Plastic strain at failure	2.0	